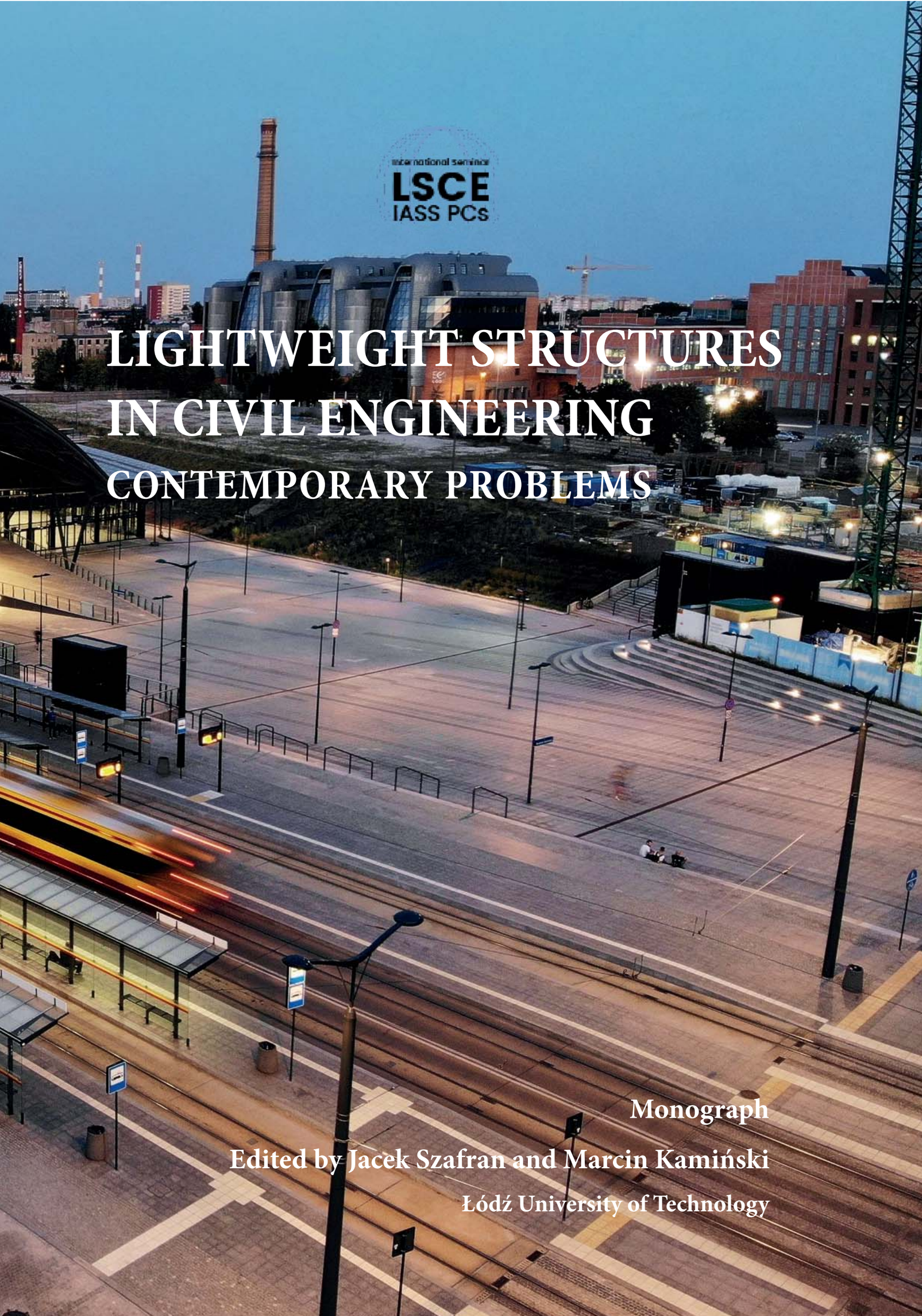

LIGHTWEIGHT STRUCTURES IN CIVIL ENGINEERING

CONTEMPORARY PROBLEMS

Monograph

Edited by Jacek Szafran and Marcin Kamiński

Łódź University of Technology

LIGHTWEIGHT STRUCTURES IN CIVIL ENGINEERING

CONTEMPORARY PROBLEMS

Monograph

Editors:
Jacek Szafran and Marcin Kamiński

Łódź University of Technology
Łódź 2022

All the papers were rewieved by minimum two members os Scientific Committee. The collected opinions were delivered to authors. Finally corrected all papers were accepted for printing. All papers were reformatted by editors. Additionally, minor changes have been made where obvious errors, faults and misprints were detected. The authors warrant that the papers are their original works and have been never published in their present form. The authors have accepted the full responsibility for the scientific content and opinions expressedin their papers.

Cover design: Ewelina Kubacka

Technical editing and typesetting: Tymoteusz Konieczny

ISBN 978-83-66741-59-1

Łódź University of Technology Press does not take responsibility
for the content and editing of this publication.

Łódź University of Technology Press
93-005 Łódź, 223 Wólczańska St.
E-mail: zamowienia@info.p.lodz.pl
www.wydawnictwo.p.lodz.pl

DOI 10.34658/9788366741591

Edition 50 copies
Printing and bookbinding: Quick-Druk, 90-562 Łódź, Łąkowa 11

TABLE OF CONTENTS

PAPERS PRESENTED ON LSCE 2021

PAPERS PRESENTED ON LSCE 2020

LIGHTWEIGHT STRUCTURES in CIVIL ENGINEERING
CONTEMPORARY PROBLEMS
Monograph from Scientific Seminar
Organized by Polish Chapters of
International Association for Shell and Spatial Structures
Łódź University of Technology
Faculty of Civil Engineering, Architecture
and Environmental Engineering
XXVII LSCE
Łódź, 2nd – 3rd of December 2021

FINITE ELEMENT METHOD SCAFFOLDINGS MODELLING BASED ON EXPERIMENTAL TESTS

E. Błazik-Borowa [1] **A. Misztela** [2] **M. Pieńko** [3] **A. Robak** [4]
[1] Professor, Faculty of Civil Engineering and Architecture, Lublin University of Technology, POLAND, *e.blazik@pollub.pl*
[2] PhD Eng., Faculty of Civil Engineering and Architecture, Lublin University of Technology, POLAND, *m.pienko@pollub.pl*
[3] PhD Eng., Faculty of Civil Engineering and Architecture, Lublin University of Technology, POLAND, *a.robak@pollub.pl*

ABSTRACT: The aim of the paper is to present the methods of FEM scaffolding model building based on laboratory test results. Scaffolds consist of various components. Stands, transoms, ledgers and braces are usually modelled as frame elements using geometric data and material properties. Decks are structures of complex geometry and their models require simplifications calibrated on the basis of scaffolding element horizontal stiffness tests. The flexibility of stand-ledger joints is modelled following laboratory tests of the nodes subject to moments acting on two planes. The numerical model of the entire scaffold must be then verified by means of a global test examining the behaviour of the entire structure resulting from the application of a set of horizontal and vertical forces. Each simplification applied must ensure that the results obtained in the calculations guarantee the safe use of the structure. On the other hand, the differences between the results of calculations and laboratory tests are mostly due to the said simplifications.

Keywords: scaffolding, numerical simulation, finite element method, global test.

1. INTRODUCTION

The finite element method has been developed since 1940s. One of the first papers in this field is by Hrennikoff (1941). The greatest development of FEM took place in the 1960/70s (e.g. thanks to Wilson and Clough 1963, Zienkiewicz and Cheung 1967, Aziz 1972). As far as static analyses with small strains are concerned, it seems that almost everything has already been done. Nevertheless, the modelling of more complex objects is often encumbered with problems. These are, e.g., limitations of software, the level of task complexity, the occurrence of peculiarities, etc. In nonlinear calculations performed by means of various software, it is difficult or even impossible to find the equilibrium path after passing the maximum. In this light, it turns out that, although the finite element method is an accomplished tool, using it requires knowledge and the ability to model objects and, subsequently, verification of the obtained results. The verification can consist in assessing the correctness of the behaviour of simple structures under the influence of a simple load system or on the basis of laboratory tests. Still, one should also take a critical approach towards laboratory tests, as test stands, methods and samples may be defective or may have features that are difficult to take into account in computer simulation. The said features may result from an inaccurate in the completion of test stands, e.g. the implementation of an articulated support in a laboratory is difficult and one

should bear in mind that differences between the boundary conditions of the numerical model and during laboratory tests may occur. The paper presents the main elements of the scaffold modelling process. An emphasis is placed on the modelling of the joint flexibility and horizontal stiffness of platforms in modular scaffolds, and the methods presented can be used in engineering practice. The paper also discusses the differences in the approach to the verification of models that are used for the purposes of research and design. The analysis uses the example of the ROTAX system of Altrad Mostostal in Siedlce. The presented computer simulations were conducted by means of Autodesk Simulation Multiphysics 2013 (called in the paper ASM 2013).

2. THE DESCRIPTION OF SCAFFOLDS

In the process of scaffolding system development and non-standard engineering solution design, accurate nonlinear static-strength analyses are required (Figure 1). Scaffoldings are assembled from components with different levels of geometry complexity. Stands, transoms, ledgers and bracings can be modelled with the use of frame elements. It is much more difficult to model decks which are usually stiffened with profiles of complex geometry and their surfaces are made of a perforated sheet. Another problem is the modelling of the joints between elements. Since a scaffold must be assembled quickly and safely, joints are also adapted to this task and, therefore, cannot be clearly classified as articulated or rigid. In addition, joints of scaffolding components allow for the occurrence of clearances and cause imperfections. Such a number of conditions can lead to differences between the behaviour of an actual structure and its numerical model, which, in turn, may result in a scaffold failure. For this reason, a procedure for building numerical scaffolding models has been developed, which consists of the following stages:

– laboratory tests of the material properties of scaffolding components,
– laboratory tests of the load-bearing capacity, stiffness or flexibility of individual components,
– laboratory tests of the load-bearing capacity of the scaffold with a predefined configuration, known as a global test,
– development of a numerical model, calibrated on the basis of the component laboratory test results and verified by means of the global test.

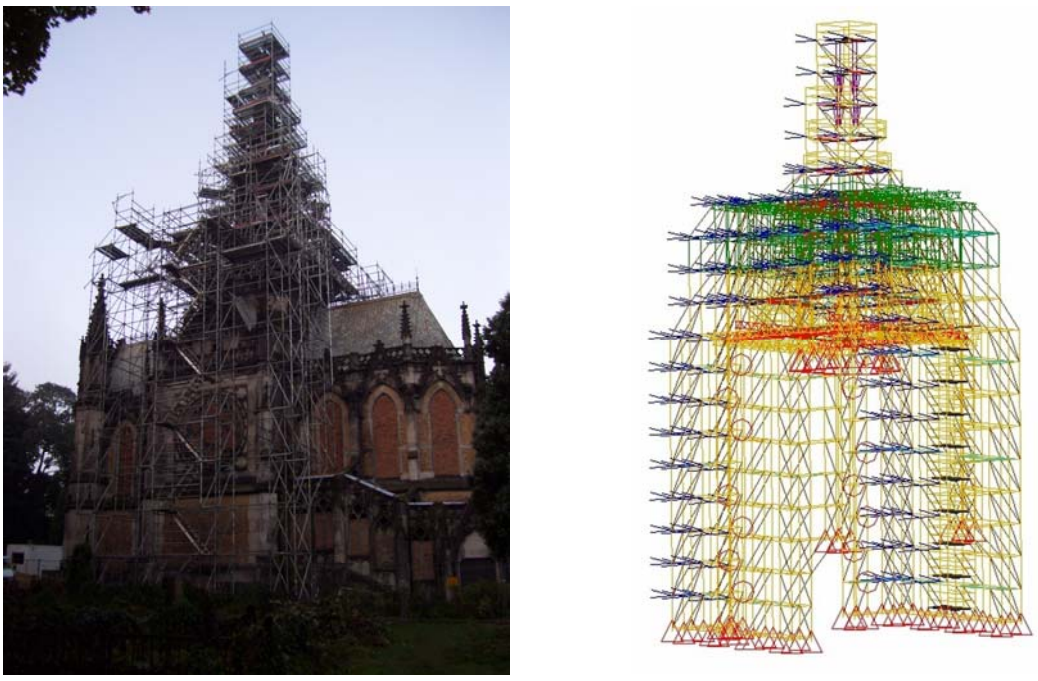

a) b)

Fig. 1. The scaffolding around the Scheibler Chapel in Łódź: a) photo, b) numerical model.

The methodology for carrying out laboratory tests, assumption of loads and part of the boundary conditions in the calculations are adopted on the basis of standards: EN 12810-1, EN 12810-2, EN 12811-1, EN 12811-3. The final numerical model constitutes the basis for nonlinear numerical analyses of typical scaffolds, the description of which is included in the technical documentation of the scaffolds and which authorises users to assemble such scaffolds without additional calculations and designs.

3. NUMERICAL MODELS OF SCAFFOLDING COMPONENTS

3.1. Laboratory tests and numerical models of scaffolding joints

In a modular scaffold, one finds rosettes with holes for attaching ledgers, mounted on a stand pipe. The geometry of such a joint is very complex – is characterised by clearances and friction. On the basis of laboratory tests of joints, force-displacement relationships for shearing and normal forces, as well as moment-rotation angle relationships for bending and torsional moments can be obtained. Some examples of test stands for joints examination are shown in Figure 2a (Pienko 2019) and Figure 3 (Błazik-Borowa et al. 2017). On the basis of the moment-rotation relationship, the stiffness of a connection is determined, which is then classified as rigid, flexible or pinned. Table 1 summarizes the test results for the same joint using three different test stands: two at the Lublin University of Technology (LUT) and one at the Institute of Mechanised Construction and Rock Mining (IMBiGS). In addition, four methods of determining stiffness are given for one of the test stands. As demonstrated, the discrepancies are large, therefore the calculations of a completed scaffold should be preceded by a sensitivity analysis of the numerical simulation results to individual parameters, as presented in Section 4.2. Furthermore, important information with regard to further analyses is that the values of the stiffness $k\varphi$, which are used in the final model, are smaller than the average values, and are determined from the following formula (EN 12811-3):

$$k_{\varphi} = \kappa(v_c)\cdot\bar{c} = \kappa(v_c)\frac{n}{\sum_{i=1}^{n}\frac{1}{c_i}}, \tag{1}$$

where: c_i – the result of the i-th stiffness measurement, $\kappa(v_c)$ – coefficient depending on the variation coefficient:

$$v_c = \frac{\sigma_c}{\bar{c}}, \tag{2}$$

$\sigma_c^2 = \frac{1}{n}\sum_{i=1}^{n}(c_i - \bar{c})^2$ – the standard deviation. (3)

The method of modelling joints depends on the features of the available software. Joint flexibility can be taken into account by means of changes in global stiffness matrices. This flexibility consideration method requires that the program have such a functionality. This approach does not allow for the control of joint effort. Therefore, in this paper the method consisting in the insertion of transition elements between nodes and components is used, described by Blazik-Borowa et al. (2017). Geometric and material parameters are selected to reflect joint flexibility in the vertical and horizontal planes.

With regard to the material of these elements, an elastic-plastic model with strengthening is used to describe the relationship between strains and stresses. The geometric and material parameters are selected to reflect the joint bending stiffness in the vertical plane ($k_{\varphi y}$ = 31.18kNm/rad), the joint bending stiffness in the

horizontal plane (kφz=12.80kNm/rad),and the load-bearing capacity expressed as the bending moment with respect to the horizontal (Mycr=0.8833kNm) and vertical (Mzcr=0.1711kNm) axes.

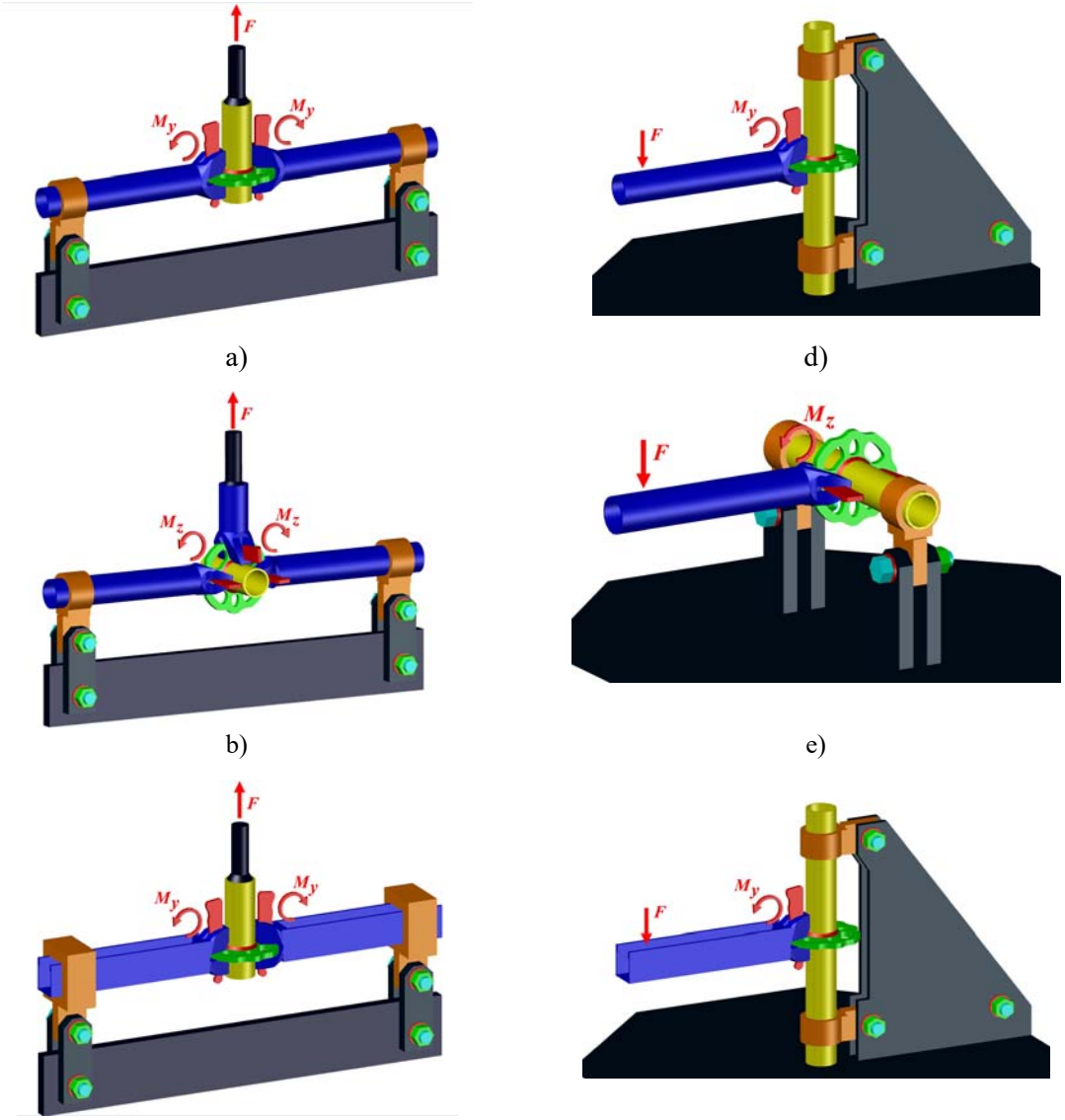

Fig. 2. The schemes of laboratory stands for testing the load bearing capacity and stiffness of joints when rotated about the horizontal axis *y* (a, c, d, f) and vertical axis *z* (b, e): a, b and c – LUT (Pieńko (2019)), d, e and f – IMBiGS (Misztela (2016)).

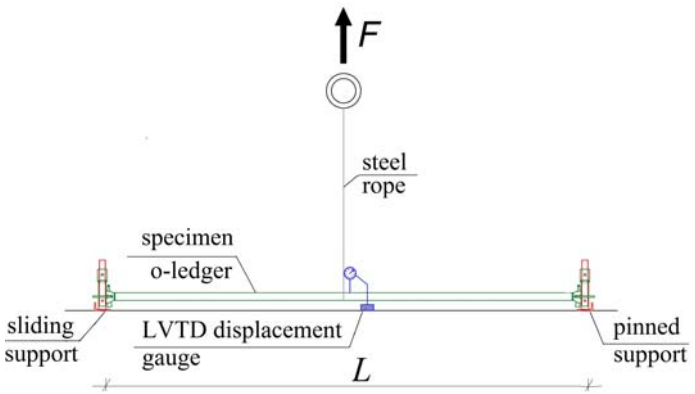

Fig. 3. The scheme of the laboratory stand for testing the load-bearing capacity of a ledger and the stiffness of joints when rotated in respect to the horizontal axis *y* (Błazik-Borowa et al. (2017)).

Tab. 1. The values of the joint stiffness in the vertical plane (action of moment My) obtained by means of various procedures.

Source, Figure	Method	Stiffness $k_{\varphi y}$ [kNm/rad]	
Pieńko (2019), Figure 2a	one linear function - loading the joint	33.74	
	two linear functions based on laboratory measurement results	φ=0.0-0.015 [rad]	φ=0.015-0.035 [rad]
		37.64	20.28φ+0.26
	one linear function - unloading the joint	53.42	
	the condition of equal fields on the graph with the results of laboratory measurements	33.46	
Misztela (2016), Figure 2d	IMBIGS – testing of the stand and o-ledger joint	31.18	
Misztela (2016), Figure 2f	IMBIGS – testing of the stand and u-ledger joint	78.18	
Błazik-Borowa et al. (2017) Figure 3	on the basis of test of the deflection of the o-ledger	34.86	

The algorithm for determining geometric characteristics and material properties includes the following stages:

I. Determination of the moments of inertia regards to:

- vertical axis y

$$J_y = \frac{k_{\varphi y} l}{E}, \tag{4}$$

- horizontal axis z

$$J_z = \frac{k_{\varphi z} l}{E}, \tag{5}$$

where: E=2.05·10^8 kPa – Young's modulus, l=0.05m – the length of the element which models of joint stiffness.

II. Determining geometric parameters of the cross-section based on the information about the moments of inertia J_y and J_z and, optionally, the condition described by the formula:

$$f_y = \frac{M_{ycr}}{W_y} = \frac{M_{zcr}}{W_z}, \tag{6}$$

where: f_y – the yield strength, W_y and W_z – section modulus.

Tab. 2. Calculation of geometric parameters and material properties for the transition element.

Stage	Transition element with a rectangular cross-section with dimensions $b\times h$	A transition element with a rectangular pipe cross-section with dimensions $b\times h$ and thickness g
Average values from the paper of Misztela (2016):	$k_{\varphi y,avr}$=48.34kNm/rad, $k_{\varphi z,avr}$=17.63kNm/rad; $M_{ycr,avr}$=1.4839kNm; $M_{zcr,avr}$=0.5663kNm	
Data to calculation from the paper of Misztela (2016):	$k_{\varphi y}$=31.18kNm/rad, $k_{\varphi z}$=12.80kNm/rad; M_{ycr}=0.8833kNm; M_{zcr}=0.1711kNm;	
Other data:	$E=2.05\cdot 10^8$ kPa; l=0.05m; m=0.53kg	
I	$J_y=\frac{k_{\varphi y}l}{E}=\frac{31.18\text{kNm/rad}\cdot 0.05\text{m}}{2\cdot 10^8\text{kPa}}=76.0488\cdot 10^{-10}\text{m}^4$ $J_z=\frac{k_{\varphi z}l}{E}=\frac{12.80\text{kNm/rad}\cdot 0.05\text{m}}{2\cdot 10^8\text{kPa}}=31.2195\cdot 10^{-10}\text{m}^4$	
II	$\begin{cases}J_y=\frac{b\cdot h^3}{12}\\ J_z=\frac{b^3\cdot h}{12}\end{cases}\Rightarrow b,h$ $\begin{cases}76.0488\cdot 10^{-10}\text{m}^4=\frac{b\cdot h^3}{12}\\ 31.2195\cdot 10^{-10}\text{m}^4=\frac{b^3\cdot h}{12}\end{cases}$ **b=0.01245m, h=0.01943m**	$\begin{cases}J_y=\frac{b\cdot h^3}{12}-\frac{(b-2g)\cdot(h-2g)^3}{12}\\ J_z=\frac{b^3\cdot h}{12}-\frac{(b-2g)^3\cdot(h-2g)}{12}\\ \frac{M_{ycr}}{W_y}=\frac{M_{zcr}}{W_z}\end{cases}\Rightarrow b,h,g$ $\begin{cases}76.0488\cdot 10^{-10}\text{m}^4=\frac{b\cdot h^3}{12}-\frac{(b-2g)\cdot(h-2g)^3}{12}\\ 31.2195\cdot 10^{-10}\text{m}^4=\frac{b^3\cdot h}{12}-\frac{(b-2g)^3\cdot(h-2g)}{12}\\ \frac{0.5h\cdot 0.8833\text{kNm}}{76.0488\cdot 10^{-10}\text{m}^4}=\frac{0.5b\cdot 0.1711\text{kNm}}{31.2195\cdot 10^{-10}\text{m}^4}\end{cases}$ **There is no physically justified solution**
III	$W_y=\frac{J_y}{0.5h}=$ $=\frac{76.0488\cdot 10^{-10}\text{m}^4}{0.5\cdot 0.01943\text{m}}=$ $=78.2926\cdot 10^{-8}\text{m}^3$ $f_{yz}=\frac{M_{ycr}}{W_y}=$ $=\frac{0.8833\text{kNm}}{78.2926\cdot 10^{-8}\text{m}^3}$ **f_{yz}=1.1282·10^{6}kPa** $\rho_z=\frac{m}{bhl}=$ $=\frac{0.53\text{kg}}{0.01245\text{m}\cdot 0.01943\text{m}\cdot 0.05\text{m}}$ **ρz=44.02t/m^3**	

III. Determining material properties

– surrogate yield strength

$$f_{yz} = \frac{M_{ycr}}{W_y}, \tag{7}$$

– surrogate mass density

$$\rho_z = \frac{m}{A}, \tag{8}$$

where: m – mass of the joint part replaced by a transition element, A – cross-section area of the transition element. The equations (5)÷(8) require the assumption of a type of cross-section. The cross-section type depends primarily on how many unknowns one can determine on the basis of the set of the equations from 2nd stage, and whether the solution of the non-linear set of equations is justified by physical conditions, e.g. whether a dimension does not obtain a negative value. The set of equations is non-linear and, despite the fact that there are several solutions, they may not be applicable. Therefore, the cross-section can be described with three parameters, but sometimes one must abandon one parameter. Table 2 summarizes the formulas and calculations for two cross-sections: a rectangle and a rectangular pipe. The results in the left column of Table 2 were used in Section 4 as master data for the numerical model to be used to simulate a global test.

In Table 2, in the right-hand column, three equations were used to determine the dimensions of the cross-section. However, a very low value of the thickness g was obtained, which could lead to numerical errors due to rounding. The results on the left side are closer to the values consistent with the physical conditions, but in this case the limit bending moment M_{ycr} is correctly determined, while the other limit bending moment M_{zcr} is not correct. Therefore, during the calculations, it is necessary to make sure that the value M_{zcr} is not exceeded.

3.2. Laboratory tests and a numerical model of horizontal stiffness for platforms

Scaffold platforms are formed by a set of decks of complex geometry. The level of simplification applied in the model depends on the purpose of the calculations performed (comp. Błazik-Borowa and Robak 2017). In the case where the load-bearing capacity of a single deck subject to vertical loads is determined, tests or calculations can be performed, but if computer simulations are selected, the model must quite accurately represent the geometry of the plate perforation and of the other elements. Such a model is shown in Figure 4. The intermediate model (Figure 5), in which the deck is replaced with a set of frame and shell elements, can be used as a deck model in calculations aimed at an accurate determination of the manner in which the load is transferred from the platforms to the other scaffolding components. This model is used in the case of a modular scaffold with complex geometry or with unusual loads.

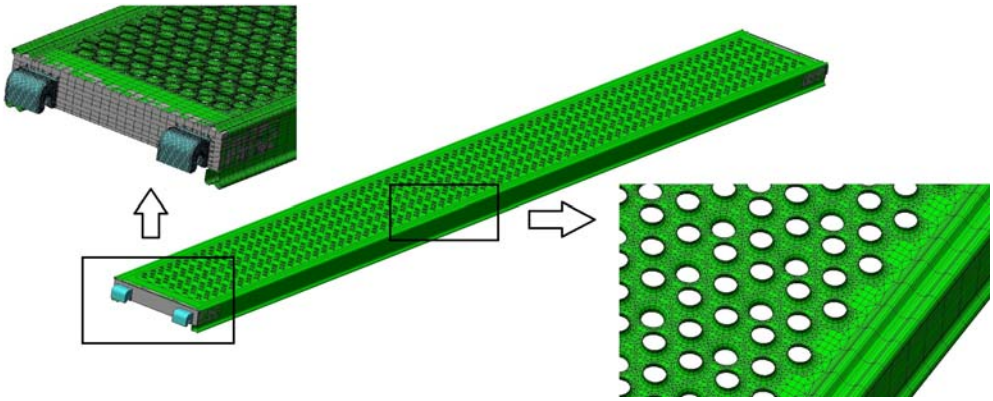

Fig. 4. The shell model of the deck.

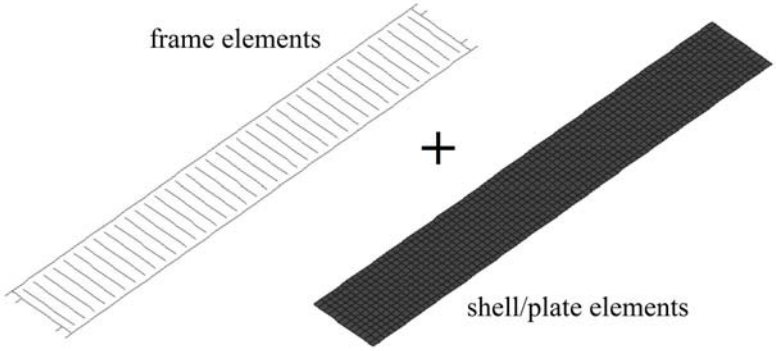

Fig. 5. The shell-frame model of the deck.

a) b)

Fig. 6. Test stands for (Misztela (2020)): a) platforms with a perpendicular load; b) platforms with a parallel load.

In the case of modelling an entire scaffold, it is enough to take into account the horizontal stiffness of the platforms. The set of decks, called a platform, is modelled with four truss elements: two ones along the platform, called longitudinal elements, and two crossing elements. The material properties of lattice elements are determined on the basis of the measurement results of the force-displacement relationship for the scaffolding fragment with the platforms. Tests are performed for two directions of the force: perpendicular and parallel to the platform. The test stands are shown in Figure 6 and the corresponding numerical models of the tested scaffolding fragments are shown in Figure 7. Table 3 lists the laboratory measurement results with the markings which will be used to determine the parameters of the truss elements.

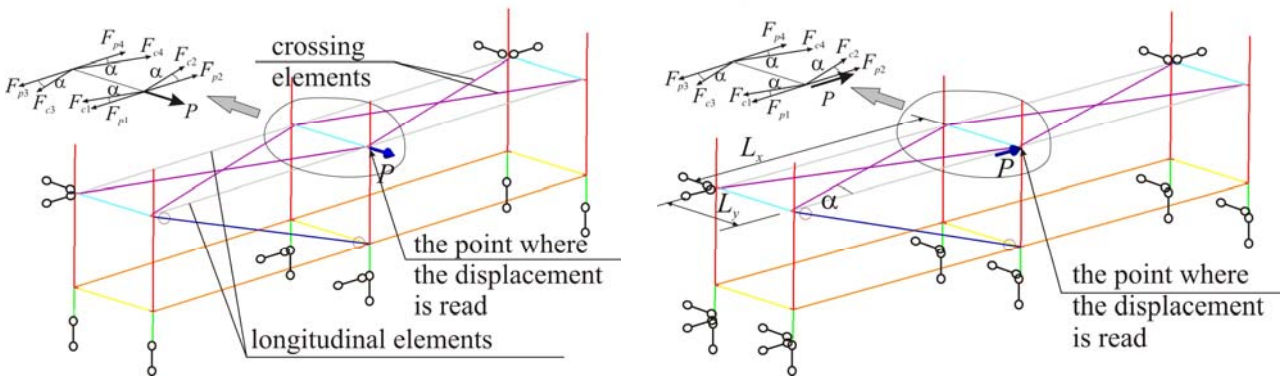

a) b)

Fig. 7. Numerical models of test sites for: a) platforms at the perpendicular load; b) platforms at the parallel load.

Tab. 3. The results of horizontal stiffness tests of the platform.

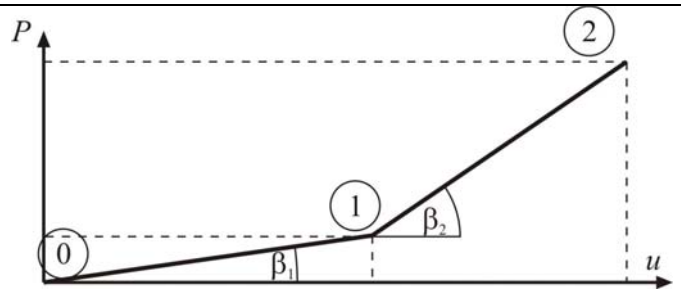

Point	The load perpendicular to the structure (Figure 6a)	The load parallel to the structure (Figure.6b)
0	$u_{\perp 0}$=0.0mm	$u_{\mathrm{II}0}$=0.0mm
	$P_{\perp 0}$=0.0mm	$P_{\mathrm{II}0}$=0.0mm
0-1	$c_{\perp 1} = tg\beta_1$=3.7kN/m	$c_{\mathrm{II}1} = tg\beta_1$=34.0kN/m
1	$u_{\perp 1}$=51.3mm	$u_{\mathrm{II}1}$=18.0mm
	$P_{\perp 1} = u_{\perp 1}c_{\perp 1} = 0$.19kN	$P_{\mathrm{II}1} = u_{\mathrm{II}1}c_{\mathrm{II}1}$
1-2	$c_{\perp 2} = tg\beta_2$=96.0kN/m	$c_{\mathrm{II}2} = tg\beta_2$=341.0kN/m
2	$u_{\perp 2}$=90.0mm (the end of graph)	$u_{\mathrm{II}2}$=25.0mm (the end of graph)
	$P_{\perp 2} = P_{\perp 1} + (u_{\perp 2} - u_{\perp 1})c_{\perp 2}$=3.91kN	$P_{\mathrm{II}2} = P_{\mathrm{II}1} + (u_{\mathrm{II}2} - u_{\mathrm{II}1})c_{\perp\mathrm{II}}$

The material properties of the truss elements are determined in two stages. In the first stage, the properties are estimated on the basis of the following assumptions and formulas:

– the elements have the same material properties in compression and tension,
– the cross-sectional area for all the truss elements is the same and equals A=0.001m^2,
– each fragment of the σ-ε graphs is determined separately,
– the term "the first part of the σ-ε graph" refers to the fragment from the beginning of the coordinate system to the turning point of the graph, and the remaining parts of the σ-ε graph are referred to as the "second part of the σ-ε graph",
– the influence of the longitudinal elements on the horizontal stiffness of the platform when a force is applied in the direction perpendicular to the decks (Figure 6a and Figure 7a) is negligible and therefore the σ-ε characteristic for the crossing elements is determined based on the measurement in the perpendicular direction.

The following is the order of the 1st stage calculations, the purpose of which is to determine the dependence σ-ε for the crossing and longitudinal elements, and the corresponding relationships:

A. The first part of the force-displacement plot in Figure 8a represents the clearances obtained in the model as a result of the introduction of the first horizontal part of the σ-ε graph (Figure 9a) for the crossing elements. The first coordinate (abscissa) of the turning point is determined with the assumption of small displacements on the basis of the following formula:

$$\varepsilon_{c1} = \frac{\sqrt{L_x^2 + \left(L_y + u_{\perp 1}\right)^2} - L_c}{L_c}, \tag{9}$$

where: L_x i L_y - platform dimensions shown in Figure 7b, $L_c = \sqrt{L_x^2 + L_y^2}$ - length of the crossing elements.

The slope of the second part of the σ-ε graph for the crossing elements was obtained on the basis of the sum of projections of forces for the separated fragment of the scaffold (Figure 7a) in the perpendicular direction *y* to the platforms:

$$\sum y = P_{\perp} - \left(F_{c1} + F_{c2} - F_{c3} - F_{c4}\right)\sin\alpha = P_{\perp} - F_{csum}\sin\alpha = 0 \Rightarrow P_{\perp} = F_{csum}\sin\alpha, \tag{10}$$

and relationships (Figure 9a):

$$\Delta\sigma_{c2} = \frac{F_{csum2} - F_{csum1}}{4 \cdot A} = \frac{P_{\perp 2} - P_{\perp 1}}{4 \cdot A \cdot \sin\alpha}, \tag{11}$$

$$\Delta\varepsilon_{c2} = \frac{\sqrt{L_x^2 + \left(L_y + u_{\perp 2} - u_{\perp 1}\right)^2} - L_c}{L_c}, \tag{12}$$

$$E_{c2} = \frac{\Delta\sigma_{c2}}{\Delta\varepsilon_{c2}}. \tag{13}$$

B. The coordinates of the turning point of the σ-ε graph for the longitudinal elements (Figure 9b) were determined on the assumption that the crossing elements do not affect the stiffness until the strain ε_{c1} is achieved, and the axial forces in these elements $F_{c1} = F_{c2} = F_{c3} = F_{c4} = 0$. Since the crossing elements did not work, each of the longitudinal elements also worked separately and as a result the axial forces $F_{p2} = F_{p3} = F_{p4} = 0$. From the formula:

$$\sum x = P_{\text{II}} - \left(F_{p1} + F_{p3} - F_{p2} - F_{p4}\right) - \left(F_{c1} + F_{c3} - F_{c2} - F_{c4}\right)\cos\alpha = P_{\text{II}} - F_{p1} = 0 \Rightarrow P_{II} = F_{p1}, \tag{14}$$

obtained on the basis of the sum of the projections of forces for the separate scaffold fragment (Figure 7b) onto the direction *x* parallel to the platforms, comes that the stiffness of the system was related to the work of only one longitudinal element. Therefore, the coordinates of the turning point of the σ-ε graph were determined from the following formulas:

$$\sigma_{p1} = \frac{F_{p1}}{A} = \frac{P_{\text{II}1}}{A}, \tag{15}$$

$$\varepsilon_{p1} = \frac{u_{\text{II}1}}{L_x}, \tag{16}$$

and the slope of the first part of the $\sigma-\varepsilon$ graph:

$$E_{p1} = \frac{\sigma_{p1}}{\varepsilon_{p1}}. \tag{17}$$

C. To estimate the slope of the second part of the σ-ε graph for longitudinal elements, the sum of the projections of forces for the separate scaffold fragment (Figure 7b) onto the direction *x* parallel to the platforms was used:

$$\sum x = P_{\mathrm{II}} - \left(F_{p1} + F_{p3} - F_{p2} - F_{p4}\right) - \left(F_{c1} + F_{c3} - F_{c2} - F_{c4}\right)\cos\alpha = 0 \Rightarrow F_{psum} = P_{\mathrm{II}} - F_{csum}\cos\alpha. \tag{18}$$

Now, all the normal forces were different from zero and their sums could be written as follows:

$$F_{csum} = F_{c1} + F_{c3} - F_{c2} - F_{c4}, \tag{19}$$

$$F_{psum} = F_{p1} + F_{p3} - F_{p2} - F_{p4}. \tag{20}$$

The stress increase for the second part of the σ-ε graph was determined as the quotient of the force difference for the second part of the force-displacement graph, obtained from the laboratory test with a load parallel to the scaffold (Fig. 8b), and the cross-sectional areas of four longitudinal elements:

$$\begin{aligned} \Delta\sigma_{p2} &= \frac{F_{psum2} - F_{psum1}}{4 \cdot A} = \frac{\left(P_{\mathrm{II}2} - F_{csum2}\cos\alpha\right) - \left(P_{\mathrm{II}1} - F_{csum1}\cos\alpha\right)}{4 \cdot A} = \\ &= \frac{\left(P_{\mathrm{II}2} - P_{\mathrm{II}1}\right)}{4 \cdot A} - \frac{\left(F_{csum2} - F_{csum1}\right)\cos\alpha}{4 \cdot A} = \frac{\left(P_{\mathrm{II}2} - P_{\mathrm{II}1}\right)}{4 \cdot A} - \Delta\sigma_{c\_\mathrm{II}}\cos\alpha\,. \end{aligned} \tag{21}$$

As demonstrated, the second part of the force-displacement relationship graph (Figure 8b) presents the result of the work of all the truss elements, both the longitudinal and the crossing ones. Therefore, to describe the behaviour of the latter elements, the slope of the second part of the σ-ε graph for the crossing elements determined earlier by means on the formula (13) should be used, and the change of normal stresses in the crossing elements, included in the formula (21), to be calculated from the following formula:

$$\Delta\sigma_{c\_\mathrm{II}} = E_{c2}\varepsilon_{c\_\mathrm{II}}, \tag{22}$$

$$\varepsilon_{c\_\mathrm{II}} = \frac{\sqrt{L_y^2 + \left(L_x + u_{\mathrm{II}2} - u_{\mathrm{II}1}\right)^2} - L_c}{L_c}. \tag{23}$$

The strain increase for the second part of the $\sigma-\varepsilon$ graph for the longitudinal elements is given by the formula:

$$\Delta\varepsilon_{p2} = \frac{u_{\mathrm{II}2} - u_{\mathrm{II}1}}{L_x}, \tag{24}$$

and the slope of this part of the graph is given by the formula:

$$E_{p2} = \frac{\Delta\sigma_{p2}}{\Delta\varepsilon_{p2}}. \tag{25}$$

The horizontal stiffness of scaffold is influenced by decks, other components, clearances at the anchors, the friction of supports, assembly inaccuracy, etc. hence, the results of the calculations with the use of the formulas (9) ÷ (25) were deemed preliminary, and in the 2nd stage iterations were performed, which consisted in the conducting of calculations with different slopes of the second parts of the σ-ε graphs to better match the results of the calculations and the laboratory measurements σ-ε. Based on the calculations for the model in Figure 7a, the relationship σ-ε for the crossing elements was determined. The result was used in the iterations for the model in Figure 7b and the relationship σ-ε for the longitudinal elements was determined. The comparison of the calculation and measurement results for the final material properties is shown in Figure 8. In turn, Table 4 summarizes the data after 1st and 2nd stages of the determination of the material properties of the truss elements modelling the horizontal stiffness of the scaffold platforms, and Figure 9 shows graphs with the final relationship σ-ε for these elements.

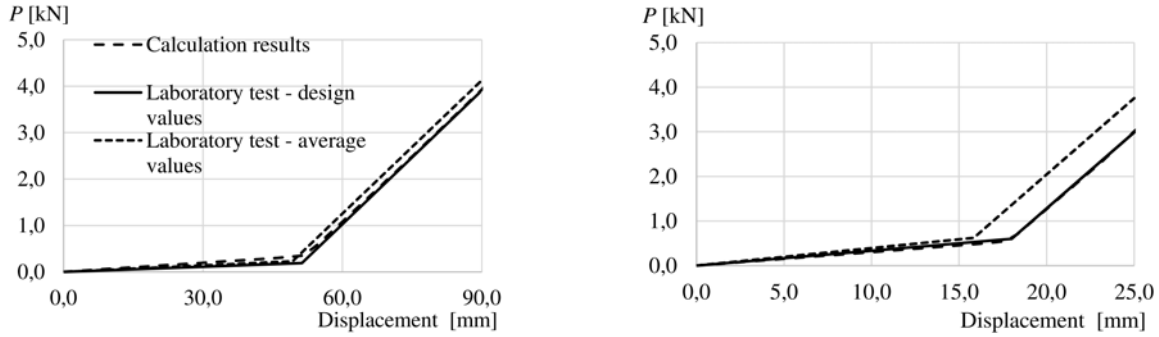

Fig. 8. The comparison of the horizontal stiffness of the platforms obtained from measurements and the calculations for the model in Figure 7: a) scaffold with a perpendicular load; b) scaffold with a parallel load.

Tab. 4. The results of the estimation of the material properties of the truss elements modelling the horizontal stiffness of the platforms.

	The value from stage I	The value from stage II
Crossing elements		
ε_{c1}	$4.981 \cdot 10^{-3}$	$5.0 \cdot 10^{-3}$
E_{c2}	$81.184 \cdot 10^{4}$ kPa	$100.0 \cdot 10^{4}$ kPa
Longitudinal elements		
ε_{p1}	$5.156 \cdot 10^{-3}$	$6.0 \cdot 10^{-3}$
E_{p1}	$26.19 \cdot 10^{4}$ kPa	$10.0 \cdot 10^{4}$ kPa
E_{p2}	$3.568 \cdot 10^{4}$ kPa	$3.56 \cdot 10^{4}$ kPa

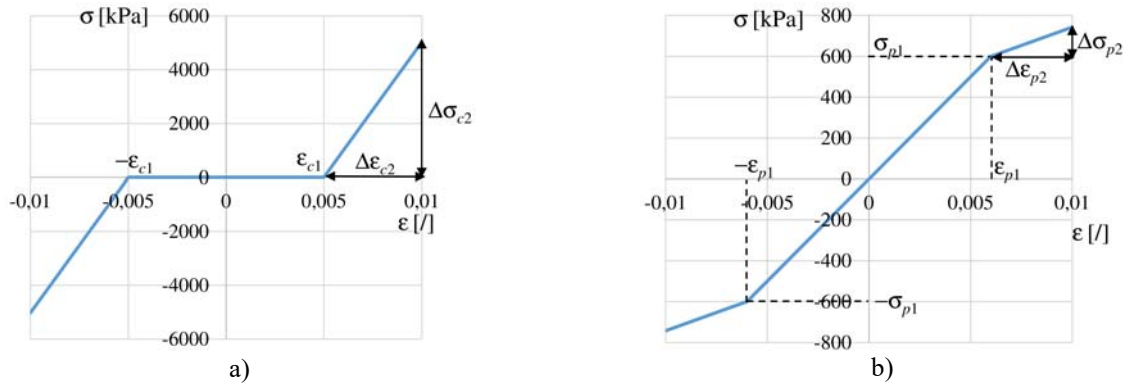

Fig. 9. Graphs of the material properties of the truss elements modelling the horizontal stiffness of the platforms: a) crossing elements, b) longitudinal elements.

Of course, the above procedure is one many possible methods. Formulas for determining material characteristics can be much more accurate. A completely different procedure for calibrating a numerical model based on dynamic measurements on the example of a bridge was described by Jukowski et al. (2018).

4. THE GLOBAL TEST AND FEM MODEL OF SCAFFOLDING

4.1. The description of the global test and numerical simulation of this research

A global test examines the behaviour of an entire scaffold, assembled from new components and shaped in accordance with EN 12810-2. In this paper the results of the research carried out by the Research Institutes of Sweden (RISE) laboratory, which are described by Snygg (2021), are used. The scaffold scheme is shown in Figure 2. The scaffold is placed on spheres as a result of which articulated supports are obtained. Anchor ties are hooked in the eyelets, which also guarantees the possibility of rotation in the connection, but blocks the components of the displacement in three directions. Before conducting the actual measurements, the scaffold is initially loaded with horizontal forces in the directions H_1, H_2, H_3 and H_4. Next, the forces are removed and an accurate measurement of the scaffold geometry is taken. The results of the measurement are used to develop the geometry of a numerical model of the scaffold, taking into account the inaccuracy of the assembly. Following the measurement of the geometry, the proper laboratory test is started. The scaffold is loaded successively with the following forces:

- F_1, F_2, F_3 and F_4 which achieve value about 1.0kN,
- H_3+H_4=0.35kN,
- H_1=0.25kN and H_2=0.35kN,
- F_1, F_2, F_3 i F_4 the values of which are increased in such proportions that F_2=F_3=2F_1=2F_4 and this process continues until the scaffolding is damaged.

Figure 2b shows the forces acting on the scaffold during the measurements, and Figure 2a – the locations and directions of the nodal displacement measurements. The results of the test concern vertical forces and nodal displacements as functions of time. In the laboratory tests also the load-bearing capacity of the scaffold, expressed by the forces F_2=F_3, and the value of F_{cr}=21.75kN were obtained.

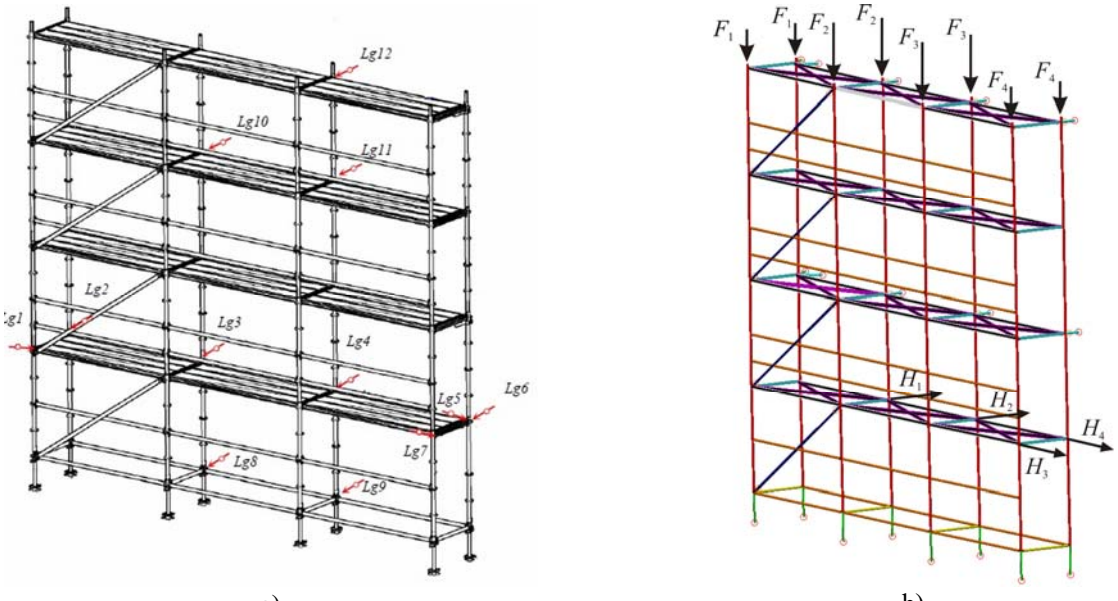

a) b)

Fig. 10. The global test: a) scheme of the scaffold with the directions of the displacement measurement marked *Lg*; b) FEM model with forces.

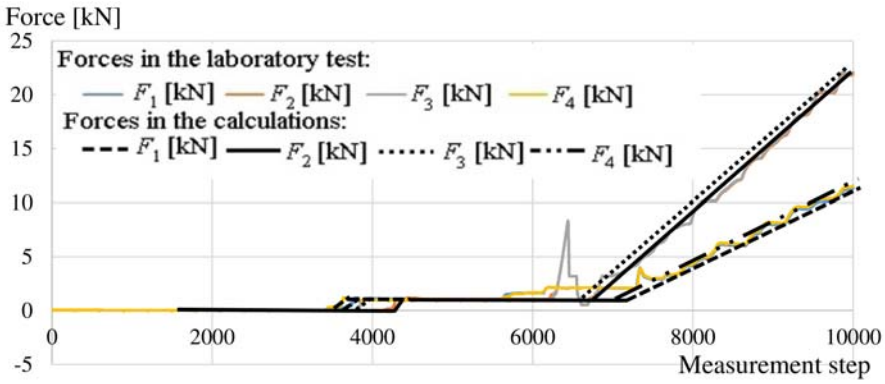

Fig. 11. Changes in the values of forces F_1, F_2, F_3 and F_4 during laboratory tests and calculations.

Tab. 5. The geometrical characteristics of element cross-sections.

Lp	Component	A [cm^2]	J_1 [cm^4]	J_2 [cm^4]	J_3 [cm^4]	W_2 [cm^3]	W_3 [cm^3]
1	Base jack	4.278	10.2676	5.1838	5.1838	2.942	2.942
2	Stand, ϕ48.3x3.2	4.5339	23.1710	11.5860	11.5860	4.7975	4.7975
	O-ledger ,1.088m ϕ48.3x3.2	4.5339	23.1710	11.5860	11.5860	4.7975	4.7975
3	U-ledger, open cross-section 53x48x2.5	3.7250	26.4610	11.0750	15.3760	2.9932	6.4067
4	O-ledger, 3.072m, ϕ48.3x2.7	3.8679	20.1780	10.0890	10.0890	4.1776	4.1776
5	Bracing, ϕ48.3x2.6	3.7328	19.5531	9. 7765	9.7765	4.0483	4.0483
6	Wall tie, ϕ48.3x2.7	3.8679	20.1780	10.0890	10.0890	4.1776	4.1776

where: A – cross-section area, J_1 – torsional resistance, J_2 and J_3 – moments of inertia with respect to 2nd and 3rd axes of the local coordinates system respectively, W_2 and W_3 – section modulus at bending with respect to 2nd and 3rd axes of the local coordinates system respectively.

Tab. 6. Material properties.

Component	Base jack	Stand ϕ48.3x3.2	O-ledger 1.088m ϕ48.3x3.2	O-ledger 3.072m ϕ48.3x2.7	Bracing ϕ48.3x2.6	U-ledger 53x48x2.5	Wall tie ϕ48.3x2.7
Material	Steel S235JRH					Steel S355J2	Steel S235JR
Density γ	78.5kN/m^3					78.5kN/m^3	78.5kN/m^3
Young's modulus E	2.05·10^8 kPa					2.05·10^8 kPa	2.05·10^8 kPa
Yield strength f_{yk}	320MPa					355MPa	235MPa
Strain hardening modulus	2.05·10^6 kPa					2.05·10^6 kPa	2.05·10^6 kPa
Poisson's ratio	0.3					0.3	0.3

The geometry in the FEM model maps the scaffold geometry in the global test. Such components as base jacks, stands, ledgers, or bracings are modelled with frame elements. Table 5 contains geometrical characteristics of cross-sections for frame elements and Table 6 contains material properties for ones. Stand-

transom and stand-ledger connections are modelled as flexible for bending in two planes, as described in Section 3.1, and for other types and directions of interactions - as rigid. Stand-stand and stand-base jack connections are modelled as rigid. Stand-anchor tie connections are modelled as articulated. The platforms are modelled as described in Section 3.2. Nonlinear calculations taking into account large displacements and material nonlinearities were performed in ASM 2013. In the numerical simulations of the global test, the self-weight was applied first followed by forces applied in the same order as in laboratory tests. Figure 11 shows a graph of changes in the values of the forces F_1, F_2, F_3 and F_4 during laboratory tests and calculations. The model developed in such a way does not take into account the fact that:
each stand-ledger joint has a different moment-angle rotation characteristic due to, among others, a different force of the hammer hitting the wedge during the assembly, decks can be installed in various ways, e.g. they can block each other, during the initial loading, the deck movement can also be blocked and the free movement of the decks was not unlocked during unloading, when anchor ties are secured to the steel frame of the test stand clearances occur, during the measurements, there was a sudden increase in one of the vertical forces, which could cause dynamic effects.

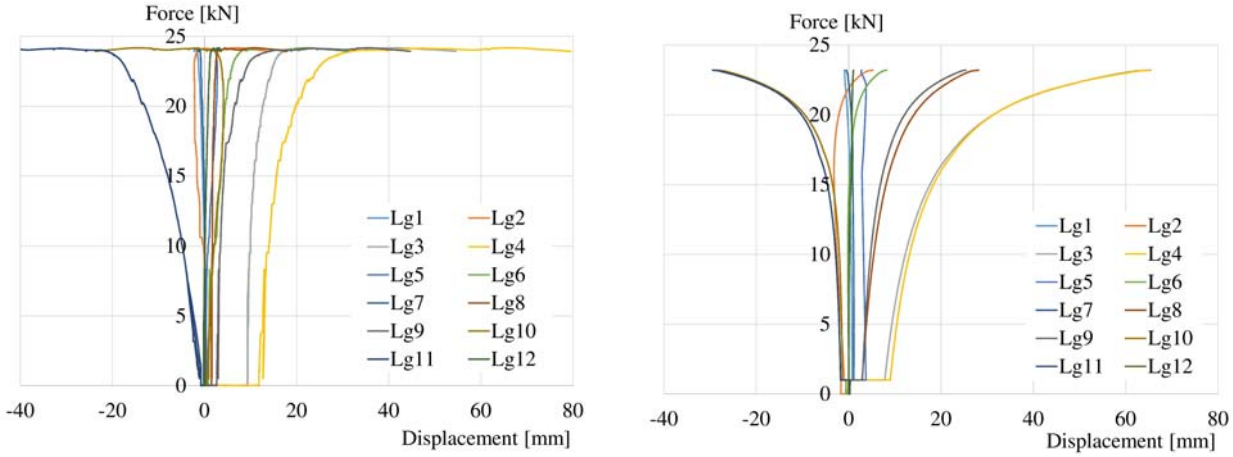

a) b)

Fig. 12. The numerical and laboratory results: a) global test results, b) results of the calculations using design data.

Figure 12 shows the results of the measurements and calculations in the form of force-displacement graphs. The displacements are measured at 12 points, the location of which is shown in Figure 10. The force F_2 is on the vertical axis. At this stage, the results of the measurements (Figure 12a) and the results of the calculations with data (material properties and geometric characteristics), determined in such a way that they could be used for designing (Figure 12b), i.e. as characteristic values, are shown. The verification and discussion of the results is carried out in the following sections.

4.2. The sensitivity analysis of calculations to the input data

When developing the numerical model of a structure, it is worth assessing the influence of individual input data on the calculation results. This enables an conscious calibration of the model. In other words, when selecting the data and the boundary conditions of the model, one knows which errors to avoid or for which parameters more precise tests or calculations should be performed. There are two types of data in the case of the analysed structure:

– data assumed on the basis of the component geometry and material properties declared by the scaffolding manufacturer as characteristic values, i.e. those for which the probability of the occurrence of worse values is usually set at 5%;
– data estimated on the basis of laboratory tests of the elements that are used in the tested scaffold.

The best option when developing a numerical model is to conduct one's own laboratory tests of the material properties of all the components. An example of such numerical modelling based on own research is the development of a modular scaffolding node model, the process of which was presented by Pieńko (2019). However, even with this approach, there can be a significant scattering of the measurement results, so the sensitivity analysis of the calculation results to the input data should be performed.
In the global test simulation, substitute scaffold fragment models were used. The quality of such models has the greatest impact on the correctness of the obtained results, therefore a simplified sensitivity analysis was carried out for the parameters of the task related to the selection of parameters for simplified models of the stand-ledger joint and the horizontal stiffness of the platforms, namely for:
– stiffness of the stand-ledger joint at bending with respect to the horizontal axis – $k_{\varphi y}$,
– stiffness of the stand-ledger joint at bending with respect to the vertical axis – $k_{\varphi z}$,
– slope of the second part of the σ-ε graph for crossing elements – module E_{c2},
– slope of the first part of the σ-ε graph for longitudinal elements – module E_{p1},
– slope of the second part of the σ-ε graph for longitudinal elements – module $E_{p2.}$

A simplified sensitivity analysis consists in the performance of a series of calculations at different value ranges and in examining the influence of the input parameters on the load-bearing capacity of the scaffold, represented by the force F_2max (or F_3max). The exceedance of one of the following conditions was assumed as the criterion for achieving the load-bearing capacity:
– for transitional elements modeling the stand-ledger joints

$$\left|\frac{M_y}{M_{ycr}}\right|+\left|\frac{M_z}{M_{zcr}}\right|\le 1, \tag{26}$$

where: M_y and M_z – bending moments at nodes with respect to the horizontal and vertical axes, respectively,
– for the other frame elements

$$\sigma=\left|\frac{N}{A}\right|+\left|\frac{M_2}{W_2}\right|+\left|\frac{M_3}{W_3}\right|<f_{yk}, \tag{27}$$

where: N – axial force, M_2 and M_3 – bending moments at nodes with respect to 2nd and 3rd axes of the local coordinates system, respectively, A – cross-section area, W_2 and W_3 – section modulus at bending with respect to 2nd and 3rd axes of the local coordinates system respectively.
The results of the sensitivity analysis are shown in Figure 13 ÷ Figure 18. Figures 13 and 14 present the influence of the stiffness of the transition elements on the relationship between the load value, represented by the force F_2, and the horizontal displacements Lg4 and Lg11. For all the calculations, the values of the critical forces F_{cr}, defining the load-bearing capacity of the scaffold were determined, and the results of the analyses are shown in Figure 15. In Figure 16 and Figure 17 the influence of the slope of the first part of the σ-ε curve concerning the longitudinal elements E_{p1} and the second part of the σ-ε curve regarding the crossing elements E_{c2} on the behaviour of the scaffold is demonstrated. The values of the critical forces F_{cr} obtained at different values of the modules E_{p1} and E_{c2} are shown in Figure 18.

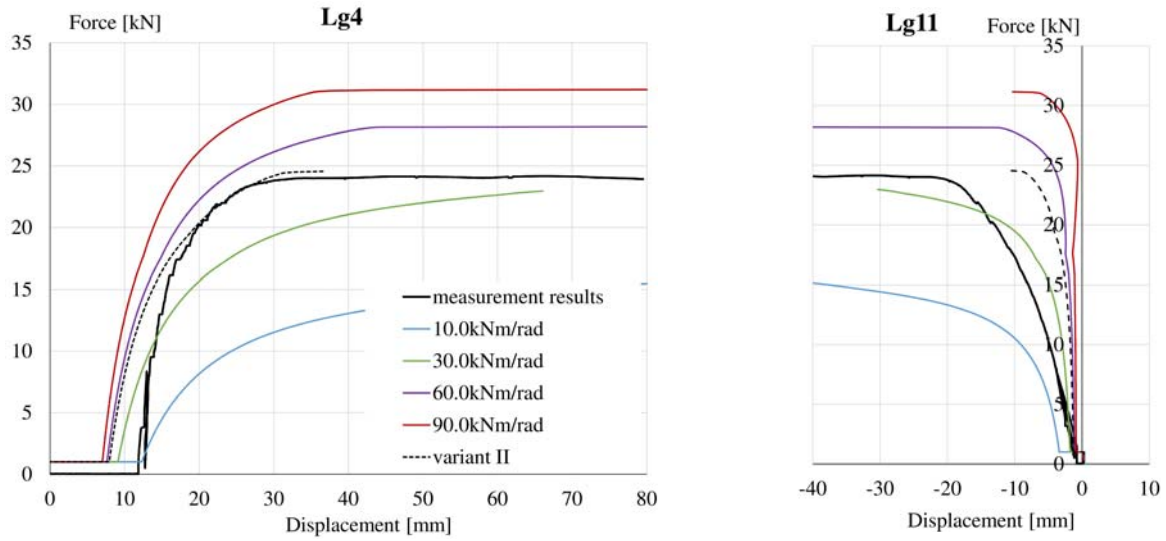

a) b)

Fig. 13. Influence of the stiffness of the joint $k_{\varphi y}$ on the force-displacement relationship for the displacement in the direction: a) Lg4, b) Lg11.

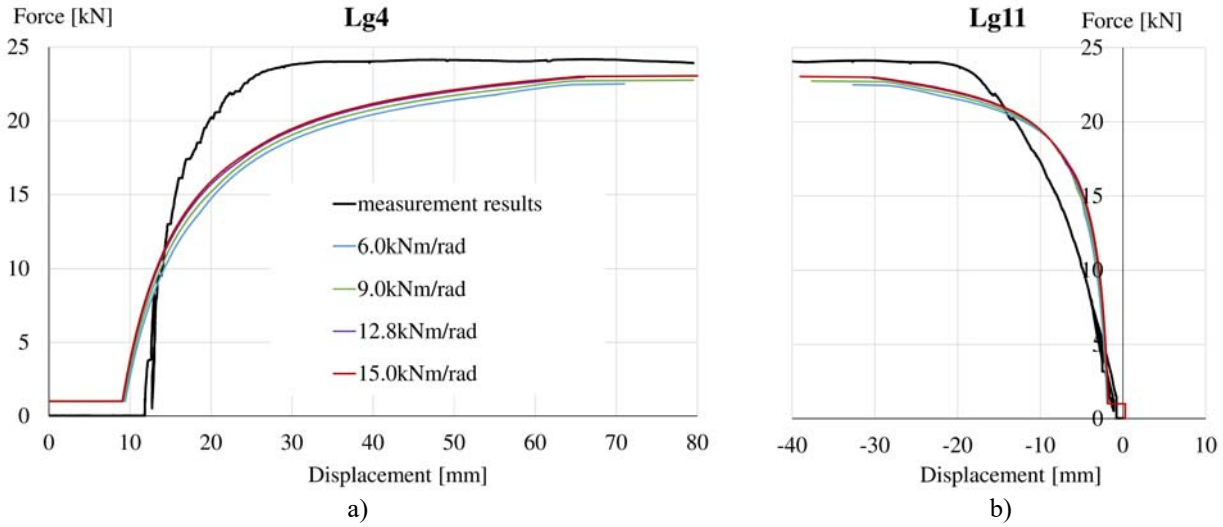

a) b)

Fig. 14. Influence of the stiffness of the joint $k_{\varphi z}$ on the force-displacement relationship for the displacement in the direction: a) Lg4, b) Lg11.

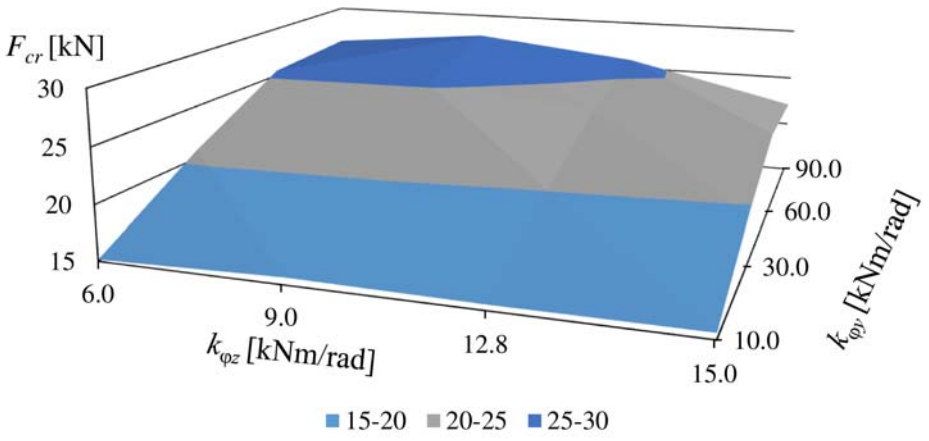

Fig. 15. Influence of the stiffness of the joints $k_{\varphi y}$ and $k_{\varphi z}$ on the load-bearing capacity expressed as F_{cr}.

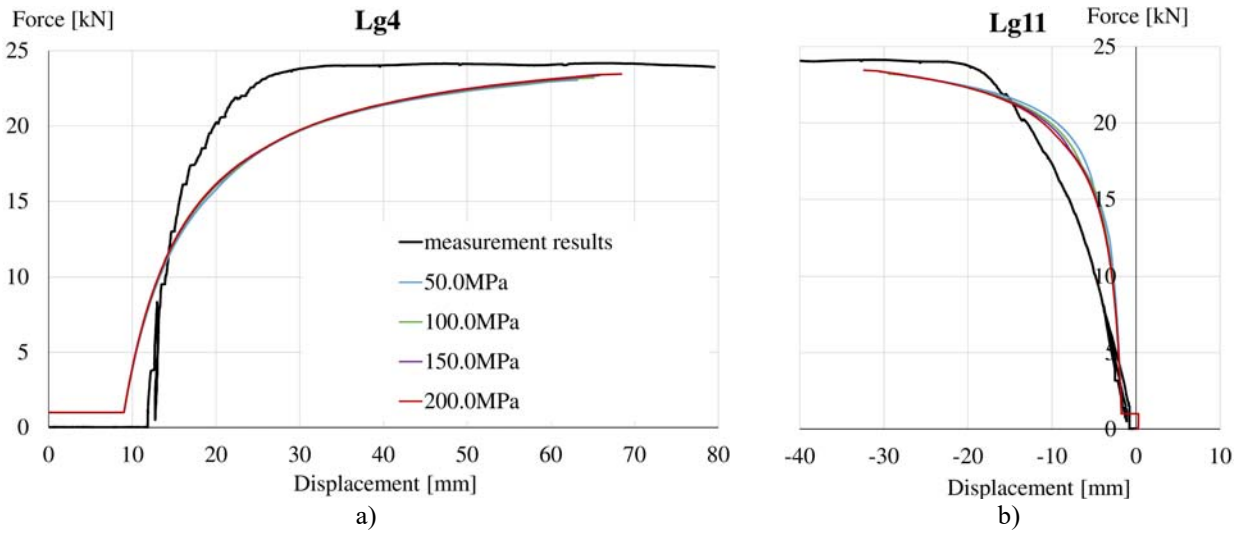

Fig. 16. Influence of the first part of the σ–ε graph concerning longitudinal elements (modulus E_{p1}) on the force-displacement relationship for the displacement in the direction: a) Lg4, b) Lg11.

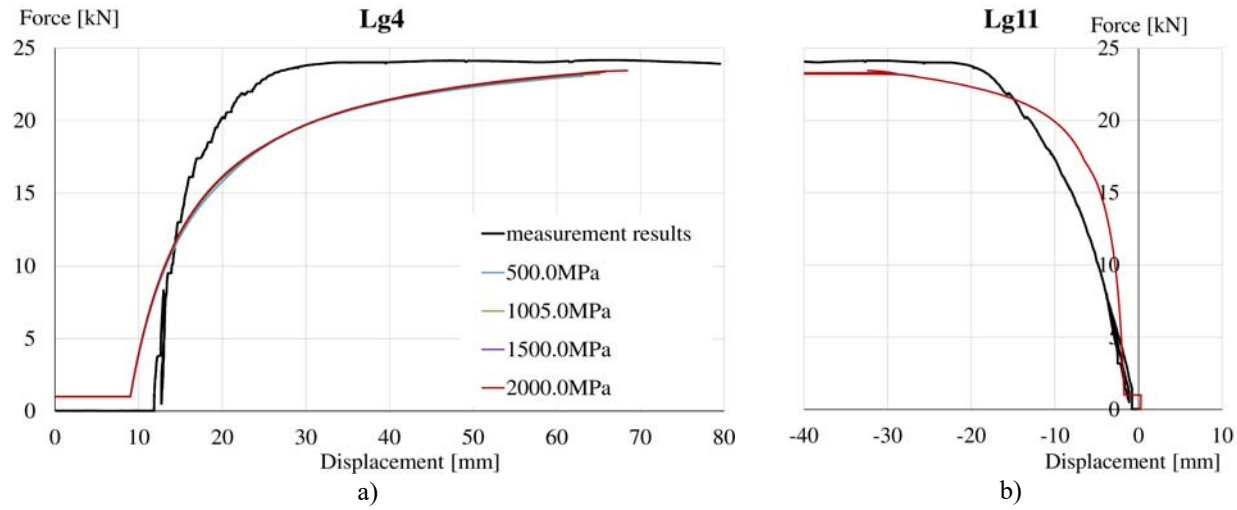

Fig. 17. Influence of the second part of the σ–ε graph concerning crossing elements (modulus E_{c2}) on the force-displacement relationship for the displacement in the direction: a) Lg4, b) Lg11.

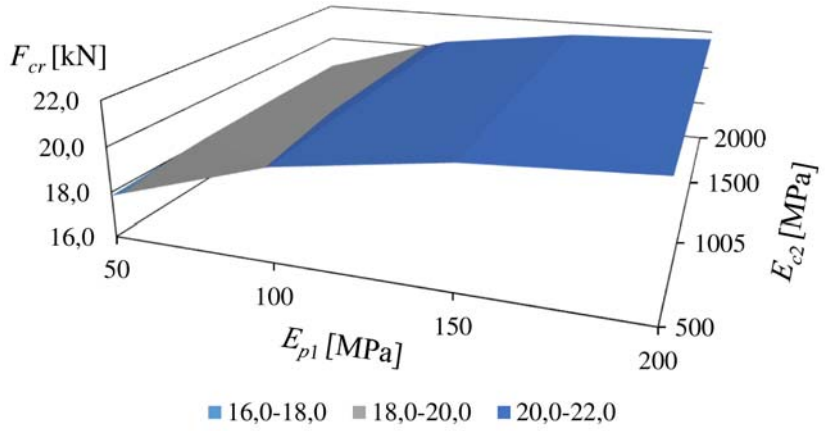

Fig. 18. Influence of the modules E_{p1} and E_{c2} on the load-bearing capacity expressed as F_{cr}.

As shown in Figure 13 ÷ Figure 18, the stiffness of the joint $k_{\varphi y}$ has the greatest influence on the load-bearing capacity of the structure and its behaviour. The stiffness of the joint $k_{\varphi z}$ impacts the results from the beginning of the calculations, but the influence is much smaller. The remaining parameters do not influence

the behaviour of the scaffold in the first phase of its operation, which can be described with the linear relationship between the load and the structural response. The influence of the other parameters is revealed only upon reaching the non-linear range of calculations, when the modules E_{p1} and E_{c2} also have an impact on the operation of the scaffold. The modulus E_{p2}, i.e. the slope of the second part of the σ-ε graph concerning the longitudinal elements, has a negligible impact on the results in the examined case, hence, the results of the sensitivity analysis for this parameter are not shown in the figures.

4.3. Model verification and discussion of the results

The scaffold model described in Section 4.1 was verified by means of a comparison of the calculation results and the results of the global test measurements. Figure 19 shows the displacements in the directions indicated in Fig. 10a, obtained in global tests and computer calculations. The simulation results were obtained for two data sets:

– Variant I – the properties of the stand-ledger joints and the truss elements modelling the horizontal stiffness of the platform were estimated on the basis of the measurement values that can be used for the design of a scaffold, i.e. the characteristic values defined as 5% quantiles at the confidence level of 75%, according to EN 12811-3,
– Variant II – the properties of the stand-ledger joints and the truss elements modelling the horizontal stiffness of the platform, were estimated on the basis of the average measurement results.

An assessment of the presented simulation results requires the determination of the criteria for the verification of a numerical model. The calibration methods discussed in the article are used in engineering practice for the purposes of developing scaffold models. In engineering practice, a model should primarily give results ensuring the safety of the structure. The major model verification criterion is not the exact overlap of the measurement and calculation paths, but smaller displacements obtained with the same loads in practice. As demonstrated in Figure 19, the graphs differ slightly, but the result has been found acceptable for use in the calculations of real structures. On the basis of the models presented in this paper, scaffolding systems and non-standard scaffolds are designed in Poland and many other European countries.

In the case of scientific research, the model simulation verification criterion regards the most faithful and accurate representation of the behaviour of the tested object when loaded. This means that the geometric parameters and material properties that better reflect the behaviour of the structure should be used. The simplest method is to use average values and, as shown in Figure 19, simulations made in such a way give results which are more similar to the ones obtained in the tests. Still, in order to fully describe the behaviour of a scaffold, it is planned to perform analyses using random values of the most important parameters of the numerical model in future.

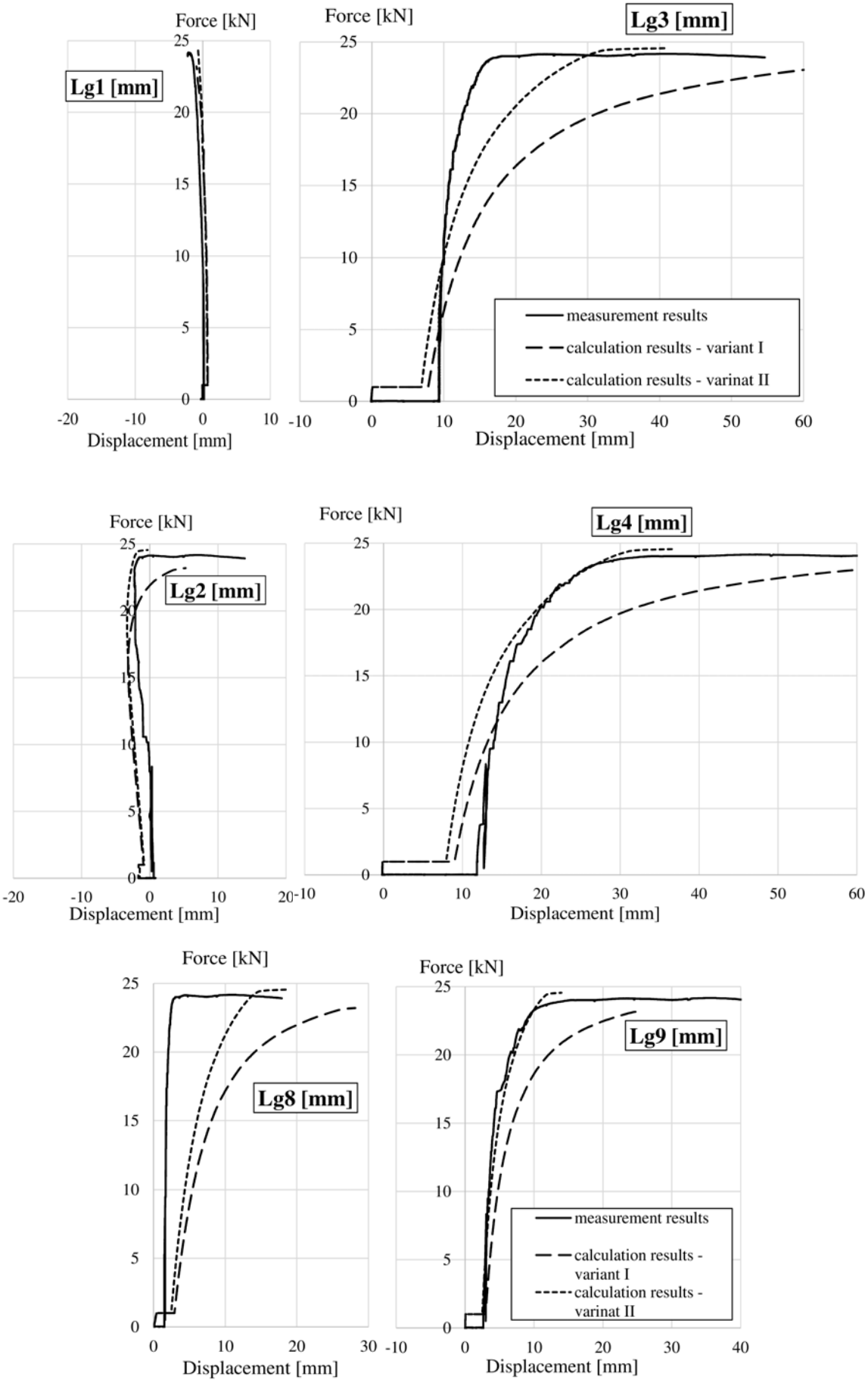

Fig. 19. The comparison of the measurements and calculations results based on the force-displacement relationships.

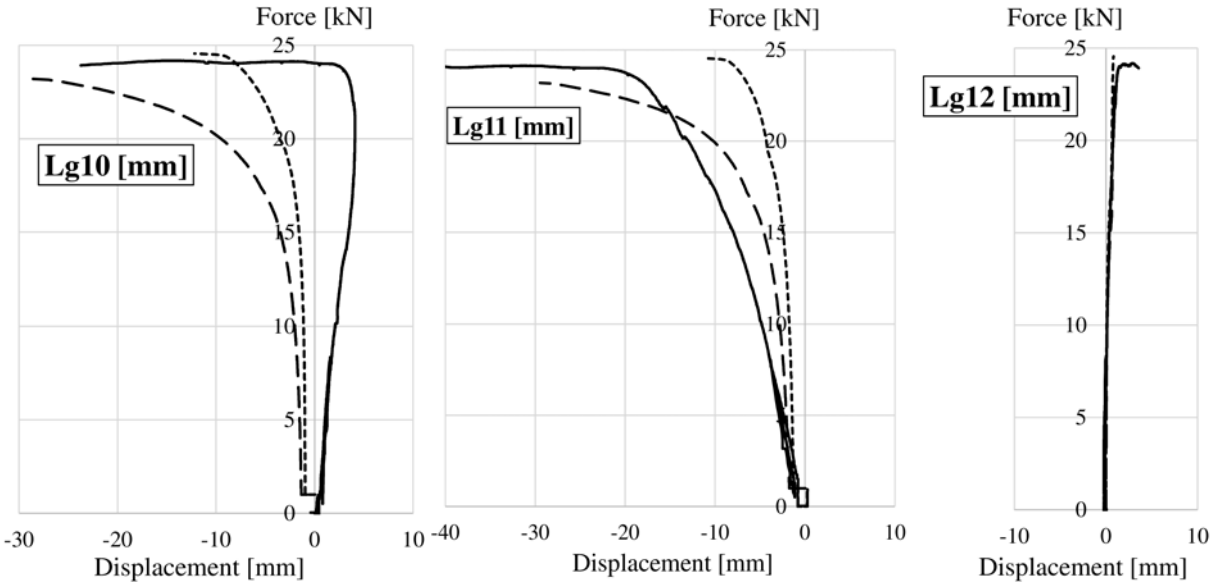

Fig.19. cont. The comparison of the measurements and calculations results based on the force-displacement relationships.

5. CONCLUSIONS

Scaffolds are light structures. This is achieved by using slender frame elements and perforated sheet decks. Due to a varying degree of the complexity of scaffold component geometry, a numerical simulation of the scaffold operation requires the use of special methods. Numerical calculations should be preceded by an assessment of the influence of the parameters adopted in the numerical model on the simulation results. In particular, the introduced simplifications must be carefully analysed. In the presented case, it regards the modelling of the stiffness of the stand-ledger joints, which have a significant impact on the results, and the model of the decks. The first part of the σ-ε graph concerning the longitudinal elements has a much greater influence on the calculation results than the second part of this curve and the σ-ε graph regarding the crossing elements. As can be seen, the calculations results are similar to the laboratory test results, but it cannot be claimed that they perfectly reflect them. This difference results from the following:

– there are too many constituents which may not approach the ideal, such as: the material properties of the scaffold components, the stiffness of the stand-ledger joints, clearances of decks mounted on transoms, the method of anchoring;
– the characteristics determined on the basis of laboratory tests are burdened with error, e.g. support construction inaccuracy, clearances in joints, components not checked in terms of material properties,
– the method of transferring loads and a possible occurrence of dynamic effects during tests,
– in Variant 1, in the numerical calculations of the scaffold, parameters selected to ensure the safety of the structure are used, which, by definition, differ from the average values.

If one wants to compare the results of measurements and computer simulations, one either tries to "take care" of the laboratory test stand and the method of applying a load in the laboratory, one inventories them in terms of possible imperfections, or one takes into account possible deficiencies. In the case of the problem presented in the paper, the most important thing is to create a model that will guarantee the safety of the scaffold users. Each simplification applied must ensure that the results obtained in the calculations will guarantee the safe use of the structure. It may seem that scaffolds are not very interesting structures, but it is demonstrably not true. Due to the nature of the scaffold structure, it is necessary to demonstrate knowledge, experience and solve many scientific problems when conducting a numerical analysis of its behaviour.

ACKNOWLEDGMENT

The research, of which results are presented in the paper, were financed by ALTRAD-Mostostal in Siedlce.

REFERENCES

Aziz, A.K. 1972. *The mathematical foundations of the Finite Element Method with applications to partial differential equations*, New York: Academic Press.

Błazik-Borowa, E., Pieńko, M., Robak, A., Borowa, A. & Jamińska-Gadomska, P. 2017. *Analysis of ledger-stand joints in the aluminium modular scaffold*. Archives of Civil Engineering, LXIII (1/2017): 17-31.

Błazik-Borowa, E. & Robak, A. 2017. *Numerical models of scaffolding decks and their applications*. International Journal of Civil Engineering 15 (7): 979-989.

EN 12810-1. 2004. *Façade scaffolds made of prefabricated components. Part 1: Product specifications*, Brussels: European Committee for Standardization.

EN 12810-2. 2004. *Facade scaffolds made of prefabricated components Part 2: Particular methods of structural design*, Brussels: European Committee for Standardization.

EN 12811-1. 2004. *Temporary works equipment – Part 1: Scaffolds – Performance requirements and general design*, Brussels: European Committee for Standardization.

EN 12811-3. 2003. *Temporary works equipment – Part 3: Load testing*, Brussels: European Committee for Standardization.

Hrennikoff, A. 1941. *Solution of problems of elasticity by the framework method*. Journal of Applied Mechanics 8 (4): 169-175.

Jukowski, M., Błazik-Borowa, E., Bohatkiewicz, J., Bęc, J. & Hypki, M. 2018. *The influence of the composite bridge exploitation on the behavior of the structure subjected to a dynamic load*. In: Bily P., Kohoutkova A., Vitek J., Frantova M. (eds). 12th fib International PhD Symposium in Civil Engineering: proceedings. Praga: Czech Technical University.

Misztela, A. 2016. *Badania węzła rusztowania Altrad Mostostal ROTAX-PLUS (The research of a node of Altrad Mostostal ROTAX-PLUS scaffolding)*, Reports No. 13823/MR, Warsaw: Institute of Mechanised Construction and Rock Mining.

Misztela, A. 2020. *The research of the horizontal stiffness of aluminum decks E491530 cooperating with u-transom 1.09m E372411 as a component the ROTAX-PLUS system*, Reports No. 14730/BZ, Warsaw: Institute of Mechanised Construction and Rock Mining.

Pieńko, M. 2019. *Selection of criteria for estimation of load-bearing capacity of scaffolding joints*. Lublin: Publisher of Lublin University of Technology.

Snygg, H. 2021. *Rotax Scaffolding System - Global Tes*t, Report No. P103877, Borås: Research Institute of Sweden.

Wilson, E.L. & Clough, R.W. 1963. *Finite element analysis of two-dimensional structures*. Berkeley: Structural Engineering Laboratory, University of California.

Zienkiewicz, O.C. & Cheung, Y.K. 1967. *The Finite Element Method in Structural Mechanics*, London: McGraw-Hill.

LIGHTWEIGHT STRUCTURES in CIVIL ENGINEERING
CONTEMPORARY PROBLEMS
Monograph from Scientific Seminar
Organized by Polish Chapters of
International Association for Shell and Spatial Structures
Łódź University of Technology
Faculty of Civil Engineering, Architecture
and Environmental Engineering
XXVII LSCE
Łódź, 2nd – 3rd of December 2021

ECONOMIC AND RELIABILITY ASSESSMENT OF TWCFS STRUCTURES STRENGTHENED WITH CFRP COMPOSITES

M.A. Dybizbański [1] **M.W. Hązła** [2] **K. Rzeszut** [3] **I. Szewczak** [4]
[1] MEng, Faculty of Civil Engineering and Transport, Poznań University of Technology, POLAND, *maciej.dybizbanski@doctorate.put.poznan.pl*
[2] BEc, Faculty of International Business and Economics, Poznań University of Economics and Business, POLAND, *marcelihazla@gmail.com*
[3] PhD, DSc , Eng., Faculty of Civil Engineering and Transport, Poznań University of Technology, POLAND, *katarzyna.rzeszut@put.poznan.pl*
[4] PhD, Eng., Faculty of Civil Engineering, Lublin University of Technology, POLAND, *i.szewczak@pollub.pl*

ABSTRACT: This paper presents the analysis of steel market and its future prospects, as well as discusses the possible usage of thin-walled cold-formed steel (TWCFS) elements strengthened with CFRP composites. Economic analysis was carried out based on literature, professional media and market trends review.
A reliability analysis was carried out for TWCFS elements strengthened with CFRP on the basis of laboratory and numerical tests and selected examples from the existing literature. On the basis of the above analyses, two main conclusions were drawn. Firstly, amidst increasing global demand for steel, the vulnerability of the global steel market to distortions and the rising costs of steel production, it will be beneficial for companies to reduce their demand for steel. Secondly, one possible way of reducing steel consumption in construction industry may be the usage of TWCFS elements strengthened with CFRP composites on the wider scale.

Keywords: thin-walled structures, steel market, CFRP composites.

1. INTRODUCTION

As steel prices continue to rise, there is an increasing need to find an optimal way to reduce steel consumption. One that would enable costs to be reduced in such a way that adverse effects are minimised for various industries, including the construction industry. One possible way to find this solution is to extend the usage of thin-walled steel elements. In this case, they would need to be reinforced, where potential can be found in the application of CFRP composites. This solution would allow for the reinforcement of cold-formed metal elements to such an extent that they could be used in a wider range of structures, especially as the main load-bearing elements. This would reduce the impact of steel costs on the construction market. Currently, the number of publications on the issue is very limited, and most of them are focused on the analysis of compressed elements. Due to the increasing use of thin-walled elements in steel structures, it becomes necessary to optimize the methods of their reinforcement. It is a fact that the principles of using CFRP tapes to strengthen concrete structures are now widely known, however, there are no design guidelines for steel structures. Therefore this paper presents the analysis of current state of steel market and its future

prospects, as well as the possible usage of thin-walled, cold-formed steel elements strengthened with CFRP composites.

2. CONDUCTED RESEARCH

2.1. Economic

Iron has accompanied mankind for millennia. Although the oldest known iron artefacts date to around 3200 BC (Rehren et al. 2013), most historians consider not until the Iron Age of the 1st millennium BC as the period when this material became widespread (Hummel 1998). For hundreds of years, however, it remained a rather luxurious raw material, used mainly for weapons, jewellery and other small objects (Lucas 2005). Its mass usage did not really take place until the Industrial Revolution, since the process of transforming grey iron into wrought iron using puddling furnaces was developed in 1784 (Morton and Mutton 1967). However, the advancing industrialisation of the United Kingdom and the United States in the 19th century began to require increasingly flexible metals, largely linked to the intensive development of railway networks (Bogart et al. 2021). A key turning point for the industrial use of iron came with H. Bessemer's 1856 patent on the process of de-carbonising pig iron by oxidising excess carbon in a refractory ladle, which ushered in an era of affordable steel, enabling its mass usage. Due to declining production costs, steel saw a considerable growth in worldwide demand throughout the twentieth century, owing to its numerous applications in the electrical, automotive, and building industries. Steel output increased by 30 times over this time span, from 28.3 Mt in 1900 to 850 Mt in 2000 (Kelly and Matos 2021). Given that the world population nearly quadrupled from 1.6 billion in 1900 to 6.1 billion in 2000 (NEAA 2013), it is clear that the twentieth century saw a considerable increase in global per capita steel consumption, which increased from 17.7 kg to 139.3 kg[1]. In 2019, global steel output reached 1870 Mt, with the Asian area accounting for 70% (1314.6 Mt) and China accounting for 53.5 % (996.3 Mt) (WPR 2021). Multiple economic conditions in the twentieth century for East Asian nations that have been extensively industrializing their economies have resulted in such a high degree of steel production density. The goal was to reduce the risk of excessive specialisation in the export of low-processed goods and raw materials (Chang 2006). These processes accelerated in the 1990s due to the increasing globalisation of capital markets and inflow of FDIs into emerging economies (Eichengreen 2006). As a result, in 2020, of the world's 20 largest (by volume) steel-producing companies, 16 were based in East Asian countries, with as many as 12 of them in China (WSA 2021). However, excessive production concentration is a significant risk factor for global supply chains. In March 2011, as a result of the earthquake and subsequent tsunami in Japan, 656 companies supplying components to Japanese and US buyers in the automotive, electronics and metals industries went bankrupt, contributing to significant delays and supply shortages that were still being felt 6 months after the disaster (Suzuki and Kaneko 2013). The global economy was similarly impacted by the COVID-19 pandemic, the effects of which some industries are still struggling with today.

One of the markets that has been severely affected in 2020 is the global steel market. As mentioned earlier, the global economy is increasingly dependent on this raw material, making macroeconomic shocks to the steel market cause far-reaching implications. With the outbreak of the COVID-19 pandemic and lockdowns in many countries[2], many steel mills halted production in the face of uncertainty over future steel demand, disrupting the global steel production cycle and causing a decline in global steel stocks (Monarch Metal

[1] It is also worth noting that steel consumption per unit of GDP produced has also intensified over this period. The value of world GDP at 1900 prices increased from USD 1.9 trillion in 1900 to USD 36.7 trillion in 2000 (OECD, 2006), meaning that world steel consumption per unit of GDP increased from 14.9 g to 23.16 g. Thus, the above measure clearly indicates the growing importance of this material to the global economy.

[2] Which was particularly hard felt by China's economy (accounting for more than half the world's steel production), where the most stringent lockdowns took place (Mokyr, 1998).

2021). However, the decline in steel demand was lesser than expected and by the second half of 2020 it was already back to pre-pandemic levels. This was largely related to a shift in demand for consumer goods, as during the lockdowns in the first half of 2020, consumers purchased steel-intensive products such as cars, refrigerators and other household appliances instead of going on holiday (Miningtechnology.com 2022). Demand for steel significantly exceeded its supply, which led to a surge in steel prices once stocks were depleted. In the second half of 2020, steel contract prices rose from the vicinity of USD 500 to USD 1000, reaching USD 1945 per tonne in August 2021 (Figure 1), an increase of more than 280% year-on-year. However, current steel futures prices suggest that a tipping point has already been passed, with contract prices for the second half of 2022 ranging around USD 900, which could imply a new long-term equilibrium.

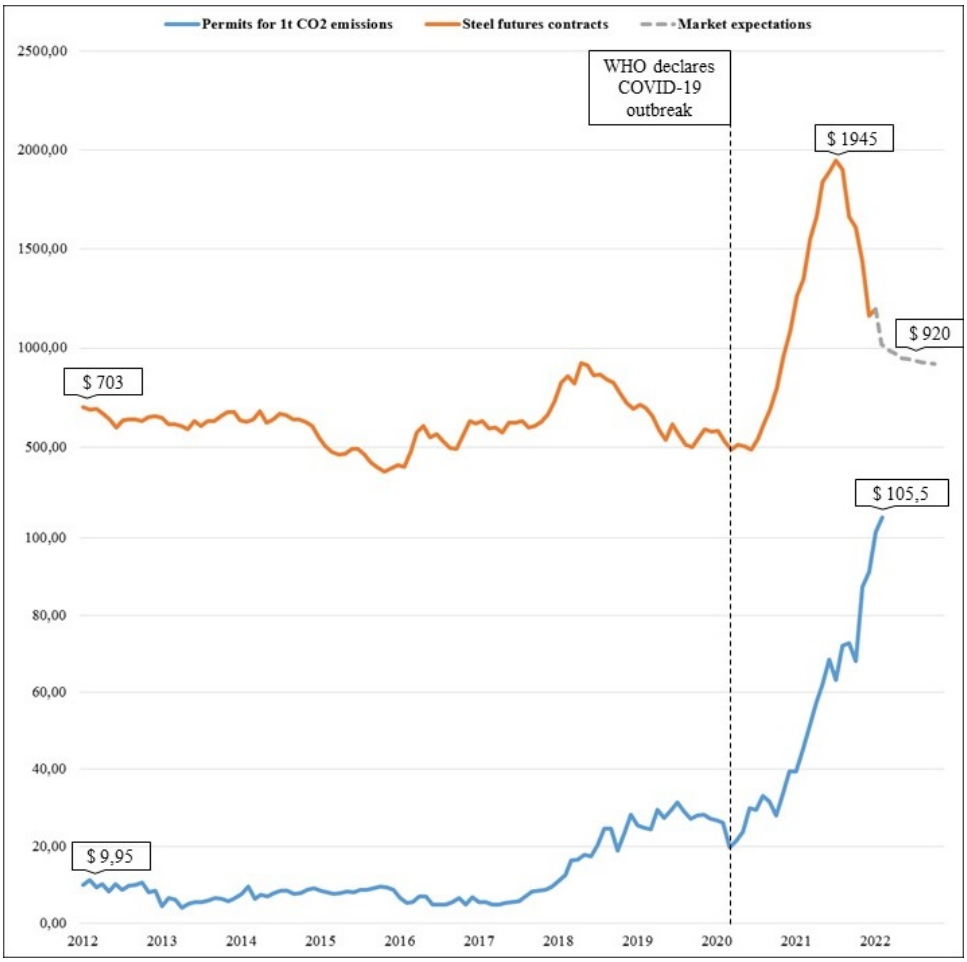

Fig. 1. Prices of steel tonne futures and European permits for 1t CO2 emissions in 2012-2022, USD (as of 02.02.2022) (Macrotrends, 2022; Market Watch, 2022; Trading Economics, 2022)

Although market expectations do not fully reflect the reality until the end of 2022, it can be assumed that steel prices will start to gradually decrease over the course of 2022. Of course, it cannot be said that steel prices will return to their pre-pandemic levels in the near future - in the long term, other factors than those already cited will have an impact on steel prices. One of the main reasons for this is the high CO2 emission of the steel production process. Currently, the production of 1t of steel emits 1.8t of carbon dioxide. As a result, global steel manufacturing contributes around 6.6 percent of world CO2 emissions, amounting to approximately 51Gt (Gates 2021, World Population Review 2022). Meanwhile, given the growing climate problems over the 21st century, an increasing number of developed countries are beginning to move towards

decarbonising their economies[3]. The most developed system supporting the pursuit of this goal can be found in the European Union, where since 2005 permits to emit 1t of CO2 have been treated as a financial instrument (European Commission 2021b). In Figure 1 it can be observed that between 2012 and 2022 the price of a permit to emit a tonne of carbon dioxide increased from around USD 10 to over USD 100, which means that in EU the share of the price of CO2 emission permits in steel prices rose from 2.5% in 2012 to 15.9% in 2022. Given the convergence of the objectives of most countries in the world in terms of reducing CO2 emissions in their economies, it can therefore be assumed that the trend in the granting of emission permits initiated by the EU will, over time, begin to influence (increase) steel prices around the world[4]. The technology of trapping carbon dioxide in the steel manufacturing cycle, which may cut emissions by up to 90% (European Commission 2014), could be a substitute to purchasing increasingly expensive emission permits. The anticipated costs of widespread deployment of this technology vary from 16 to 29% of the steel value, implying that 'green' steel[5] might cost between USD 871 and 964 per tonne in the coming years, assuming an average price per tonne of roughly USD 750 for the previous ten years. It appears to be in line with current market expectations (Gates 2021, Rhodium Group 2020).

2.2. Reliability

Information on thin-walled steel structures

Thin-walled bars are distinguished by a certain geometric dimension ratio. The cross-wall section's thickness is considerably lower than its transverse dimensions, and the element's length is significantly bigger than the cross-dimensions. The works (Gosowski 2004, Piechnik 2000, Gosowski 2015) include detailed instructions for the limit values of transverse dimensions for thin-walled components.

Thin-walled structures found wide application in civil engineering practice not only as the secondary steelwork but also as main bearing capacity members (Fig. 2), due to several benefits they can provide. Among them its lightness, namely high strength in relation to weight, which causes significant reduction in costs. It should be noted that the two requirements are fulfilled by all cold-formed steel sections and only a few hot-rolled steel sections. Thin-walled bars are classified as open, closed, or open-closed based on their cross-sectional geometry.

Fig. 2. System of steel halls made of cold-formed profiles “Blachy Pruszyński” company

[3] According to the European Green Deal strategy, Europe is to become a continent with zero CO2 emissions by 2050 (Ministry of Economy, Trade and Industry, 2022). Japan has also adopted a similar resolution for its economy (European Commission, 2021a). Given the lower level of development of its economy, China does not plan to reach this goal until 2060 (United Nations, 2022).

[4] This is confirmed by the launch in July 2021 of the Chinese platform for trading CO2 emissions permits (Nogrady 2021), which means that their quotations are already influencing steel prices in countries accounting for more than half of global steel production.

[5] In August 2021, the Swedish company Volvo produced its first batch of 'green' steel, while announcing that industrial application of the technology would not be possible until around 2026 (Kindy, 2021).

The abundance of available thin-walled cross-section shapes not only provides steel structure designers with a diverse set of elements, but also, as the author notes (Ostwald and Magnucki 2008), contributes to the emergence of new design problems due to the interaction of global and local forms of loss of stability. Contrary to popular belief, the more time and attention spent to laboratory and numerical analysis of thin-walled steel structures, the more fascinating research topics emerge. As a result, several research institutions are still conducting active research on thin-walled steel structures.

Basic information on composite materials

FRP composite materials are made of high-strength nonmetallic fibers embedded in an epoxy matrix (Kałuża and Bartosik 2015). Currently, three types of composite materials are frequently used in construction, each with a different material from which the fibers are made: CFRP (Carbon Fiber Reinforced Polymer), GFRP (Glass Fiber Reinforced Polymer), and AFRP (Aramid Fiber Reinforced Polymer). Since carbon fibers have very strong strength properties when compared to other materials, CFRP tapes and mats with carbon fiber matrices are the most extensively utilized composite material for reinforcing building structures. Composite material manufacturers assert a wide range of applications for CFRP tapes (Aleksandrowicz 2005). They can be utilized anywhere it is necessary to reinforce the existing structure owing to increasing operating loads (e.g., due to a change in the building's function) or the appearance of new loads, such as the installation of heavy devices. According to studies undertaken by CFRP tape producers (Aleksandrowicz 2005), the basic advantages of CFRP composite materials include the following characteristics: resistance to aggressive agents, corrosion resistance, and no maintenance. An undeniable benefit of CFRP tapes is their low weight (1.6–2.0 g / cm) and narrow cross-section, which allows for nearly imperceptible reinforcement of the structure while also allowing the tapes to be coated. CFRP tapes may be used to strengthen constructions made of diverse materials due to their great variety, which allows for the selection of a tape with the right modulus of elasticity, tensile strength, or cross-sectional dimensions (concrete, steel, wood). It is also critical to be able to reinforce the structure using tensioned straps secured with anchoring devices. All of these benefits are topped off by the simplicity and speed with which they can be applied, as well as the minimal labor costs and convenience with which they can be transported. Despite their numerous advantages, these materials have drawbacks that restrict their usage. Anisotropic strength qualities characterize tapes made with unidirectional carbon fiber. The stiffness and strength of the tapes are quite high along the fibers, however they are substantially weaker perpendicular to the fibers (Linghoff et al. 2009). They have a poor compressive strength, around 10% of the tensile strength, and considerably lower for interlayer shear (debonding) (Mażulis et al. 2011).

Strengthening technology for cold-formed steel structures

Research on the strengthening method by gluing CFRP composites to TWCFS elements is being conducted on a global scale. In the work (Bambach et al. 2007) a method of determining the axial compressive strength of elements reinforced with CFRP composites was developed. The performance of axially compressed, thin-walled hollow sections (SHS - Steel Hollow Sections) strengthened with CFRP was explained in the subsequent years as a continuation of this study (Bambach et al. 2009). The tapes were bonded in layers around the cross-section during the test, with the fibers in the first layer perpendicular to the load direction and parallel in the following layer. The acquired findings show that CFRP application greatly diminished local buckling and enhanced elastic buckling strength. Scheme of spot-welded SHS test column subjected to compression is presented in Figure 3. In the case of axial compression, as described in (Bambach 2014), the main objective of the tests is to enable the control of buckling deformations and to ensure increased compressive strength. The strengthening of bonded CFRP mats was wrapped across the whole cross-section of the test column with square SHS in the work (Imran et al. 2018). The samples were subjected to compression. Figure 3. presents an example of such test subject.

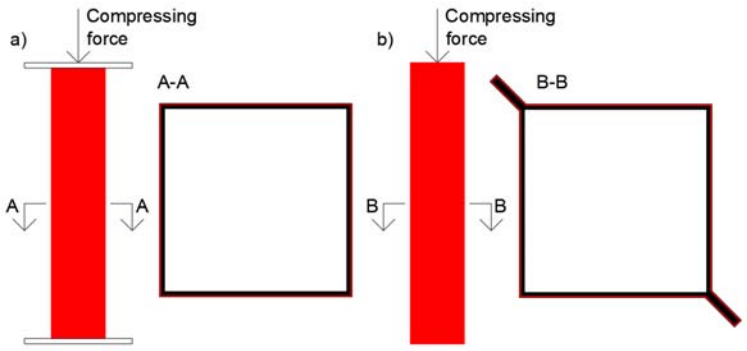

Fig. 3. CFRP strengthened: a) SHS test column (Imran et al. 2018) and b) spot-welded SHS column (Bambach et al. 2009)

Vertical and horizontal displacements can be greatly decreased depending on the location of the bonded CFRP tapes on thin-walled sigma cross-section subjected to bending as reported in (Szewczak et al. 2020) and (Szewczak et al. 2021). An illustrations of the test beams are presented in Figure 4.

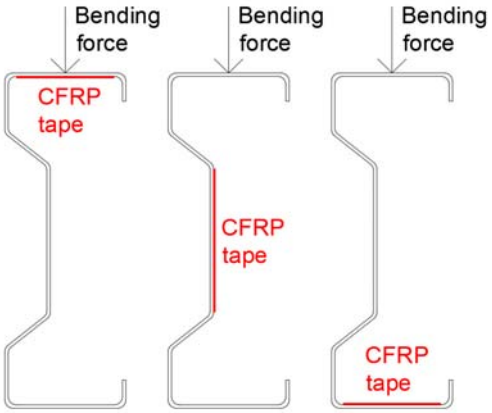

Fig. 4. Sigma cross-sections with CFRP tapes locations (Szewczak et al., 2020)

The study carried out in (Tafsirojjaman et al., 2021) on the cyclically loaded welded beam-column connection built of square SHS components revealed, among other things, that utilizing three layers of CFRP tapes may significantly enhance the bending resistance of such a connection. Figure 5. shows the scheme of described strengthened connection. Example results of strengthening TWCFS elements with CFRP composites are shown in Table 2. It can be observed, that the usage of CFRP composites may provide significant improvement in different aspects of resistance and stability of TWCFS elements.

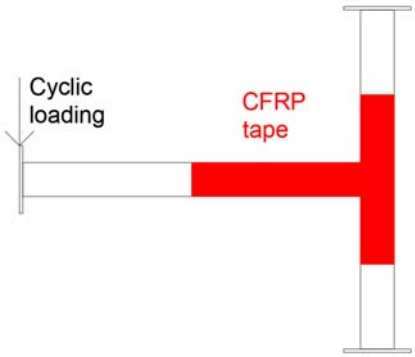

Fig. 5. Schematic of the CFRP strengthened connection (Tafsirojjaman et al., 2021)

Tab. 1. Results of strengthening TWCFS elements with CFRP composites

No	Sources	Conducted research	Results
1.	(Szewczak et al., 2020; Szewczak et al., 2021)	Bending tests performed on thin-walled beams with a cross-section of 200x70x2 reinforced with CFRP.	Horizontal displacements can be decreased by up to 45 percent, while vertical by 17.6%.
2.	(Tafsirojjaman et al., 2021)	Cyclically loaded welded beam-column connection composed of square SHS pieces, with the beam being SHS100x100x3 and the column being SHS100x100x9.	By utilizing three layers of CFRP tapes, the bending resistance of such a connection may be enhanced by up to 41.3 percent.
3.	(Imran et al., 2018)	Bonded CFRP mat reinforcement was wrapped around the whole cross-section.	Reinforced specimens transferred 260 percent more compressive force before the first local buckling forms appeared than unreinforced ones.
4.	(Bambach et al., 2009)	Axially compressed, thin-walled SHS reinforced with CFRP.	The usage of CFRP greatly postponed local buckling and enhanced elastic buckling strength up to 400% of the initial value.

3. RESULTS

3.1. Economic

Because of the increasing worldwide demand for steel, the international steel market's sensitivity to distortions due to its high density of production, and the rising cost of steelmaking, it will be advantageous for corporations to decrease demand for steel. Figure 6 shows a graphical representation of the reasoning behind this assertion.

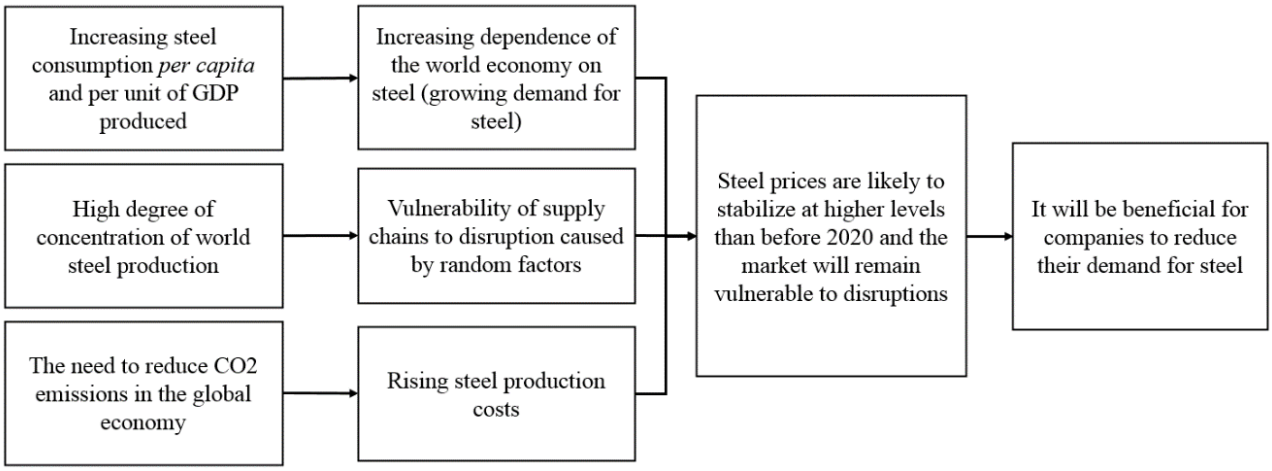

Fig. 6. Factors justifying the need for companies to reduce their steel demand.

In line with recent concerns, there is a growing need to develop a solution that will allow for a reduction in the material input to construction in the face of rising steel costs and projections for their future. One strategy to minimize steel demand is to build thin-walled constructions. In the light of the above, as well as due to the needs of the construction market and the requirements of investors, designers of steel structures are constantly working on designing safe and economical structures. The aim is to reduce the weight of the structure and shorten the assembly time, while meeting the required load-bearing and serviceability conditions. These requirements can be achieved by using a light steel structure made of thin-walled elements. The use of modern, highly automated bending, cutting and drilling processes for the production of cold-formed steel structures, described e.g. in (Bródka et al. 2006), significantly reduces costs. Compared to traditional construction solutions, cold-formed elements have one of the highest indexes determining the strength-to-weight ratio of materials used in their production. According to (Bródka and Łubiński 1978), the development of thin-walled structures allowed for up to a 50% reduction in steel consumption compared to standard structures composed of hot-rolled profiles, as well as a 60% reduction in assembly time and a 25% reduction in construction costs.

3.2. Reliability

Thin-walled steel constructions have become more common in recent years as the major parts of load-bearing structures. As a result, there could be a necessity reinforce them in the future, for example, due to higher external loads. Composites based on high-strength non-metallic fibres contained in an epoxy resin matrix (Fiber Reinforced Polymer), such as CFRP, GFRP, and AFRP tapes, are one of the futuristic techniques. These tapes are bonded to the structure to ensure rapid and effective strengthening while not interfering with the operation's continuity. Section 2.2 summarizes some of the research that has been done thus far. Furthermore, it can be observed that this innovative method may provide significant performance improvements for thin-walled elements. The quantity of publications on this subject is currently relatively low. As a result, more study on the issue discussed in this work is required.

4. CONCLUSIONS

A steel market analysis was conducted based on a review of the literature, industry media and market trends, and a reliability analysis of cold-formed thin-walled steel elements strengthened with CFRP composites was conducted based on a review of laboratory and numerical tests as well as selected examples from the existing literature. Based on the above analyses, two main conclusions were drawn. Firstly, in the light of the increasing global demand for steel, the vulnerability of the global steel market to distortions arising from high concentrations of production and the rising costs of steel production, it will be beneficial for companies to reduce their demand for steel. Secondly, one possible way of reducing steel consumption in construction industry and therefore construction costs may be the usage of cold-formed thin-walled steel elements strengthened with CFRP composites on the wider scale. While it remains true that the principles of using CFRP tapes to strengthen concrete structures are now well established, there is a lack of design guidance for steel structures. At present, the number of publications on this matter is very limited and most of them focus on the analysis of compressed elements. As a result, it is necessary to carry out further research on the subject described in this paper.

ACKNOWLEDGEMENTS

Funding: This paper was financially supported by Poznan University of Technology: 0412/SBAD/0060, FN-4/2021 WBIA

REFERENCES

Aleksandrowicz, M. 2005. Podstawowe informacje o systemach wzmacniania konstrukcji budowlanych i inżynierskich za pomocą materiałów kompozytowych Sika CarboDur System, http://www.bzg.pl/node/282 [accessed: 30.01.2022].

Bambach, M.R. & Elchalakani, M. 2007. Plastic mechanism analysis of steel SHS strengthened with CFRP under large axial deformation. Thin-Walled Structures 45(2): 159–170.

Bambach, M.R., Jama, H.H., Elchalakani, M. 2009. Axial capacity and design of thin-walled steel SHS strengthened with CFRP. Thin Walled Structures 47(10): 1112–1121.

Bambach, M.R. 2014. Strengthening of thin-walled (hollow) steel sections using fibre-reinforced polymer (FRP) composites. In: Karbhari V.M. (Ed.), Rehabilitation of Metallic Civil Infrastructure Using Fiber Reinforced Polymer (FRP) Composites (p. 140-168). Sawston: Woodhead Publishing.

BBC 2021. Wuhan lockdown: A year of China's fight against the Covid pandemic, https://www.bbc.com/news/world-asia-china-55628488 [accessed: 07.10.2021].

Bogart, D., You, X., Alvarez-Palau, E., Satchell, M., Shaw-Taylor, L. 2021. Railways, divergence, and structural change in 19th century England and Wales. Journal of Urban Economics. 103390.

Bródka, J., Łubiński, M. 1978. Lekkie konstrukcje stalowe. Warszawa: Arkady.

Bródka, J., Broniewicz, M., Giżejowski, M. 2006. Kształtowniki gięte: poradnik projektanta. Rzeszów: Polskie Wydawnictwo Techniczne.

Chang, H-J. 2006. The East Asian Model of Economic Policy. In: The East Asian Development Experience: The Miracle, the Crisis and the Future (p. 13-62). London: Zed Books.

Eichengreen, B. 2006. Managing the world economy in the 1990s. In: Rhode P., Toniolo G. (Eds.), The Global Economy in the 1990s: A Long-Run Perspective (p. 43-68). Cambridge: Cambridge University Press.

European Commission. 2021a. European Green Deal, https://ec.europa.eu/clima/eu-action/european-green-deal_en [accessed: 08.10.2021].

European Commission. 2021b. EU Emissions Trading System (EU ETS), https://ec.europa.eu/clima/eu-action/eu-emissions-trading-system-eu-ets_en [accessed: 08.10.2021].

European Commission. 2014. ULCOS top gas recycling blast furnace process (ULCOS TGRBF): final report. Luxembourg: Publications Office of the European Union.

Gates, B. 2021. Jak ocalić świat od katastrofy klimatycznej. Warszawa: Wydawnictwo Agora.

Gosowski, B. 2004. Skręcanie i zginanie otwartych elementów konstrukcji metalowych. Wrocław: Oficyna Wydawnicza Politechniki Wrocławskiej.

Gosowski, B. 2015. Zginanie i skręcanie cienkościennych elementów konstrukcji metalowych. Wrocław: Oficyna Wydawnicza Politechniki Wrocławskiej.

Hummel, R.E. 1998. The Iron Age. In: Understanding Materials Science (p. 123-137). New York: Springer.

Imran, M., Mahendran, M., Keerthan, P. 2018. Experimental and numerical investigations of CFRP strengthened short SHS steel columns. Engineering Structures 175: 879-894.

Kałuża, M., Bartosik, T. 2015. Wzmacnianie konstrukcji budowlanych materiałami kompozytowymi FRP, https://inzynierbudownictwa.pl/wzmacnianie-konstrukcji-budowlanych-materialami-kompozytowymi-frp/ [accessed: 12.10.2021].

Kelly, T. D., Matos, G.R. 2013. Historical Statistics for Mineral and Material Commodities in the United States, https://www.usgs.gov/centers/nmic/historical-statistics-mineral-and-material-commodities-united-states [accessed: 30.09.2021].

Kindy, D. 2021. Fossil Fuel–Free 'Green' Steel Produced for the First Time, https://www.smithsonianmag.com/smart-news/green-steel-produced-first-time-180978550/ [accessed: 08.10.2021].

Linghoff, D., Haghani, R., Al-Emrani, M. 2009. Carbon-fibre composites for strengthening steel structures. Thin-Walled Structures 47(10): 1048–1058.

Lucas, A.R. 2005. Industrial Milling in the Ancient and Medieval Worlds: A Survey of the Evidence for an Industrial

Revolution in Medieval Europe. Technology and Culture 46(1): 1-30.
Macrotrends. 2022. Euro Dollar Exchange Rate (EUR USD) - Historical Chart, https://www.macrotrends.net/2548/euro-dollar-exchange-rate-historical-chart [accessed: 02.02.2022].
MarketLine. 2021. US steel prices are up over 200% and expected to remain high into 2022, https://www.mining-technology.com/comment/us-steel-prices-remain-high-into-2022/ [accessed: 07.10.2021].
Market Watch. 2022. HRC Steel Futures Continuous Contract, https://www.marketwatch.com/investing/future/hrn00 [accessed: 02.01.2022].
Mażulis, J., Wrzesiński, M., Bierońska, K. 2011. Efekt wzmocnienia konstrukcji stalowych przy użyciu włókien węglowych. Przetwórstwo Tworzyw 17(6): 475–478.
Ministry of Economy, Trade and Industry. 2021. Japan's Roadmap to "Beyond-Zero" Carbon, https://www.meti.go.jp/english/policy/energy_environment/global_warming/roadmap/index.html [accessed: 08.10.2021].
Mokyr, J. 1998. The Second Industrial Revolution, 1870-1914, https://faculty.wcas.northwestern.edu/~jmokyr/castronovo.pdf [accessed: 01.10.2021].
Monarch Metal. 2021. 3 Reasons Steel Prices Skyrocketed in 2020, https://www.monarchmetal.com/blog/steel-prices-expected-to-continue-rising-in-2021/ [accessed: 07.10.2021].
Morton, G.R., Mutton, N. 1967. The transition to Cort's pudding process. Journal of Iron and Steel Institute 205(7): 722-728.
Netherlands Environmental Assessment Agency. 2013. History database of the Global Environment, https://www.pbl.nl/en/image/links/hyde [accessed: 30.09.2021].
Nogrady, B. 2021. China launches world's largest carbon market: but is it ambitious enough?, https://www.nature.com/articles/d41586-021-01989-7 [accessed: 08.10.2021].
Organisation of Economic Co-Operation and Development. 2006. The World Economy: Volume 1: A Millennial Perspective and Volume 2: Historical Statistics. Paris: OECD Publishing.
Oswald, M., Magnucki, K. 2008. Optymalne projektowanie belek cienkościennych walcowanych na zimno o przekrojach otwartych. Poznań: Agencja Reklamowa Comprint.
Piechnik, S. 2000. Pręty cienkościenne – otwarte. Kraków: Wydawnictwo Politechniki Krakowskiej.
Rehren, T. et al. 2013. 5,000 years old Egyptian iron beads made from hammered meteoritic iron. Journal of Archaeological Science 40(12): 4785–4792.
Rhodium Group. 2020. Clean Products Standard. A New Approach to Industrial Decarbonization. New York: Rhodium Group LLC.
Suzuki, I., Kaneko, Y. 2013. Japan's disaster governance: how was the 3.11 crisis managed?. New York: Springer.
Szewczak, I., Rzeszut, K., Różyło, P., Samborski, S. 2020. Laboratory and Numerical Analysis of Steel Cold-Formed Sigma Beams Retrofitted by Bonded CFRP Tapes. Materials, 13(19): 4339.
Szewczak, I., Rozylo, P. & Rzeszut, K. 2021. Influence of Mechanical Properties of Steel and CFRP Tapes on the Effectiveness of Strengthening Thin-Walled Beams. Materials, 14(9): 2388.
Tafsirojjaman, T., Fawzia, S., Thambiratnam, D. & Zhao, X. 2021. FRP strengthened SHS beam-column connection under monotonic and large-deformation cyclic loading. Thin Walled Structures 161: 107518.
Trading Economics. 2022. EU Carbon Permits, https://tradingeconomics.com/commodity/carbon [accessed: 02.01.2022].
United Nations. 2021. China headed towards carbon neutrality by 2060; President Xi Jinping vows to halt new coal plants abroad, https://news.un.org/en/story/2021/09/1100642 [accessed: 08.10.2021].
World Population Review. 2021. Steel Production By Country 2021, https://worldpopulationreview.com/country-rankings/steel-production-by-country [accessed: 01.10.2021].
World Steel Association. 2021. 2021 World Steel in Figures. Brussels: World Steel Association.

LIGHTWEIGHT STRUCTURES in CIVIL ENGINEERING
CONTEMPORARY PROBLEMS
Monograph from Scientific Seminar
Organized by Polish Chapters of
International Association for Shell and Spatial Structures
Łódź University of Technology
Faculty of Civil Engineering, Architecture
and Environmental Engineering
XXVII LSCE
Łódź, 2nd – 3rd of December 2021

OPTIMUM DESIGN OF BARREL VAULTS STRUCTURES USING RAO ALGORITHM

M. Grzywiński [1] **T. Dede** [2] **B. Atmaca** [3]
[1] Dr, Faculty of Civil Eng., Czestochowa University of Technology, POLAND,
maksym.grzywinski@pcz.pl
[2] Prof, Department of Civil Eng., Karadeniz Technical University, TURKEY, *dtayfun@ktu.edu.tr*
[3] Dr, Department of Civil Eng., Karadeniz Technical University, TURKEY, *atmaca@ktu.edu.tr*

ABSTRACT: The aim of this study is to present the optimization of double-layer barrel vault structures taking into account the stresses and buckling of compression structural members and nodal displacements as constraints. The buckling is calculated according to the AISC-ASD. In the optimization process a new proposed algorithm named Rao-1 is preferred. The finite element analysis of barrel vault structures is carried out by using applicable programming interface properties of SAP2000 program. The MATLAB programming is used to data transfer from the SAP2000 for sending design variables and getting the stresses and nodal displacement of the structure analysis.

Keywords: Rao-1 algorithm, barrel vaults, optimization, buckling analysis, OAPI-SAP2000.

1. INTRODUCTION

Barrel vault structures can be considered as special roof to cover large span areas such as stadium, shopping center and exhibition halls. These types of structures are usually designed double or single layer geometry in one direction curve form. In the case of the double layer barrel vault structures (DLBV), the bottom and top barrel vaults are connected to each other by braced line elements keeping the symmetry of the structure.
Like the other civil engineering structures the barrel vaults are optimized for the minimum weight of total structure without violating some structural constraints such as nodal displacement and the buckling of compression line element. In the literature there are some paper related to the barrel vaults structures. The aim of these studies is to find a global optimal solution by using metaheuristic algorithm instead of using a mathematical explanation.
Kaveh and Eftekhar (2012) presented optimal design of barrel vaults using the improved big bang-big crunch (IBB-BC) method. This method can be used for problems with continuous and discrete variables. Kaveh *et al.* (2014) used improved magnetic charged system search (IMCSS) for the optimal design of the DLBV. They used open application programming interface (OAPI) properties of SAP2000 for optimization of DLBV. Kaveh and Moradveisi (2016) applied two different optimization methods, colliding bodies (CBO) and its enhanced version (ECBO) for DLBV structures under the static loads.
Hasançebi *et al.* (2011) presented a conference paper on large scale structural optimization by using ant colony optimization algorithm (ACO). They optimized 693-bar braced barrel vault structure with the discrete set design variables and compared their optimal results with those of other methods, such as particle swarm

optimization (PSO), harmony search optimization (HSO) and genetic algorithms (GA). Hasançebi and Kazemzadeh (2013) used big bang-big crunch algorithm (BB-BC) for discrete structural design optimization of barrel, grill and 3D framed structures. They used AISC standard sections for design variables and taken into account stress, stability and geometric constraints according to AISC-ASD. Hasançebi and Kazemzadeh (2015) presented study a new metaheuristic algorithm called adaptive dimensional search (ADS) is proposed for discrete truss sizing optimization problems.

Grzywiński (2015) presented optimization algorithm available in Autodesk Robot Structural Professional for design of the double layer barrel vaults. Grzywiński *et al.* (2019) used teaching-learning-based optimization algorithm (TLBO) to solve the weight minimization problem of truss structures considering shape, and sizing design variables. Tunca *et al.* (2017) made a study on optimum design of braced barrel vault systems using cold-formed steel sections. The authors of that paper used the artificial bee colony algorithm (ABC) to optimize the structure. Dede *et al.* (2020) presented the Rao-1 algorithm for optimization of 384-bar double layer barrel vault structure without violating structural constraints such as nodal displacement, stresses and the buckling.

In this study, optimization of DLBV using a new proposed algorithm named Rao-1 is presented. This new optimization algorithm is firstly presented by Rao (2020). The allowable steel pipe sections for the cross-sectional areas of the bar elements of DLBV are taken from AISC-LRFD (1989). The nodal displacement and the tension or compression stresses are taken into account as constraints for the optimization process. The allowable tensile and compressive stresses are calculated according to the AISC-ASD (1994).

2. RAO ALGORITHM

After developing several successful optimization algorithms such as TLBO (Rao 2011) and Jaya (Rao 2016), Rao proposed a new algorithms named: Rao-1, Rao-2, and Rao-3 (Rao 2020). Like his previous optimization algorithms, the Rao algorithms does not need any algorithm-specific parameters. Rao algorithms is a population-based optimization technique.

Let f(x) is the objective function to be minimized (or maximized). At any iteration "i", assume that there are "m" number of design variables, "n" number of candidate solutions (i.e. population size, k=1,2,…,n). Let the best candidate *best* obtains the best value of f(x) (i.e. $f(x)_{best}$) in the entire candidate solutions and the worst candidate *worst* obtains the worst value of f(x) (i.e. $f(x)_{worst}$) in the entire candidate solutions. If $X_{j,k,i}$ is the value of the "j-th" variable for the "k-th" candidate during the "i-th" iteration, then this value is modified as per the following equations:

$$\text{Rao-1: } X'_{j,k,i} = X_{j,k,i} + r1_{j,i}\left(X_{j,best,i} - X_{j,worst,i}\right), \tag{1}$$

$$\text{Rao-2: } X'_{j,k,i} = X_{j,k,i} + r1_{j,i}\left(X_{j,best,i} - X_{j,worst,i}\right) + r2_{j,i}\left(\left|X_{j,k,i} \text{ or } X_{j,l,i}\right| - \left|X_{j,l,i} \text{ or } X_{j,k,i}\right|\right), \tag{2}$$

$$\text{Rao-3: } X'_{j,k,i} = X_{j,k,i} + r1_{j,i}\left(X_{j,best,i} - \left|X_{j,worst,i}\right|\right) + r2_{j,i}\left(\left|X_{j,k,i} \text{ or } X_{j,l,i}\right| - \left|X_{j,l,i} \text{ or } X_{j,k,i}\right|\right), \tag{3}$$

where: $r1_{j,i}$ and $r2_{j,i}$ are a randomly number in the range [0, 1].

In Eqs.(2) and (3) the term $X_{j,k,i}$ *or* $X_{j,l,i}$ indicates that the candidate solution "k" is compared with any randomly picked candidate solution "l" and the information is exchanged based on their fitness values. If the fitness value of "k-th" solution is better than the fitness value of "l-th" solution then the term $X_{j,k,i}$ *or* $X_{j,l,i}$ becomes $X_{j,k,i}$. On the other hand, if the fitness value of "l-th" solution is better than the fitness value of "k-th" solution then the term $X_{j,k,i}$ *or* $X_{j,l,i}$ becomes $X_{j,l,i}$. The flowchart of Rao-1 algorithm is shown in Figure 1. Rao algorithms are given in the following web page: https://sites.google.com/view/raoalgorithms/.

The Rao-2 algorithm looks structurally very similar to the Particle Swarm Optimization algorithm (Kennedy and Eberhart, 1995), but is designed to be even simpler and without parameters. A particle in this algorithm, instead heading to the personal best and the global best simultaneously, it heads towards the best and away from the worst, and it has no inertia.

A PSO method performs search using particles population. During the search process, the searching velocity is updated $V_{jk}(t+1)$ to be used to determine the following position $X_{jk}(t+1)$. The current position $X_{jk}(t)$ and velocity of each particle $V_{jk}(t)$ can be modified by the following Eqs. (4) and (5).

$$V_{jk}(t+1) = wV_{jk}(t) + C_1 r_1 \left(X_{pbest,jk} - X_{jk}(t)\right) + C_2 r_2 \left(X_{gbest,jk} - X_{jk}(t)\right), \tag{4}$$

$$X_{jk}(t+1) = X_{jk}(t) + V_{jk}(t+1), \tag{5}$$

where: r_1 and r_2 represent random numbers C_1 and C_2: cognitive and social acceleration constant respectively, w: inertia weight factor.

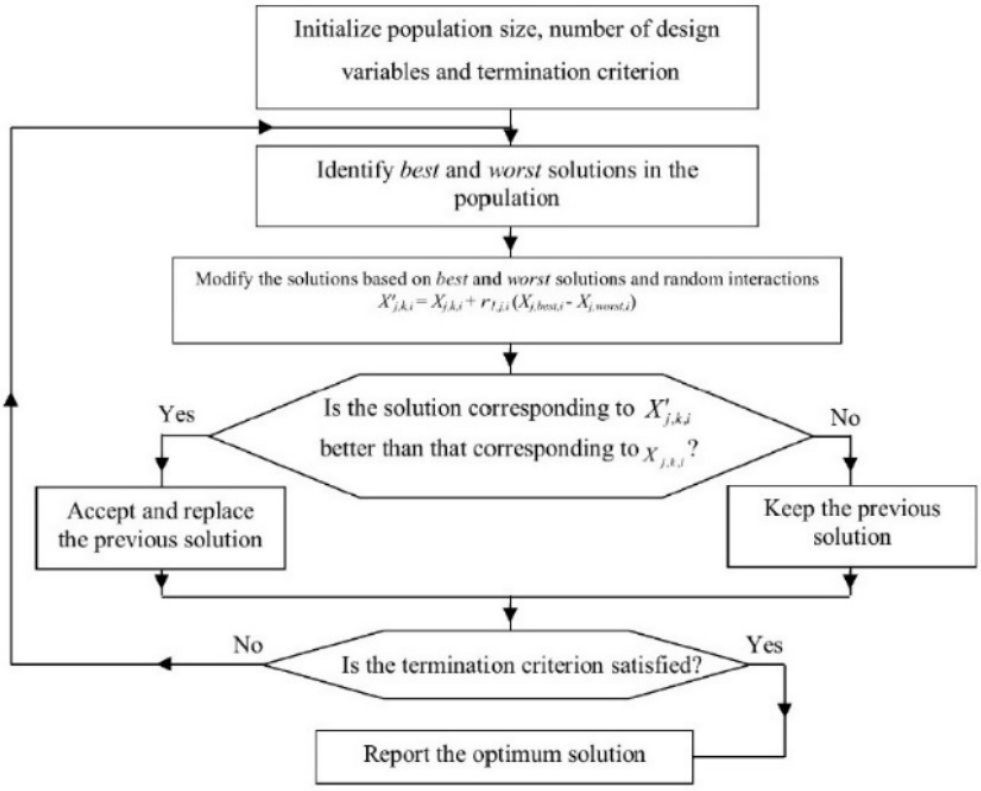

Fig.1 Flowchart of Rao-1 algorithm.

3. FINITE ELEMENT ANALYSIS OF BARREL VAULT STRUCTURES

Finite element method (FEM) is very well represented in many articles and books. As an example is recommended (Lewiński *et al.* 2019). Barrel vault structures can be analysis like a 3D truss structures. A bar element for barrel vault structure is given in the Figure 2. As seen from this figure, 3D bar element has two nodal points and three degree of freedom in each node. These freedoms are the displacements in x, y and z directions.

Where, “i”, “j” are the nodal points, x, y, z are the element axis sets, u_{ix}, v_{iy}, w_{iz} are displacements for node “i” in x, y, z direction, respectively. u_{jx}, v_{jy}, w_{jz} are displacements for node “j" in x, y, z direction, respectively. The nodal displacements $\{U\}$ and load forces $\{F\}$ are shown in the vector form given below:

$$\{U\}=\begin{Bmatrix} u_{ix} \\ v_{iy} \\ w_{iz} \\ u_{jx} \\ v_{jy} \\ w_{jz} \end{Bmatrix}, \quad \{F\}=\begin{Bmatrix} f_{ix} \\ f_{iy} \\ f_{iz} \\ f_{jx} \\ f_{jy} \\ f_{jz} \end{Bmatrix}. \tag{6}$$

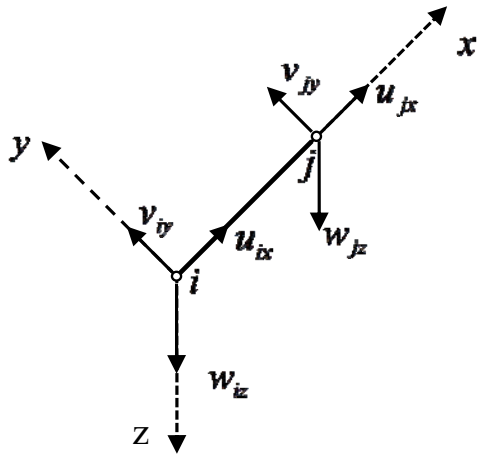

Fig.2 A bar element in 3D for barrel vault structure.

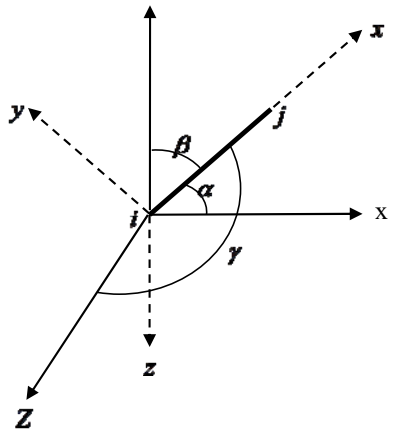

Fig. 3. Local and global axes for 3D truss element.

Element stiffness matrix for the barrel vault structure is calculated by the using Eq. 7.

$$\left[K\right]_{ij}^{e}=\frac{EA}{L}\begin{bmatrix} 1 & 0 & 0 & -1 & 0 & 0 \\ 0 & 0 & 0 & 0 & 0 & 0 \\ 0 & 0 & 0 & 0 & 0 & 0 \\ -1 & 0 & 0 & 1 & 0 & 0 \\ 0 & 0 & 0 & 0 & 0 & 0 \\ 0 & 0 & 0 & 0 & 0 & 0 \end{bmatrix}, \tag{7}$$

where E is Young modulus, L is length of the bar element and A is the cross-sectional area of the bar element.

The element stiffness matrix created in the element axes must be transformed to the global axes by using the transformation matrix. To calculate the transformation matrix, direction cosines given in the Figure 3 are used. Where X, Y, Z are the global axes, x, y, z are the local axes, and α, β, γ are the angles for the bar element with the global direction X, Y and Z, respectively.

$$T=\begin{bmatrix} \gamma_X & \gamma_Y & \gamma_Z & 0 & 0 & 0 \\ 0 & 0 & 0 & 0 & 0 & 0 \\ 0 & 0 & 0 & 0 & 0 & 0 \\ 0 & 0 & 0 & \gamma_X & \gamma_Y & \gamma_Z \\ 0 & 0 & 0 & 0 & 0 & 0 \\ 0 & 0 & 0 & 0 & 0 & 0 \end{bmatrix}. \tag{8}$$

The transformation matrix T is given in the Eq. 8, where the γ_X, γ_Y, γ_Z are the cosine angles of the α, β, γ, respectively.

$$\gamma_X = \cos\alpha = \frac{x_j - x_j}{L}, \tag{9}$$

$$\gamma_Y = \cos\beta = \frac{y_j - y_j}{L}, \tag{10}$$

$$\gamma_Z = \cos\gamma = \frac{z_j - z_j}{L}. \tag{11}$$

The element stiffness matrix in the global axes can be formed by the following equation. Then, the stiffness matrix for all structure is created by assembling the element stiffness matrix.

$$\left[K\right]_{ij}^{s} = \left[T\right]^{T} . \left[K\right]_{ij}^{e} . \left[T\right], \tag{12}$$

$$\left[K\right] = \sum_{k=1}^{n} \left[K\right]_{ij}^{s} . \tag{13}$$

Where “n” is the number of elements. After the assembling, structural stiffness matrix and load vector, the general equation of nodal deformation of the structures can be written as:

$$\left[K\right]\left\{U\right\} = \left\{F\right\}. \tag{14}$$

4. NUMERICAL EXAMPLE

The objective function of the present study is to minimize the weight of the barrel vaults structures. For this purpose, the general equation can be written as follow.

$$F_{obj} = \rho \sum_{i=1}^{m} L_i A_i \quad i = 1,2,...,m, \tag{15}$$

where “F_{obj}” is the objective function, “ρ” is the material density, “L” is the elements length in vault structure, “A” is the cross-sectional area and “m” is the number of elements. In this study, the nodal displacement of the free nodes, the allowable stresses and the slenderness ratio for tensile and compressive member are taken as design constraints:

$$\sigma_j^t < \sigma_{j,all}^t \text{ and } \sigma_j^c < \sigma_{j,all}^c \qquad i=1,2,...,nm, \tag{16}$$

$$\sigma_j^t < \sigma_{j,all}^t \text{ and } \sigma_j^c < \sigma_{j,all}^c$$
$$\lambda_j^t < \lambda_{j,all}^t \text{ and } \lambda_j^c < \lambda_{j,all}^c \qquad j=1,2,...,nm, \tag{17}$$

where "δ_i" is the nodal displacement, "δ_{max}" is the maximum displacement, "nn" is the number of nodes, "σ_j^t" is the tensile stress and "$\sigma_{j,all}^t$" is the allowable tensile stresses, "σ_j^c" is compression stress, "$\sigma_{j,all}^c$" allowable compression stress, "nm" is the number member and the "λ" is the slenderness ratio both tensile and compression members. If the design variables violate the constraint, the penalty function in terms of the total weight and the violated constraints are calculated as given below.

$$f_{penalty} = W\left(1+\varepsilon_1 C\right)^{\varepsilon_2}, \tag{18}$$

$$\varepsilon_1 = 1.0 \text{ and } \varepsilon_2 = 1.5 + 1.5\frac{Iter}{MaxIter}, \tag{19}$$

where "*Iter*" is the current iteration number and the "*MaxIter*" is the maximum iteration number. So, the "ε_2" will be gradually equal to 3. The penalty function "*C*" is calculated as given below:

$$C = C_\delta + C_\sigma + C_\lambda, \tag{20}$$

$$C_\delta = \sum_{i=1}^{\text{nm}} max\left(\left|\frac{\delta_i}{\delta_{max}}\right| - 1.0\right),\ C_\sigma = \sum_{j=1}^{\text{nm}} max\left(\left|\frac{\sigma_i}{\sigma_{all}}\right| - 1.0\right),\ C_\lambda = \sum_{j=1}^{\text{nm}} max\left(\left|\frac{\lambda_i}{\lambda_{all}}\right| - 1.0\right). \tag{21}$$

At the end of the optimization process, the penalized objective function must be equal to the objective function. That is, the penalty function must be equal to zero. By using the penalty function, the penalized objective function can be written as given below. By using the penalized objective function at all steps of the optimization process, it is hoped that the final candidate solutions will yield the best solution and do not violate the constraints. If the final candidate solutions don't violate the constraints of the optimization problem, the penalized objective function will be equal to the objective function.

$$\left\{\Phi_{obj}\right\} = \left\{F_{obj}\right\} \cdot \left[1 + C\right]. \tag{22}$$

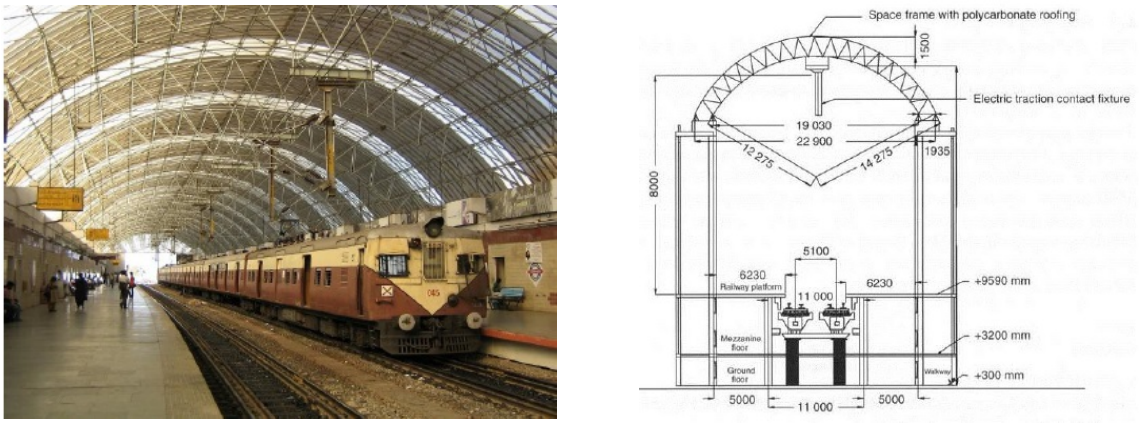

a) b)

Fig. 1. a) The platform shelter at Thirumailai Station, b) the cross-section of the parallel vault and railway tracks.

5. NUMERICAL EXAMPLE

The example is a three-dimensional DLBV structure which was already built for roofing the platform shelters at the Thirumailai Railway Station in Chennai, India as shown in Fig. 1(a) and 1(b). The braced barrel vault contains 259 joints and 693 bars which are linked into 23 independent size variables considering the symmetry about centerline as shown in Fig. 2a. The member grouping scheme is shown in Fig. 2(a) and the front and plan view are provided in Fig. 2(b) and Fig. 2(c), respectively.

It is assumed that the barrel vault is subjected to a uniform dead load (DL) pressure of 35 kg/m^2, a positive wind load (WL) pressure of 160 kg/m^2, and a negative wind load (WL) pressure of 240 kg/m^2 which are combined under two separate load cases for design purposes as follows:

(i) 1.5(DL+WL) = 1.5(35 +160) = + 292.5 kg/m^2 (+2.87 kN/m^2)

(ii) 1.5(DL–WL) = 1.5(35 – 240) = –307.5 kg/m^2 (–3.00 kN/m^2), along z direction.

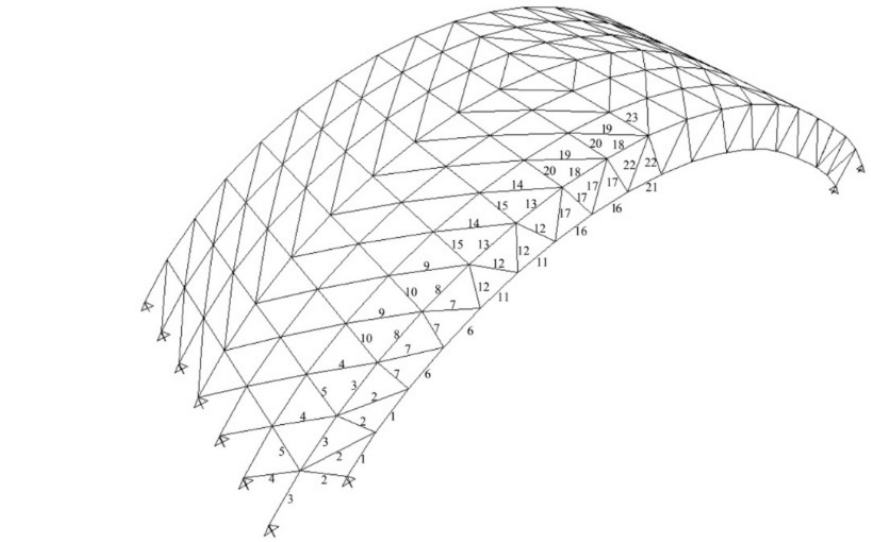

a)

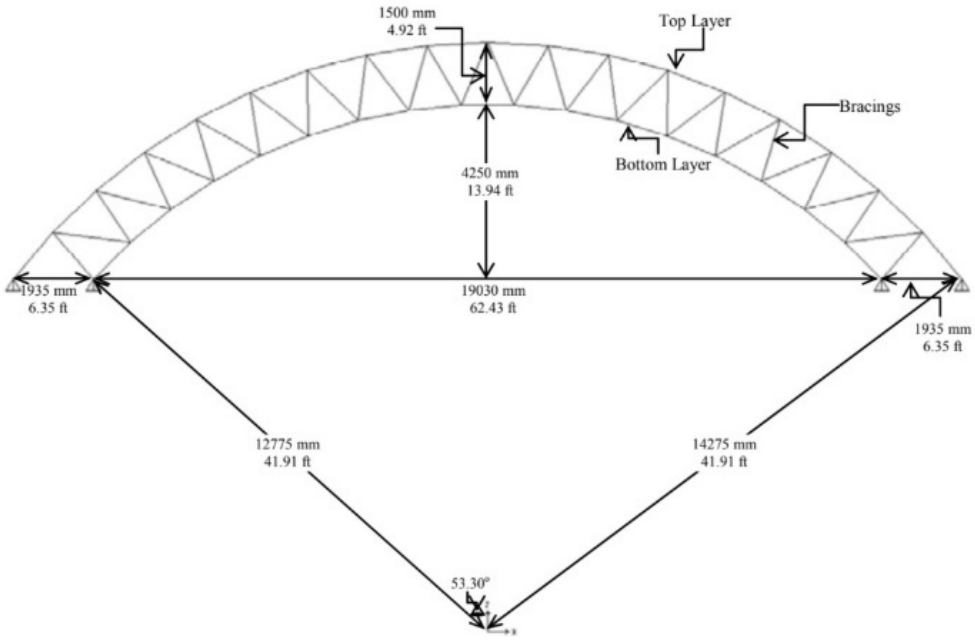

b)

Fig. 2. The 693-bar braced vault: a) 3-D view, b) front view.

The displacements of all joints in any direction are restricted to a maximum value of 0.254 cm (0.1 in). The strength and stability requirements of steel members are imposed according to Allowable Stress Design of the American Institute of Steel Construction (ASD-AISC). In Table 1 the structural members are adopted from a list of 37 circular hollow sections. The obtained optimal design variables and the value of objective function are given in Table 2 by comparing the previous study given in literature.

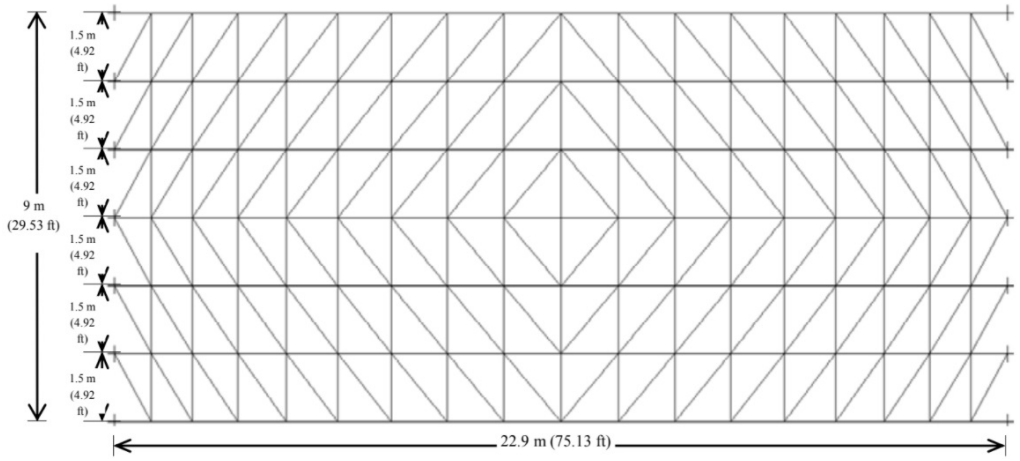

c)

Fig. 2 The 693-bar braced vault: c) plan view.

Tab. 1. Allowable set of steel pipe sections.

No	Type	D (in)	No	Type	D (in)	No	Type	D (in)
1	ST	½	16	EST	½			
2	ST	¾	17	EST	¾			
3	ST	1	18	EST	1			
4	ST	1 ¼	19	EST	1 ¼			
5	ST	1 ½	20	EST	1 ½			
6	ST	2	21	EST	2	31	DEST	2
7	ST	2 ½	22	EST	2 ½	32	DEST	2 ½
8	ST	3	23	EST	3	33	DEST	3
9	ST	3 ½	24	EST	3 ½			
10	ST	4	25	EST	4	34	DEST	4
11	ST	5	26	EST	5	35	DEST	5
12	ST	6	27	EST	6	36	DEST	6
13	ST	8	28	EST	8	37	DEST	8
14	ST	10	29	EST	10			
15	ST	12	30	EST	12			

ST=standard weight, EST=extra strong, DEST=double-extra strong

Tab. 2. Comparative results for the 693-bar braced barrel vault structure.

Element	Hasançebi *et al.* (2011)		Kaveh *et al.* (2014)		This study
group	ACO	HS	MCSS	IMCSS	Rao-1
1	DEST 2 ½	EST 3 ½	EST 3	EST 3 ½	DEST 2 ½
2	ST 1	EST ¾	ST 1	ST 1	ST 1
3	ST 1	ST 1	EST ¾	EST 1	ST ¾
4	ST 1	ST 1	EST ½	ST ¾	ST 1
5	ST 1	EST ¾	EST ½	ST 1	ST ¾
6	ST ¾	ST 4	EST 3	DEST 2	EST 3 ½
7	EST 1	ST 1 ¼	EST 1 ¼	ST 1	ST 1
8	ST ¾	ST ¾	ST 1	ST 1 ¼	ST 1
9	ST 3 ½	ST 3 ½	ST ¾	EST ½	ST 1
10	DEST 2 ½	ST 1	EST ½	ST ½	ST ¾
11	ST 1	ST 1 ¼	EST 2 ½	ST 3	DEST 2

Tab. 2. Comparative results for the 693-bar braced barrel vault structure.

12	EST 1	EST 1 ¼	EST 1 ½	EST 1 ¼	EST 1
13	EST 1 ¼	EST 1 ½	ST 2 ½	EST 2	ST 2
14	EST 1	EST 1 ¼	ST ¾	ST ½	ST 1
15	ST ¾	ST ¾	ST ¾	ST ¾	ST ¾
16	EST 1	EST 1 ¼	ST 1 ¼	EST 1 ¼	ST 2
17	EST 1 ¼	EST 1 ¼	ST 1 ½	ST 1 ½	ST 1 ¼
18	ST 1	ST 1 ¼	ST 3	ST 3	ST 2 ½
19	ST 1 ¼	EST 1	EST ¾	ST ¾	ST 1
20	ST ¾	ST ¾	ST ½	ST ¾	ST ¾
21	ST 2 ½	ST 2 ½	ST 1 ¼	ST 1	ST 1
22	ST 1 ¼	ST 1	EST ¾	EST 1	ST ¾
23	ST 1	EST 1	ST ¾	EST ¾	ST ¾
Weight (kg)	**4989.15**	**5095.07**	**4904.42**	**4785.81**	**4810.03**
NA	45650	48150	14300	9200	17280

NA – number of analysis

6. CONCLUSION

The main purpose of this study is to make the optimal design of the double-layer barrel vault structure using a metaheuristic algorithm named Rao-1. For this aim, 693-member barrel vault structure is examined. To carry out the optimization process the required computer codes are developed in MATLAB. This program can transfer data from the SAP2000. The optimal result obtained from this study shows that the proposed algorithm can be effectively used for the optimization of the structures.

REFERENCES

AISC-ASD 1989. *Manual of Steel Construction: Allowable Stress Design*, 9th edition, Chicago: American Institute of Steel Construction.

AISC-LRFD 1994. *Manual of Steel Construction: Load & Resistance Factor Design*. 2nd edition, Chicago: American Institute of Steel Construction.

Dede, T., Grzywiński, M., Rao, R.V. & Atmaca B. 2020. *The size optimization of steel braced barrel vault structure by using Rao-1 algorithm*. Sigma Journal of Engineering and Natural Sciences 38(3):1415-1425.

Grzywiński, M. 2015. *Optimization of double-layer braced barrel vaults*, Transactions of the VŠB – Technical University of Ostrava, Civil Engineering Series 15(2):paper #06

Grzywiński, M., Selejdak, J. & Dede, T. 2019. *Shape and size optimization of trusses with dynamic constraints using a metaheuristic algorithm*. Steel and Composite Structures 33(5):747–753.

Hasançebi, O., Çarbas, S. & Saka, M.P. 2011. *A reformulation of the ant colony optimization algorithm for large scale structural optimization*, Proceedings of the Second International Conference on Soft Computing Technology in Civil, Structural and Environmental Engineering, Civil-Comp Press, Stirlingshire, UK, Paper 12.

Hasançebi, O. & Kazemzadeh Azad, S. 2013. *Reformulations of big bang-big crunch algorithm for discrete structural design optimization.* International Journal of Civil and Environmental Engineering 7(2):139-150.

Hasançebi, O. & Kazemzadeh Azad, S. 2015. *Adaptive dimensional search: A new metaheuristic algorithm for discrete truss sizing optimization.* Computers & Structures 154:1-16.

Kaveh, A. & Eftekhar, B. 2012. *Optimal design of double layer barrel vaults using an improved hybrid big bang-big crunch method*. Asian Journal of Civil Engineering 13(4):465-487.

Kaveh, A., Mirzaei, B. & Jafarvand, A. 2014. *Optimal design of double layer barrel vaults using improved magnetic charged system search*, Asian Journal of Civil Engineering 15(1):135-154.

Kaveh, A. & Moradveisi, M. 2016. *Optimal design of double-layer barrel vaults using CBO and ECBO algorithms*. Iranian Journal of Science and Technology, Transactions of Civil Engineering 40(3):167-178.

Kennedy, J. & Eberhart, R. 1995. *Particle Swarm Optimization*. Proceedings of the IEEE International Conference on Neural Networks, 4:1942-1948.

Lewiński, T., Sokół, T. & Graczykowski C. 2019. *Michell Structures*, Springer.

Rao, R.V., Savsani, V.J. & Vakharia D.P. 2011. *Teaching-learning based optimization: A novel method for constrained mechanical design optimization problems*. Computer-Aided Design 43(3), 303-315

Rao, R.V. 2016. *Jaya: A simple and new optimization algorithm for solving constrained and unconstrained optimization problems*. International Journal of Industrial Engineering Computations 7(1):19-34.

Rao, R.V. 2020. *Rao algorithms: Three metaphor-less simple algorithms for solving optimization problems*. International Journal of Industrial Engineering Computations 11(1):107-130.

Tunca, O., Aydogdu, I. & Carbas, S. 2017. *Optimum design of braced barrel vault systems using cold-formed steel sections*, E-Journal European Council of Civil Engineering 15:9-16.

LIGHTWEIGHT STRUCTURES in CIVIL ENGINEERING
CONTEMPORARY PROBLEMS
Monograph from Scientific Seminar
Organized by Polish Chapters of
International Association for Shell and Spatial Structures
Łódź University of Technology
Faculty of Civil Engineering, Architecture
and Environmental Engineering
XXVII LSCE
Łódź, 2nd – 3rd of December 2021

AN APPLICATION OF THE DISCRETE WAVELET TRANSFORM TO DAMAGE DETECTION IN FLAT TRUSS GIRDERS

A. Knitter-Piątkowska [1] **O. Kawa** [2] **M.J. Guminiak** [3]
[1] Ph.D. Eng., Faculty of Civil and Transport Engineering, Poznan University of Technology, POLAND,
anna.knitter-piatkowska@put.poznan.pl
[2] Ph.D. Eng., Faculty of Civil and Transport Engineering, Poznan University of Technology, POLAND,
olga.kawa@put.poznan.pl
[3] Ph.D. Habil. Eng., Faculty of Civil and Transport Engineering, Poznan University of Technology, POLAND,
michal.guminiak@put.poznan.pl

ABSTRACT: The paper presents the problem of damage detection in flat truss girders while considering the static external loadings. The presented issue of flat truss girders statics is described and solved by the Finite Element Method (FEM). Damage in truss is modeled as local stiffness reduction of one chord element. The analyses of static structural responses are carried out with the use of Discrete Wavelet Transform (DWT). Signal decomposition according to the Mallat pyramid algorithm is applied. The measured variables are static vertical deflections and angles of rotation. All of them have been established at selected nodes of finite elements. The numerical examples are presented.

Keywords: truss structures, finite element method, damage detection, discrete wavelet transform.

1. INTRODUCTION

Damage detection has focused much attention over the last decades. There are different non-destructive techniques which enable the identification of defective part of a structure. This problem was investigated by many scientists and developed while using some approaches based on e.g. optimization of loads (Mróz & Garstecki, 2005), information on natural frequencies (Dems & Mróz 2001) and others, which belongs to the class of soft computing methods, e.g. (Burczyński et al. 2004) and (Rucka and Wilde 2010). Another approach in this field may be the application of Discrete Wavelet Transform (DWT) to the structural response signal analysis, e.g. (Knitter-Piątkowska 2011), (Knitter-Piątkowska et al. 2016), (Guminiak and Knitter-Piątkowska 2018) which allows to locate areas of the structure where damage (defects) can be expected, e.g. in the form of local stiffness loss. Wavelet functions proved to be highly useful in many applications, including their implementation to the theory of homogenization (Kamiński 2002).

1.1. Theoretical foundations of the Discrete Wavelet Transform (DWT)

Let the function $\psi(t)$, called the wavelet function (mother function), be continuous and belong to the field of $L^2(\mathbf{R})$. Additionally, the function $\psi(t)$ must satisfy the condition of admissibility (Mallat 1999). The mother function may be real- or complex-valued. The real-valued wavelets will be applied in the considered

cases. For signal decomposition the set of wavelets (wavelet family) is needed. This set of functions is obtained by translating and scaling the function ψ what can be written by means of the relation:

$$\psi_{a,b} = \frac{1}{\sqrt{|a|}} \cdot \psi\left(\frac{t-b}{a}\right), \tag{1}$$

where t is a time or space coordinate, a and b are the scale and translation parameters respectively. The parameters a and b take real values $(a, b \in (\mathbf{R}))$ and additionally $a \neq 0$. The element $|a|^{-1/2}$ expresses the scale factor which ensures the constant wavelet energy regardless of the scale, i.e. $\|\psi_{a,b}\| = \|\psi\| = 1$.
In the present analysis, Discrete Wavelet Transform (DWT) plays the leading role. The wavelet family can be obtained by substitution $a = 1/2^j$ and $b = k/2^j$ in the equation (1). This leads to the relation:

$$\psi_{j,k}(t) = 2^{(j/2)} \cdot \psi\left(2^j \cdot t - k\right), \tag{2}$$

in which k and j are scale and translation parameters, respectively.
The Discrete Wavelet Transformation (DWT) of the signal (e.g. the response function of the structure) $f(t)$ is expressed by the equation:

$$Wf(j,k) = 2^{j/2} \cdot \int_{-\infty}^{\infty} f(t) \cdot \psi\left(2^j \cdot t - k\right) \cdot dt = \left\langle f(t), \psi_{j,k} \right\rangle. \tag{3}$$

The scalar product of the response function $f(t)$ and the wavelet function allows to find the set of wavelet coefficients $d_{j,k} = \left\langle f(t), \psi_{j,k} \right\rangle$. This enables the discrete signal to be represented in the form of the combination of linear wavelet functions $\psi_{j,k}$ with wavelet coefficients $d_{j,k}$ which can be written as:

$$f(t) = \sum_{j=0}^{J-1} \sum_{k} d_{j,k} \cdot \psi_{j,k}(t), \tag{4}$$

for the number of discrete input data equal to 2^J.
The multi-resolution analysis is performed with the use of the scaling wavelet function (father function) $\varphi_{j,k}(t)$ in the following form:

$$\varphi_{j,k}(t) = 2^{j/2} \cdot \varphi\left(2^j \cdot t - k\right). \tag{5}$$

The scaling function $\varphi_{j,k}(t)$ limits the unit area and has the unit energy. This condition describes the following relation:

$$\int_{-\infty}^{\infty} \varphi(t) \cdot dt = 1. \tag{6}$$

This function fulfills the orthogonality and the translation conditions what can be written in the form:

$$\langle \varphi(t), \varphi(t) \rangle = \int_{-\infty}^{\infty} |\varphi(t)|^2 \cdot dt = 1, \ \langle \phi(t), \phi(t-n) \rangle = 0, \quad n \neq 0, \tag{7}$$

$$\langle \varphi(t), \varphi(t-n) \rangle = 0, \quad n \neq 0 . \tag{8}$$

The input function $f(t)$ is developed in series while using the basic (mother) function $\psi(t)$ and the scaling (father) function $\varphi(t)$

$$f(t) = \sum_{k=-\infty}^{\infty} a_{j,k} \cdot \phi_{j,k}(t) + \sum_{k=-\infty}^{\infty} \sum_{j=0}^{\infty} d_{j,k} \cdot \psi_{j,k}(t), \tag{9}$$

where $a_{j,k}$ are the coefficients of the scaling wavelet determined as follows:

$$a_{j,k} = \langle f(t), \varphi_{j,k} \rangle . \tag{10}$$

For 1-D DWT analysis, decomposition of the discrete signal is carried out according to the Mallat pyramid algorithm (Mallat, 1999):

$$f_J = S_J + D_J + ... + D_n + ... + D_1, \quad n = J - j , \tag{11}$$

where each component in signal representation is coupled with a specific range of frequency and provides information at the scale level $(j = 1, ..., J)$. The Mallat pyramid algorithm is presented in Figure 1.

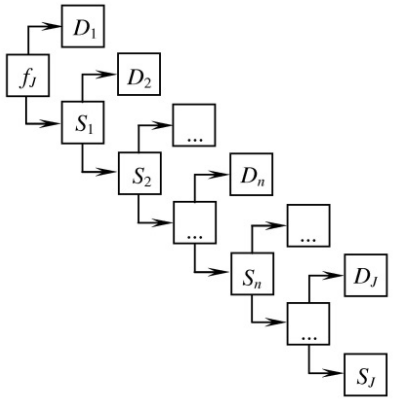

Fig. 1. Mallat pyramid algorithm for 1-D analysis.

The discrete parameter J describes the level of a multi-resolution analysis (MRA), S_J expresses the smooth signal representation, D_n and S_n are the details and rough parts of the transformed signal respectively and D_1 corresponds to the most detailed representation of the transformed signal. The function f_J must be approximated by $N = 2^J$ discrete values to fulfill the dyadic requirements of DWT. Basic and scaling functions of Daubechies 4 wavelets are presented in Fig. 2.

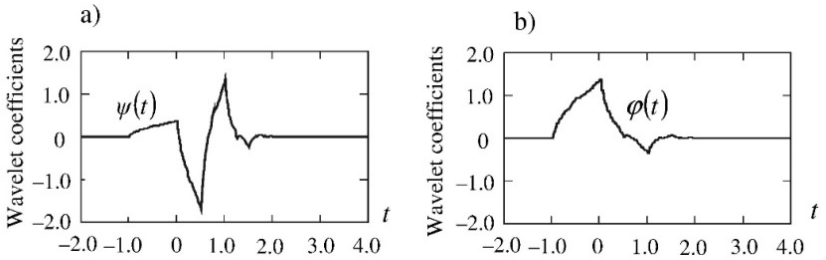

Fig. 2. Daubechies 4 wavelet function: a) – basic (mother) and b) – scaling function (father).

2. FINITE ELEMENT ANALYSIS

The statics of a system of flat truss girders is described and solved in terms of the Finite Element Method:

$$\mathbf{K} \cdot \mathbf{q} = \mathbf{P}, \tag{12}$$

where $\mathbf{K}$, $\mathbf{q}$ and $\mathbf{P}$ are the stiffness matrix, the displacement vector and the right-hand-side vector of the whole structure respectively, with the appropriate boundary conditions introduced.
The deformation of structures is described by means of two-node spatial bar finite elements (Figure 3).

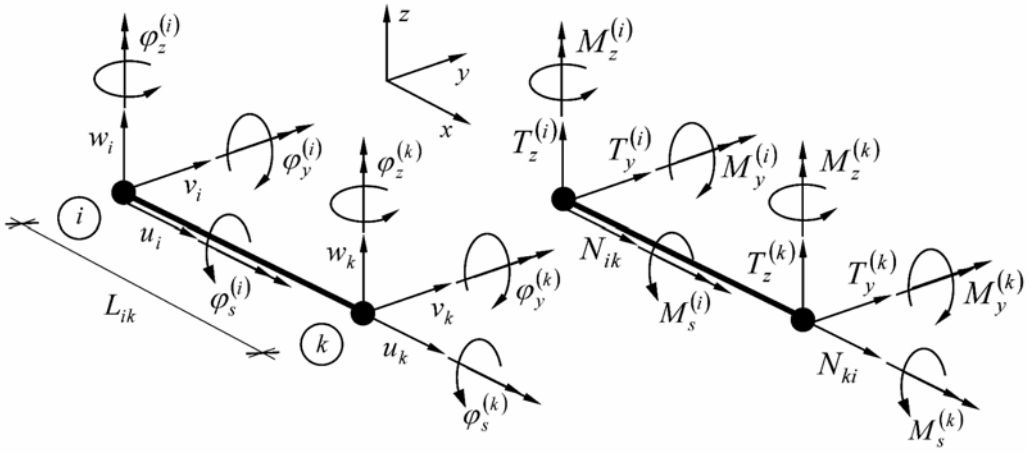

Fig. 3. Two-node spatial bar finite element.

3. NUMERICAL EXAMPLES

The aim of the present work is to detect the localization of weakened parts of the structure provided that damage (deterioration) takes place. The system of flat truss girders subjected to classic code loads has been analyzed (Figure 4). The damage was introduced by stiffness reduction of the selected chord element along a very small part of its length. The span and the height of the analyzed truss girder are 24.0 m and 1.65 m respectively. The upper and lower chords are made of steel hot-rolled profiles such as HEB 300 and HEB 200 respectively whereas the diagonals are made of thin wall pipe 120×120×6 mm. The lower chord was divided into 160 finite elements, wherein the damaged part is modeled by HEB 180 profile. Numerical investigation has been carried out while basing on the signal analysis of structural static response which has been obtained while using the Finite Element Method (FEM) in terms of 3D two--nodes finite elements and ROBOT Structural Analysis computational program.

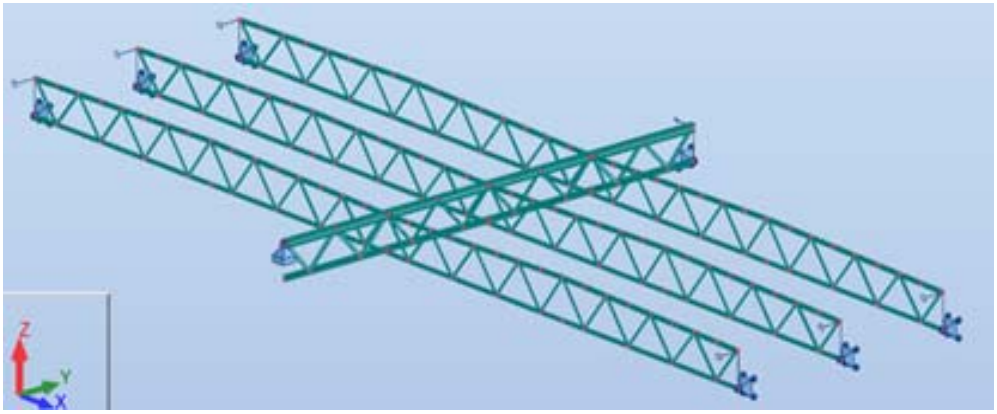

Fig. 4. Analyzed system of flat truss girders.

Table 1 presents the basic dimensions and material properties for steel structural elements.

Tab. 1. Element and material properties

Element	Profile	Material	Young modulus [kPa]
Upper chord	HEB 300	S355	$210 \cdot 10^6$
Lower chord	HEB 200	S355	$210 \cdot 10^6$
Chords (defects)	HEB 180	S355	$210 \cdot 10^6$
Diagonals	RK 120×120×6	S355	$210 \cdot 10^6$
Diagonals (defects)	RK 90×90×5	S355	$210 \cdot 10^6$

Tables 2 and 3 provide a set of permanent and variable loadings acting on the entire structure.

Tab. 2. Loadings: permanent loading

Permanent loading	Label	Value	Width	Characteristic value
Calc. coeff. $\gamma_f = 1.35$		[kN/m^2]	[m]	[kN/m]
The weight of the structure	Permanent	Included in the computational program		
Self-weight of the roof	Self-weight	0.32	6.0	1.92

Tab. 3. Loadings: variable loading

Variable loading	Label	Value	Width	Characteristic value
Calc. coeff. $\gamma_f = 1.5$		[kN/m^2]	[m]	[kN/m]
Hangers, installations	Variable	0.15	6.0	0.9
Snow loading	Snow	0.72	6.0	4.32
Wind, zone H – suction	Wind suction	− 0.51	6.0	3.06
Wind, zone I – pressure	Wind pressure	0.15	6.0	0.9

The analyzed structure response signals will be: the deflection line and angle of rotation of the lower chord girder and in addition, horizontal displacements of the selected diagonal. The most unfavorable load combinations were selected for the analysis in accordance with the applied engineering practice.

3.1. Example 1. Deterioration of the lower chord

The response signal in the form of deflections of the lower truss chord has been analyzed and transformed while using DWT procedures. The set of Daubechies 4 and 8 families of wavelet functions has been applied to the preliminary analysis. The introduced weakening of the cross-section is shown in the Figure 5 in the relation to the entire single girder. Figure 6 shows the weakened cross-section in the relation to finite element division. Introduced weakening part of the lower chord is marked with a red circle.

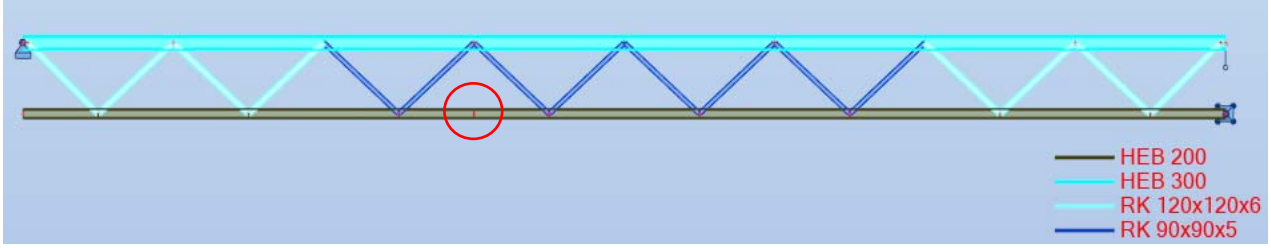

Fig. 5. The place of introduction of the weakening cross-section in the relation to the entire girder.

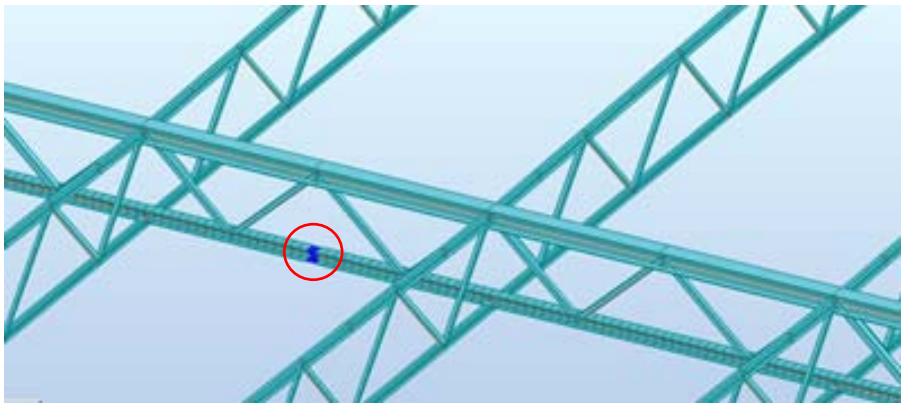

Fig. 6. The place of introduction of the weakened cross-section in relation to the entire girder with the division into finite elements.

The detail of the impairment of the lower chord cross-section is presented in the Figure 7 and indicated with a red circle.

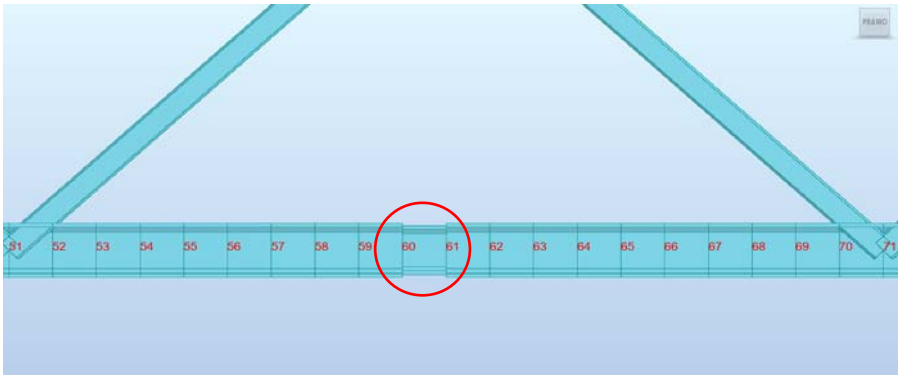

Fig. 7. Reduction of cross-sectional stiffness in the relation to the set of finite elements.

The damage position is sufficiently precisely indicated while employing DWT procedure and Daubechies 4, 6 and 8 sets of wavelet functions what is shown in Figures 8–10. One can observe an evident disturbance of the transformed signals and high peaks in the expected defective area in every of discussed cases.

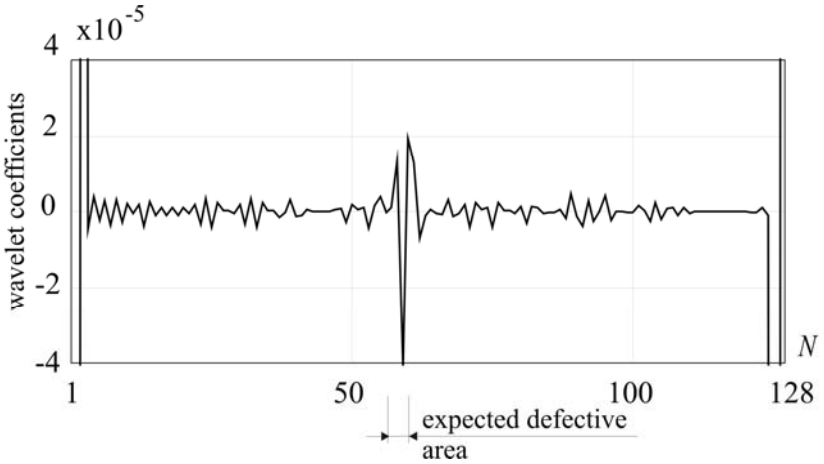

Fig. 8. 1-D DWT of vertical displacements for Daubechies 4 (detail 1) and $N = 128$ number of measurements.

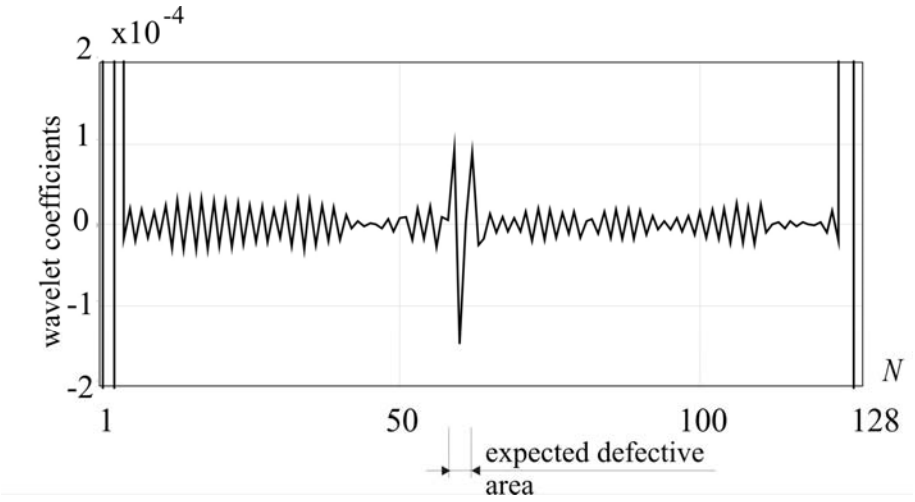

Fig. 9. 1-D DWT of vertical displacements for Daubechies 6 (detail 1) and $N = 128$ number of measurements.

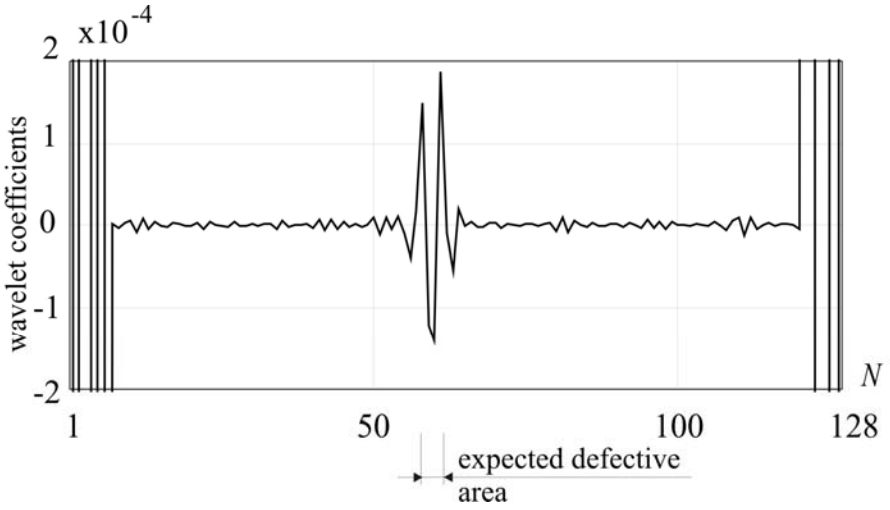

Fig. 10. 1-D DWT of vertical displacements for Daubechies 8 set of wavelets (detail 1) and $N = 128$ number of measurements.

3.2. Example 2. Deterioration of the diagonals

In this example, two failures of the selected diagonals have been introduced. These weakening part of the diagonals are shown in Figures 11 and 12 marked with a red circle. The response signal in the form of deflections of the lower truss chord has been analyzed and transformed while using DWT procedures. The set of Daubechies 8 family of wavelet functions has been applied to the preliminary analysis.

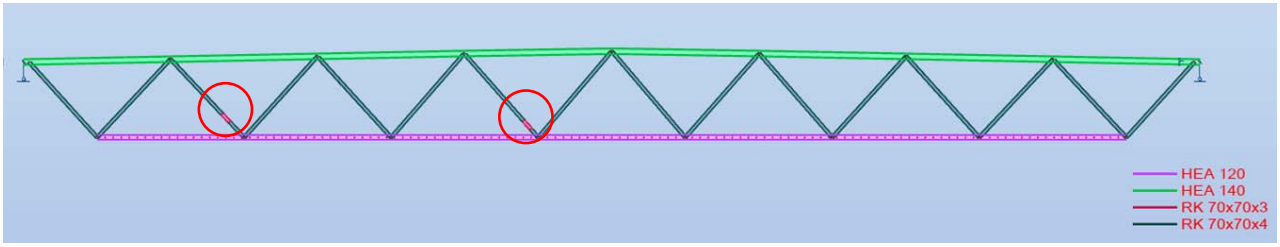

Fig. 11. The places of introduction of the weakening cross-sections in the relation to the entire girder.

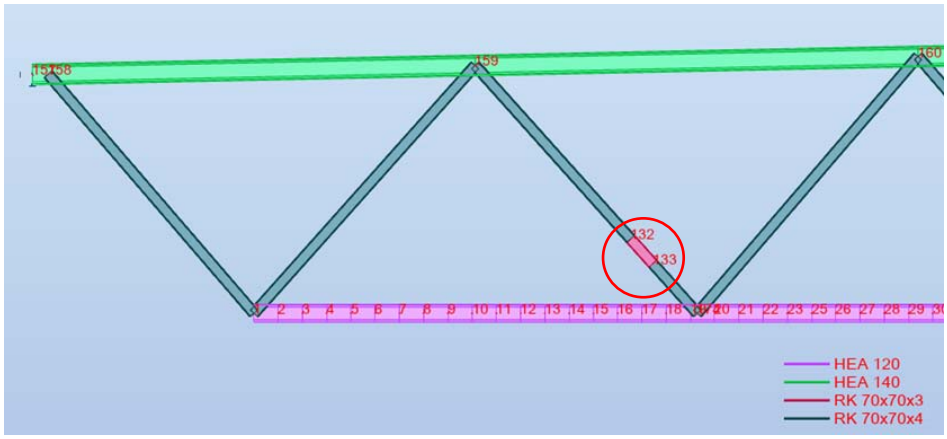

Fig. 12. Reduction of cross-sectional stiffness in the relation to the set of finite elements.

Damaged parts of the structure can be sufficiently precisely indicated which is shown in Figure 13 where evident disturbances of the transformed signal are visible.

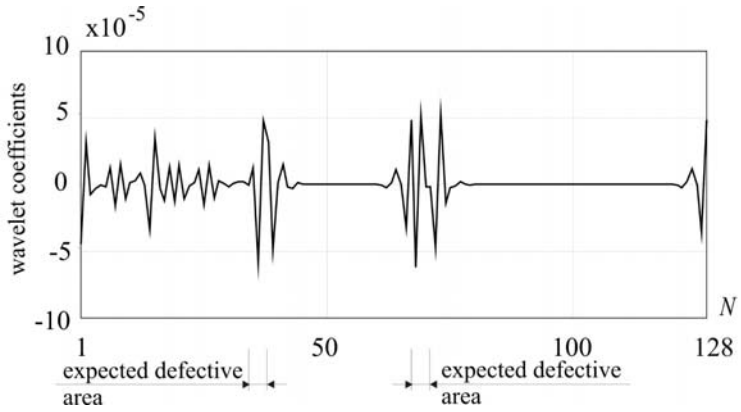

Fig. 13. 1-D DWT of the difference between angle of rotations φ_y for undamaged and defective structure for Daubechies 8 set of wavelets (detail 1) and $N = 128$ number of measurements.

3.3. Example 3. Deterioration of one diagonal - change in the thickness of the walls

In this example, one failure of the selected diagonal will be introduced. This weakening part of the diagonal is shown in Figure 14 and 15 marked with a red circle. The response signal in the form of horizontal displacements has been analyzed and transformed while employing DWT procedures. The set of Daubechies 8 families of wavelet functions has been applied to the preliminary analysis.

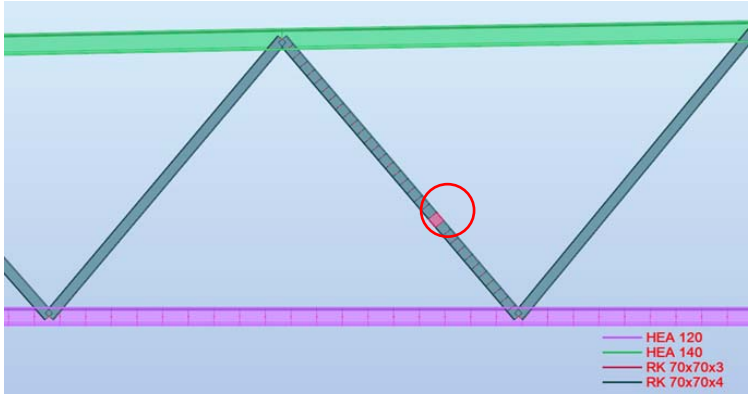

Fig. 14. The place of introduction of the weakening cross-section in relation to the diagonal with the division into finite elements.

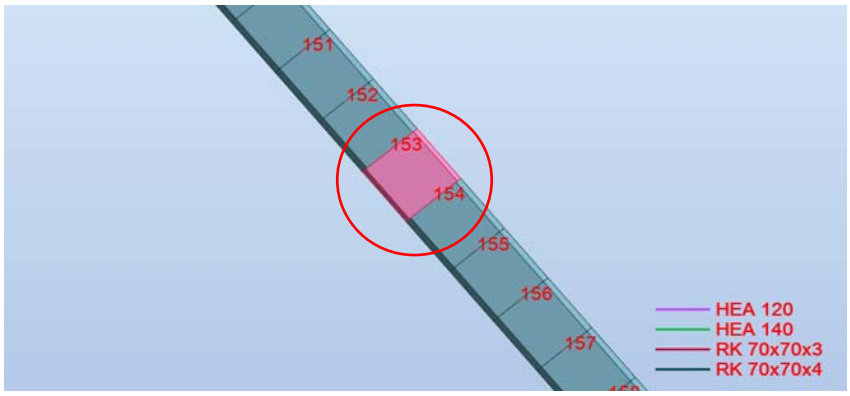

Fig. 15. Reduction of cross-sectional stiffness in the relation to the set of finite elements.

Damaged parts of the structure can be sufficiently precisely indicated which is shown in Figures 16 and 17 where evident disturbances of the transformed signals are visible in the area of the expected occurrence of the defect. Transformation disorders at the boundaries of the transformation window are common, one can avoid them, e.g. by reducing the area under study and compacting discrete points.

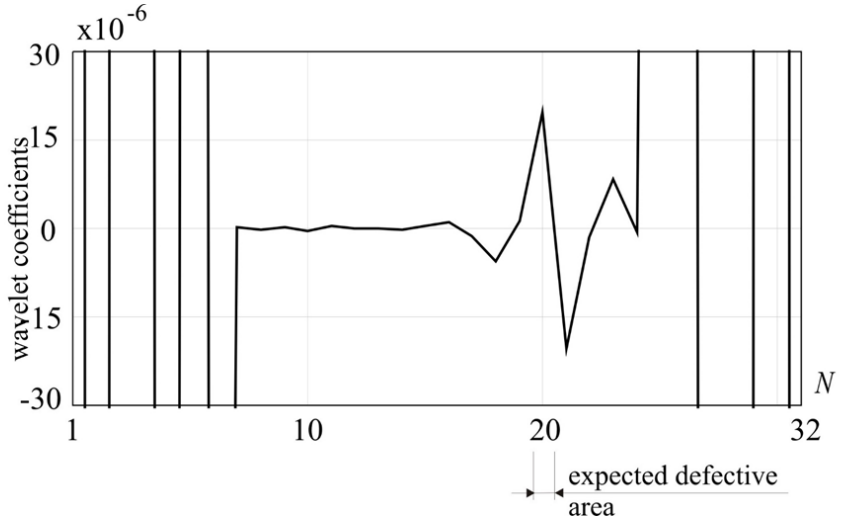

Fig. 16. 1-D DWT of vertical displacements for Daubechies 8 set of wavelets (detail 1) and $N = 32$ number of measurements.

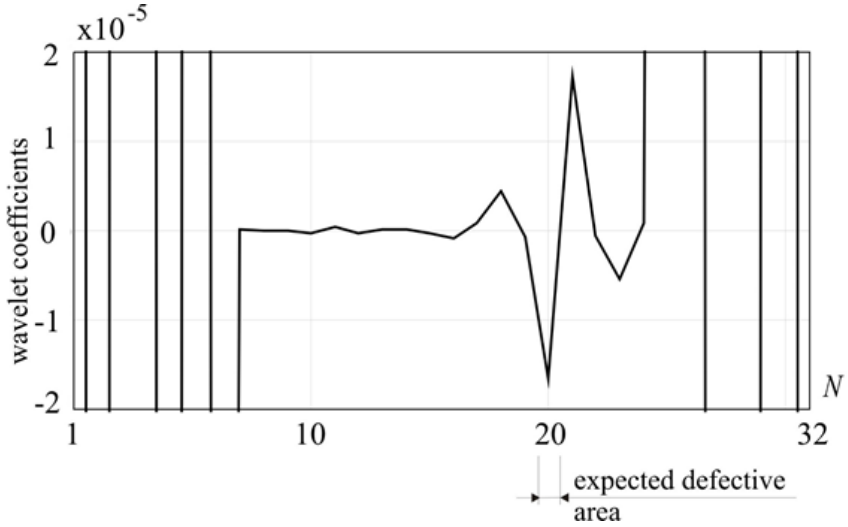

Fig. 17. 1-D DWT of horizontal displacements for Daubechies 8 set of wavelets (detail 1) and $N = 32$ number of measurements.

4. CONCLUSIONS

Application of discrete 1-D Discrete Wavelet Transformation (DWT) to recognition of structural response signal discontinuity in the analysis of flat truss girders is discussed in the paper. Measured response signals were assumed as the static vertical and horizontal deflection as well as the angles of rotations given at the selected, discrete points. In general, the proposed method was highly efficient while applied only to the decomposition of the data set obtained from undamaged structure. However, in one discussed case, while transforming the angle of rotations signal, the data set from undamaged structured occurred to be indispensable. All defects were properly localized while using asymmetric Daubechies 4, 6 and 8 set of wavelets. The minimum number of measurements was assumed as thirty two. The position of defects was quite correctly identified by the high peak and evident disturbances of the transformed data. The presented analyzes have shown that the DWT tool can be successfully used in the process of detecting damage in engineering structures. The analyzed response signal can be basically any discrete function, e.g. the function of the influence line of a given static or geometric quantity (Knitter-Piątkowska et al. 2016), (Guminiak and Knitter-Piątkowska 2018). However, the deflection function is most often used as a set of numbers that can be obtained in a relatively simply manner both numerically and experimentally.

REFERENCES

Burczyński, T., Kuś, W., Długosz, A. & Orantek, P. 2004. *Optimization and defect identification using distributed evolutionary algorithms*. Engineering Applications of Artificial Intelligence 17: 337–344.

Dems, K. & Mróz, Z. 2001. *Identification of damage in beam and plate structures using parameter dependent frequency changes*. Engineering Computation 18 (1/2): 96–120.

Guminiak, M & Knitter-Piątkowska, A. 2018. *Selected problems of damage detections in internally supported plates using one-dimensional Discrete Wavelet Transform*. Journal of Theoretical and Applied Mechanics, 56(3): 631–644.

Kamiński, M. 2002. *Wavelet-based Finite Element analysis of composites*. Fifth World Congress on Computational Mechanics, July 7– 2, 2002, Vienna, Austria, eds.: H.A. Mang, F.G. Rammerstorfer, J. Eberhardsteiner.

Knitter-Piątkowska, A. 2011. *Application of Wavelet Transform to detect damage in statically and dynamically loaded structures*. Poznań: Poznań University of Technology Publishing House (in Polish).

Knitter-Piątkowska, A., Guminiak, M. & Przychodzki, M. 2016. *Application of Discrete Wavelet Transformation to defect detection in truss structures with rigidly connected bars*. Engineering Transactions 64(2): 157–170.

Mallat, S.G. 1999. *A wavelet tour of signal processing*. San Diego: Academic Press.

Mróz, Z. & Garstecki, A. 2005. *Optimal loading conditions in design and identification of structures. Part 1: Discrete formulation*. Int. J. Struct. and Multidisciplinary Optim. 29: 11–18.

Rucka, M. & Wilde, K. 2010. *Neuro-wavelet damage detection technique in beam, plate and shell structures with experimental validation*. Journal of Theoretical and Applied Mechanics 48(3): 579–604.

LIGHTWEIGHT STRUCTURES in CIVIL ENGINEERING
CONTEMPORARY PROBLEMS
Monograph from Scientific Seminar
Organized by Polish Chapters of
International Association for Shell and Spatial Structures
Łódź University of Technology
Faculty of Civil Engineering, Architecture
and Environmental Engineering
XXVII LSCE
Łódź, 2nd – 3rd of December 2021

INFLUENCE OF THE ROTATIONAL FLEXIBILITY OF SUPPORTS ON THE DYNAMIC PARAMETERS OF THE ARCH STRUCTURE

M. Łasecka-Plura [1] **Z.M. Pawlak** [2] **M. Żak-Sawiak** [3]
[1] Dr. Eng., Faculty of Civil and Transport Engineering, Poznan University of Technology, POLAND,
magdalena.lasecka-plura@put.poznan.pl
[2] Dr. Hab. Eng., Faculty of Civil and Transport Engineering, Poznan University of Technology, POLAND,
zdzislaw.pawlak@put.poznan.pl
[3] MSc., Faculty of Civil and Transport Engineering, Poznan University of Technology, POLAND,
martyna.zak-sawiak@put.poznan.pl

ABSTRACT: The article examines bar structures modelled by finite elements, in which nodes are flexibly connected to the supports. Two-node elements with three degrees of freedom at each node and non-curved axis were used. Polynomial shape functions were adopted to derive the stiffness and mass matrices, but they were modified by introducing rotational flexibility in the boundary supports. The determined finite element matrices were used for the numerical analysis of the circular arch to determine its dynamic parameters. Changes in the frequency of free vibrations of arches of different heights with changing rotational elasticity of supports were determined.

Keywords: flexible connections, arched structures, dynamic characteristics, semi-rigid nodes, finite element.

1. INTRODUCTION

The free vibration analysis of circular arches is widely described in the literature due to their wide application in civil engineering (e.g., bridges, covering of large-scale buildings or underground structures). Lamb wrote one of the first papers about this issue (Lamb 1887).

Analysis of arch structures requires a six-order differential equation to be solved. The basic model adopted for the analysis of arches is based on the Euler-Bernoulli theory, which states that displacements are caused only by bending, while the effects of shear deformation, rotary inertia and the influence of axial extensibility are neglected. An exact solution for such an arch, also called the Euler-Bernoulli arch, can be found in the work by Wasserman (1977), where both free and forced vibrations are considered. Euler-Bernoulli model is often sufficient for most engineering problems, but for thick and shallow arches it does not give sufficiently accurate results. In such cases, the authors use a model that includes the effects of axial extensibility, shear deformation and rotary inertia – Timoshenko circular arches. The exact solution was given in the work Rao and Sundararajan (1969).

In the analysis of modern and complex structures, the finite element method is primarily used and therefore it is developed by many authors. An exact dynamic stiffness matrix for in-plane and out-of-plane vibrations was derived by Calio et al. (2014). Many authors have also studied influence of rotatory inertia and shear deformation (Tufekci and Arpaci 1998) or axial extensibility (Chidamparam and Leissa 1995).

The researchers analyzed arches with different boundary conditions, including those supported by flexible supports. The latter are important, especially when dynamic effects are taken into account and reduction of vibration is necessary. Yang et al. (2004) showed that the introduction of flexible supports significantly reduces the natural frequency of the structures. Xu et al. (2002) analyzed shallow arch with flexible supports subjected to impulse load. Flexible supports were also considered in the paper by Zhuo et al. (2021). The authors proved the effectiveness of flexible supports in reducing the damage of the underground arch structure. Closed-form solution for dynamic analysis of circular beam with elastic boundary conditions can be found in paper by Lin et al. (2001).

In this paper the dynamic parameters of a circular arch with flexible boundary supports are analyzed using the finite element method. It was assumed that the supports have a rotational flexibility modelled by an elastic spring. Two-node elements with three degrees of freedom at each node and non-curved axis were used. Polynomial shape functions were adopted to derive the stiffness and mass matrices, but they were modified by introducing rotational stiffness in the boundary supports (Seculovic et al. 2002, Ozturk and Catal 2005). In Section 2 the formulation of dynamic problem is presented and the stiffness and mass matrices for element with rotational stiffnesses are derived. In Section 3 numerical examples are showed. Several circular arches of various heights and stiffnesses of boundary supports were analyzed. The paper ends with final conclusions in Section 4.

2. DYNAMIC PROBLEM

In order to determine the dynamic parameters of the structure, the stiffness matrix and the mass matrix of the beam element were determined.

2.1. Stiffness matrix

In a beam finite element, the rotational stiffnesses at the nodes are denoted as k_0 and k_l, respectively. Figure 1 shows that the beam element is connected to the supports by rotating elastic elements, while the sections marked as e_0 and e_l are assumed to be infinitely short and have infinitely high stiffness.

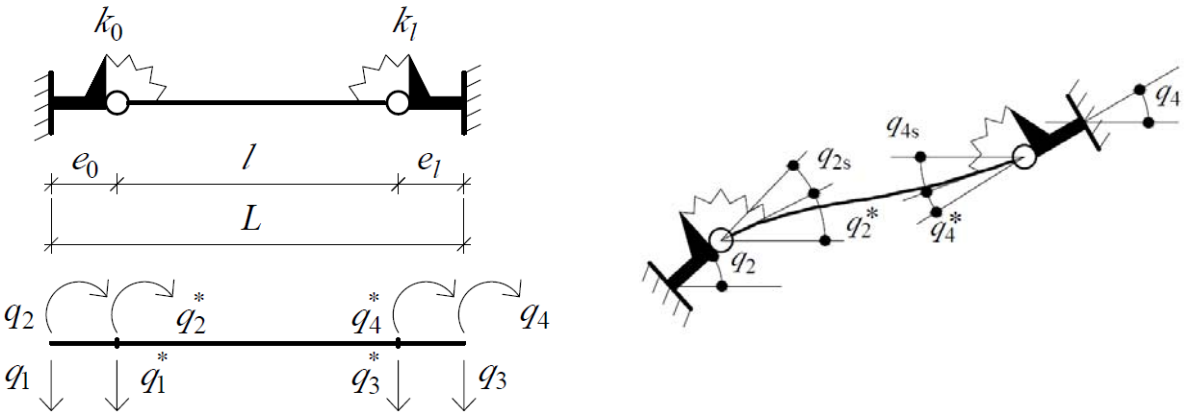

Fig. 1. Beam finite element with flexible connections.

The displacements of the beam element at the nodes are marked with asterisks. The translational displacements of the beam element nodes and the supports are the same, i.e. $q_1 = q_1^*$, $q_3 = q_3^*$, while the rotations of the supports and ends of the beam element differ due to the rotational flexibility of the connections:

$$q_2 = q_2^* + q_{2s},\ q_4 = q_4^* + q_{4s}. \tag{1}$$

In addition, the bending moments in the beam nodes (Q_2^* and Q_4^*) determine the values of the rotation angles in the elastic constrains:

$$q_{2s} = \frac{Q_2^*}{k_0},\ q_{4s} = \frac{Q_4^*}{k_l}. \tag{2}$$

Using the well-known relationships between nodal forces and displacements in a beam element and taking into account the relationships given in Eq. (1), one can write:

$$\begin{bmatrix} Q_2^* \\ Q_4^* \end{bmatrix} = \frac{EI}{l^2}\begin{bmatrix} 6 & 4l & -6 & 2l \\ 6 & 2l & -6 & 4l \end{bmatrix}\begin{bmatrix} q_1 \\ q_2^* \\ q_3 \\ q_4^* \end{bmatrix} = \frac{EI}{l^2}\begin{bmatrix} 6 & 4l & -6 & 2l \\ 6 & 2l & -6 & 4l \end{bmatrix}\begin{bmatrix} q_1 \\ q_2 - q_{2s} \\ q_3 \\ q_4 - q_{4s} \end{bmatrix}. \tag{3}$$

After substituting Eq. (2) into Eq. (3) and some transformations, the forces Q_i^* can be expressed as follows:

$$\begin{bmatrix} Q_2^* \\ Q_4^* \end{bmatrix} = \frac{EI}{\gamma l}\begin{bmatrix} 6k_0\left(k_l l + 2EI\right) & 4lk_0\left(k_l l + 3EI\right) & -6k_0\left(k_l l + 2EI\right) & 2k_0 k_l l \\ 6k_l\left(k_0 l + 2EI\right) & 2k_l k_0 l & -6k_l\left(k_0 l + 2EI\right) & 4lk_l\left(k_0 l + 3EI\right) \end{bmatrix}\begin{bmatrix} q_1 \\ q_2 \\ q_3 \\ q_4 \end{bmatrix}, \tag{4}$$

where $\gamma = 12\left(EI\right)^2 + 4k_0 lEI + 4k_l lEI + k_0 k_l l^2$. Substituting Eq. (4) into Eq. (2), the rotations in the elastic constraints can be written in the matrix form:

$$\mathbf{q}_s = \begin{bmatrix} 0 \\ q_{2s} \\ 0 \\ q_{4s} \end{bmatrix} = \begin{bmatrix} 0 \\ Q_2^*/k_0 \\ 0 \\ Q_4^*/k_l \end{bmatrix} = \frac{EI}{\gamma l}\begin{bmatrix} 0 & 0 & 0 & 0 \\ 6\left(k_l l + 2EI\right) & 4l\left(k_l l + 3EI\right) & -6\left(k_l l + 2EI\right) & 2k_l l \\ 0 & 0 & 0 & 0 \\ 6\left(k_0 l + 2EI\right) & 2k_0 l & -6\left(k_0 l + 2EI\right) & 4l\left(k_0 l + 3EI\right) \end{bmatrix}\begin{bmatrix} q_1 \\ q_2 \\ q_3 \\ q_4 \end{bmatrix}. \tag{5}$$

Finally, the vector of rotations in the flexible constraints is as follows:

$$\mathbf{q}_s = \mathbf{D}\mathbf{q}, \tag{6}$$

where**:**

$$\mathbf{D} = \frac{EI}{\gamma l}\begin{bmatrix} 0 & 0 & 0 & 0 \\ 6\left(k_l l + 2EI\right) & 4l\left(k_l l + 3EI\right) & -6\left(k_l l + 2EI\right) & 2k_l l \\ 0 & 0 & 0 & 0 \\ 6\left(k_0 l + 2EI\right) & 2k_0 l & -6\left(k_0 l + 2EI\right) & 4l\left(k_0 l + 3EI\right) \end{bmatrix}. \tag{6}$$

If the displacement field for a beam with flexible supports is approximated by the functions:

$$w(x) = \mathbf{N}(x)\mathbf{q}^* = \mathbf{N}(x)\left(\mathbf{I} - \mathbf{D}\right)\mathbf{q}, \tag{7}$$

where $\mathbf{N}(x) = [N_1(x)\ N_2(x)\ N_3(x)\ N_4(x)]$ is the set of shape functions for the beam element fixed at both ends:

$$
\begin{aligned}
N_1(x) &= 1 - 3\left(\frac{x}{l}\right)^2 + 2\left(\frac{x}{l}\right)^3, \\
N_2(x) &= x\left(1 - \left(\frac{x}{l}\right)^2\right), \\
N_3(x) &= \left(\frac{x}{l}\right)^2 \left(3 - 2\frac{x}{l}\right), \\
N_4(x) &= \left(\frac{x}{l}\right)^2 \left(\frac{x}{l} - 1\right) l,
\end{aligned}
\tag{8}
$$

and $\mathbf{q}^*$ is the vector of beam displacements (Fig. 1).

Then the expression for potential energy can be written as:

$$
\Pi = \frac{EI}{2}\mathbf{q}^T \left[\int_0^l (\mathbf{I} - \mathbf{D})^T \left(\frac{d^2\mathbf{N}(x)}{dx^2} \right)^T \frac{d^2\mathbf{N}(x)}{dx^2} (\mathbf{I} - \mathbf{D})\, dx \right] \mathbf{q} + \frac{1}{2}\mathbf{q}^T \mathbf{D}^T \mathbf{S} \mathbf{D} \mathbf{q} = \frac{1}{2}\mathbf{q}^T \left(\mathbf{K}_1 + \mathbf{K}_s \right) \mathbf{q} \tag{9}
$$

where $\mathbf{N}(x)$ is the set of the shape functions for the beam element fixed at both ends, $\mathbf{I}$ is the identity matrix and $\mathbf{S}$ is the matrix containing rotational stiffnesses of nodes:

$$
\mathbf{S} = \begin{bmatrix} 0 & 0 & 0 & 0 \\ 0 & k_0 & 0 & 0 \\ 0 & 0 & 0 & 0 \\ 0 & 0 & 0 & k_l \end{bmatrix}. \tag{10}
$$

Matrices $\mathbf{K}_1$ and $\mathbf{K}_S$ are as follows:

$$
\begin{aligned}
\mathbf{K}_1 &= EI (\mathbf{I} - \mathbf{D})^T \int_0^l \left(\frac{d^2\mathbf{N}(x)}{dx^2} \right)^T \frac{d^2\mathbf{N}(x)}{dx^2} dx (\mathbf{I} - \mathbf{D}), \\
\mathbf{K}_S &= \mathbf{D}^T \mathbf{S} \mathbf{D}.
\end{aligned}
\tag{11}
$$

Then, both the stiffness matrix and the mass matrix were supplemented with elements related to the axial degrees of freedom. These additional elements are the same as in the classical stiffness and mass matrices for a bar element, since they are not affected by rotational stiffness.
Finally, the stiffness matrix for a beam element with rotational flexibility is a sum of matrices given in (11):

$$
\mathbf{K} = \mathbf{K}_1 + \mathbf{K}_s, \tag{12}
$$

and can be expressed in the following form:

$$\mathbf{K}=\begin{bmatrix} k_{11} & 0 & 0 & k_{14} & 0 & 0 \\ 0 & k_{22} & k_{23} & 0 & k_{25} & k_{26} \\ 0 & k_{32} & k_{33} & 0 & k_{35} & k_{36} \\ k_{41} & 0 & 0 & k_{44} & 0 & 0 \\ 0 & k_{52} & k_{53} & 0 & k_{55} & k_{56} \\ 0 & k_{62} & k_{63} & 0 & k_{65} & k_{66} \end{bmatrix}, \tag{13}$$

where:

$$k_{11}=k_{44}=-k_{14}=-k_{41}=\frac{EA}{l},$$
$$k_{22}=k_{44}=\frac{12EI}{l^3\Omega}\left(1+\mu_0+\mu_l\right),\ k_{23}=k_{32}=-k_{35}=-k_{53}=\frac{6EI}{l^2\Omega}\left(1+2\mu_l\right),$$
$$k_{25}=k_{52}=-\frac{12EI}{l^2\Omega}\left(1+\mu_0+\mu_l\right),\ k_{26}=k_{62}=-k_{56}=-k_{65}=\frac{6EI}{l^2\Omega}\left(1+2\mu_0\right),$$
$$k_{33}=\frac{4EI}{l\Omega}\left(1+3\mu_l\right),\ k_{36}=\frac{2EI}{l\Omega},\ k_{66}=\frac{4EI}{l\Omega}\left(1+3\mu_0\right),$$
$$\mu_0=\frac{EI}{k_0 l},\ \mu_l=\frac{EI}{k_l l},\ \Omega=\left(1+4\mu_0+4\mu_l+12\mu_0\mu_l\right).$$

2.2. Mass matrix

Assuming that the mass density ρ is constant along the element, the element consistent mass matrix for beam with the rotational flexibility at nodes can be formulated as:

$$\mathbf{M}=\rho\left(\mathbf{I}-\mathbf{D}\right)^T\int_0^l\mathbf{N}\left(x\right)^T\mathbf{N}\left(x\right)dx\left(\mathbf{I}-\mathbf{D}\right). \tag{14}$$

Finally, the mass matrix of the considered element can be written in the following form:

$$\mathbf{M}=\frac{\rho l}{420}\begin{bmatrix} m_{11} & 0 & 0 & m_{14} & 0 & 0 \\ 0 & m_{22} & m_{23} & 0 & m_{25} & m_{26} \\ 0 & m_{32} & m_{33} & 0 & m_{35} & m_{36} \\ m_{41} & 0 & 0 & m_{44} & 0 & 0 \\ 0 & m_{52} & m_{53} & 0 & m_{55} & m_{56} \\ 0 & m_{62} & m_{63} & 0 & m_{65} & m_{66} \end{bmatrix}, \tag{15}$$

where:

$$m_{11}=m_{44}=140,\ m_{14}=m_{41}=70,$$
$$m_{22}=\frac{12}{\Omega^2}\left(g_{1,l}+\mu_0 g_{2,l}+\mu_0^2 g_{3,l}\right),\ m_{23}=m_{32}=\frac{2l}{\Omega^2}\left(g_{4,l}+\mu_0 g_{5,l}\right),$$
$$m_{25}=m_{52}=\frac{18}{\Omega^2}\left(s_1+\mu_l s_2+\mu_l^2 s_3\right),\ m_{26}=m_{62}=-\frac{l}{\Omega^2}\left(g_{6,0}+\mu_l g_{7,0}\right),$$
$$m_{33}=\frac{4l^2}{\Omega^2}g_{8,l},\ m_{35}=m_{53}=\frac{l}{\Omega^2}\left(g_{6,l}+\mu_0 g_{7,l}\right),$$

$$m_{36} = m_{63} = -\frac{l^2}{\Omega^2}\left(s_4 + \mu_l s_5\right),\ m_{55} = \frac{12}{\Omega^2}\left(g_{1,0} + \mu_l g_{2,0} + \mu_l^2 g_{3,0}\right),$$

$$m_{56} = m_{65} = -\frac{2l}{\Omega^2}\left(g_{4,0} + \mu_l g_{5,0}\right),\ m_{66} = \frac{4l^2}{\Omega^2} g_{8,0}, g_{1,i} = 13 + 117\mu_i + 272\mu_i^2,\ g_{2,i} = 82 + 656\mu_i + 1344\mu_i^2,$$

$$g_{3,i} = 132 + 924\mu_i + 1680\mu_i^2,\ g_{4,i} = 11 + 110\mu_i + 288\mu_i^2,\ g_{5,i} = 32 + 288\mu_i + 672\mu_i^2,$$

$$g_{6,i} = 13 + 130\mu_i + 264\mu_i^2,\ g_{7,i} = 76 + 684\mu_i + 1176\mu_i^2,\ g_{8,i} = 1 + 11\mu_i + 32\mu_i^2,\ i = 0 \text{ or } i = l,$$

$$s_1 = 3 + 27\mu_0 + 52\mu_0^2,\ s_2 = 27 + 216\mu_0 + 364\mu_0^2,\ s_3 = 52 + 364\mu_0 + 560\mu_0^2,\ s_4 = 3 + 20\mu_0,\ s_5 = 20 + 124\mu_0.$$

3. NUMERICAL EXAMPLE

A circular arch with a span of 20 m, made of the HEA300 steel I-section, was selected for numerical analyses (Fig. 2). Several cases of structures have been studied in which the height of the arch was different, and thus also the radius of curvature varied. The values of the rotational stiffness coefficients in the supports were also changed from zero till the value several times higher than the bending stiffness of the bar elements *EI*.

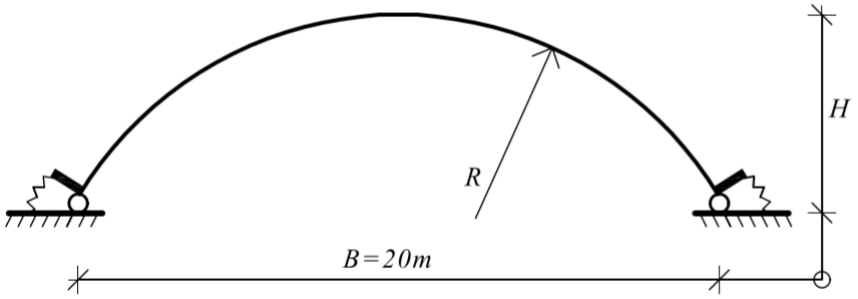

Fig. 2. The circular arch structure.

The structure at both ends has supports, in which the rotational stiffness has been varied. The obtained solution can be used to analyse any boundary conditions. In the case when the stiffness of the flexible supports tends to infinity ($k_0 \to \infty$, $k_l \to \infty$) the solution for fixed-fixed boundary conditions is obtained, while when the stiffness tends to zero ($k_0 \to 0$, $k_l \to 0$), the solution of pinned-pinned boundary conditions is obtained. In the first step the influence of finite element mesh density was investigated. The analysis was performed for arch with span of 20 m, height of 10 m and various types of supports. The division into 8, 18, 30 and 50 elements was considered. The first three natural frequencies were compared. In Tables 1 and 2 the relative difference between the results obtained for a given mesh and for the finest division into 50 elements was presented. The comparison presented for two different types of supports allows to conclude that the difference between the results for 18 and 50 elements is very small. In the case of three compared natural frequencies, it does not exceed 0.6%. Therefore, it was decided to use the division into 18 elements in further analyses.

Tab.1. Comparison of natural frequencies for division into a different number of finite elements – fixed-fixed arch

mode	Natural frequency [Hz]						
	8 finite elements	Relative difference [%]	18 finite elements	Relative difference [%]	30 finite elements	Relative difference [%]	50 finite elements
1	4.6818	1.83	4.6129	0.33	4.6017	0.09	4.5977
2	10.2973	1.97	10.1335	0.34	10.1081	0.09	10.0988
3	19.1924	2.27	18.8341	0.36	18.7845	0.09	18.7670

Tab. 2. Comparison of natural frequencies for division into a different number of finite elements – flexible supports $k_0 = k_l = 0.4EI$ 1/(m·rad)

mode	Natural frequency [Hz]						
	8 finite elements	Relative difference [%]	18 finite elements	Relative difference [%]	30 finite elements	Relative difference [%]	50 finite elements
1	3.6594	2.15	3.5961	0.38	3.5860	0.10	3.5824
2	8.7415	2.95	8.5346	0.51	8.5026	0.14	8.4911
3	16.7040	3.16	16.2760	0.52	16.2143	0.14	16.1923

As the first, the influence of arch height on the first natural frequency was investigated with various supports. Fixed-fixed arch (Fig. 3a), pinned-pinned arch (Fig. 3c) and arch with flexible supports (Fig. 3b) were taken into consideration. The rotational stiffness of $0.4EI$ was assumed for flexible supports. The results are presented in Table 3.

Tab. 3. Comparison of first natural frequencies f_1 for different supports and different height of arch.

Arch height [m]	First natural frequency [Hz]		
	Fixed-fixed (Fig. 3a)	Flexible supports $k_0 = k_l = 0.4EI$ (Fig. 3b)	Pinned-pinned (Fig. 3c)
3.0	13.6375	10.7114	8.4936
6.0	9.0013	7.0082	5.2417
10.0	4.6129	3.5961	2.3924

Based on the results presented in Table 3, it can be concluded that the natural frequency decreases with the height of the structure and increases with the increasing stiffness of the supports. It is also worth noting that the introduction of flexible supports reduces the value of the natural frequency of structure.

The influence of the stiffness value of flexible supports on natural frequencies was also analysed. As a result, a graph of the dependence of the fundamental frequency of free vibrations on the coefficient of rotational stiffness in the supports was presented. Such a change of the natural frequency depending on the support stiffness for a few selected arch heights is shown in Fig. 4.

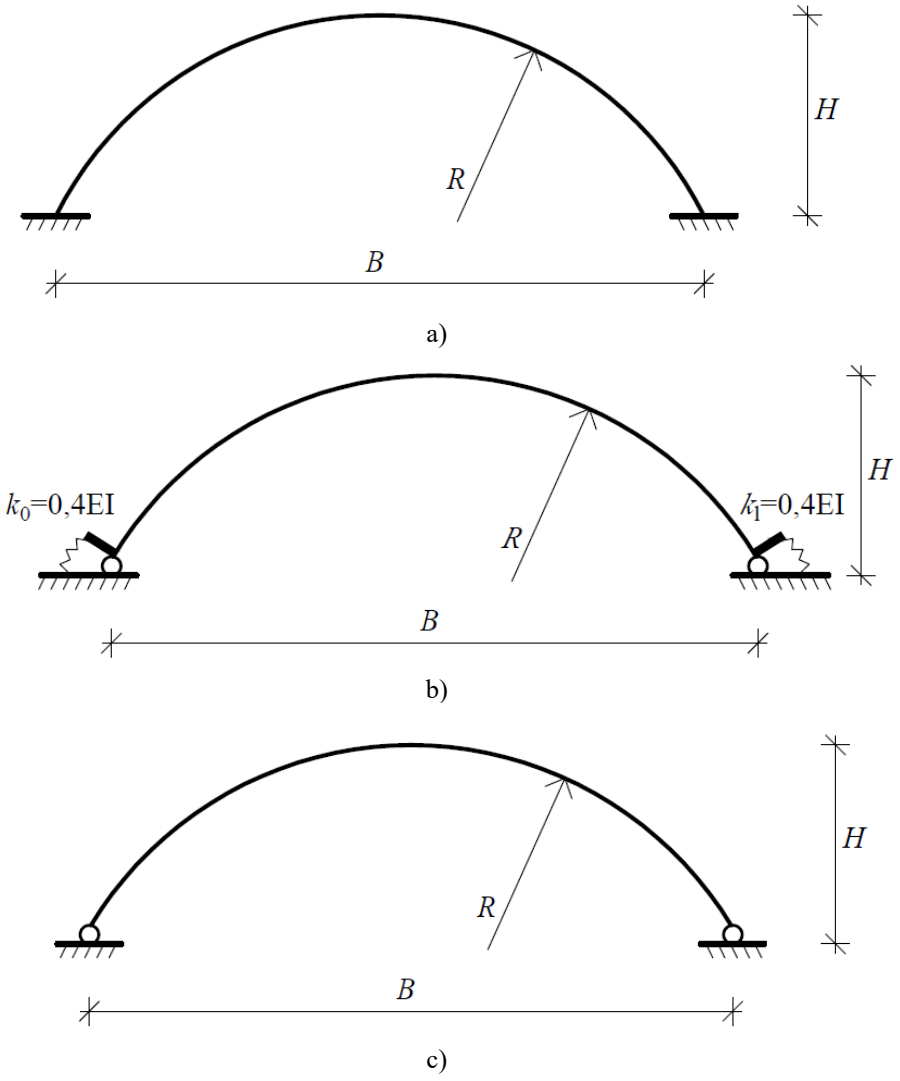

Fig. 3. Diagrams of arch structures with different types of supports
a) fixed-fixed b) flexible supports c) pinned-pinned.

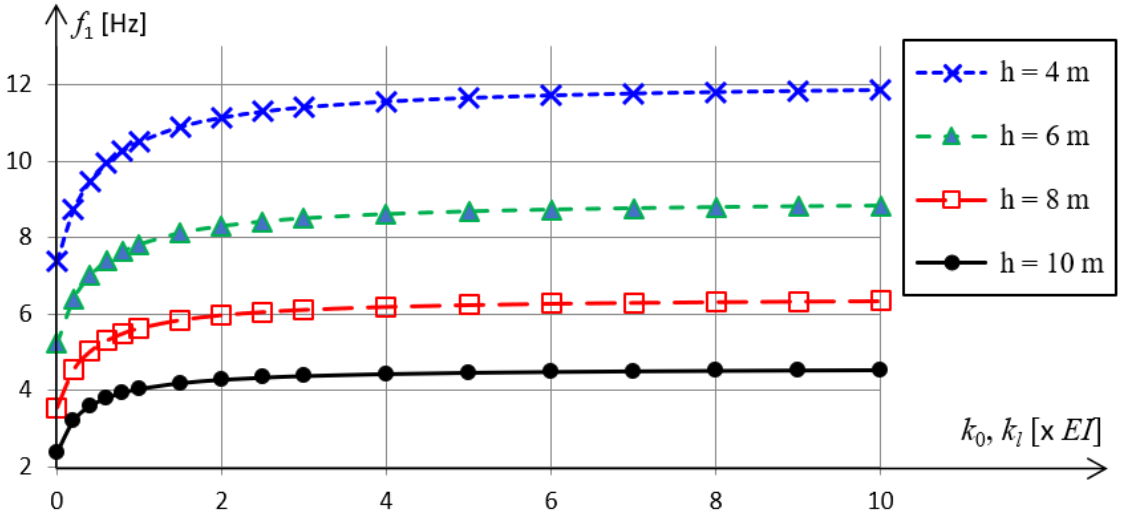

Fig. 4. Fundamental, natural frequency of arch versus the rotational stiffness of the supports.

In the case of a 10 m high arch (half of circle), it can be concluded that the supports behave as completely rigid when the rotational stiffness is twice as high as the bending stiffness of the bars. The variability of the first natural frequency is greater in the range of stiffness from 0 to 2*EI* for smaller arches.
Analysis of the variability of the first natural frequency was also carried out for arch with height of 10m for different values of the stiffness of flexible supports. Stiffnesses varied from 0 to 2*EI*. The results are shown in Figure 5.

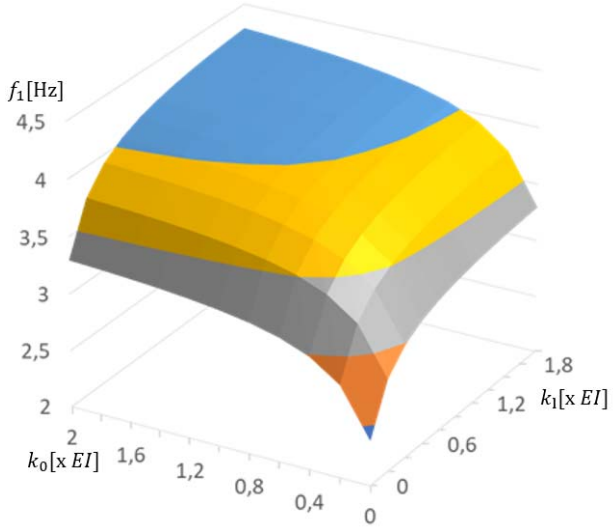

Fig. 5. First natural frequency f_1 for different stiffnesses of flexible support.

The values of the first three natural frequencies were also compared for arches with different supports. The analysis was carried out for arch with height of 3m. The results are presented in Table 4.

Tab. 4. Comparison of first three natural frequencies for different supports, height of arch is 3m.

Mode	Natural frequency [Hz]		
	Fixed-fixed	Flexible supports $k_0 = k_l = 0.4EI$	Pinned-pinned
1	13.6375	10.7114	8.4936
2	24.2266	20.7968	18.9323
3	43.8505	38.9871	36.1855

As expected, the frequencies are higher for fixed supports than for pinned supports. Since the stiffness of the flexible supports is between these two cases, the natural frequencies also take the corresponding intermediate values. The variability of the first three natural frequencies was also examined for the flexible supports with stiffnesses $k_0 = k_l = 0.4EI$ for changing height of arch. The results are listed in Table 5. The values of natural frequencies decrease with increasing arches height.

Tab. 5. Comparison of first three natural frequencies for different height of arch, stiffnesses are $k_0 = k_l = 0.4EI$

Mode	Natural frequency [Hz]		
	H = 3m	H = 6m	H = 10m
1	10.7114	7.0082	3.5961
2	20.7968	15.0515	8.5346
3	38.9871	28.0804	16.2760

4. CONCLUSIONS

The proposed method makes it possible to assess the influence of the rotational flexibility of connections in nodes on the static and dynamic parameters of bar structures. The derived formulas allow for the analysis of both external flexible support and for internal ones. Based on measurements in the actual structure and on the basis of the calculation results, it can be stated when the connection can be treated as rigid, i.e. when a change in the rotational flexibility causes a negligible change in the value of dynamic parameters.
The next stage of the research will be the use of the shape functions of a different type and comparison of obtained results, as well as the analysis of the influence of the applied flexible boundary supports on the seismic response of the structures.

ACKNOWLEDGEMENTS

The study has been supported by the University internal grant No. SBAD 0411/SBAD/0004. This support is gratefully acknowledged.

REFERENCES

Calio, I., Greco, A., D'Urso D. 2014. *Free vibrations of spatial Timoshenko arches*. Journal of Sound and Vibration 333: 4543-4561.

Chidamparam, P., Leissa, A.W. 1995. *Influence of centerline extensibility on the in-plane free vibrations of loaded circular arches*. Journal of Sound and Vibration 183(5):779-795.

Lamb, H. 1887. *On the Flexure and the Vibrations of a Curved Bar*. Proceedings of the London Mathematical Society 1-19(1): 365-377.

Lin, S.M., Lee, S.Y. 2001. *Closed-form solutions for dynamic analysis of extensional circular Timoshenko beams with general elastic boundary conditions*. International Journal of Solids and Structures 38:227-240.

Ozturk, A.U., Catal, H.M. 2005. *Dynamic Analysis of semi-rigid frames*. Mathematical and Computational Applications 10(1):1-8.

Rao, S.S, Sundararajan, V. 1969. *In-plane Flexural Vibrations of Circular Rings*. Journal of Applied Mechanics 36(3):620-625.

Sekulovic, M., Salatic, R., Nefrovska, M. 2002. *Dynamic analysis of steel frames with flexible connections*. Computers and Structures. 80:935-955.

Tufekci, E., Arpaci, A. 1998. *Exact solution of in-plane vibrations of circular arches with account taken of axial extension, transverse shear and rotatory inertia effects*. Journal of Sound and Vibration 209(5):845-856.

Wasserman, Y. 1977. *The influence of the behaviour of the load on the frequencies and critical loads of arches with flexibly supported ends.* Journal of Sound and Vibration 54(4):515-526.

Xu, J.X., Huang, H., Zhang, P.Z., Zhou, J.Q. 2002. *Dynamic stability of shallow arch with elastic supports – application in the dynamic stability analysis of inner winding of transformer during short circuit.* International Journal of Non-Linear Mechanics 37:909-920.

Yang, Y.B., Lin, C.L., Yau, J.D., Chang, D.W. 2004. *Mechanism of resonance and cancellation for train-induced vibrations on bridges with elastic bearings*. Journal of Sound and Vibration 269:345-360.

Zhuo, C., Xiang, S.X., Yingje, Y. 2021. Modal Research of underground arch structure with elastic support. *Journal of Physics: Conference Series* 1972 012131.

LIGHTWEIGHT STRUCTURES in CIVIL ENGINEERING
CONTEMPORARY PROBLEMS
Monograph from Scientific Seminar
Organized by Polish Chapters of
International Association for Shell and Spatial Structures
Łódź University of Technology
Faculty of Civil Engineering, Architecture
and Environmental Engineering
XXVII LSCE
Łódź, 2nd – 3rd of December 2021

THE DESIGN OF A 3D TENSEGRITY MODULE TO EC3 – NUMERICAL EXAMPLES

L. Małyszko [1] **A. Rutkiewicz** [2]
[1] Professor, Faculty of Geoengineering, University of Warmia and Mazury in Olsztyn, POLAND,
andrzej.rutkiewicz@uwm.edu.pl
[2] Assistant, Faculty of Geoengineering, University of Warmia and Mazury in Olsztyn, POLAND

ABSTRACT: The paper consists of several design worked examples of compressively loaded tensegrity T3 simplex modules. The verification of ultimate limit states according to the Eurocode 3 is performed based on the raised full scale physical model of tensegrity T3 simplex, with two different cross-sections of struts. A numerical solution to the force distribution during loading is used, as well as, resistances to buckling and rupture of elements are calculated. Based on the results, a more optimal solution is presented by following a proposed simple algorithm of design. The presented examples are aimed to connect the theoretical calculations typical for the mechanics of tensegrity structures with civil engineering approach to the design of steel structures in accordance to the Eurocode 3.

Keywords: tensegrity column, buckling resistance, Eurocode 3, structural design, self-stress, T3 simplex.

1. INTRODUCTION

Tensegrity systems are composed of compressed bars, often treated as rigid bodies, and elastic tensioned cables connected in nodes in such a way that stability of the system under external loads applied at the nodes can only be achieved by pre-stress of the cables according to the self-stress states of the structure. Tensegrity systems are usually regarded as a special class of spatial truss structures where members are assembled in a self-equilibrated system providing stability and the geometrical stiffness to the structure. The fundamental three-dimensional module, called a simplex module $T3$ or a regular minimal tensegrity prism is shown in Figure 1a.

The T3 Simplex module is the most well-known tensegrity structure and the one, which was first patented (Fuller 1959, Emmerich 1963, Snelson 1965). It is constructed from three bars (struts) of length b, three cross cables of length s, and six base cables of length l. The topological structure of the T3 simplex module can be completely described by the three parameters: the module height h, the length l and the angle of rotation of the upper base triangle versus the lower base triangle – the twist φ, because the bar length and cross cable length can both be expressed as their function. The self-stressed stable equilibrium configuration of the T3 simplex module without an external force is provided by the twist $\varphi = \pm 5\pi / 6$ for a left-handed and a right-handed module, respectively, which means that any pairs of self-stressed element length s_0, l_0, b_0 or h_0 can be obtained by the other pair. More information on the tensegrity structures can be found for example in (Morto 2003, Skelton and de Olivera 2009, Al Sabouni-Zawadzka and Gilewski 2019, Obara 2019).

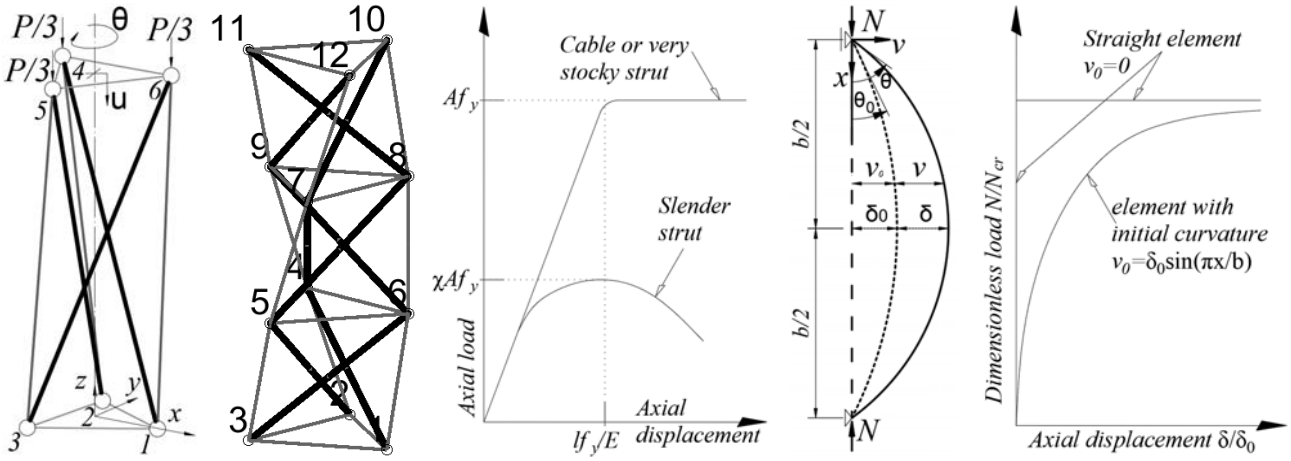

Fig. 1. (a) The T3 simplex, (b) the T3 tower, (c) resistance of elements, (d) strut and (e) elastic flexural buckling.

A larger column can be created by connecting several modules of the T3 simplex by base-to-base connection (Fig. 1b). The column in civil engineering should be designed to carry main vertical loads, as well as, transversal loads (i.e. winds, impacts) or additional loads from eccentric loading, depending on the type of the structure and the location of the column in the structure. The aim of this study is to present some worked examples of the verification of the ultimate limit states in accordance to the Eurocode 3, as well as, following a simple algorithm, to propose a more optimal solution in which the limit states in all members are exceeded at almost the same time under the external compressive force. Additional information on the authors' research on tensegrity structures has been described in (Małyszko 2016, 2017, Małyszko et al. 2018, Małyszko and Rutkiewicz 2020), both under static and dynamic loads.

2. FLEXURAL BUCKLING OF COMPRESION MEMBERS

In the tensegrity module the strut is the axially loaded structural element whose compression resistance decreases as its length increases, in contrast to the axially loaded cable whose tension resistance is independent of its length and which is taken as the yield (or plastic) resistance of the cross-section (Fig. 1c). The decrease in resistance is caused by the bending in the strut with initial curvature (Fig. 1d). The so-called flexural buckling, i.e. the action of lateral deflections growing during the bending until failure occurs at the beginning of compressive yielding, may occur both under the applied external load as well in the self-stress state. Figure 1e presents the behaviour of the straight and the initially curved element. The bending of the strut with initial curvature can be analysed by considering the differential equilibrium equation (Trahair et al. 2008):

$$E_b I \frac{d^2 v}{dx^2} = -N(v - v_0), \tag{1}$$

where E_b is the Young's modulus, I is the moment of inertia, v is the actual horizontal deflection and $v_0 = \delta_0 \sin(\pi x / b)$ is the initial curvature. The solution of equation (1) is the deflected shape:

$$v = \delta \sin(\pi x / b), \quad \text{where} \quad \delta / \delta_0 = \left(N/N_{cr}\right) / \left(1 - N/N_{cr}\right). \tag{2}$$

From the expression of the maximum bending stress $\sigma_{\max}$, where $W_{el} = 2I/D$ is the elastic section modulus, the limiting axial load N_L (i.e. the characteristic buckling strength) for which the above analysis is valid is given by:

$$\sigma_{\max} = \frac{N}{A_b} + \frac{N(\delta+\delta_0)}{W_{el}} \quad \rightarrow \quad N_L = N_y - \frac{N_L(\delta+\delta_0)}{(1-N_L/N_{cr})}\frac{\delta_0 D}{2i^2}, \tag{3}$$

where $N_y = A_b f_{yb}$ is the squash force, D is the strut diameter and i is the radius of gyration. The equation (3) can be solved for the dimensionless limiting load N_L/N_y as:

$$\frac{N_L}{N_y} = \frac{1}{\Phi + \sqrt{\Phi^2 - \overline{\lambda}^2}}, \quad \Phi = 0.5(1+\eta+\overline{\lambda}^2), \quad \eta = \frac{\delta_0 D}{2i^2}, \quad \overline{\lambda} = \sqrt{N_y/N_{cr}}. \tag{4}$$

In the axially loaded module without lateral wind loads, the struts can be treated as the pin-ended column with the bending stiffness $E_b I$, for which the Eurocode buckling curves can be applied (EC3-1-1 2004). The Eurocode curves are based on a probabilistic approach using the experimental strength with a theoretical analysis and describe column strength both for the elastic as well the elastic-plastic buckling. The curves give the value for the reduction factor χ of the strut resistance as a function of the non-dimensional slenderness $\overline{\lambda}$ for different kinds of cross-sections referred to different values of the imperfect factor α are drawn according to the following expression:

$$\chi = \frac{1}{\Phi + \sqrt{\Phi^2 - \overline{\lambda}^2}}, \quad \Phi = 0.5[1+0.49(\overline{\lambda}-0.2)+\overline{\lambda}^2], \quad \overline{\lambda} = \lambda/(\pi\sqrt{E_b/f_{yb}}), \tag{5}$$

where λ is the slenderness and f_{yb} is the yield strength. To illustrate the design worked examples the curve c is chosen with the imperfection factor $\alpha = 0.49$. The curve (5) is shown in Figure 2a for both slender and stocky struts. The non-dimensional slenderness are $\overline{\lambda}_{sl} = 4.01$ and $\overline{\lambda}_{st} = 1.21$ of the slender and stocky struts, respectively. Note that the limit value of the slenderness corresponding to the elastic proportionality is shown in Figure 2, above which fully elastic buckling should be expected for the slender strut, while the behaviour of the stocky strut is elastoplastic with a tangential bending stiffness varying continuously as the load is increased.

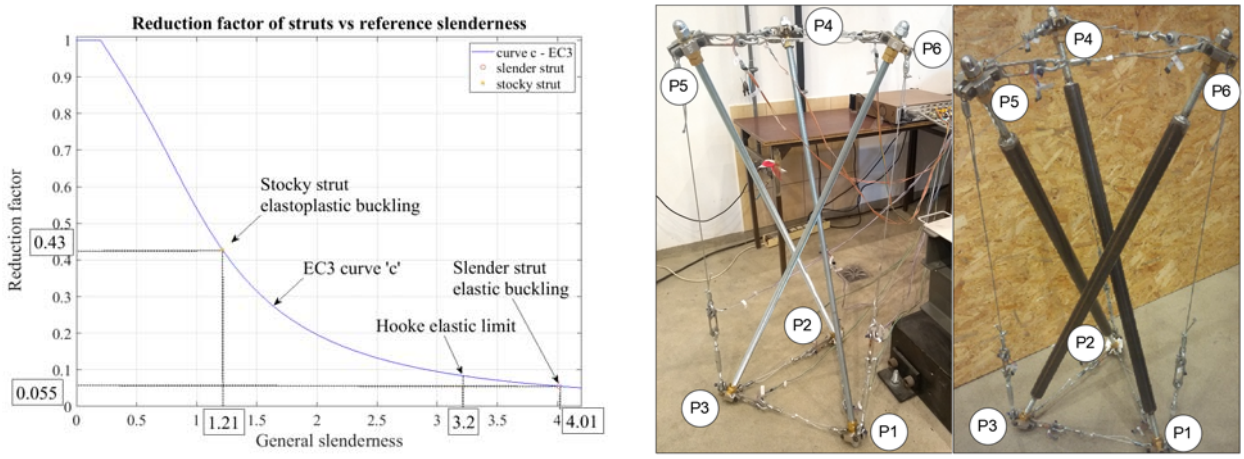

a) b)

Fig. 2. (a) The design curve of the buckling reduction factor χ of the strut resistance as the function of the general slenderness and (b) the slender (left) and stocky (right) tensegrity modules.

3. DESIGN OF TENSEGRITY MODULE ACCORDING TO EUROCODES

The design axial forces in elements of the tensegrity module originate from the pre-straining and the design external compressive load and can be denoted as:

$$N_{Ed} = \gamma_0 N_0 + \gamma_P N_P = \gamma_{0P} N_{Ek}, \tag{6}$$

where N_{Ed} are the design axial forces in struts, cross cables and base cables induced by pre-straining and external compressive force, γ_0 is the partial factor for forces generated by pre-strain, γ_P is a mean partial factor for dead and live loads $(\gamma_G = 1.35 \le \gamma_P \le \gamma_Q = 1.5)$ (EC0, 2004), N_0, N_P are the characteristic values of axial forces induced by the pre-strain and compressive loading, respectively. In other cases we can present general characteristic values of axial forces as N_{Ek} and mean values of the partial factors are calculated as $\gamma_{0P} = N_{Ed} / N_{Ek}$. Since in general, the structure elements dimensions are different before and after pre-straining, the indexes 'n' and '0' are used to distinguish between the natural (unstrained) and the pre-strained configuration, respectively.

Calculating the values of internal forces is based on the theoretical model presented in (Fraternali et al. 2015) together with the computer program discussed in (Małyszko 2016) and design examples from (Małyszko 2017), where the force density method was used. According to this theoretical model the characteristic pre-strain $p_{0,Ek}$ is denoted as the strain value in the cross cables $p_0 = (s_0 - s_n)/s_n$ and the axial forces N_{b0}, N_{s0} and N_{l0} in struts, cross and base cables of the self-stressed state are:

$$\begin{aligned} &N_{s0} = E_s A_s p_{0,Ek}, \quad x_s = N_{s0}/s_n\left(1+p_{0,Ek}\right), \quad N_{l0} = \frac{x_s l_0}{\sqrt{3}} = \frac{x_s}{\sqrt{3}} \frac{E_l A_l (1+p_{0,Ek}) l_n s_n}{p_{0,Ek}(E_l A_l s_n - \sqrt{3} E_s A_s l_n/3) + E_l A_l s_n}, \\ &N_{b0} = -x_s b_0 = -E_s A_s p_{0,Ek} \sqrt{1 + \frac{6\sqrt{3}\, E_l^2 A_l^2 l_n^2}{\left[p_{0,Ek}(3E_l A_l s_n - \sqrt{3} E_s A_s l_n) + 3E_l A_l s_n\right]^2}}, \end{aligned} \tag{7}$$

where $E_b A_b$, $E_s A_s$, $E_l A_l$ are the modules of elasticity and the cross-section areas of the struts, cross cables and base cables, respectively. The variable $x_s = k_s (s - s_n)/s$ is called the force density in the cross cable, i.e. a ratio between the force in the cross cable N_{s0} and its length s_0, and $k_s = E_s A_s / s_n$ is the truss stiffness of cross-cables.

The solution to the axial forces in the compressively loaded tensegrity module under the vertical force needs an incremental-iterative solutions, since the T3 simplex experiences large displacements. In any node of the tensegrity T3 simplex, the force equilibrium equations along the three Cartesian directions can be expressed in the following manner:

$$x_s - x_b/2 + \left(x_s + 3x_l + x_b\right)\cos\left(\varphi + \pi/3\right) = 0, \; -x_b\sqrt{3}/2 + \left(x_s + 3x_l + x_b\right)\sin\left(\varphi + \pi/3\right) = 0, \; -h(x_s + x_b) + P_{Ek}/3 = 0. \tag{8}$$

where $x_b = k_b (b - b_n)/b$ and $x_l = k_l (l - l_n)/l$ are the actual force densities in the struts and base cables, respectively, and P_{Ek} is the actual, external, characteristic, vertical force. The computer program to find the equilibrium path of the nonlinear system of the equations (8) with 3 unknow parameters $(h, l \text{ and } \varphi)$ is given in (Małyszko 2016) in the form of Matlab scripts.

After the solution, values of the axial forces are compared to the resistances of tensegrity module elements. The ultimate limit states (ULS) of cross and base cables are performed by the condition (6.2) of the standard (EC3-1-11, 2008) when (assumption on the linearly elastic phase of work on cables is made):

$$N_{s,Ed}/F_{Rd} = 1.5\gamma_R N_{s,Ed}/F_{uk} \le 1.0 \quad \text{and} \quad N_{s,Ed}/F_{Rd} = 1.5\gamma_R N_{l,Ed}/F_{uk} \le 1.0, \tag{9}$$

where γ_R is a partial safety factor in case of usage of special anchorage ($\gamma_R = 1.0$ without special anchorage), F_{uk} is a characteristic value of the rupture force and F_{Rd} is the design strength. The ultimate limit states of struts are meet based on the condition (6.46) of the standard (EC3-1-1, 2004) when:

$$\left|N_{b,Ed}\right| / N_{b,Rd} \leq 1,0, \tag{10}$$

where $N_{b,Ed} = N_L / \gamma_{M1}$ is the design buckling resistance, γ_{M1} is the partial factor for member instability (recommended as $\gamma_{M1} = 1.0$).

Finally, taking into account the presented design axial forces and resistances, as well as, geometric assumptions an algorithm of the design process of the tensegrity column is given in Figure 3. The pre-straining values were set in accordance to the recommendations of one of the cable manufacturers (Halfen 2020), although the system cables were not used. This simple requirements propose, that the pre-strain generated axial forces in elements cannot exceed 40% and 50% of its load bearing capacities in the prestressing state for cables and struts. Moreover, the presented graph (Fig. 3) has its limitations – i.e. it is restricted to circular cross sections of at least 3rd class for struts, as well as, the cable design is in accordance to the EC3-1-11. Also, it does not consider the serviceability limit states. Such states should be considered in case of columns, for example restricting the maximum vertical deflection under applied vertical loas to avoid large displacements of the leaning elements. This can be restricted only to live loads, since the deflection originated from the dead load is known at the stage of design and can be added to the column height to obtain the desired height. Such a serviceability limit state could be considered as:

$$u^{live} / u_{sls} \leq 1.0 \rightarrow u^{live} \leq h_n / 250, \tag{11}$$

for a limited vertical deflection $u_{sls} = h / 250,$ where u is the actual vertical displacement and h_n is the initial height of the column.

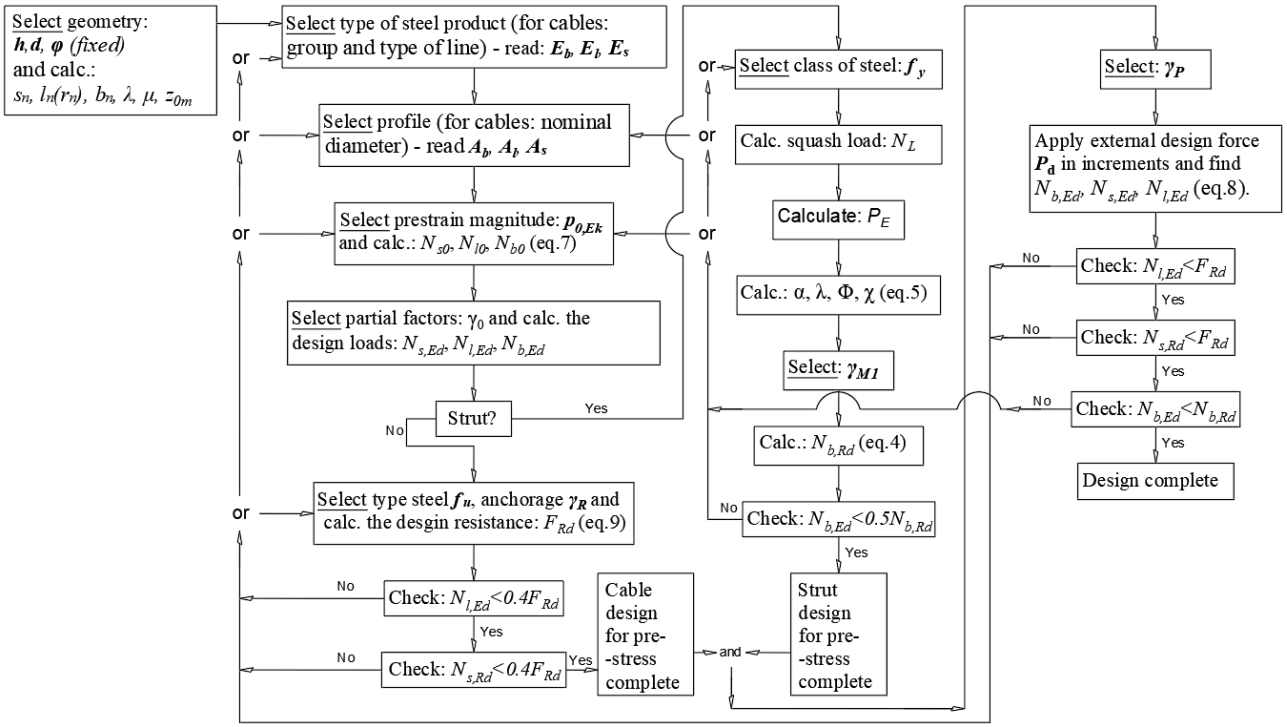

Fig. 3. Flow chart for the design of tensegrity column.

4. WORKED EXAMPLES

As a first step, the verification of the load bearing capacity of the physical model of the tensegrity module is checked for the self-stress phase, loading phase with no pre-strain and finally, for the loaded and pre-strained module. Please note, that two modules are verified and the calculations for the stocky module are written on the left side, while for the slender module one on the right side of the page.

4.1. The T3 simplex models and resistances of their members

Let us consider a specific case of tensegrity module, presented in Figure 2b, which is a physical model build by the authors. There are two variations of this structure, each with different struts – i.e. a so called slender struts (Fig. 2b – left, $\overline{\lambda}_{sl} = 4.01$, indexed sl, CHS 42.4x2) and stocky struts (Fig. 2b - right, $\overline{\lambda}_{st} = 1.21$, indexed st, M20 bar) which leads to two different structures, called the slender-strut and the stocky-strut module. The model is fully build out of steel components. The cables are made out of 1x19 strand, 3mm diameter, steel line. Additionally, each cable has attached a force sensor, while three cross-cables has also additionally attached a roman screw in order to induce and control the prestress level. Also, the model is equipped with force sensors (Wheatstone half-bridge principle of work) attached to all cables. Natural dimensions are given in Table 1, while material and geometry of sections are given in Table 2.

Tab. 1. Tensegrity modules natural dimensions.

s_n	l_n	r_n	b_n	δ_0	h_n	$\lambda = b_n / r_n$	$\mu = h_n / (2r_n)$
m	m	m	m	m	m	–	–
1.193	0.431	0.249	1.280	6.4e-3	1.186	5.141	2.382

Tab. 2. Material and geometry of cross-sections of tensegrity modules.

T3 simplex	E_b GPa	m_b kg/m	I mm^4	W mm^3	A_b mm^2	E_l GPa	E_s GPa	f_{yb} MPa	$f_{us} = f_{ul}$ MPa	$A_{m,l} = A_{m,s}$ mm^2	$m_s = m_l$ kg/m
Stocky	197.8[2]	1.99	51 916	2 448.8	253.8	56.0[3]	81.0[3]	355	1570[4]	5.25[5]	$4.4 \cdot 10^{-3}$
Slender	204.1[1]	1.92	4 036	476.7	225.2						

[1] Value from the own compression test, [2] equivalent moduli, [3] values form the own uniaxial tension tests on full elements (composites), [4] rupture strength, [5] *Am* denotes the metallic cross section (without spaces between wires).

Before calculating the resistance of the members, partial factors need to be assumed - these are given in Table 3. For simplification, only dead load and pre-strain generated forces are considered (therefore the partial factor is set to 1.35), as well as, only the upper values of these factors are considered (the '*sub*' index values in the Eurocodes). The basic values of resistances and other parameters for the analysed elements are gathered in Table 4.

Tab. 3. Partial safety factors.

$\gamma_{0,\mathrm{sup}}$	$\gamma_{P,\mathrm{sup}}$	γ_R[1]	γ_{M1}	$\gamma_{0P,\mathrm{sup}}$
1.35	1.35	1.0	1.0	1.35

[1] Partial factor for cable twist protection, see EC3-1-11.

Starting with the design resistance of the cables, the characteristic resistance F_{uk} and design resistance F_{Rd} of the cables are calculated as follows:

$$F_{uk} = k_e d^2 f_{us} K / 1000 = 0.9 \cdot 3^2 \cdot 1570 \cdot 0.525 / 1000 = 6.68kN,\ F_{Rd} = F_{uk} / \left(1.5\gamma_R\right) = 6.68 / \left(1.5 \cdot 1.0\right) = 4.45kN$$

where k_e is a partial factor for type of anchorage and K is the factor for rupture force (EC3-1-11). Calculations necessary for strut design buckling resistances are given below as:

$$\bar{\lambda}_{st} = \sqrt{\frac{N_{Rk,st}}{P_{E,st}}} = \sqrt{\frac{90.099}{61.860}} = 1.21, \qquad \bar{\lambda}_{sl} = \sqrt{\frac{N_{Rk,sl}}{P_{E,sl}}} = \sqrt{\frac{79.946}{4.962}} = 4.01,$$

$$\alpha = 0.49, \quad \Phi_{st} = 0.5\left(1+\bar{\lambda}^2 + \alpha\left(\bar{\lambda}-0.2\right)\right) =$$

$$= 0.5\left(1+1.21^2+0.49\left(1.21-0.2\right)\right) = 1.4795, \qquad \Phi_{sl} = 0.5\left(1+4.01^2+0.49\left(4.01-0.2\right)\right) = 9.5161,$$

$$\chi_{st} = \left(\Phi + \sqrt{\Phi^2 - \bar{\lambda}^2}\right)^{-1} =$$

$$= \left(1.4795 + \sqrt{1.4795^2 - 1.21^2}\right)^{-1} = 0.43, \qquad \chi_{sl} = \left(9.5161 + \sqrt{9.5161^2 - 4.01^2}\right)^{-1} = 0.055.$$

Tab. 4. Load bearing capacities of tensegrity module elements.

Element	P_E kN	N_{Rk} kN	$\bar{\lambda}$ –	χ –	$N_{b,Rd}$ kN	Element	F_{Rd} N
Stocky strut	61.86	90.10	1.21	0.430	38.74	Base & cross cables	4.45
Slender strut	4.96	79.95	4.01	0.055	4.40		

4.2. Self-stress state of modules

Firstly, the self-stress phase of work is considered, where only the pre-strain is applied. The axial forces are calculated based on equation (7). For design purposes a maximum value of pre-strain $p_{0,Ek,\max}$ for ultimate limit states is found for both modules, on the conditions that for the arising values of axial forces generated by arising pre-strain, based on equations (9) for cables and (10) for struts, we find the first value of the pre-strain for which the ultimate limit state is equal to 1.0, separately for stocky and slender module elements.

This value is equal to: $p_{0,k,\max,st} = 0.007752$ for stocky and $p_{0,k,\max,sl} = 0.007223$ for slender module.

The axial forces are:

$N_{b0,st} = -3495N,\ N_{s0,st} = 3297N,\ N_{l0,st} = 684N,$ $\qquad N_{b0,sl} = -3257N,\ N_{s0,sl} = 3072N,\ N_{l0,sl} = 637N.$

The design axial forces are:

$N_{b,Ed,st} = -4718N,\ N_{s,Ed,st} = 4450N,\ N_{l,Ed,st} = 923N,$ $\qquad N_{b,Ed,sl} = -4397N,\ N_{s,Ed,sl} = 4147N,\ N_{l,Ed,sl} = 860N.$

The ultimate limit states are as follows:

$N_{s,Ed,st} / N_{s,Rd,st} = 4450 / 4450 = 1.0,$ $\qquad \left|N_{b,Ed,sl}\right| / N_{b,Rd,sl} = \left|-4400\right| / 4400 = 1.0,$

$\left|N_{b,Ed,st}\right| / N_{b,Rd,st} = \left|-4718\right| / 38740 = 0.12,$ $\qquad N_{s,Ed,sl} / N_{s,Rd,sl} = 4147 / 4450 = 0.93,$

$N_{l,Ed,st} / N_{l,Rd,st} = 923 / 4450 = 0.21,$ $\qquad N_{l,Ed,sl} / N_{l,Rd,sl} = 860 / 4450 = 0.19.$

Therefore, in the self-stress phase, the stocky module fails by the cross cable rupture, while the slender module fails by struts failure. The ultimate limit states (the design exertion) of element in a function of the pre-strain value $p_{0,Ek}$ is presented in Figure 4a, i.e. one can adjust the pre-strain in order to find the related exertion measured by the Eurocode 3 ultimate limit states – equation (9) for cables and equation (10) for struts.

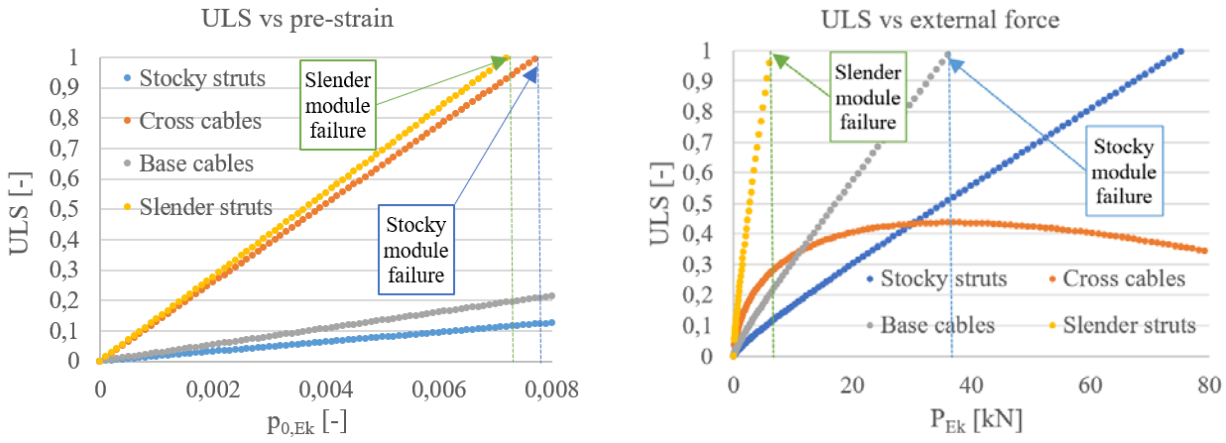

a) b)

Fig. 4. ULS in a function of characteristic (a) pre-strain $p_{0.Ek}$ and (b) external force P_{Ek}.

4.3. External loading with zero self-stress

Secondly, the consideration on the behaviour of the nonself-stressed module is performed (the actual value of pre-strain is equal to $p_{0,Ed} = 10^{-5}$, $N_{s0} = 4.3N$ for avoiding numerical calculation problems with zero stiffness of the column). It should be mentioned, that due to the direction of the compressive loading, the stiffness of the module will increase during the process of loading by force P. Also, since the only difference between the two compared modules, in case of numerical calculations for the presented mathematical model (Małyszko, 2016), is the stiffness of the struts (linearly elastic material) – a mean value of this parameter will be taken. The slender strut axial stiffness is equal to $k_b^{sl} = E_b^{sl} A_b^{sl} / b_n = 204100 \cdot 225.2 / 1280 = 35909N / m$ and the stocky strut axial stiffness is equal to $k_b^{st} = E_b^{st} A_b^{st} / b_n = 197800 \cdot 253.8 / 1280 = 39220N / m.$ The mean value used in the numerical calculations is $k_b = 37565N / m,$ i.e. within a 4.5% difference. In this task, we seek numerically based on equation (8) axial forces in elements caused by external loading P_{Ek} that fulfil equations (9) for cables and (10) for struts – i.e. the value of $P_{Ek,\max}$ for both struts.

The maximum value of characteristic external load $P_{k,\max}$ for which the modules meets the ultimate limit states is equal to: $P_{Ek,\max,st} = 36.9kN$ and $P_{Ek,\max,sl} = 6.42kN$ for the stocky and slender segment, respectively. As can be seen, also the corresponding displacements are given.

The design values are: $P_{Ed,\max,st} = 49.87kN$ for stocky and $P_{d,\max,sl} = 8.68kN$ for slender module.

The design axial forces in elements are:

$N_{b,Ed,st} = -20168N,\ N_{s,Ed,st} = 1944N,\ N_{l,Ed,st} = 4450N,\quad N_{b,Ed,sl} = -4397N,\ N_{s,Ed,sl} = 1233N,\ N_{l,Ed,sl} = 945N.$

The ultimate limit states are as follows:

$N_{l,Ed,st} / N_{l,Rd,st} = \sim 4450 / 4450 = 1.0$

$\left|N_{b,Ed,st}\right| / N_{b,Rd,st} = \left|-20168\right| / 38740 = 0.52,$

$N_{s,Ed,st} / N_{s,Rd,st} = 1944 / 4450 = 0.44,$,

$\left|N_{b,Ed,sl}\right| / N_{b,Rd,sl} = \left|\sim -4400\right| / 4400 = 1.0,$

$N_{s,Ed,sl} / N_{s,Rd,sl} = 1233 / 4450 = 0.28,$

$N_{l,Ed,sl} / N_{l,Rd,sl} = 945 / 4450 = 0.21.$

Therefore, in the external loading phase of module work, the stocky one fails this time by the base cable rupture, while the slender one fails again by struts failure. A relation between the ULS element exertion versus the characteristic external loading P_{Ek}, is presented in Figure 4b. Note that for cables equation (9) is drawn, while for struts equation (10) is drawn.

4.4. External loading with self-stress

This time, the behaviour of the self-stressed tensegrity module in the external loading phase is considered (a typical state). The pre-strain values $p_{0,Ek}$ were set in a way, that the generated forces in elements cannot exceed 40% and 50% of its resistance in the self-stress state for cables and struts, respectively. Therefore, one can easily set the values of forces in the self-stressed state as 40% of pre-strain value for the stocky column module and as 50% of the pre-strain value of the slender module from the maximal values found in subchapter 4.2 (with partial factor). These values are: $p_{0,Ed,st} = 0.4 \cdot 1.35 \cdot 0.007752 = 0.004186$ for the stocky and $p_{0,Ed,sl} = 0.4 \cdot 1.35 \cdot 0.00544 = 0.002938$ for the slender module, respectively.

The maximum value of characteristic external load $P_{Ek,\max}$ for which the module meets the ultimate limit states is equal to: $P_{Ek,\max,st} = 34.4kN$ and $P_{Ek,\max,sl} = 4.96kN$ for the stocky and slender module, respectively.

The design values are: $P_{Ed,\max,st} = 46.47kN$ and $P_{Ed,\max,sl} = 6.69kN$.

The design axial forces are:

$N_{b,Ed,st} = -20242N,\ N_{s,Ed,st} = 3172N,\ N_{l,Ed,st} = \sim 4450N,$ $N_{b,Ed,sl} = \sim -4397N,\ N_{s,Ed,sl} = 1829N,\ N_{l,Ed,sl} = 903N.$

The ultimate limit states are as follows:

$|N_{b,Ed,st}| / N_{b,Rd,st} = |-20242| / 38740 = 0.52,$ $|N_{b,Ed}| / N_{b,Rd,sl} = |\sim -4400| / 4400 = 1.0,$

$N_{s,Ed,st} / N_{s,Rd,st} = 3172 / 4450 = 0.71,$ $N_{s,Ed,sl} / N_{s,Rd,sl} = 1829 / 4450 = 0.41,$

$N_{l,Ed,st} / N_{l,Rd,st} = \sim 4450 / 4450 = 1.0,$ $N_{l,Ed,sl} / N_{l,Rd,sl} = 903 / 4450 = 0.20.$

The chart of the ultimate limit states versus the characteristic external loading P_{Ek} is presented in Figure 5 (this time the charts are separated, since the pre-strain values for both modules are different). Again, for struts equation (10) is drawn, while for cables equation (9) is drawn.

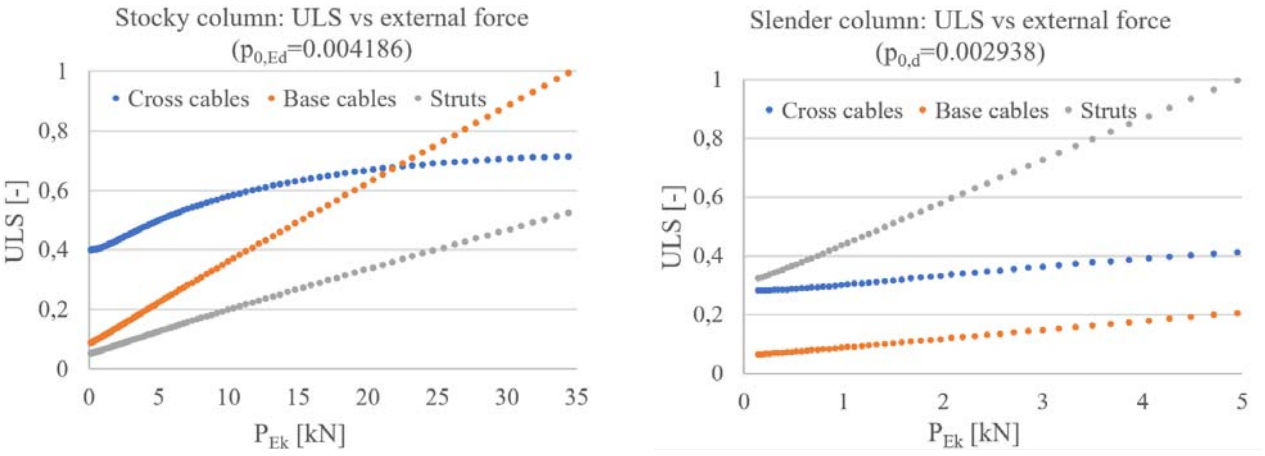

a) b)

Fig. 5. ULS in a function of characteristic external force P_{Ek} for (a) stocky and (b) slender column segment.

5. THE OPTIMAL DESIGN

Considering the presented ULS verification, one can propose an optimal solution, i.e. a solution in which the ULS in all elements are exceeded at the same or close value of the compressive force $P_{Ek,\max}$.

5.1. Self-stress at 40% of the elements resistance

Firstly, the value of generated force in the self-stress state is set to 40% of the cross cable resistance (for typical elements cross cables fail first in the self-stressing phase). The base, arbitrary chosen assumption

will be the design external load equal to $P_{Ed,\max} = 50kN$ $\left(P_{Ek,\max} = 37kN\right)$, which is a close value to the obtained from the stocky module from the subchapters 4.2 and 4.3 ($P_{Ed,\max} = 49.87kN$ and $P_{Ed,\max} = 46.47kN$, respectively). The geometry of the module and values of Young's moduli, as well as, the partial factors, are similar to the ones given in Tables 1, 2 (stocky column) and 4. The cables are 1x19 strand lines and the permitted strengths are $f_u = 1450$, 1570, 1770, $1960MPa$ (each cable strengths and diameter can differ). The struts are CHS and the permitted yield strengths are $f_y = 235$, 275, 355, 420, $460MPa$. Cables and lines are taken from typical profile catalogues. Therefore, using the iterative process and algorithm given in Figure 3, the proposed elements are given in Table 5.

In the self-stress phase, following the recommendations of the maximum 40% exertion in cables, the value was obtained for: $p_{0,Ed} = 0.00492$ and $p_{0,Ek} = 0.00364$. The design axial forces in elements are: $N_{b,Ed} = -1630.9N$, $N_{s,Ed} = 1537.9N$ and $N_{l,Ed} = 319.6N$, while the exertions are: $\left|N_{b,Ed}\right| / N_{b,Rd} = 0.061$, $N_{s,Ed} / N_{s,Rd} = 0.4$ and $N_{l,Ed} / N_{l,Rd} = 0.072$. In the loading phase, the obtained values for the defined load $P_{Ek} = 37kN$ are: $N_{b,Ed} = -22655N$, $N_{s,Ed} = 3731N$ and $N_{l,Ed} = \sim 4451N$, while the exertions are: $\left|N_{b,Ed}\right| / N_{b,Rd} = 0.88$, $N_{s,Ed} / N_{s,Rd} = 0.97$ and $N_{l,Ed} / N_{l,Rd} = 1{,}0$. Figure 6a presents the relation between the ULS and the characteristic pre-strain $p_{0,Ek}$, as well as, characteristic external force P_{Ek}.

Tab. 5. Materials and cross sections taken into the optimal design.

Element	Profile/line	A, A_m mm^2	f_{yb}, f_{us} MPa	$N_{b,Rd}, F_{Rd}$ kN	m kg/m
Strut	CHS 38x2.0	226.19	235	25.7	1.78
Cross cable	1x19, 2.5mm	3.731	1960	3.86	$3.1 \cdot 10^{-3}$
Base cable	1x19, 3.0mm	5.372	1570	4.45	$4.4 \cdot 10^{-3}$

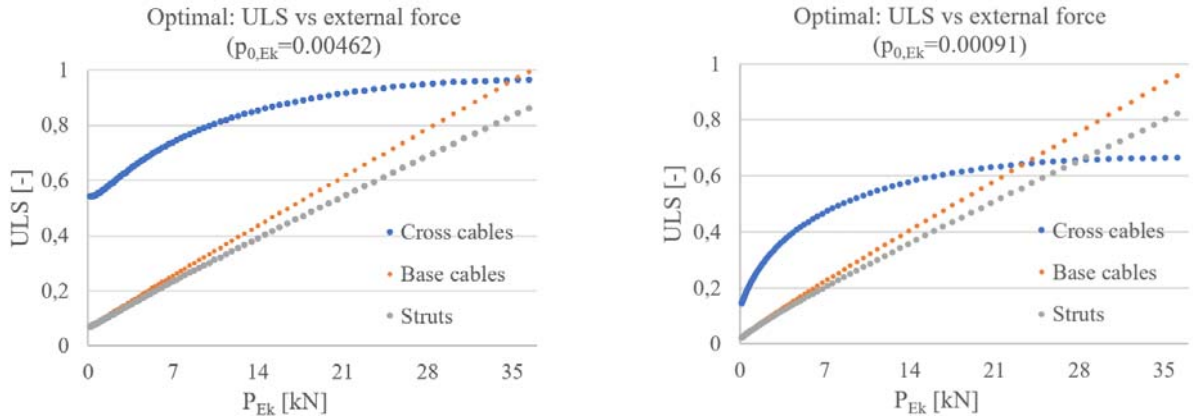

a) b)

Fig. 6. ULS in a function of characteristic (a) pre-strain $p_{0,Ek}$ and (b) external force P_{Ek} for optimal segment.

5.2. Self-stress at 10% of the element resistance

Secondly, the same calculations were set for the pre-strain values generating forces of values 10% of the cross cable resistances, i.e. for the value: $p_{0,Ed} = 0.00123$ and $p_{0,Ek} = 0.00091$.

In the self-stressed phase, the values of internal forces are obviously a quarter of the values presented in subchapter 5.1. In the loading phase, the obtained values for the defined load $P_{Ek} = 37kN$ are: $N_{b,Ed} = -21590N$, $N_{s,Ed} = 2557N$ and $N_{l,Ed} = 4372N$, while the exertions are: $\left|N_{b,Ed}\right| / N_{b,Rd} = 0.84$, $N_{s,Ed} / N_{s,Rd} = 0.57$ and $N_{l,Ed} / N_{l,Rd} = 0.98$. Figure 6b presents the relation between the ULS and the characteristic external force P_{Ek}.

6. DISCUSSION

In order to compare the load bearing capacities of tensegrity systems and typical civil engineering structures, the ratio between the load bearing capacity of the module and the load bearing capacity of only three independent vertical struts, is presented in Table 6, among other values gathered in the calculations. Please note, that we compare the buckling resistance of three independent struts of length b, where we could compare the buckling resistance of struts, taking the length h (height of the module). This means that the ratios in the last column of Table 6 would be even smaller. On the contrary, when connecting several modules in order to create a column, for example five, the length b of struts in the tensegrity structure would not change, whereas the length of the three independent struts would increase five times to the value of $5b$ or $5h$ (then, for comparison purposes we would need to consider rather a truss, than independent struts).

Tab. 6. Results.

Example	Description on loads	Chapter	$p_{0,Ek}$ -	$P_{Ek,\max}$ kN	$3N_{b,Rk}$ kN	$P_{Ek,\max} / 3N_{b,Rd}$ -	M kg
Physical segment	Only self-stress	4.1	-	-	116.2		7.669
	Only ext. load	4.2	$10^{-5} \approx 0$	36.9	116.2	0.32	7.669
	Self-stress (40%) & ext. load	4.3	$3.10 \cdot 10^{-3}$	34.4	116.2	0.30	7.669
Optimized segment	Self-stress (40%) & ext. load	5.1	$3.64 \cdot 10^{-3}$	37.0	77.1	0.48	6.858
	Self-stress (10%) & ext. load	5.2	$0.91 \cdot 10^{-3}$	37.0	77.1	0.48	6.858

In general, the load bearing capacity of the tensegrity module is three to two times lower than the capacity of the individual struts, for the physical model and optimal design, respectively. The pre-straining of elements, as well as, inclination angle of struts in regard to the applied vertical load are important factors that influence this phenomena.

As can be seen from the comparison between the stocky and the slender physical model, the buckling resistance of the struts is crucial for the load bearing capacity of the whole system, i.e. the maximal characteristic loads were $P_{Ek,\max,st} = 34.4,\ 36.9kN$ and $P_{Ek,\max,sl} = 4.96,\ 6.42kN$ for the stocky and the slender segment (chapters 4.2 and 4.3), respectively.

From the comparison between the stocky physical model in the non-self-stressed (chapter 4.2) and the self-stressed and loaded state (chapter 4.3), one can see that the pre-straining is counterproductive – the non-pre-strained module has obtained a slightly greater value of external load $P_{Ek,\max}$.

The same comparison on the maximal external force for the optimal module design shows no difference for the more and less pre-strained module. Nevertheless, the difference in pre-strain is smaller.

Comparison of total mass of elements shows a 12% reduction in mass of the elements between the optimal and physical modules. It is worth mentioning, that the cable mass has a neglected effect on the total mass of the structure.

7. CONCLUSIONS

In the paper, a proposition of an algorithm for the design of compressed tensegrity modules, using circular hollow sections and lines in accordance to the Eurocode 3, was proposed.

Several presented working examples give an insight into the connection of the mechanics of tensegrities and the standardization of the steel elements.

As can be seen, understanding the mechanic response of a single compressed module enables to understand the whole tensegrity column from which it is build. This can be helpful when considering a simple case of an uniaxially loaded column (without transversal and eccentric loads), which is not an untypical case when

considering internal columns of sheltered buildings. When considering a stiffnesses of typical civil engineering elements and the proportions of the modules analysed in this paper, i.e. $\mu \approx 2.4$ (see Tab. 1), we can approximately conclude, that in the self-stressed phase cross cables are a typical form of failure, while in the loading phase base cables are a typical form of failure. Nevertheless, the general stiffness of the structure is generated by the stiffness of the struts. The load bearing capacities of tensegrity module, compared to three vertical struts working separately, are smaller at an advantage of an interesting architectural form.

The process of design, made by hand calculations, is time consuming and requires several iterations, even for someone familiar with tensegrity structures, which is a rather an uncommon knowledge among engineers. This is due to the fact, that the equilibrium path and the individual paths of forces in elements are changing with each change of stiffness of every element (compare Fig. 5a and 6a), as well as, the prestress level (compare Fig. 5 a and b). Moreover, a numerical solver of an analytical system of equations (8) or a nonlinear FEM solver is necessary to find the forces in the loaded stage which makes the issue even more complex.

Further study is focused on extending the research for different loading types, different ratios λ and different number of segments in one column. Performing the mentioned analysis, would give an insight into creating some universal recommendations for the design of these structures.

REFERENCES

Al Sabouni-Zawadzka, A. & Gilewski, W. 2019. *Soft and Stiff Simplex Tensegrity Lattices as Extreme Smart Metamaterials*. Materials, 12, 187.

Emmerich, D.G. 1963. *Construction de reseaux autotendants.* Brevet D'invention No. 1.377.290.

European Committee for Standardisation. 2004. *Eurocode 0: Basis of structural design*.

European Committee for Standardisation. 2004. *Eurocode 3: Design of steel structures. Part 1-1: General rules and rules for buildings*.

European Committee for Standardisation. 2008. *Eurocode 3: Design of steel structures. Part 1-11: Design of structures with tension components*.

Fraternali, F., Carpentieri, G. & Amendola, A. 2015. *On the mechanical modeling of the extreme softening/stiffening response of axially loaded tensegrity prisms.* J. Mech. Phys. Solids 74: 136–157.

Fuller, R.B. 1959. US patent 3.063.521 *Tensile integrity structures.* United States Patent Office.

Halfen. *System cięgnowy Detan. Katalog Techniczny DT13-PL* (in Polish), 2020.

Małyszko, L. 2016. *Static response of axially loaded tensegrity prism. Example of using proprietary programming language.* In Małyszko, L. & Tarczewski, R. (eds.), XXII Lightweight Structures in Civil Engineering 2016. University Publishing House, Olsztyn.

Małyszko, L. 2017. *Design of tensegrity modules with UHMWPE cables based on experiments and nonlinear behavior.* In Gołębiowska, I. & Dutkiewicz M. (eds.), XXIII Lightweight Structures in Civil Engineering. Contemporary Problems. UTP University of Science and Technology in Bydgoszcz, p. 25-30.

Małyszko, L. & Rutkiewicz, A. & Bilko, P. 2018. *Dynamic response of a tensegrity simplex in impact hammer tests.* In Kamiński, M. & Szafran, J., Lightweight Structures in Civil Engineering 2018. Łódź: University Publishing House.

Małyszko, L. & Rutkiewicz, A. 2020. *Response of a tensegrity simplex in experimental tests of a modal hammer in different self-stress levels*. Applied Sciences 10: 8733.

Motro, R. 2003. *Tensegrity. Structural Systems for the Future*. London: Kogan Page Science.

Obara, P. 2019. *Dynamic and Dynamic Stability of Tensegrity Structures*. Wydawnictwo Politechniki Świętokrzyskiej, Monograph nr M116, Kielce, (In Polish).

Skelton, R.E. & de Oliveira, M.C. 2010. *Tensegrity Systems.* London: Springer.

Snelson, K. 1965. *Continuous tension, discontinuous compression structures.* United States Patent Office no. 3,169,611.

Trahair N.S., Bradford M.A., Nethercot D.A. & Gardner L., 2008. *The Behaviour and Design of Steel Structures to EC3*.- 4th ed. London and New York: Taylor & Francis.

LIGHTWEIGHT STRUCTURES in CIVIL ENGINEERING
CONTEMPORARY PROBLEMS
Monograph from Scientific Seminar
Organized by Polish Chapters of
International Association for Shell and Spatial Structures
Łódź University of Technology
Faculty of Civil Engineering, Architecture
and Environmental Engineering
XXVII LSCE
Łódź, 2nd – 3rd of December 2021

EXPERIMENTAL AND NUMERICAL ANALYSES OF AIRFLOW AROUND TWO CYLINDERS ANGLED TO THE DIRECTION OF WIND

A. Padewska-Jurczak [1] **P. Szczepaniak** [2] **R. Walentyński** [3]
[1] Ph.D., Faculty of Civil Engineering, Affiliation Silesian University of Technology, POLAND, *agnieszka.padewska-jurczak@polsl.pl*
[2] Ph.D., Faculty of Civil Engineering, Affiliation Silesian University of Technology, POLAND, *piotr.szczepaniak@polsl.pl*
[3] Ph.D., Professor at the Silesian University of Technology, Faculty of Civil Engineering, Affiliation Silesian University of Technology, POLAND, *ryszard.walentynski@polsl.pl*

ABSTRACT: The purpose of the analyses is to determine the drag coefficients in the case of air flow around two cylinders at different angles to the speed direction. Such systems may be a part of a water slide. These values differ from those given in the so-called wind Eurocode for both a single cylinder and a system of cylinders. Eurocode also does not include the case of cylinders angled to the wind direction. The aerodynamic drag force of the cylinder systems was determined on the basis of numerical Finite Volume Method analyses using the Computational Fluid Dynamics module. To verify the above results, experimental tests were also carried out in a wind tunnel.

Keywords: water slide, wind action, CFD, FVM, wind tunnel test.

1. INTRODUCTION

Lightweight structural elements with circular cross sections and various nontypical shapes are applied in engineering on a large scale. One of such examples are water slides, which can be divided into elements with a circular cross section in the shape of a torus, a helix, a single pipe, or several pipes arranged next to each other at different angles to the direction of the wind speed (see Fig. 1).

Numerical and experimental analyses of the effect of wind on systems of two or more cylinders are often found in literature e.g., in (Żurański 2000, Jester and Kallinderis 2003, Park and Lee 2003). The values of the κ factor, which increase the resulting aerodynamic force of cylinders arranged in a row, are proposed in the Eurocode (CEN 2005). These problems were also discussed in some of the works of the Authors (Padewska 2016, Padewska, Szczepaniak & Wawrzynek 2016). However, in the case of cylinders placed close to each other and concerning large Re numbers these values differ significantly from those given in the literature. The Eurocode also does not include cylinders angled to the wind direction.

The aerodynamic drag force of the cylinder systems was determined on the basis of numerical Finite Volume Method (FVM) analyses using the CFD module. To verify the above results, experimental tests were also carried out in a wind tunnel.

A fragment of a relatively rigid structure is analyzed. The review of the results presented here is mainly limited to determining the aerodynamic resistance of the cylinder systems, ignoring the vibration phenomena of a circular cylinder in the trace of another cylinder (interference galloping).

A fragment of a relatively rigid structure is analyzed. The review of the results presented here is mainly limited to determining the aerodynamic resistance of the cylinder systems, ignoring the vibration phenomena of a circular cylinder in the trace of another cylinder (interference galloping).

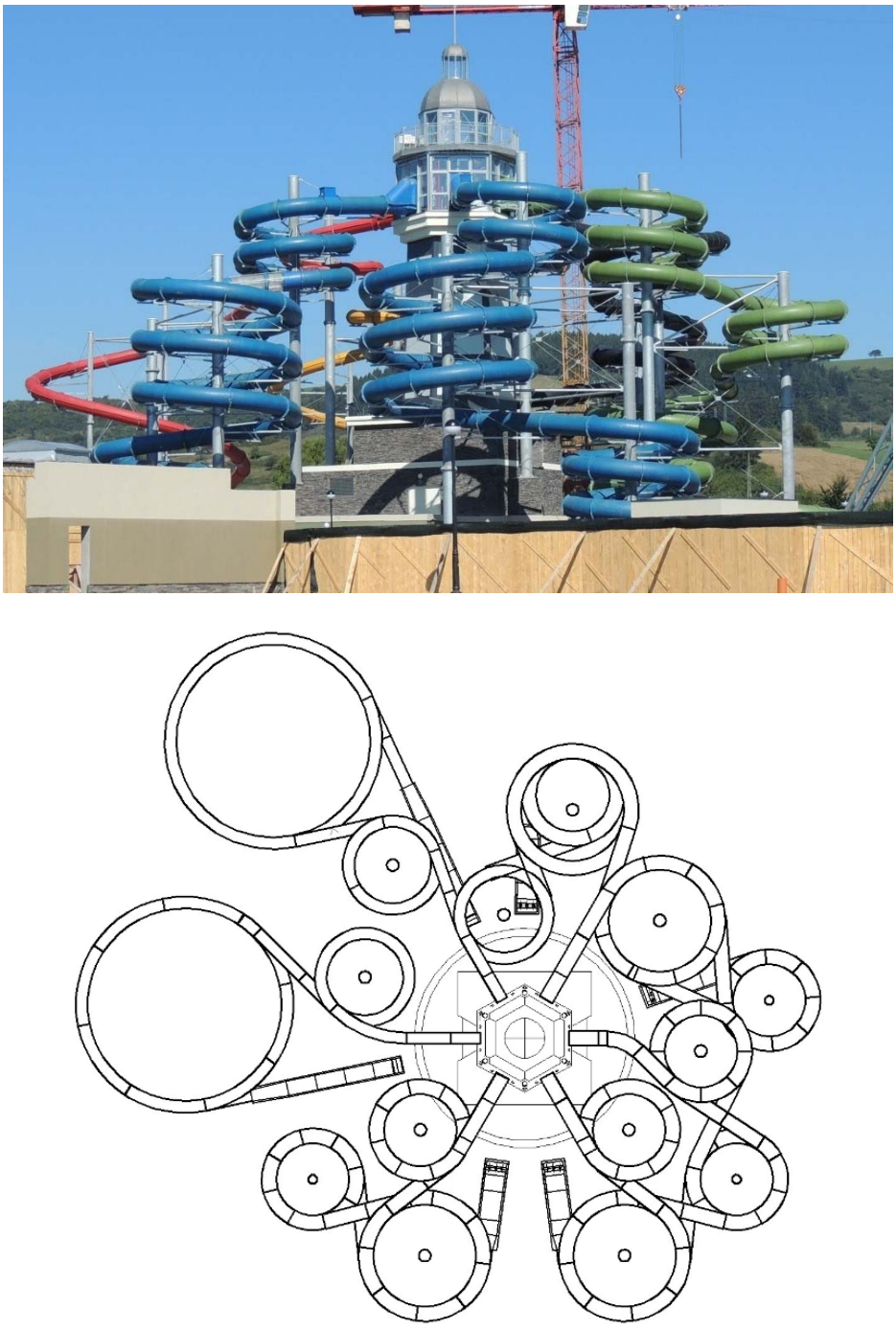

Fig. 1. General view and top view of the water slide in Gino Paradise Bešeňová in Slovakia.

2. NUMERICAL MODELS

Basic numerical model used is subject to rules as follows. The flow in the wind tunnel is modeled (see Fig. 2). The subject of the research is the airflow with Reynolds number Re ranging from 1.33·105 to 2.65·105. The distance between the cylinders with diameter Φ = 200 mm Δ is 100 mm (300 mm center to center), 150 mm (350 mm), 200 mm (400 mm) and 250 mm (450 mm). The cylinders are angled horizontally from the direction of wind velocity by: 0º, 15º, 30º and 45º. Directly at the bottom wall of the tunnel model, the FVM

mesh density is increased. The floor layer in the wind tunnel made of a dimpled foil with a height of 20 mm is considered. The Coupled scheme and Second Order in Spatial Discretization are used for the calculations. Various turbulence models for different cases of wind flow were tested in (Padewska-Jurczak, Szczepaniak and Buliński 2020) and (Padewska 2016).

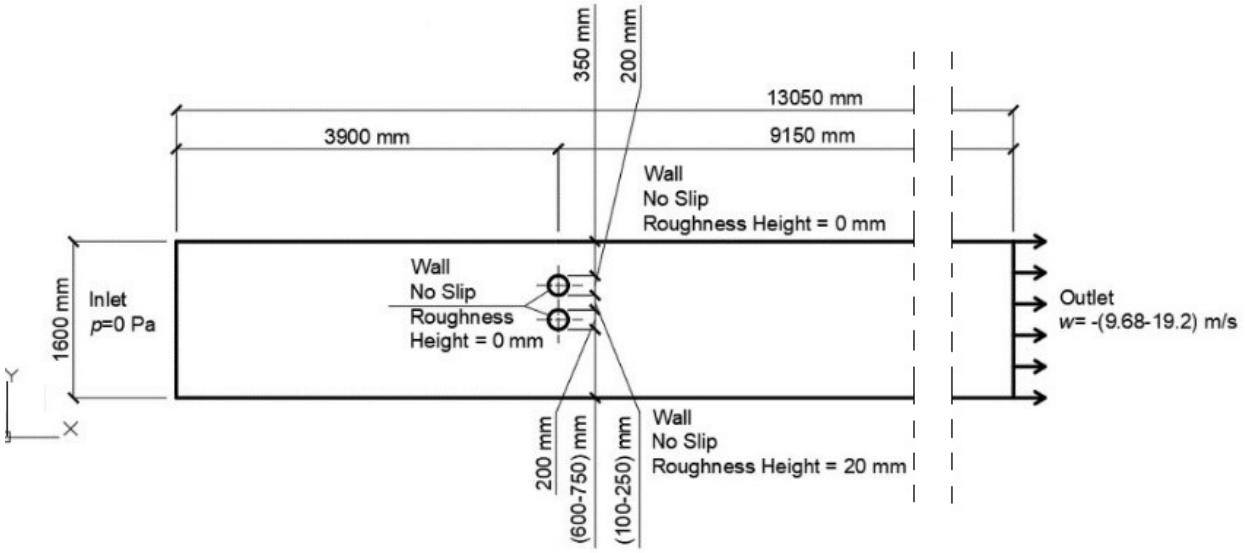

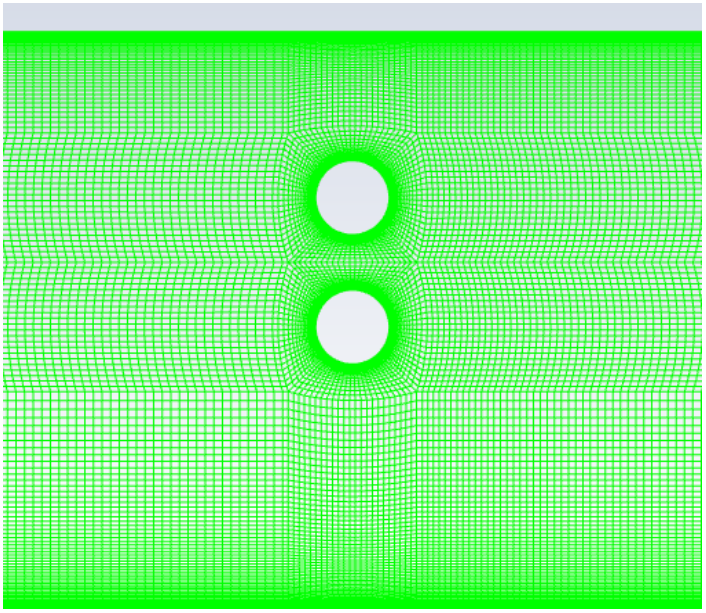

Fig. 2. Numerical model of airflow around two cylinders – dimensions, boundary conditions and sample FVM mesh.

Each of the considered flow ranges (turbulent, transitional, laminar) is characterized by a different behavior. Although all types of flows fall within the critical range (see Coutanceau and Defaye 1991), their nature is very different. Thus it is necessary to adjust the parameters of the numerical model.

The first considered case is: velocity of wind $w = 19.2$ m/s; $\mathrm{Re} = 2.6 \cdot 10^5$. The k-omega/SST turbulence model with Production Limiter is included. $y^+ = 100$ is chosen. The height of the element in the first layer of mesh near the walls of the cylinders is $h = 3.2 \cdot 10^{-3}$ m. The c_{fx} results obtained for the two cylinders differ slightly: for the first one it is 0.62 and for the second one 0.59. Thus, the average value is 0.6. After the cylinders were moved apart by a distance of 400 mm in the axes the average value of the drag coefficient is 0.49.

Another case taken into consideration is: $w = 18.23$ m/s; $\mathrm{Re} = 2.5 \cdot 10^5$. The $y^+ = 80$ ($h = 3.2 \cdot 10^{-3}$ m) is selected, which results in a resistance coefficient equal to: 0.68 and 0.64 (mean value 0.66). Then the cylinders were moved away by a distance of 400 mm in the axes. A mean c_{fx} value of 0.53 is obtained.
In the case of a wind speed of 17.14 m/s ($\mathrm{Re} = 2.3 \cdot 10^5$ m), it is only necessary to reduce the height of the FVM elements at the wall to $h = 2.2 \cdot 10^{-3}$ m ($y^+ = 60$). The result is $c_{fx} = 0.68$.
Changing the speed to 16.04 m/s ($\mathrm{Re} = 2.0 \cdot 10^5$) require reducing y^+ to 40 and the height of the elements to $h = 15 \cdot 10^{-4}$ m. Similarly, in the case of $w = 14.98$ m/s, y^+ is further reduced to the value of 20.
The flow at velocity $w = 13.92$ m/s ($\mathrm{Re} = 1.9 \cdot 10^5$) can be both laminar or turbulent. The area of viscosity influence is in the blending region. It turned out that at $y^+ = 15$ ($h = 6.6 \cdot 10^{-4}$ m) c_{fx} is 1.1.
The flow model for $w = 12.85$ m/s ($\mathrm{Re} = 1.7 \cdot 10^5$) turned out to be more complicated due to the inability to fully use the wall functions. The value of the c_{fx} coefficient equal to 1.21 is obtained for both cylinders.
For the speed $w = 11.77$ m/s ($\mathrm{Re} = 1.6 \cdot 10^5$), 10.8 m/s ($\mathrm{Re} = 1.5 \cdot 10^5$) and 9.68 m/s ($\mathrm{Re} = 1.3 \cdot 10^5$) Curvature Correction was enabled in the Transition SST model. The result in the last case is $c_{fx} = 1.39$.

3. EXPERIMENTAL RESEARCH

Experimental research was carried out at the Centrálne laboratóriá SvF STU in Bratislava. Figure 3 shows the air filter and the laminar flow section of a wind tunnel. The width and height of the measurement space are $B = 2{,}600$ mm and $H = 1{,}600$ mm, respectively (Fig. 4).

Fig. 3. Air filter and laminar flow section of the wind tunnel.

Fig. 4. Cross-section through a wind tunnel.

The subject of the investigation is the air flow around a system of two cylinders with diameter Φ = 200 mm and length L = 2,400 mm without open ends and equal to the width of the measuring section minus the width of the used connectors (Fig. 5). Re is from $1.33 \cdot 10^5$ to $2.62 \cdot 10^5$. The cylinders are angled horizontally from the direction of wind velocity by: 0°, 15°, 30° and 45°.

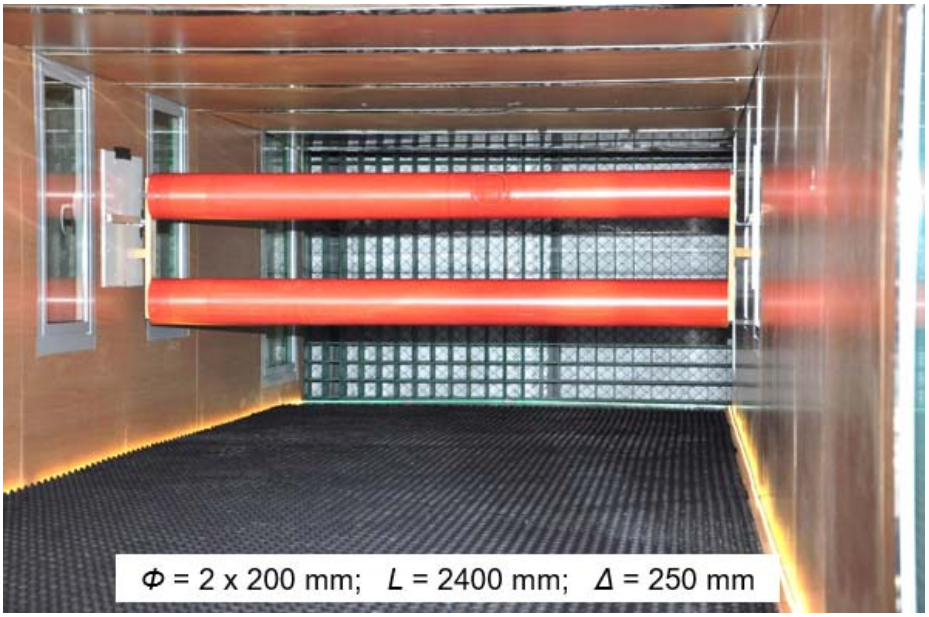

Fig. 5. A model of an arrangement of two cylinders.

Sampling points were made in the pipes to measure the pressure on their walls. Three Scanivalve DSA3217 16Px pressure gauges were used (Fig. 6).

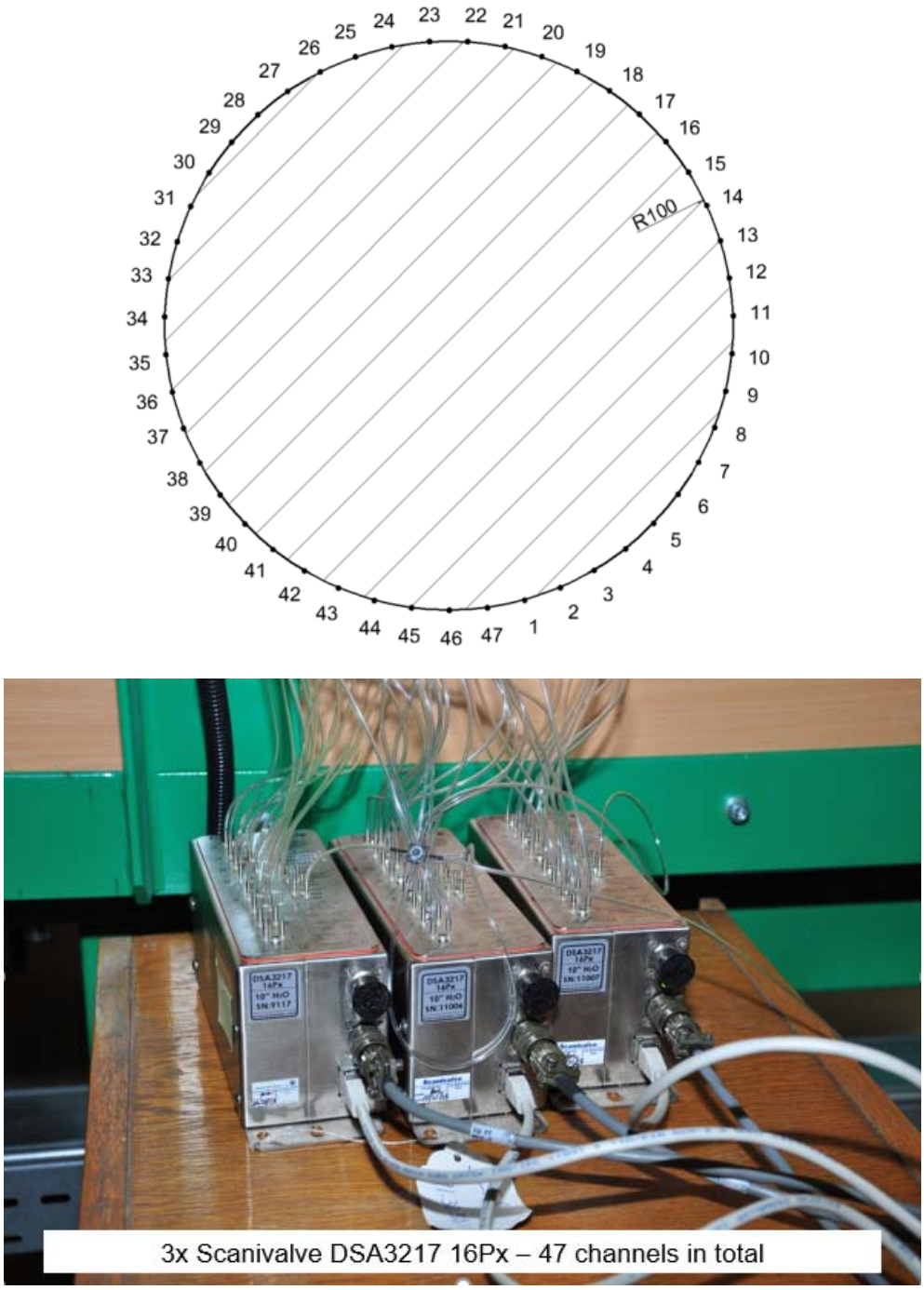

Fig. 6. Sampling points in the pipe and pressure gauges.

Temperature, density and atmospheric pressure were, respectively: 17.6 °C, 1.201 kg/m^3 and 100,680 Pa.

4. RESULTS

Figures 7 and 8 show the velocity vectors and pressure distributions around two cylinders set perpendicular to the wind speed determined from numerical analysis. In the case of speed of 19.2 m/s (Re = 2.6·105), a clear division into regions of smaller velocity and pressure values (in front of the cylinders) and region of higher values (between the cylinders) is visible. In the case of the lowest speed, this division is hardly perceptible and is difficult to model.

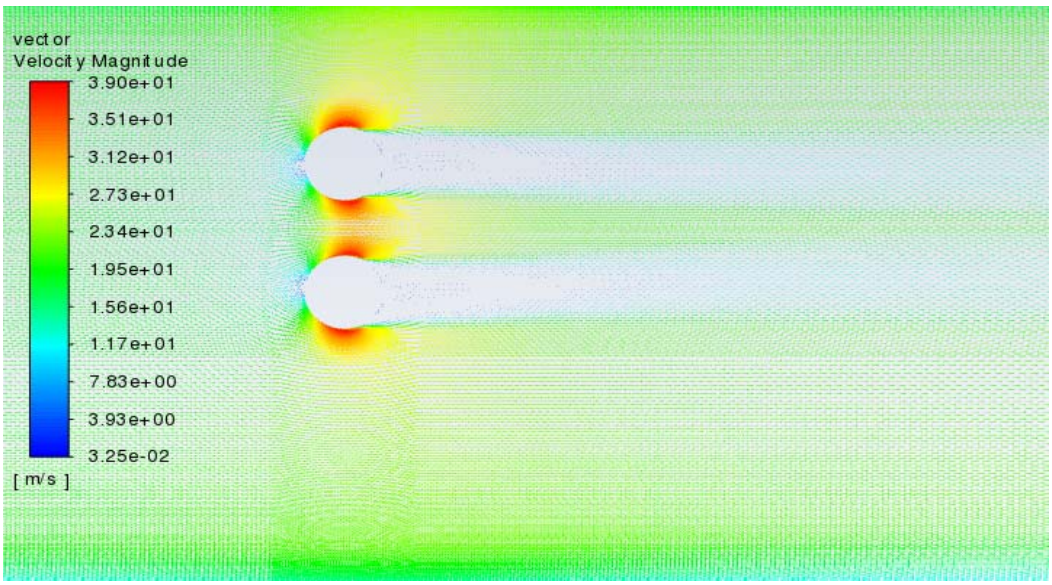

Fig. 7. Distributions of velocity vectors around two cylinders set perpendicular to the wind speed of 19.2 m/s.

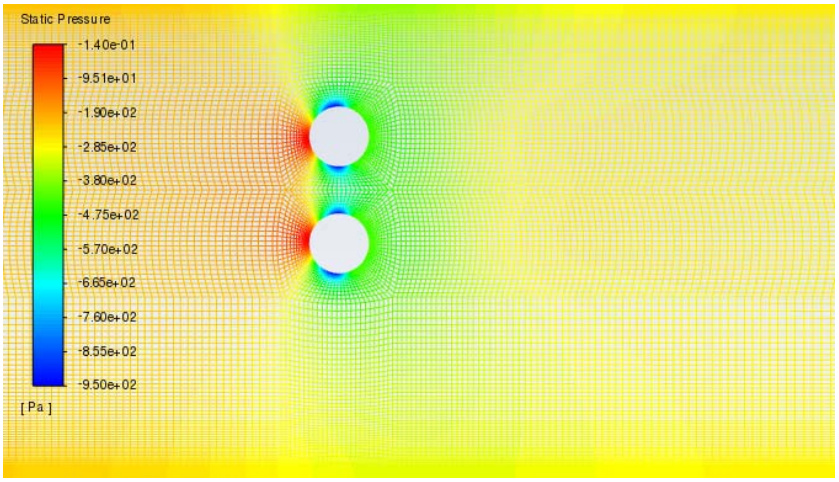

Fig. 8. Pressure distributions around two cylinders set perpendicular to the wind speed of 19.2 m/s.

Figures below (Figs. 9 and 10) show the time-averaged aerodynamic drag forces depending on the wind speed and the time-averaged coefficients of aerodynamic drag depending on the Re number. The data was determined in the wind tunnel. The highest values of drag force occur at a value of Δ equal to 100 mm, for cylinders perpendicular to the direction of the highest wind speed.

From an engineering point of view, the second graph is more useful. Up to the value of Re = 1.9·105 for Δ equal to 100 mm and 1.7·105 for the rest of the cases of cylinders perpendicular to the direction of wind velocity, the graph is very similar to that shown in the Eurocode (CEN 2005) for a single cylinder (Fig. 11). Below these values, the coefficient increases to 1.5. For angled cylinders, these values are lower. The smallest a/Φ ratio is 1.5, where $a = \Delta + \Phi$. Assuming that the drag coefficient of a single cylinder is 1.2, the interference coefficient κ is 1.25 and is greater than those given in (CEN 2005), where the maximum value of κ is 1.15. It should be noted that the British annex to the EN 1991-1-4 standard lacks guidelines to determine the value of the interference factor for a/Φ lower than 2.5. According to other authors's research, this limit could even be shifted to $a/\Phi < 3.0$. Furthermore, quoting the Eurocode: 'For cylinders near a plane surface with a distance ratio $zg/b < 1.5$ (distance between the ground and the wall of the cylinder over the

diameter of the cylinder) special advice is necessary.' This is analogous to cylinders placed close to each other. For angled cylinders, these values are similar to those given in (CEN 2005).

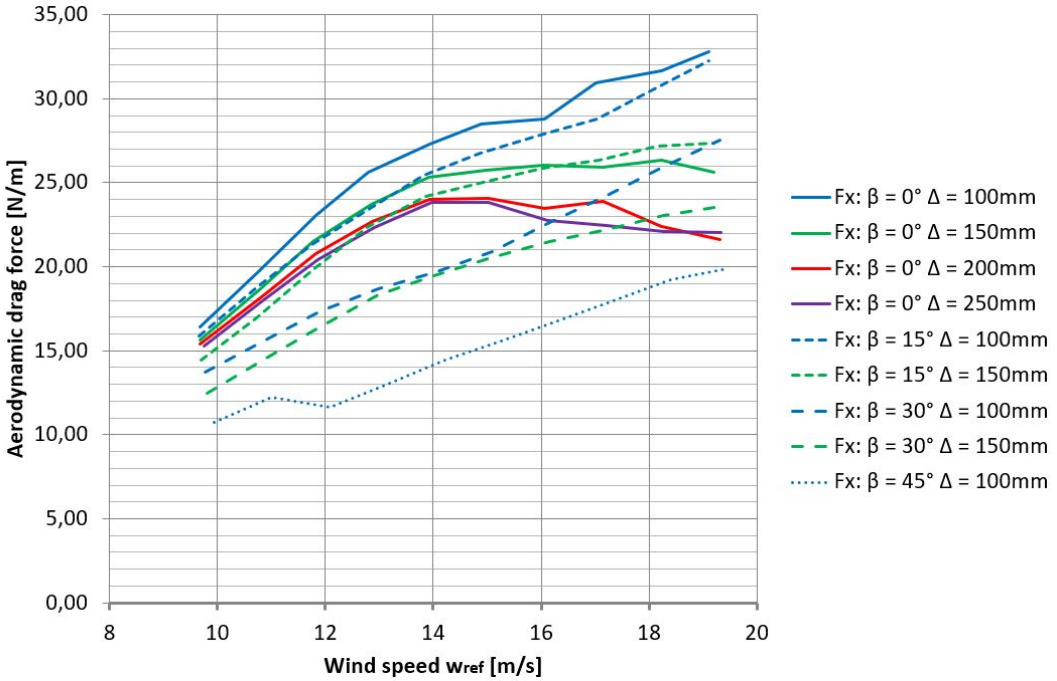

Fig. 9. Average aerodynamic drag forces on the upper cylinder for β = 0°÷45°.

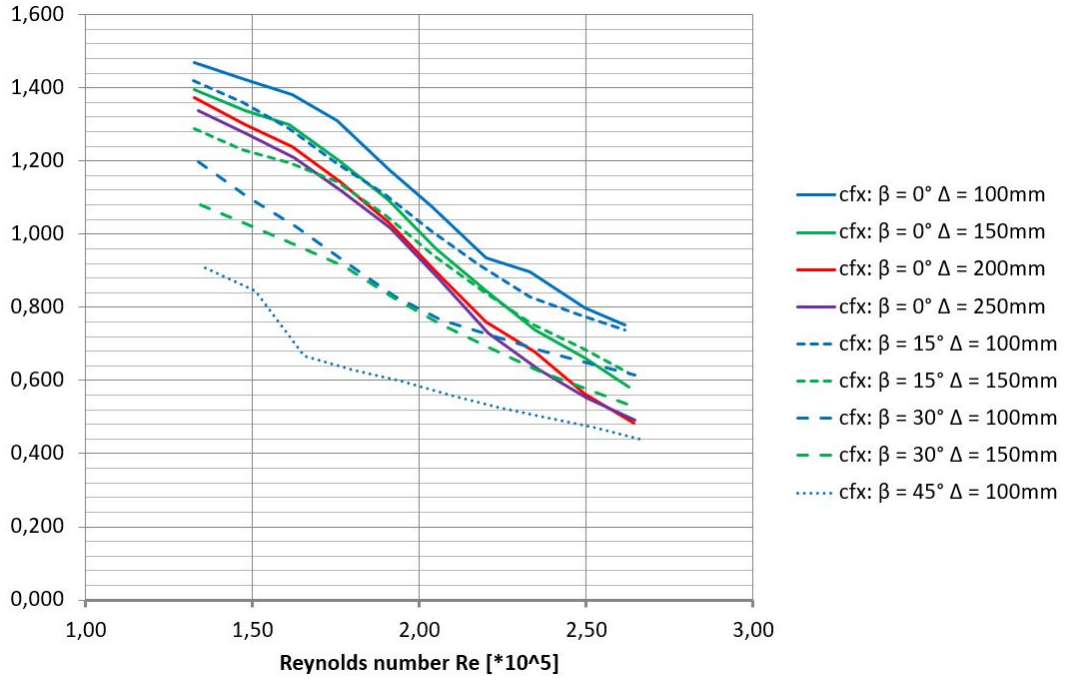

Fig. 10. Average coefficients of aerodynamic drag force on the upper cylinder for β = 0°÷45°.

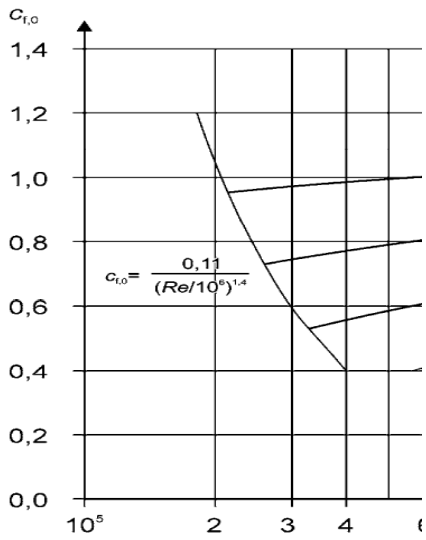

Fig. 11. Coefficients of aerodynamic drag force for one cylinder according to (CEN 2005).

Figures 12 and 13 present the time-averaged aerodynamic lift forces depending on the wind speed and the time-averaged coefficients of aerodynamic lift depending on the Re number. The greatest values of lift force occur at a value of Δ equal to 100 mm for cylinders angled horizontally from the direction of wind velocity by 15°. Only for β = 0° and Δ = 200÷250 mm the average values of the lift coefficient are similar to the data presented in (Lienhard 1966) in Fig. 9 for single circular cylinders. The remaining results shown in Figures 12 and 13 differ from these data.

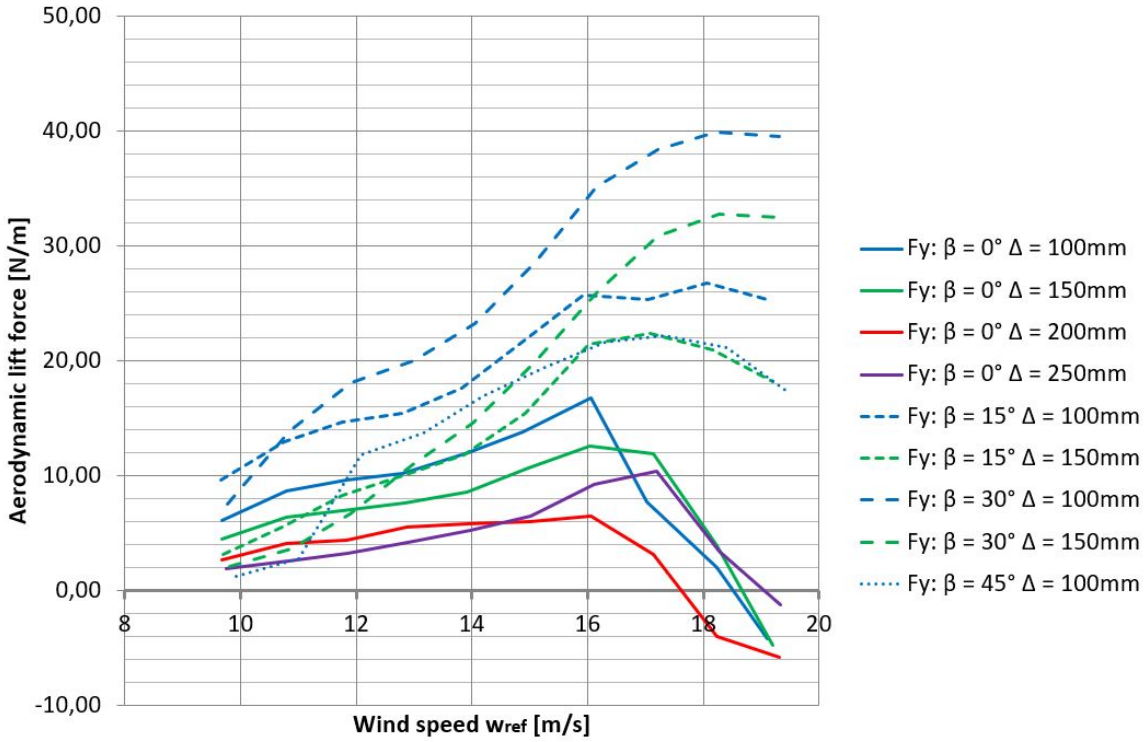

Fig. 12. Average aerodynamic lift forces on the upper cylinder for $\beta = 0°\div45°$.

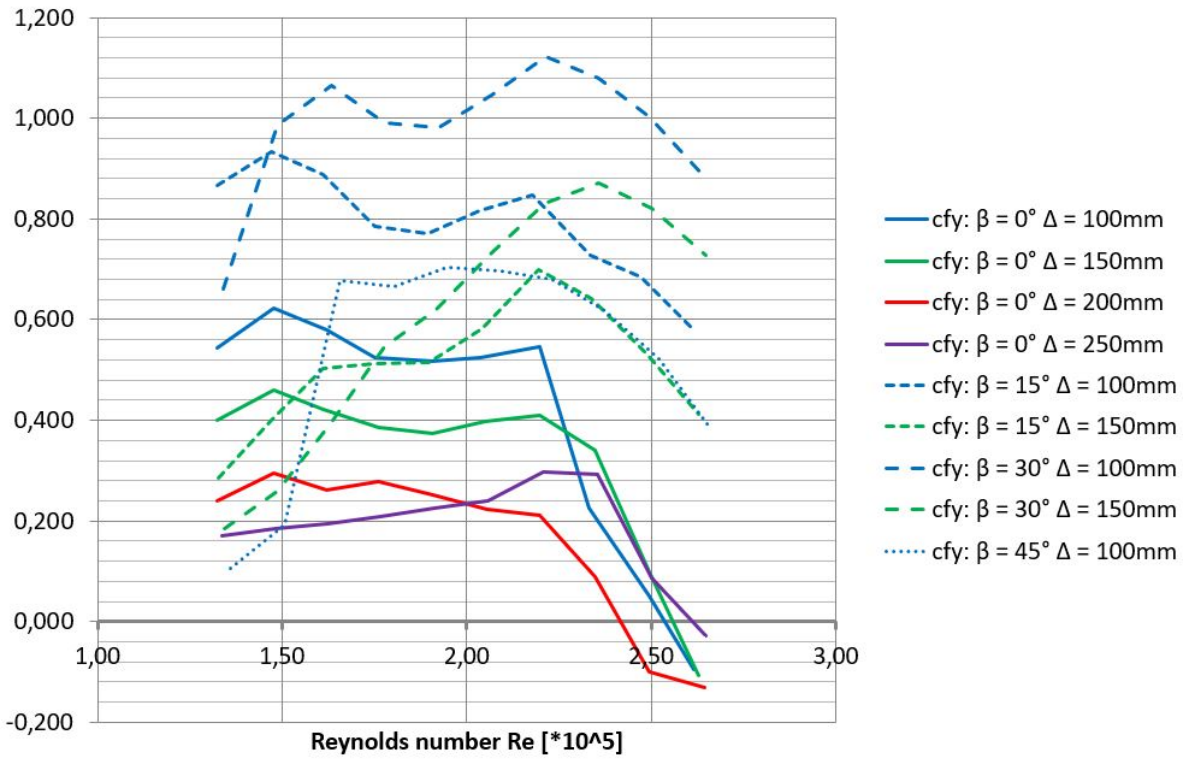

Fig. 13. Average coefficients of aerodynamic lift force on the upper cylinder for $\beta = 0° \div 45°$.

Bringing the cylinders together leaves less space between them which creates a common aerodynamic path of flow and increases the difference of observed values between the windward and leeward surfaces of the cylinders. The differences are much greater than the values given in (CEN 2005) for a single cylinder, even in case of the largest distance between the cylinders analyzed in this paper (Fig. 14). In the case of $\Delta = 250$ mm external pressure coefficient is -3.5.

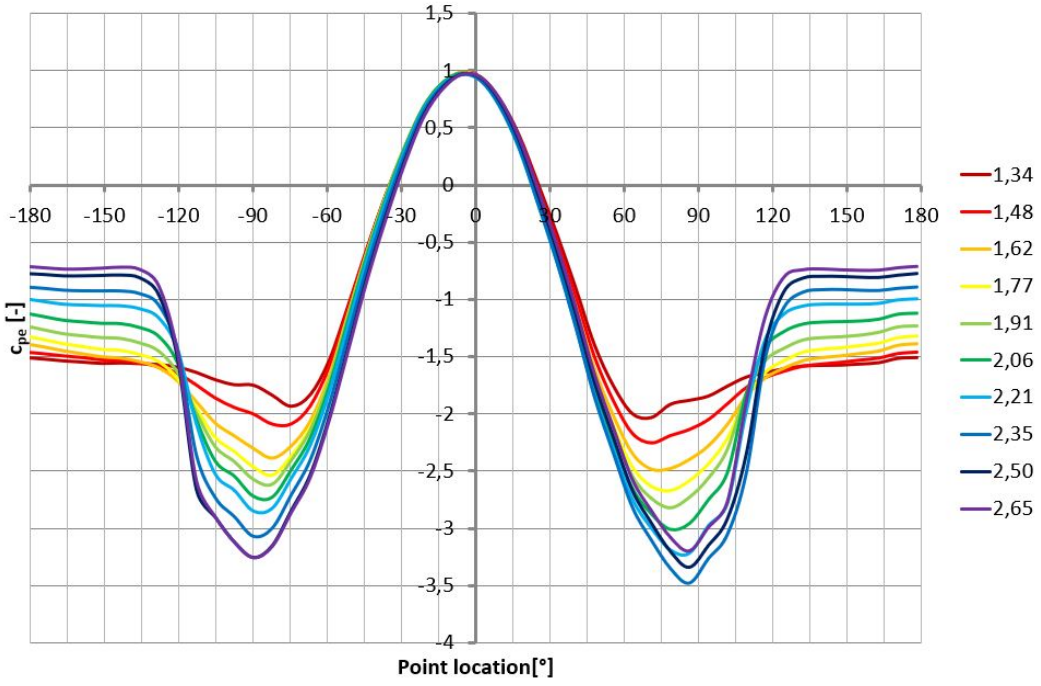

Fig. 14. External pressure coefficients for $\Delta = 250$ mm.

5. CONCLUSIONS

Numerical FVM method using the CFD module and the wind tunnel tests allow for a reliable analysis of the wind flow with high velocity near structures with circular cross sections, arranged in rows e.g. elements of a water slides. Each of the considered flow ranges (turbulent, transitional, laminar) is characterized by a different behavior. Although all types of flows fall within the critical range, their nature is very different. Thus it was necessary to adjust the parameters of the numerical model. As a result of the performed calculations in the wind tunnel the time-averaged coefficients of aerodynamic drag force on the upper cylinder depending on the Re number were presented. The distance between the cylinders with diameter Φ = 200 mm was 100 mm (300 mm center to center), 150 mm (350 mm), 200 mm (400 mm) and 250 mm (450 mm). The cylinders were angled horizontally from the direction of wind velocity by: 0º, 15º, 30º and 45º. The highest values of the drag and interference coefficient occur at a delta equal to 100 mm. These values differ from those given in (CEN 2005) for both a single cylinder and a system of cylinders. The Eurocode also does not include cylinders angled to the wind direction. In the case of speed of 19.2 m/s, a clear division into smaller pressure values (in front of the cylinders) and higher (between the cylinders) was visible. The time-averaged coefficients of aerodynamic lift depending on the Re number were also presented. The greatest values of lift force occur at a value of Δ equal to 100 mm for cylinders angled horizontally from the direction of wind velocity by 15°. Only for $\beta = 0°$ and $\Delta = 200 \div 250$ mm the average values of the lift coefficient are similar to the data presented in (Lienhard 1966) in Fig. 9 for single circular cylinders. The remaining results shown in Figures 12 and 13 differ from these data.

Analyses are used to design a structure with a circular cross section in a more detailed way. More research results will be shown in the development of this work.

To make a more complete analysis, it would be necessary to determine the aerodynamic interference coefficients of various cylinder systems and different diameters. In addition, it may be necessary to take into account in the calculations, for example, connectors or platforms with which water slides are equipped. The phenomenon of vibrations of a circular cylinder in the trace of another cylinder (the so-called interference galloping) should also be investigated.

REFERENCES

CEN. 2005. EN 1991-1-4 Eurocode 1: Actions on structures - Part 1-4: General actions - Wind actions with National Annex. CEN, PKN. Brussels, Warszawa.

Coutanceau, M. & Defaye J. 1991. *Circular Cylinder Wake Configurations: A Flow Visualization Survey*. Appl. Mech. Rewiews 44(6): 255–305. doi: https://doi.org/10.1115/1.3119504.

Jester, W. & Kallinderis, Y. 2003. *Numerical study of incompressible flow about fixed cylinder pairs*. J. Fluids Struct. 17: 561–577. doi: 10.12989/was.2020.30.1.015.

Lienhard, J.H. 1966. *Synopsis of lift, drag, and vortex frequency data for rigid circular cylinders*. Washingt. State Univ. Coll. Eng. Res. Div. Bull. 300, Tech. Ext. Serv.

Padewska-Jurczak, A., Szczepaniak P. & Buliński Z. 2020. *Numerical determination of wind forces acting on structural elements in the shape of a curved pipe.* Wind Struct. An Int. J. 30(1): 15–27. doi: 10.12989/was.2020.30.1.015.

Padewska, A. 2016. *Pogłębiona analiza numeryczna oddziaływania wiatru na obiekty budowlane o nietypowym kształcie i układzie*. Rozprawa doktorska. Politechnika Śląska.

Padewska, A., Szczepaniak P. & Wawrzynek A. 2016. *Wyznaczanie współczynników interferencji układów walców*. Proceedings of the 14th International Conference on New Trends in Statics and Dynamics of Buildings.

Park, C.W. & Lee S. 2003. *Flow structure around two finite circular cylinders located in an atmospheric boundary layer: side-by-side arrangement*. J. Fluids Struct. 17: 1043–1058. doi: 10.12989/was.2020.30.1.015.

Żurański, J.A. 2000. *Wpływ interferencji aerodynamicznej na obciążenie wiatrem stalowych kominów wieloprzewodowych*. Pr. Nauk. Inst. Tech. Bud. 2–3.

LIGHTWEIGHT STRUCTURES in CIVIL ENGINEERING
CONTEMPORARY PROBLEMS
Monograph from Scientific Seminar
Organized by Polish Chapters of
International Association for Shell and Spatial Structures
Łódź University of Technology
Faculty of Civil Engineering, Architecture
and Environmental Engineering
XXVII LSCE
Łódź, 2nd – 3rd of December 2021

OPTIMIZATION APPROACH FOR DOME STRUCTURES

D. Pilarska [1)]
[1)] PhD, Eng, Faculty of Civil Engineering and Architecture, Opole University of Technology, POLAND,
d.pilarska@po.edu.pl

ABSTRACT: The main objectives of domes constructions are to aim to the weight of the structure optimization as well as to obtain a cover with huge possibilities of large area usage thanks to the lack of internal supports. The usage of steel in such kinds of construction systems is reflected in a relatively small own weight of the construction. The other advantages of the spatial strut structures are the usage of straight struts, high rigidity of the structure, ease of shaping, relatively easy assembly. The paper presents the optimization approach of strut dome structures based on the regular octahedron, designed according to two different methods. The analysis of geometry, statics and preliminary dynamic studies of the designed innovative domes allowed to indicate the most optimal solution, taking into account the topology of the considered design methods. Usually the strut domes are cyclically symmetrical structures, having many elements with the same geometry and therefore they are suitable for modern production and assembly.

Keywords: one-layered strut structures, geodesic dome, optimization, numerical analysis, dynamic analysis.

1. INTRODUCTION

The geometric shape of the geodesic dome is used in various types of architectural solutions as an attractive, durable and self-supporting covering. The multitude of advantages of this type of construction solutions makes the dome-shaped coverings very desirable. They are used for roofing larger areas, such as halls, sports facilities, commercial facilities, planetariums and others. It is thanks to the solutions in the form of a three-way mesh stretched over the sphere that we obtain a structure characterized by a small number of different elements, which definitely facilitates prefabrication and assembly. Another advantage of this type of cover is, for example, no need to use internal supports, thus increasing the usable area and the possibility of its development. Moreover, compared to other design solutions, the smaller amount of construction material used per unit of the covered area means that geodetic dome solutions are treated as lightweight roof coverings.

The design concept of geodesic domes is based on a mesh of regular polyhedra, as they are the basis for shaping this type of cover solutions. Most of the considerations regarding the spherical structures of geodesic domes reflect the subdivision of the original icosahedron into smaller parts, using the Fuller patent - US Patent 2682235 of 29 June 1954 (Fuller 1954). Taking into account Fuller patents and projects, the geodesic dome has become the canon of modern architecture, and at the same time the subject of many scientific studies. They treat the icosahedron as well as the dodecahedron as the basis for generating large surface

coverings in the form of geodesic domes. Significant and excellent achievements in this field have been attained by Clinton (Clinton 1971, 1990), Tarnai et al (Tarnai 1987, 1996 Tarnai , Lengyel and Gaspar 2017), Huybers (Hyubers 1982, 1990, 1997, 2002), Hyubers and van der Ende (Hyubers and van der Ende 2001), Lalvani (Lalvani 1982, 1990, 1996), Lalvani and Katz (Lalvani and Katz 1993), Pavlov (Pavlov 1990, 1993), Ramaswamy et al (Ramaswamy, Eukhout and Suresh 2002), Obrębski (Obrębski 2006) and many others. A different polyhedron than the recognized icosahedron or dodecahedron, i.e. a regular octahedron, was analyzed and used as the basis for generating strut meshes of geodesic domes by Pilarska (Pilarska 2017, 2018, 2020, 2021).

A very important aspect is to optimize the geometry and topology of geodesic dome structures. Various approaches to this subject, as well as many innovative solutions, can be found in the works prepared by Kaveh and Talatahari (Kaveh and Talatahari 2011), Kaveh and Rezamei (Kaveh and Rezamei 2016), Saka (Saka 2007), Carbas and Saka (Carbas and Saka 2012), Gythiel et al. (Gythiel, Mommeyer, Raymaekers and Schevenels 2020). However, all these works take into account the optimization of various forms of geodesic domes, formed on the basis of polyhedra other than the regular octahedron.

The aim of this paper is the optimization of geodesic strut domes designed on the basis of regular octahedron. Its equilateral faces were subdivided into smaller sub-faces and taking the resulting face vertices to define the nodes of the structural grid, while the edges of the sub-faces define the axes of the structural members. Using two subdivision methods, two families of structures were designed, each consisting of 8 spherical strut structures. These are innovative domes, previously unrecognized, treating a regular octahedron as the basis for geodesic domes generating.

2. GEODESIC DOMES SHAPED ON THE BASIS OF THE REGULAR OCTAHEDRON

2.1. Applied methods of geodesic domes shaping

Two subdivision methods developed by Professor Fuliński (Fuliński 1966) were used to design two families of geodesic domes subjected to the analysis. Taking into account the regular octahedron as the basis for the geodesic domes, its initial triangular meshes were subdivided into smaller triangles. The principles of this subdivision differ depending on the method used. The subdivision points reflect the individual nodes of the structures. Appropriate connection of nodes, depending on the method used, leads to two families of strut domes, differing in mesh topology. The number of subdivisions is referred to as frequency, which is denoted by the letter “V.” Also, “2V” is shorthand of “frequency 2.” The subdivision process naturally leads to the generation of a three-way grid on every face of the basis octahedron. The central projection of this grid’s vertices on the octahedron’s circumscribed sphere, leads to a polyhedron approximating the sphere in which only the grid’s nodes lie on the sphere’s surface. Higher frequencies give smoother spheres.

In this paper, based on the regular octahedron as the so far unexplored basis for the shaping of geodesic domes, two methods of dividing the initial mesh are used. The mentioned methods were developed in detail in the papers of Pilarska 2017, 2018, 2020. Figure 1 shows graphically the principles of shaping geodesic domes, depending on the method used.

The first method involves the subdivision of each edge of the basic triangle into n parts, drawing three families of lines parallel to each of the edges. Subdivision frequencies may be even or odd. The 1V dome is made up of equilateral triangles, with all edges of every triangle being the same length. To make a 2V dome, each initial edge is broken into two parts which subdivides the triangle in the 1V dome into four triangles. The 3V dome has each initial edge of the triangle broken into three parts, which in turn gives nine triangles. The 4V dome is shaped thanks to the subdivision of each initial edge into four parts and thanks to that we get 16 triangles.

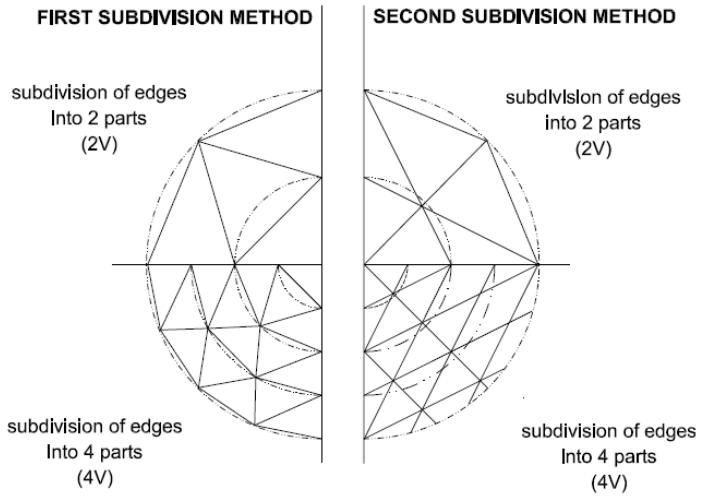

Fig. 1. Two subdivision methods used for geodesic domes designing.

In the second method, after subdividing the edges into n parts, three families of parallel lines are drawn parallel to the medians of the initial triangle, where a median runs from a vertex of the initial triangle to the mid-point of its opposite edge. Subdivision frequencies is even. Thanks to this subdivision, we deal with pairs of left and right triangles, which are combined to form an entire second method triangle, which is then projected to the sphere. The 1V dome is exactly the same as in the first method. To make a 2V dome, each initial edge is broken into two parts which subdivides the triangle in the 1V dome into three pairs of left and right triangles, therefore three entire triangles. Every edge of the basis triangle in the 4V dome is subdivided into four segments, which gives in turn 12 complete triangles. To obtain the 6V dome, each initial edge is subdivided into six parts which subdivides the triangle in the 1V dome into 27 entire triangles.
Using the first subdivision method, after division of each edge of the regular octahedron into 19, 20, 21, 22, 23, 24, 25 and 26 parts (frequencies), the following domes were obtained: 2888-hedron, 3200-hedron, 3528-hedron, 3872-hedron, 4232-hedron, 4608-hedron, 5000-hedron and 5408-hedron. The second subdivision method used, leads to the creation of 2904-hedron, 3456-hedron, 4056-hedron, 4704-hedron, 5400-hedron, 6144-hedron, 6936-hedron and 7776-hedron. These structures were shaped by the division of the regular octahedron edge into 22, 24, 26, 28, 30, 32, 34 and 36 parts (frequencies).

2.2. Description of numerical models

The commercial software Autodesk Robot Structural Analysis were used to prepare the numerical analysis. The program is based on the Finite Element Method, which is commonly used in engineering practice. All of the analysed 16 geodesic domes were made of S235 standard steel as steel struts (round pipes) according to Eurocode 3. In addition, the steel elements were modelled as a linearly elastic isotropic material and truss finite elements (without torsional effect). The properties of this steel grade were: (i) Young modulus (E) 210 GPa, (ii) Poisson ratio (ν) 0.3. Such assumptions and parameters allow for the correct representation of the work of the structure of the tested geodesic domes under a given load.

Tab. 1. Division of the analysed geodesic domes into four groups of struts.

Groups of struts	
2888-hedron (I method)	**2904-hedron (II method)**
RO 70.0 × 8.0	RO 70.0 × 7.1
RO 63.5 × 8.8	RO 63.5 × 8.0
RO 44.5 × 5.6	RO 57.0 × 5.6
RO 44.5 × 3.6	RO 51.0 × 3.2

All struts of modelled structures were grouped into four groups. On the basis of the most stressed element in a given group, struts were assigned individual cross-sections, as shown in Table 1.
The following loads were taken into account: the fixed load, i.e. own weight of construction and weight of cover constituting glass panes with a weight of 0.6 kN / m^2, as well as variable load, i.e. snow and wind for the first climate zone. From the presented interactions, the following load combinations were created: combination no 1 containing fixed influences as well as leading variable influences of the wind and accompanying variable influences of the snow, combination no 2 consisting of fixed influences as well as leading variable influences of the snow and accompanying variable influences of the wind, combination no 3 including fixed influences as well as leading variable influences of the wind.

3. GEOMETRY AND STATIC COMPARATIVE ANALYSIS

3.1. Geometry analysis results

From the geometric point of view, the number of nodes and struts, the number of supports, groups of struts of the same lengths, as well as the lengths of strut elements constituting the mesh of the domes generated were compared.
The number of nodes and struts are less for geodesic domes shaped according to the first method used. It is caused by the method of topological connection of nodes, in accordance with the assumptions of the subdivision methods used. The final number of supports for all designed geodesic domes indicates that it depends on the subdivision method used. This number is smaller for domes generated according to the first method. When considering strut elements, a very important aspect is to obtain as many struts of the same length as possible. Therefore, the geometric analysis also included the indication of the number of groups of struts of equal lengths. These tests were carried out for all modelled geodesic dome structures, shaped both according to the first and the second method. On the basis of the conducted research, it was found that in the first method there is a smaller number of struts of different lengths. This tendency is maintained in relation to all compared structures generated according to the first and the second used. Moreover, the increasing density of the structure mesh, resulting from the successive subdivisions of the initial regular octahedron, does not cause a significant increase in the number of groups of struts of equal lengths. In the case of domes created according to the first method, these amounts are on a comparable level, about 100 groups. For structures generated according to the second method, these amounts are higher and oscillate around 120 - 130 groups. The obtained results are presented in Figure 2.

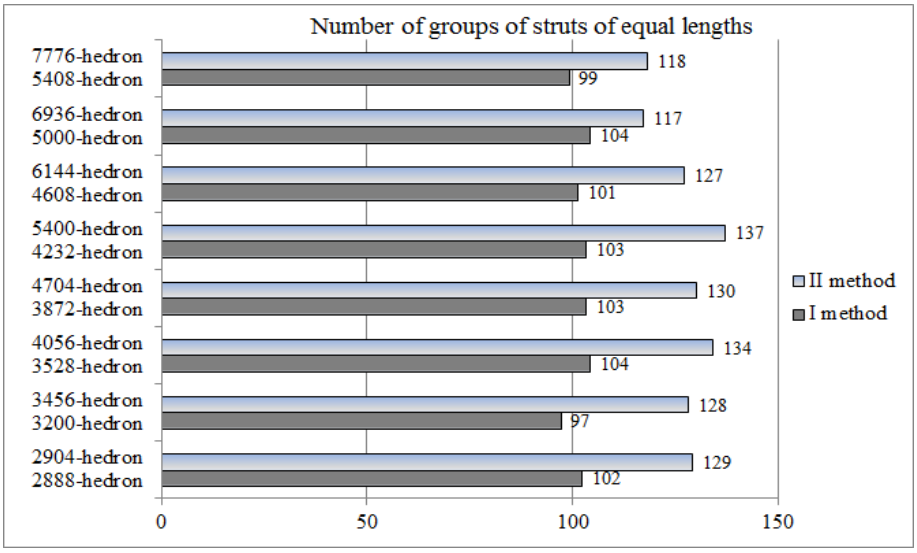

Fig. 2. Two subdivision methods used for geodesic domes designing.

The total length of the struts constituting the individual meshes of the designed geodesic domes is determined by the subdivision method used. The method of subdividing the initial mesh of regular octahedron, as well as the topology of the connected nodes resulting from this subdivision, is reflected in the smaller total length of the struts used to design the individual geodesic domes according to the first method. Only when comparing the smallest designed structures (2888-hedron according to the first method and 2904-hedron according to the second method) the total length of the struts is smaller for the second subdivision method used. In Figure 3, point A marks the place where the trend changes, and indicates the greater length of the dome struts generated according to the second method. Moreover, it can also be seen from the presented Figure 3 that with the densification of the dome meshes, the difference in the lengths of strut elements between the two designed families of structures increases more and more. In the case of domes shaped on the basis of 3200-hedron according to the first method and 4056-hedron according to the second method the difference is 1.5 %, while for structures generated on the basis of 5408-hedron for the first method and 7776-hedron for the second method the difference is 18 %.

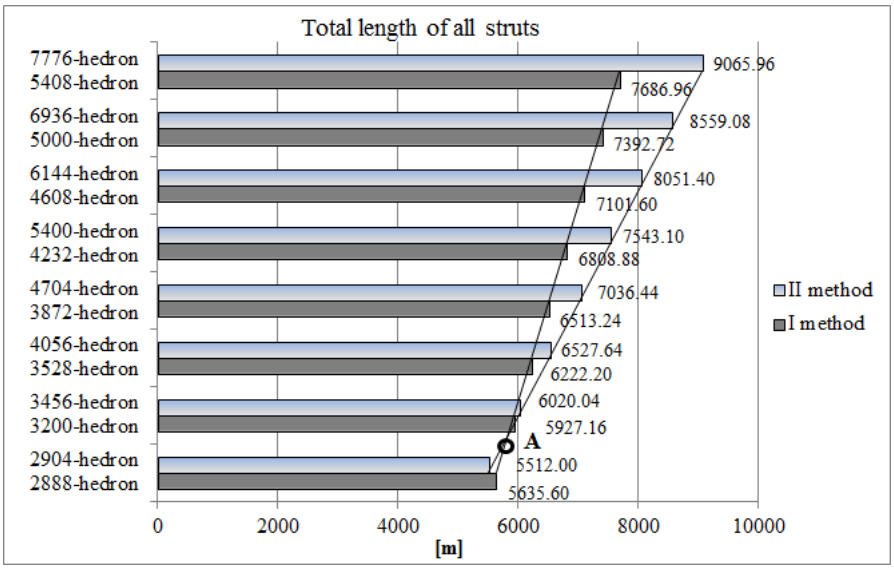

Fig. 3. Total length of all struts in each analysed dome shaped on the basis of the first and the second method.

3.2. Static analysis results

Two families of geodesic domes, shaped on the basis of a regular octahedron, were also subjected to static analysis, the aim of which was the comparison of the values of axial forces and stresses in struts, as well as vertical and horizontal displacements of nodes. The static analysis was carried out using the commercial software. All analysed aspects indicate the lower values obtained for geodesic domes designed according to the first method of subdividing the regular octahedron. Figure 4 and 5 show the vertical and horizontal displacements of nodes, confirming the conclusion that the structures created according to the first method are characterized by lower values. The vertical displacements for structures designed according to the second method are about 30 – 40 % higher than for structures shaped according to the first method. The differences in horizontal displacements are definitely smaller and oscillate about 4 – 15 %. There are 2 cases where this difference is higher, especially for domes generated from 4234-hedron due to the first method and 5400-hedron due to the second method (32 %).

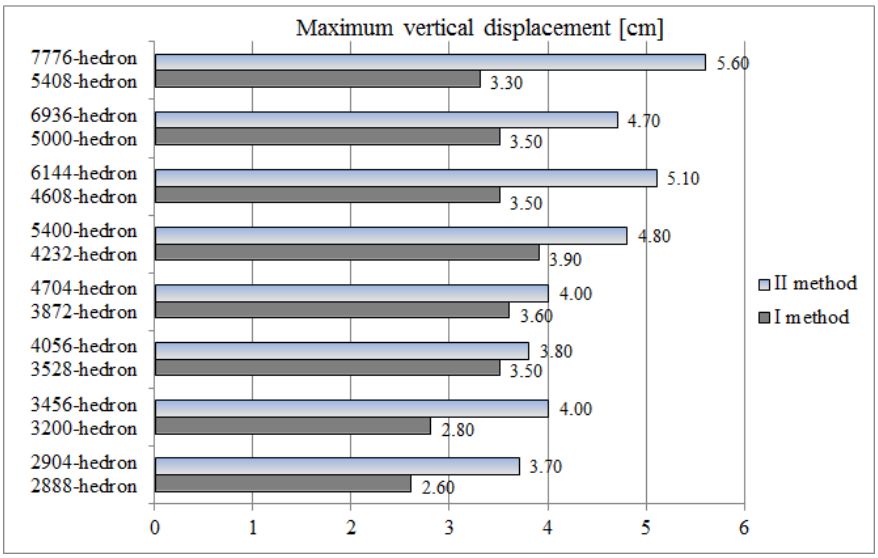

Fig. 4. Maximum vertical displacements of nodes occurred in each analysed dome shaped on the basis of the first and the second method

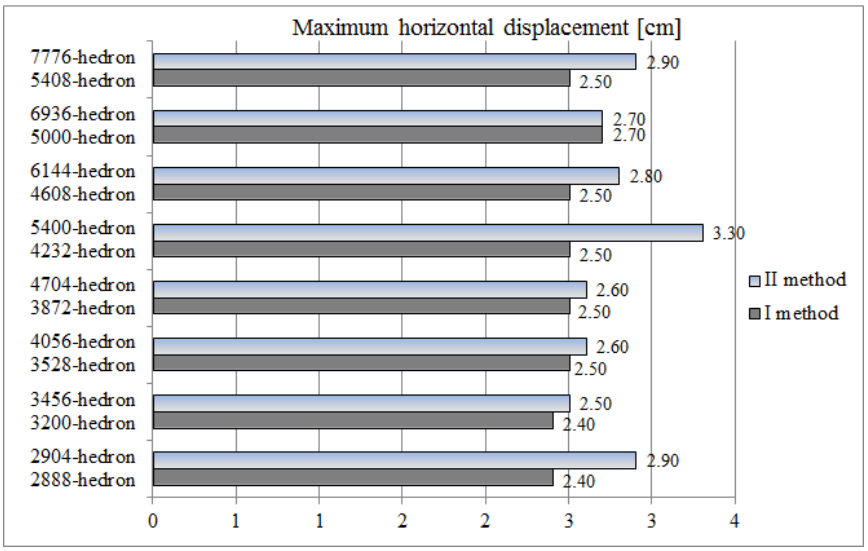

Fig. 5. Maximum horizontal displacements of nodes occurred in each analysed dome shaped on the basis of the first and the second method

4. OPTIMIZATION OF STRUTS CROSS - SECTIONS

Firstly, all elements of the strut structures designed according to the first and the second method were assigned with an identical cross-sections, taking into account the use of the most stressed strut in a given dome at the level of about 90%. On this basis, the weight of the structures were determined, as shown in Figure 6a. The greater weights appear for the two domes with the smallest mesh density generated due to the first method used, in compare to the smallest dense meshes of structures shaped on the basis of the second method. The next designed domes indicate the reverse tendency, that is the greater weight of all struts in geodesic domes generated on the basis of the second method. The moment of change is presented in the graph as point A.

The next step was to group strut elements of each designed structures into four groups, indicating the most optimal struts cross-sections for each of them and determining the new weight of the entire structures. The trend turned out to be the same as in the case of considering domes having all strut elements with the same cross-section. The first two analysed structures, that are the structures with the smallest density of struts,

show the higher weights for domes generated according to the first method. Increasing mesh density (higher frequency of the subdivision) cause the higher weight of domes designed due to the second method (Figure 6b).

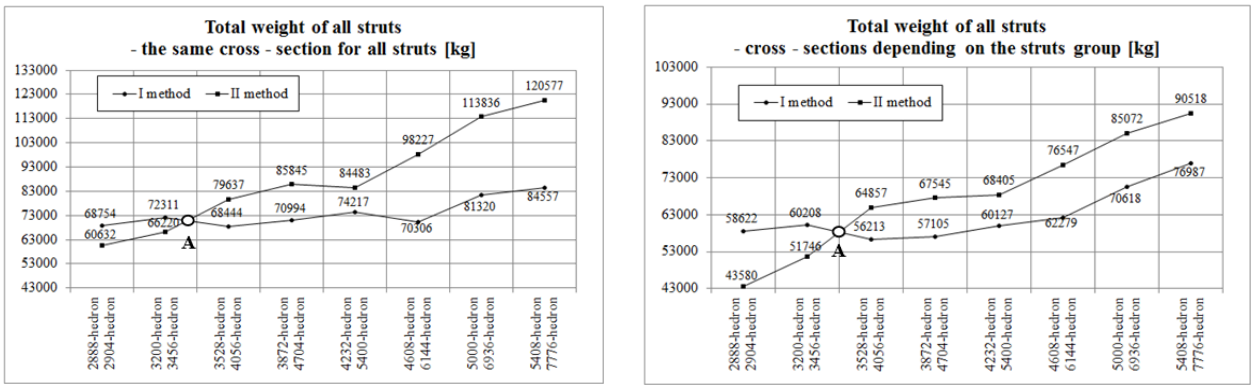

a) b)

Fig. 6. Total weight of all struts in the individual dome shaped according to the first and the second method a) the same cross – section for all struts, b) cross – sections depending on the struts group.

Optimization of the cross-sections of the struts allowed to reduce the consumption of construction material (steel), as well as to reduce the weight of the domes by about 15-20% for structures designed according to the first method and 25-30% for structures designed according to the second method (Fig. 7).

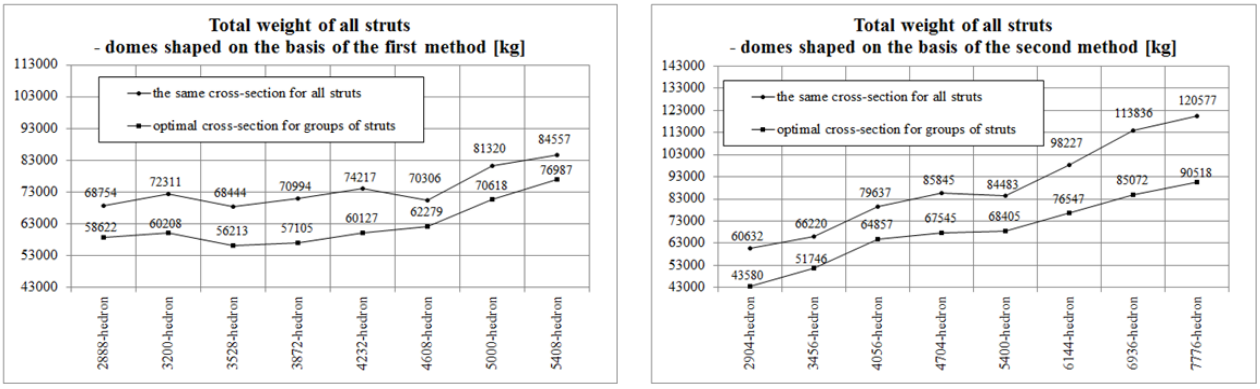

a) b)

Fig. 7. Total weight of all struts in the individual dome: a) domes shaped on the basis of the first method, qb) domes shaped on the basis of the second method

5. SEISMIC EXCITATIONS ANALYSIS RESULTS

Additionally, preliminary studies were conducted including seismic excitations. Using the DLUBAL RFEM 5.21.01 (2020, Dlubal Software GmbH from Tiefenbach, Germany) program, the performed numerical analysis allowed to determine how seismic excitation affects the dome shaping method. The following aspects were analysed: displacements, axial forces, velocities and accelerations. Figure 8 shows maximum displacements in strut domes, constructed according to the first method (for 2888-hedron) and to the second method (for 2904-hedron).

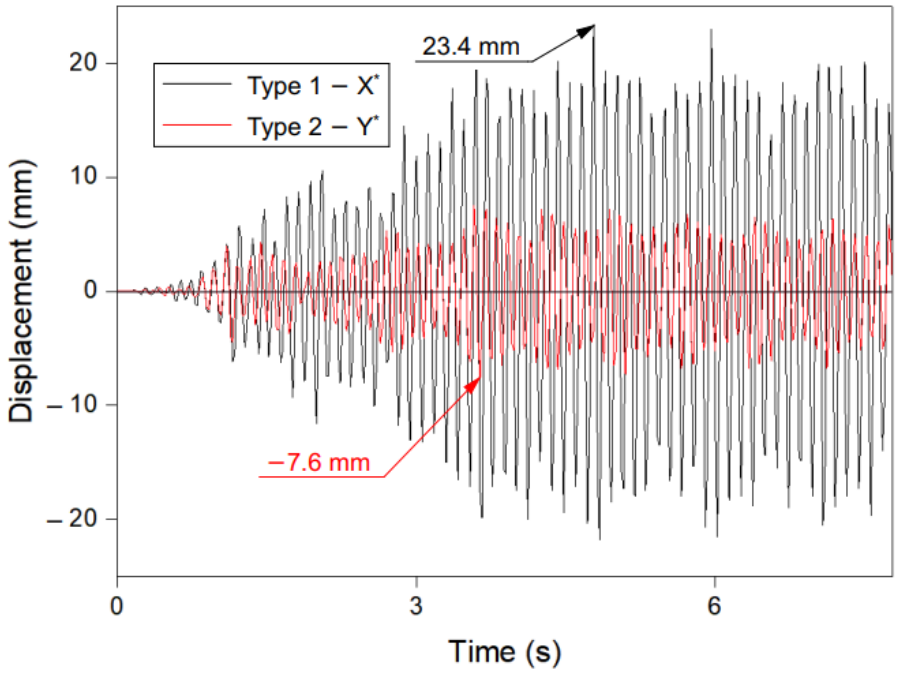

Fig. 8. Maximum displacements in numerical model of record of Ancona (*Type 1 – 2888-hedron designed according to the first method; Type 2 – 2904-hedron designed according to the second method*).

6. CONCLUSIONS

Grouping the strut elements of the designed geodesic domes into four groups and assigning them an optimized cross-sections allowed to reduce the consumption of construction material and, consequently, to minimize the weight of the structure by about 15-20% for structures designed according to the first method and 25-30% for structures designed according to the second method The other advantages are as follows:

– The geometrical analysis carried out for eight domes designed using the first method and eight domes using the second method showed that the structures generated based on the first method are characterized by: (i) less structural elements, such as nodes and struts, (ii) about 45–70 % more supports, (iii) about 20–30 % lower number of groups of struts of equal lengths, (iv) lower total length of all strut elements, which in turn leads to less use of construction material needed to produce all strut elements.
– The static analysis carried out for eight domes designed using the first method and eight domes using the second method showed that the structures generated based on the first method are characterized by: (i) smaller values of tensile forces (by approx. 8–25 %) and compressive forces (by approx. 25–47 %) in struts, (ii) smaller (by approx. 10–20 %) maximum stresses occurring in the struts, (iii) smaller maximum vertical and horizontal displacements of nodes.
– On the basis of the preliminary research taking into account seismic excitations, it can be concluded that the method of shaping the steel structure of the dome has a significant impact on the obtained values of displacements, axial forces, velocities and accelerations.

REFERENCES

Çarbas, S. & Saka, P.M. 2012. *Optimum topology design of various geometrically nonlinear latticed domes using improved harmony search method*. Struct Multidiscipl Optim. 45(3): 377–399.

Clinton, J.D. 1971. *Advanced structural geometry studies. Part I, Polyhedral subdivision concept for structural application*. NASA contractor report, NASA CR-1734. Washington, DC: NASA.

Clinton, J.D. 1990. *Lowest common frequency: b2 + bc + c2*. Int J Space Struct. 7(3&4): 213–222.

Fuller, B. 1954. *Geodesic Dome, Patent no. US2682235 A. www.google.com/patents/US2682235?hl=pl&dq=2682235*

Gythiel, W., Mommeyer, C., Raymaekers, T. & Schevenels, M. 2020. *A Comparative Study of the Structural Performance of Different Types of Reticulated Dome Subjected to Distributed Loads*. Front. Built Environ. 6:56. doi: 10.3389/fbuil.2020.00056.

Huybers, P. 1982. *The use of polyhedral for building structures*. Struct Topol. 6: 33–42.

Huybers, P. 1990. *Dome-type space structures of ellipsoidal form*. Int J Space Struct. 7(3&4): 299–310.

Huybers, P. 1997. *The polyhedral world*. In: Gabriel JF (ed.) Beyond the cube. The architecture of space frames and polyhedra. New York/Chichester/Weinheim/Brisbane/Singapore/ Toronto: John Wiley & Sons, Inc. pp. 243–279.

Huybers, P. 2002. *The morphology of building structures*. In: ICCS'02: Proceedings of the international conference on computational science – Part III. pp. 85–94. London: Springer-Verlag.

Huybers P & van der Ende G. 2001. *Polyhedral patterns*. In: Kunieda H (ed.) International symposium on theory, design and realization of shell and spatial structures, Nagoya, Japan, 9–13 October 2001, pp. 290–291. Madrid: IASS & Architectural Institute of Japan.

Kaveh, A. & Rezamei, M. 2016. *Topology and geometry optimization of different types of domes using ECBO*. Adv Comput Des. 1(1): 1–25.

Kaveh, A. & Talatahari, S. 2011. *Geometry and topology optimization of geodesic domes using charged system search*. Struct Multidiscipl Optim. 43(2): 215–229.

Lalvani, H. 1982. *Structures on hyper-structures*. Struct Topol. 6: 13–16.

Lalvani, H. 1990. *Continuous transformations of subdivided periodic surfaces*. Int J Space Struct. 5(3&4): 255–279.

Lalvani, H. 1996. *Higher dimension periodic table of regular and semi-regular polytopes*. Int J Space Struct. 11(1&2): 27–57.

Lalvani, H & Katz N. 1993. *Computer-generated transformations of geodesic spheres*. In: Parke GAR and Howard CM (eds) Space structures 4. London: Thomas Telford. pp. 1202–1212.

Obrębski, J.B. 2006. *Unidom-space bar system*. In: Local seminar of IASS Polish charter; XII LSCE. Warsaw.

Pavlov, G.N. 1990. *Determination of parameters of crystal latticed surfaces composed of hexagonal plane faces*. Int J Space Struct. 7(3&4): 169–187.

Pavlov, G.N. 1993. *Calculation of geometrical parameters and projection of geodesic domes and shells based on the network subdivision of the system D*. In: Parke GAR and Howard CM (eds) Space structures 4. London: Thomas Telford. pp. 1128–1137.

Pilarska, D. 2017. *Covers of large areas in the form of octahedron - based spatial bar structures*. XXIII Lightweight Structures in Civil Engineering. Bydgoszcz.

Pilarska, D. 2018. *Octahedron - based spatial bar structures – the form of large areas covers,* 3RD Scientific Conference ENVIRONMENTAL CHALLENGES IN CIVIL ENGINEERING (ECCE). Opole. Poland. MATEC Web Conf. Volume 174. Article Number: 03007. https://doi.org/10.1051/matecconf/201817403007.

Pilarska, D. 2018. *Comparative analysis of various design solutions of octahedron - based spatial bar structures*, XXIV Lightweight Structures in Civil Engineering. 103-108.

Pilarska, D. 2020. *Two subdivision methods based on the regular octahedron for single-and double-layer spherical geodesic domes*. International Journal of Space Structures. SAGE Publications. https://doi.org/10.1177/0956059920956944. Volume: 35 issue: 4. page(s): 160-173.

Pilarska, D. & Maleska, T. 2021. *Numerical Analysis of Steel Geodesic Dome under Seismic Excitations*. MDPI. Materials. 14(16), 4493. https://doi.org/10.3390/ma14164493.

Ramaswamy, S.G., Eukhout, M. & Suresh, R.G. 2002. *Analysis, design and construction of steel space frames*. London: Thomas Telford Ltd.

Saka, M.P. 2007. *Optimum geometry design of geodesic domes using harmony search algorithm.* Adv Struct Eng. 10: 595–606.

Tarnai, T. 1987. *Spherical grid structures: geometric essays on geodesic domes*. Budapest: Hungarian Institute for Building Science.

Tarnai, T. 1996. *Geodesic domes: natural and man-made*. Int J Space Struct. 11(1&2): 13–25.

Tarnai, T, Lengyel, A & Gaspar Z. 2017. *The roundest polyhedral with symmetry constraints*. Symmetry 9(3): 41.

LIGHTWEIGHT STRUCTURES in CIVIL ENGINEERING
CONTEMPORARY PROBLEMS
Monograph from Scientific Seminar
Organized by Polish Chapters of
International Association for Shell and Spatial Structures
Łódź University of Technology
Faculty of Civil Engineering, Architecture
and Environmental Engineering
XXVII LSCE
Łódź, 2nd – 3rd of December 2021

SIMPLIFIED MODELING OF STRESS AND DEFLECTION LIMIT STATES OF UNDERGROUND TANKS

P. Sorn [1] **M. Sondej** [2] **J. Górski** [3]
[1] KB Pomorze Sp. z o.o, Faculty of Civil and Environmental Engineering, Gdańsk University of Technology, POLAND, *p.sorn@kbpomorze.pl*
[2] Faculty of Civil and Environmental Engineering, Gdańsk University of Technology, POLAND, *matsonde@pg.edu.pl*
[3] Faculty of Civil and Environmental Engineering, Gdańsk University of Technology, POLAND, *jgorski@pg.edu.pl*

ABSTRACT: Fuel tanks are designed with regard to standard actions and operating conditions. The work analyses the impact of corrosion and other means to variation of stresses and deformation of a horizontal underground tank shell. The computations are preliminary. Due to the long computational time of the entire tank the analysis is restricted to its part only. The full analysis is bound to assess structural reliability, further allowing for its optimization.

Keywords: underground fuel tanks, shell corrosion, non-standard actions.

1. INTRODUCTION

Pressure tanks belong to the most responsible structures in present design. Possible failure affects a huge financial loss due to the loss of stored or processed material, technological break and tank refurbish, it also affects human health and life. The consequences of failure may be as well environmental due to the medium exposition into the surrounding environment, possibly bringing environmental degradation like ground water pollution, etc..

The present EU regulations bring the so-called pressure directive PED with a requirement to satisfy basic safety conditions in the Appendix I to the directive 2014/68/UE. To assure the accordance of pressure tank design with the PED directive the designer may apply a set of standards harmonized with the directive, e.g. EN 13445 or other standards or codes to assure fulfilling the directive requirements e.g. The Conditions of Technical Supervision Agency (WUDT) or ASME Boiler and Pressure Vessel Code and other. All the enlisted standards emphasize operational safety and durability of tanks. The prior assumptions state that relevant ultimate and serviceability limit states and appropriate structural solutions assure a proper safety level and durability. None of the sources distinguishes the way the safety level is quantified.

The answer may be partial or an entire application of Eurocodes, say, EN 1990 - Fundamentals of structural design and EN 1993-4-2, Eurocode 3 - Design of steel structures, the standards of the Eurocode series. The EN 1990 code regards structural safety in terms of its reliability, introducing the reliability index beta. The index is affected by the so-called consequence class: CC1 (the lowest), CC2 and CC3 (the highest).

The standard allows for introducing partial safety factors, moreover, it allows to estimate the index beta and compare it with the limit value included in Table 2 of EN 1990.
The FE models of fuel tanks should exceed the deterministic analytical standards for perfect structures, to consider the issues like material and geometric imperfections and post-welding stresses (Rasiulis et al. 2006). The problem of determining the limit values of the parameters of imperfections and their impact on the stress/strain state of a shell structure is the subject of many papers, e.g. (Rotter 2011, Górski et al. 2015, Górski et al. 2020).
It is important that the pressure tanks (pressure devices covered by the directive PED) is assumed the CC3 class. Thus we are able to state that taking a 50 year reference period the reliability index of pressure tanks is estimated 4.3, corresponding to failure probability lower than 0.00001. Hence it is reasonable to assess structural reliability of the tanks designed by the non-Eurocode standards (Gwóźdź and Michałowski 2012, Kamiński and Świta 2015). Reliability assessment is incorporated to address the impact of corrosion-based degradation (Geary and Hobbs 2013).
The work presents preliminary analysis of a simplified model of an underground fuel tank. Some parameters are selected, e.g. softening (thickness reduction) of sheets because of corrosion (Melchers 2010) and the number of stiffeners, a check is completed of their impact to critical states due to negative pressure.

2. THE UNDERGROUND FUEL TANK MODEL

The analysis concerns a standard underground storage horizontal tank. The tank length is 72599 mm, outer diameter 5600 mm (Fig. 1). Spherical end caps are assumed for the analysis. The base material used for tank manufacture is steel P355NL2, 28 mm thick for cylindrical shell and 26 mm thick for the caps. The cylindrical shell is stiffened with 13 T-shaped rings. The tank features five manholes in the upper tank region.
The commercial engineering software allows to perform LBA (Linear Bifurcation Analysis) and GMNA (Geometrically and Materially Non-linear Analysis) [Hotała et al. 2014]. While the tanks are often loaded by negative pressure, it is crucial to consider imperfections during analysis i.e. GNIA (geometrically non-linear analysis of imperfect structures) or GMNIA (geometrically and physically non-linear analysis of imperfect structures). This sort of sensitivity and reliability assessment is complex and time-consuming.
The work presents preliminary analysis of a half shell. It is aimed at sensitivity assessment of the structure to cross-sectional variations, e.g. in the case of corrosion, including the non-uniform case.

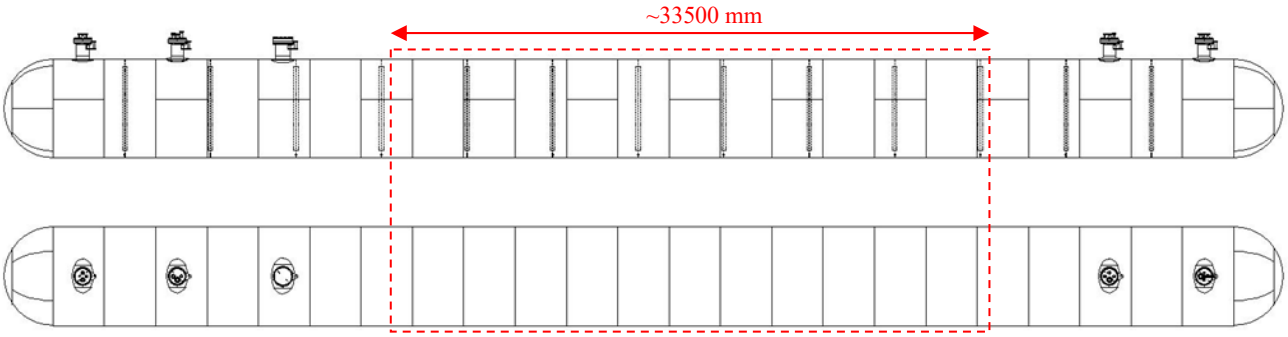

Fig. 1. Example - the analysed underground fuel storage tank

3. THE TANK FEM MODEL

The preliminary analysis was completed of the simplified tank models (Fig. 2). The computations are performed for the cylindrical shell with following parameters: length L=33500 mm (half of the real tank length) and diameter d_c=5600 mm (Fig. 1). The computations are conducted using the ABAQUS software (Smith 2009). The model incorporates 37632 shell elements. Simplified boundary conditions are modelled

by restraining the translations at both edges. This modelling pattern of boundary conditions is possible because of specific loading, i.e. negative pressure. The edges of a simplified tank model are stiffened (Fig. 1), and it is possible to represent them by the restraint upon all modes. Negative pressure was assumed of an initial value of $p = -1.0$ MPa. The negative pressure multiplier p was investigated to yield global or local stability loss (Burkacki et al. 2013). The computations are directed to the corrosion check by means of sheet thickness reduction in the case of overall or partial tank analysis. The influence of stiffener spacing was also analyzed.

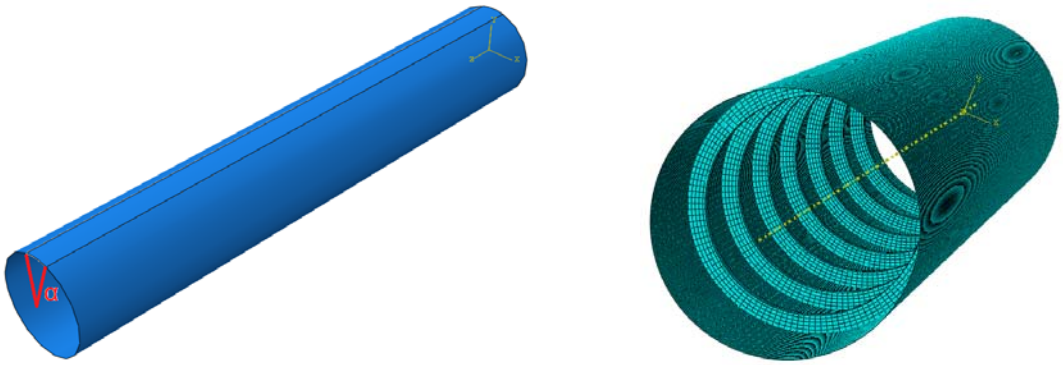

a) b)

Fig. 2. Simplified models of an underground fuel tank (ABAQUS)
a) without ribs and b) including stiffening ribs.

The following variants of tank loading are assumed (Fig. 3):
a) internal radial pressure p_n,
b) compressive load in longitudinal direction, the derivative of internal pressure p_x,
c) the combination of internal radial pressure p_n and compressive load in longitudinal direction p_x.

The longitudinal load p_x is a function of radial load p_n:

$$\pi R^2 p_n = 2\pi R p_x \quad \rightarrow \quad p_x = 1400\, p_n, \tag{1}$$

where R is the tank radius.

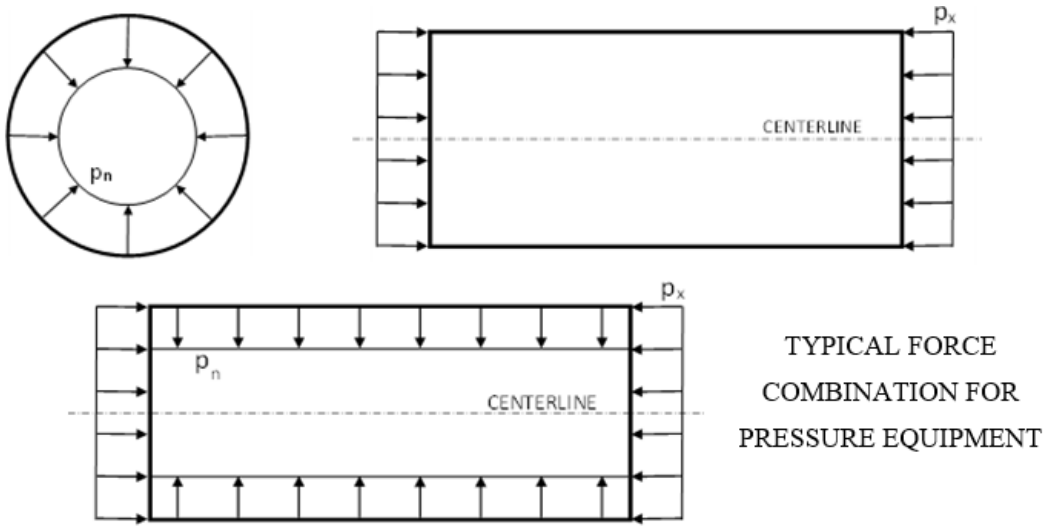

Fig. 3. Three loading variants of a tank (details in the text).

4. THE RESULTS OF SENSITIVITY ANALYSIS

The following computational variants were conducted:

1) unstiffened cylindrical shell with uniform thickness, impact of the overall tank thickness variation to buckling,
2) unstiffened cylindrical shell with a constant basic thickness equal 28 mm, reduced thickness along the generating line, the reduced strip is denoted by the angle □ = 30, 90, 180 [deg].
3) stiffened cylindrical shell with a variable number of stiffeners (1, 2, 3, 6) impact analysis of the number of stiffeners to buckling.

Figures 4 and 5 compares the critical pressure results with regard to variable sheet thickness *t* and two different loading schemes. The variation of sheet thickness *t* reflects the corrosion processes which may happen in a long-term tank operation. It was assumed that reduction of sheet thickness is uniform throughout the entire shell.

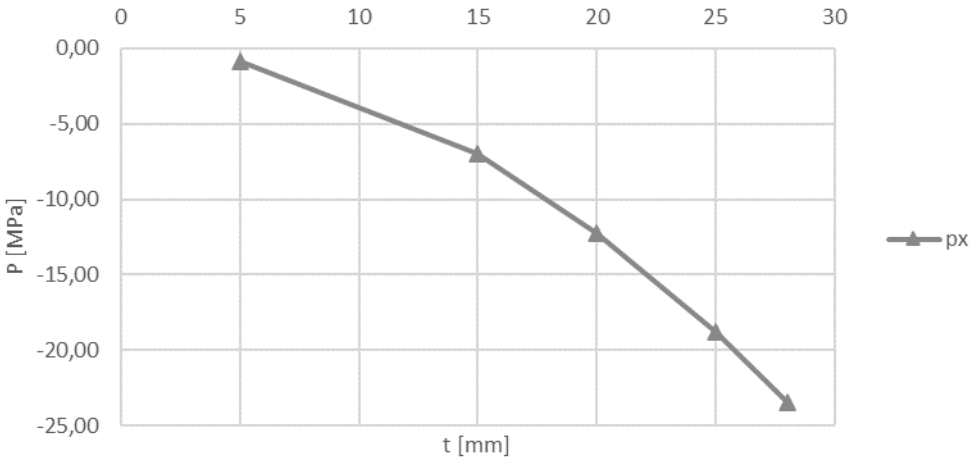

Fig. 4. Unstiffened cylindrical shell with uniform thickness: the impact of sheet thickness t on critical pressure p_x

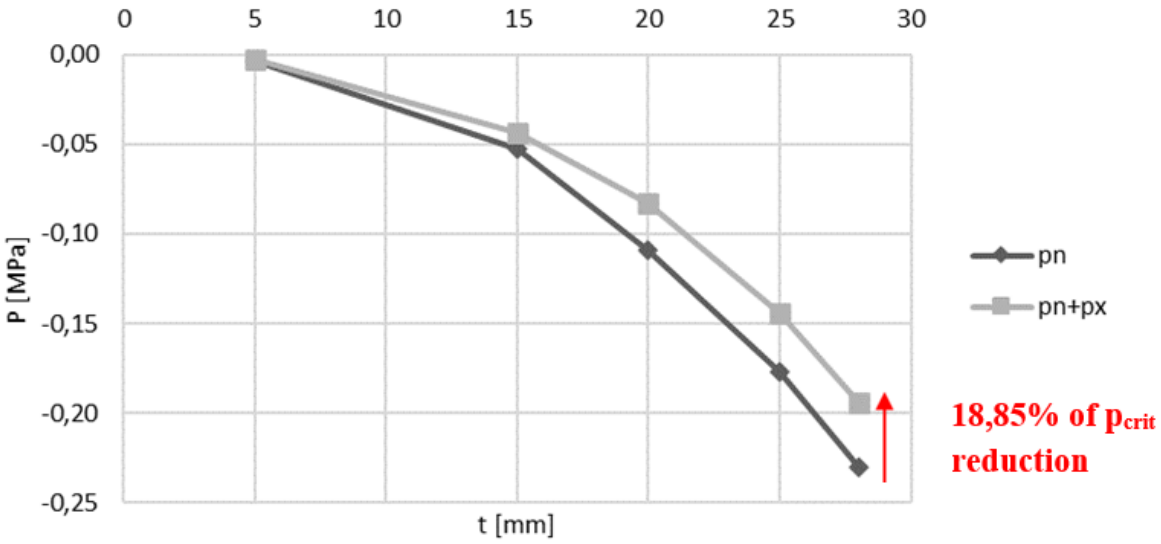

Fig. 5. Unstiffened cylindrical shell with uniform thickness: the impact of sheet thickness t and two different loading patterns on critical pressure p_n and p_x.

The preliminary computations concerned a perfect tank, free of geometric imperfections. A high impact was observed of longitudinal load p_x (Fig. 4), radial load p_n and the combination of both p_n and p_x (Fig. 5). A 20% critical pressure drop is observed in the combination case of p_n and p_x. The computations proved the necessity to consider these loads in the analysis of pressure tanks. The examples of type the computations are included in Fig. 6.

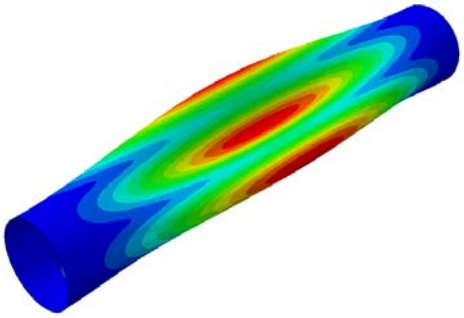

Fig. 6. Buckling modes of a tank subjected to uniform corrosion (ABAQUS).

The second analysed model consider corrosion on the part of a tank shell only. The computations define the weakened part by the angle α (Fig. 7).

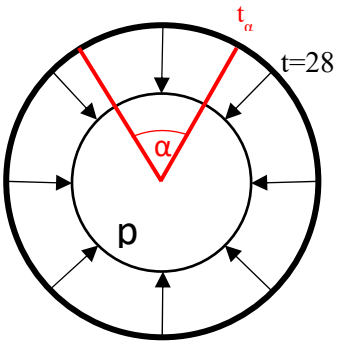

Fig. 7. Illustration of the assumed shell part of reduced sheet thickness (the impact of corrosion process)

Figure 8 presents the diagrams of breaking load change with regard to tank shell thickness. In this case the critical state involves a local buckling mode. This mode ($\alpha = 30^{o}$) is presented in Fig. 9.

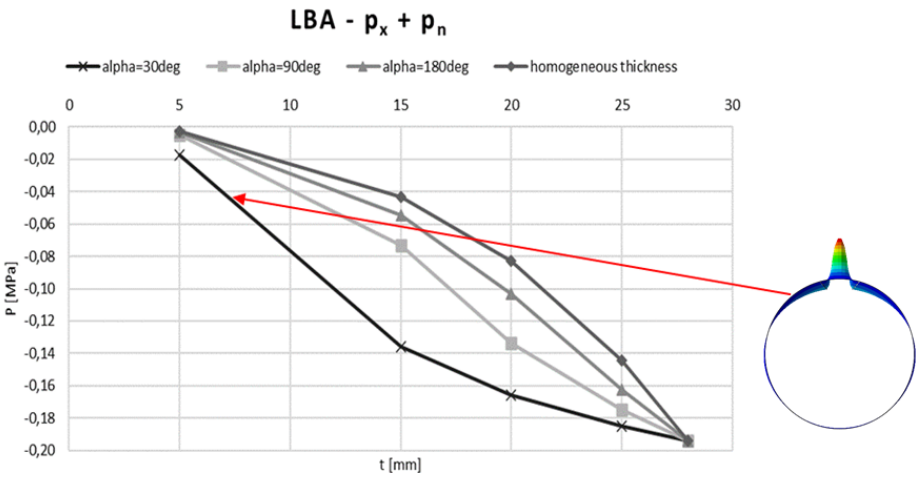

Fig. 8. Unstiffened cylindrical shell with partially reduced thickness:
the impact of range and thickness reduction on the critical load

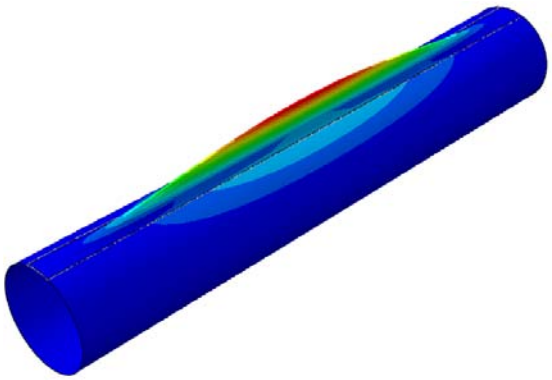

Fig. 9. Unstiffened cylindrical shell with partially reduced thickness: buckling mode of a tank subjected to corrosion covering part of the tank $\alpha = 30$ deg

The third computational series is intended to check the necessary number of stiffeners preventing the tank from reaching its critical states. Assuming an optimal spacing between the stiffeners is essential to assess the mechanical response of the structure to negative pressure. Figure 10 shows the impact of the number of stiffeners on the critical pressure calculated by LBA.

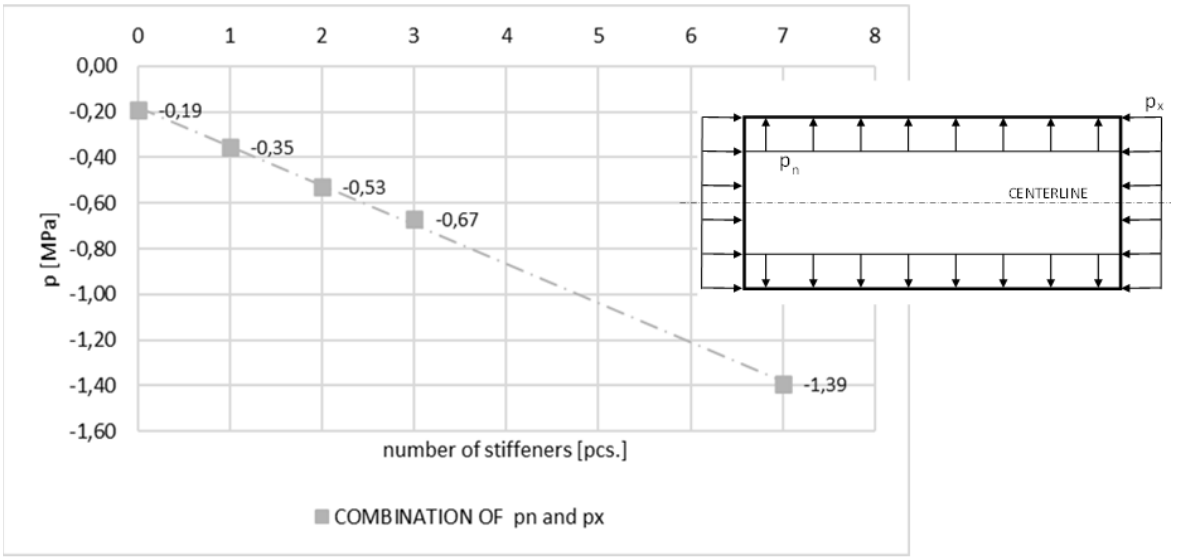

Fig. 10. Unstiffened cylindrical shell with uniform thickness: the impact of the number of stiffeners on the critical pressure (ABAQUS).

The computational results presented in Fig. 10 allow to conclude the following:

– linear relation is achieved between the critical pressure and the number of stiffeners in each loading scheme,
– in the case of internal pressure of the models with a single stiffener and seven rings a 700% rise of critical pressure is observed,
– a 6% rise of critical pressure is denoted in the case of longitudinal compressive force for the models with one and seven stiffeners

The last stage of the preliminary analysis compares the design critical stresses of the stiffened cylindrical shell subjected to longitudinal compressive force and internal pressure. It is shown(Fig. 11) that the critical stresses due to the standard formula is higher than the corresponding numerical result.

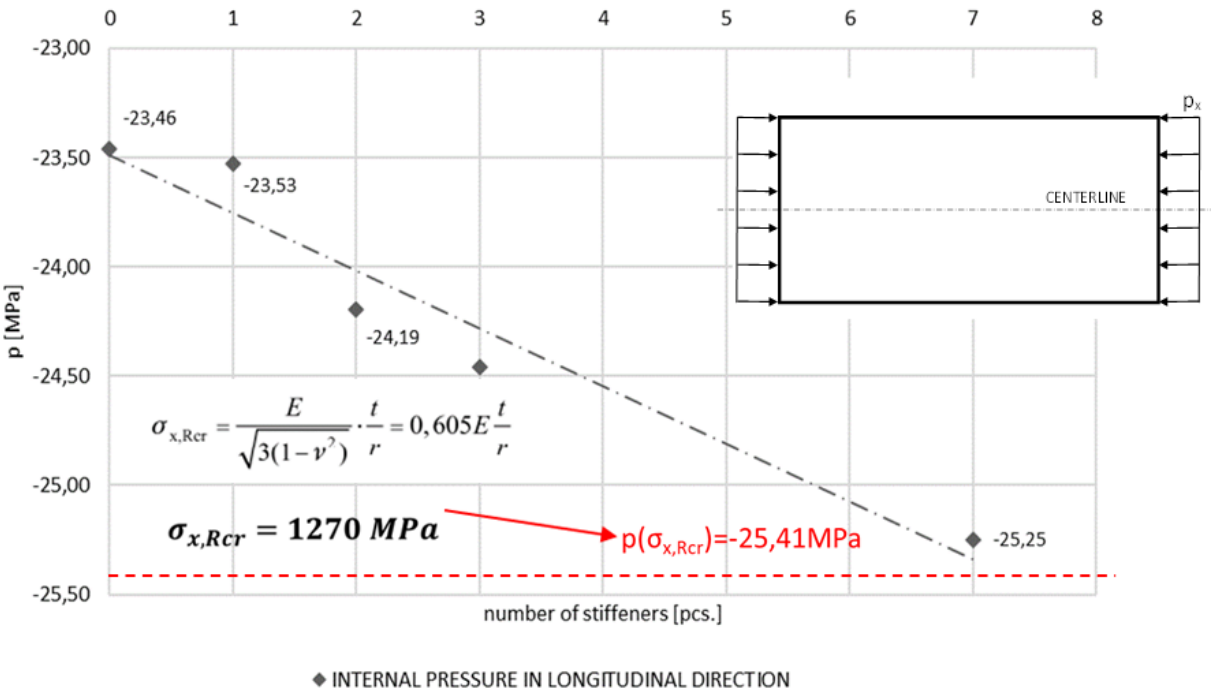

Fig. 11. Critical load of the stiffened cylindrical shell subjected to longitudinal compressive force and internal pressure in function of stiffeners number.

5. CONCLUSIONS

Preliminary analysis of this tank proved the following:

– the variation in tank thickness decreases the negative pressure bringing stability loss,
– local reduction of shell thickness yields reduction of negative pressure causing stability loss,
– while the difference between the nominal shell thickness and its reduced value is substantial local stability loss occurs in the reduced thickness region,
– the use of reinforcing stiffeners of appropriately high stiffness increases the cylinder load-carrying capacity, and the required negative pressure to yield stability loss is higher than the one for the unstiffened shell.

The conducted computations and further conclusions are bound to accelerate the computations in the complex FEM model.

6. ACKNOWLEDGMENTS

The authors acknowledge the access to computational software provided by the Centre of Informatics – Tricity Academic Supercomputer & network (CI TASK) and the financial support by the Innovative Economy Operational Programme [POIG.01.04.00-24-073/09-03].

REFERENCES

Burkacki, D., Wójcik, M. & Jankowski R. 2013. *Analiza modalna stalowego zbiornika walcowego z dachem stałym przy różnym poziomie wypełnienia.* Budownictwo i Architektura 12(2): 205-212.

EN 1990 Eurocode - Fundamentals of structural design.

EN 1993-6 Eurocode 3 - Design of steel structures part 4-2. Tanks.

EN 13445-3 Non-flame-heated pressure tanks Part 3. Design.

Geary, W. & Hobbs, J. 2013. *Catastrophic failure of a carbon steel storage tank due to internal corrosion*. Case Studies in Engineering Failure Analysis 1: 257–264.

Górski J., Mikulski T., Oziębło M., Sorn P. & Winkelmann K. 2020. *Modelling of random geometric imperfections of three-dimensional steal structures*. Inżynieria i Budownictwo 1-2 (in Polish).

Górski J., Mikulski T., Oziębło M. & Winkelmann K. 2015. *Effect of geometric imperfections on aluminium silo capacities*. Stahlbau 84.

Gwóźdź, M. & Michałowski T. 2012. *Elements of the structural reliability of steel welded tanks liquids and gases in liquid*. *Weld. Tech. Rev.* 84(3) (in Polish).

Hotała E., Skotny Ł., Drużbiak I. & Boniecka J. 2014. *Behavior analysis of steel silo shell according to different code defined procedures.* Building Materials 5(501) (in Polish).

Kamiński, M. & Świta, P. 2015. *Structural stability and reliability of the underground steel tanks with the Stochastic Finite Element Method*. Archives of Civil and Mechanical Engineering 15: 593-602.

Melchers, R.E. 2010. *Estimating uncertainty in maximum pit depth from limited observational data.* Corrosion Engineering, Science and Technology 45(3): 240-248.

Pressure directive PED 2014/68/ue.

Rasiulis, K., Šapalas, A., Vadlūga, R. & Samofalov, M. 2006. *Stress/strain state investigations for extreme points of thin wall cylindrical tanks*. Journal of Constructional Steel Research 62: 1232–1237.

Rotter, J. M. 2011. *Shell buckling design and assessment and the LBA-MNA methodology*. Stahlbau 80(11): 791-803.

Smith M., 2009. ABAQUS/Standard User's Manual, Version 6.9, Dassault Systèmes Simulia Corp, Providence, RI.

LIGHTWEIGHT STRUCTURES in CIVIL ENGINEERING
CONTEMPORARY PROBLEMS
Monograph from Scientific Seminar
Organized by Polish Chapters of
International Association for Shell and Spatial Structures
Łódź University of Technology
Faculty of Civil Engineering, Architecture
and Environmental Engineering
XXVII LSCE
Łódź, 2nd – 3rd of December 2021

DETERMINING PROPERTIES OF POLYUREA COATINGS AS A MATERIAL POTENTIALLY STRENGTHENING STRUCTURAL ELEMENTS

J. Szafran [1] **A. Matusiak** [2]
[1] BEng, PhD, DSc, Faculty of Civil Engineering, Architecture and Environmental Engineering,
Lodz University of Technology, POLAND, *jacek.szafran@p.lodz.pl*
[2] BEng, MSc, Faculty of Civil Engineering, Architecture and Environmental Engineering,
Lodz University of Technology, POLAND, *artur.matusiak@dokt.p.lodz.pl*

ABSTRACT: The paper discusses the results of experimental research on polyurea. In authors' opinion, this material could be used to improve load-carrying capacity and integrity of structural elements made of various materials. The paper presents the results of research on basic mechanical properties of polyurea, its impact on integrity of cellular concrete specimens and full-scale concrete rings. The additional polyurea layer on outer surfaces of test specimens improves mainly their integrity following their complete failure. It must be noted, however, that when the additional layer is present, it does not improve all strength properties of test specimens such as resistance to compression of cellular concrete specimens. It was revealed that this property may be negatively influenced by the level of constrainment.

Keywords: corrosion, durability of concrete elements, polyurea coatings system, concrete rings.

1. INTRODUCTION

Industrialization and improper management of natural resources have led to changes in the environment exerting adverse impact on building structures. Such changes combined with often inadequate building operation practices result in deterioration of durability of structural elements, which in numerous cases makes a building less safe to use. Building operation, mechanical and corrosion-related damage, and material aging are aspects that are closely related with each other. Wrong practices of building operation or incorrect technical solutions are the reasons why repairs, refurbishments, renovations and reinforcements of structural elements often have to be made (Badowska et al. 1974, Baszkiewicz and Kamiński 2006, Bródka 1995).
Corrosion processes combined with improper operation and aging of structural elements lead to damage to building components, which necessitates additional spending during their lifetime. The severity of this global issue depends on the environment, climate zone, and quality of materials. Traditional building materials, such as concrete, steel, wood and isolating materials, are often characterized by inadequate durability and poor functional properties. This speeds up corrosion processes on the one hand and decreases strength of structural elements over time on the other so finally works are required to reinforce such elements. Thus, products that make it possible to improve a number of functional properties of a structure are gaining interest. The characteristics of building materials that are sought after include both protecting building

elements against corrosion and aging and reinforcing them at the same time. Polyurea can be listed among products that have all the above characteristics (Banera et al. 2017, Gruener 1983).
This paper presents the application of polyurea coatings as a product used to reinforce structural elements and improve their functional properties such as protection against corrosion and aging. The focus is on demonstrating polyurea as a functional product suitable for reinforcing structures to ensure that their integrity is maintained after load-carrying capacities of structural elements have been exceeded.

2. POLYUREA COATINGS SYSTEM

Polyurea, a modern material unique in terms of its characteristics, was invented in 1980s in the United States. Polyurea coatings were used in Europe for the first time in 1990s, and the beginning of the 21st century saw a dynamic growth in the number of applications of this technology. In terms of materials science, polyurea is derived from the reaction of an isocyanate component and an amine blend and has a chain structure composed of 'n' molecules that are strongly cross-linked with each other (Fig. 1). Polyurea is an elastomer that is derived from the chemical reaction (polyaddition) of an aromatic or aliphatic isocyanate component and a multifunctional amine or an amine blend. Aromatic polyureas are derived from methylenediphenyl diisocyanate (MDI) while aliphatic polyureas from hexamethylene diisocyanate (HDI) or isophorone diisocyanate (IPDI), which form a stiff chain section (Banera et al. 2017, Szafran and Matusiak 2016, Szafran and Matusiak 2017).

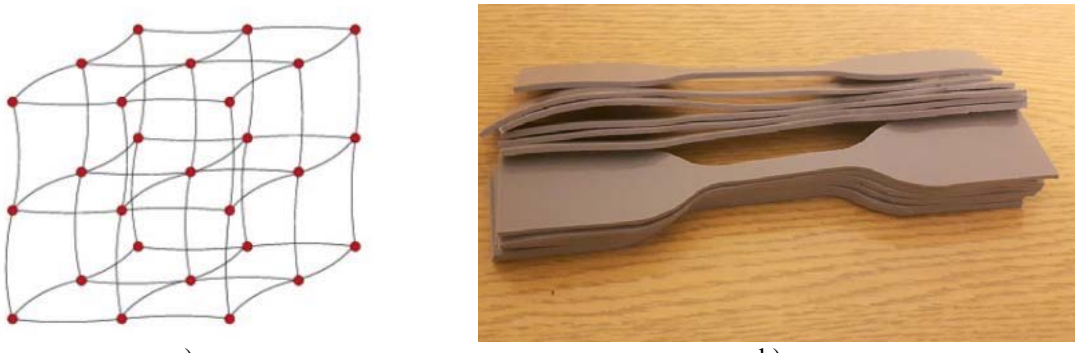

a) b)

Fig. 1. Polyurea: a) chain structure, b) photo of samples.

3. POLYUREA – ADVANTAGES AND DISADVANTAGES

3.1. Advantages

In contrast to traditional isolating materials, polyurea membranes have excellent functional properties, chemical resistance, and mechanical strength. The material properties of polyurea that make it usable in a wide range of applications and are at the same time its advantages include (Banera et al. 2017, Szafran and Matusiak 2016, Szafran and Matusiak 2017):

- fast reactivity and bonding, which significantly reduces the time required to apply the product;
- adherence to most building materials after preparing the substrate for product application;
- resilience and elasticity in a wide range of temperatures below and above 0°C;
- high mechanical strength, with tensile strength of over 20 MPa and tear strength of over 50 MPa;
- high chemical resistance to most organic and inorganic acids, bases, salt solutions and amines;
- effective crack bridging; experimental studies have shown that a coating can bridge cracks up to 5 mm in width;
- UV resistance.

3.2. Disadvantages

In addition to unquestionable advantages, the polyurea coating technology has also its flaws which should be known to justify the use of the product. The main weakness of the technology is that certain technological rules have to be observed and special equipment is necessary to apply the system. Another requirement is preparation of the substrate before polyurea is applied with the preparation method depending on the type of the substrate. What also needs to be stressed is that you must not apply polyurea on surfaces that are dirty, oily and unprepared or in adverse ambient conditions, for instance when it is raining.

4. BASIC EXPERIMENTAL RESEARCH

Basic properties of polyurea coatings were determined for aromatic polyurea as the most common type of coating utilized in the construction industry. Basic tests were designed to determine mechanical properties of polyurea in terms of static tension according to EN ISO 527:2012. The tests were done to evaluate tensile strength of polyurea using dumbbell-shaped samples. The tensile strength of the material was determined for three test speeds of 50, 100, and 500 mm/min on a custom test bench (Fig. 2). All tensile tests were done on the INSTRON 5582 tensile tester. The results of polyurea tensile tests are shown in Figure 3 and Table 1.

Fig. 2. Tensile strength test of polyurea - test bench.

Tab. 1. Strength characteristics of a polyurea coating.

Test speed [mm/min]	Number of tests [-]	Tensile strength [MPa]	Engineering strain [%]
50	5	24.08	417
100	5	23.03	391
500	3	19.47	332

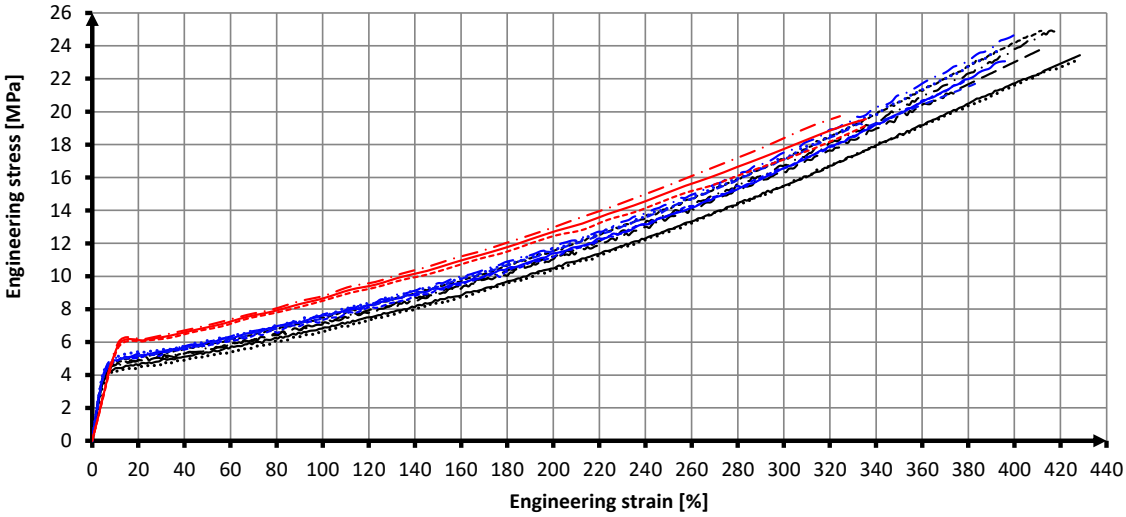

Fig. 3. Diagram – engineering stress vs. engineering strain.

The coating tensile strength was 24.08 MPa with engineering strain of 417% at the test speed of 50 mm/min, 23.03 MPa with engineering strain of 391% at the test speed of 100 mm/min, and 19.47 MPa with engineering strain of 332% at the test speed of 500 mm/min (Table 1). The analysis of the results confirmed that the tensile strength and the nominal engineering strain of the membrane depend on the test speed, and these properties are lower at higher specimen loading speeds.

The test stand was also equipped with an infrared camera which recorded changes in temperature of specimens while they were subjected to tension. Thermal imaging is currently used in a number of industries such as the construction industry, in laboratory tests and during inspections of building facilities. Thermal images can help localize defects (failures) in construction materials during their normal operation (Szczepanik et al. 2008). Thermal imaging was used during the tests of all batches of specimens to record their temperature distribution on an ongoing basis during the tensile test. All the specimens were positioned at the same distance from the infrared camera, and their surface temperatures were measured over time. The graph of specimen surface temperature vs. time is shown in Figure 4.

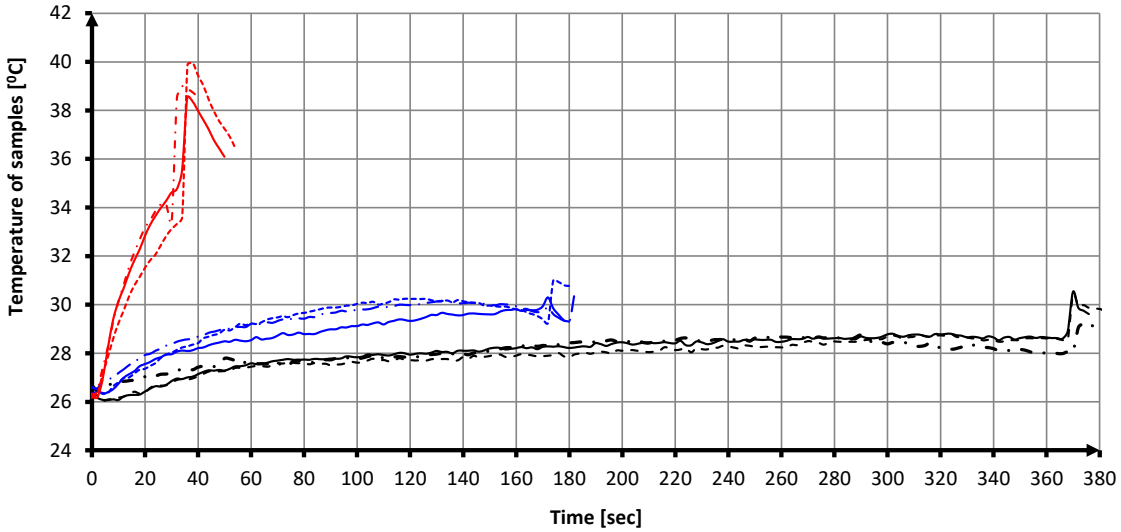

Fig. 4. Diagram – temperature of specimens vs. time.

The average maximum recorded temperature was 28.8°C at the test speed of 50 mm/min, 30.6°C at the test speed of 100 mm/min, and 39.2°C at the test speed of 500 mm/min (Fig. 4). The analysis of the results indicates that stretching polyurea specimens is an exothermic process during which the material warms up

and transfers heat to the environment. Peaks of the maximum recorded temperatures depend on the coating test speed, and their values are higher at higher specimen loading speeds. It can be also concluded that the recorded temperature gradients will have no significant effect on the performance of polyurea-coated structural elements.

5. SIMPLE PHYSICAL TESTS

Examples of simple physical tests of polyurea coatings were tests designed to determine compressive strength of cellular concrete specimens covered with a polyurea coating. The tests were done according to EN 772-1:2015 on three types of cylindrical specimens 10 cm in diameter: type I – control samples without any coating, type II – samples with a polyurea coating on their circumference, and type III – cylindrical samples covered with polyurea on their whole surface (Fig. 5). The compression strength of cellular concrete specimens was determined using a specially designed test stand (Fig. 6) at a test speed of 3.0 mm/min. All compression tests were done on one INSTRON 3384 tensile tester. The results of the cellular concrete compression strength tests are listed in Table 2.

a) b) c)

Fig. 5. Cellular concrete samples: a) type I - control sample, b) type II - sample with a polyurea on its circumference, c) type III - sample with polyurea on its whole surface.

Tab. 2. Strength properties of cellular concrete specimens.

Specimen batch designation [-]	Test speed [mm/min]	Number of tests [-]	Breaking force [kN]	Breaking stress [MPa]
Type I	3.0	8	24.21	3.08
Type II	3.0	8	23.95	3.05
Type III	3.0	8	18.65	2.37

Compressive strength of cellular concrete specimens was 24.21 kN at the breaking stress of 3.08 MPa for the uncoated elements, 23.95 kN at the breaking stress of 3.05 MPa for the elements with the coating on their circumference, and 18.65 kN at the breaking stress of 2.37 MPa for specimens with the coating on their whole surface. For the cylindrical specimens, breaking forces and breaking stresses depend on how the polyurea coating was applied. The results indicate that both these properties are lower for the polyurea-coated specimens. The reason for this might be that constrained specimens have no capacity to deform, which is more evident at a higher level of constrainment.

Fig. 6. Compressive strength test of cellular concrete - the test bench.

The cracking pattern in the specimens was in line with deformation of cylindrical elements under compressive load. In the case of the uncoated specimens (type I), slightly oblique vertical cracks appeared already at small values of the compressive force, and when it increased, the cracks lengthened and their number grew at the circumference of the specimens. Finally, the specimens undergone a complete failure after cracks occurred in the whole volume of the specimens and the internal structure of the material delaminated (Fig. 7a). In the case of the polyurea-coated specimens (types II and III), cracks appeared according to the same mechanism as for the uncoated elements. The polyurea coating efficiently covered the surface cracking to the extent that the cracks were not visible even at high levels of deformation of the specimens (Fig. 7b).

a) b)

Fig. 7. Deformations and failures of specimens under load:
a) type I - control sample, b) type III - sample with polyurea on its whole surface.

All the specimens failed in a characteristic conical way similar to that of concrete specimens in compression strength tests (Fig. 8). In contrast to control samples (type I), the polyurea-coated specimens (types II and III) kept their integrity after the maximum load was exceeded.

Fig. 8. Cellular concrete samples after the failure.

6. FULL-SCALE TEST

Tests of full-scale structural components were done using concrete rings of 800 mm in inner diameter and 900 mm in height with a shell of 100 mm in thickness. The tests aimed at assessing the crushing strength of concrete rings reinforced with a polyurea coating. The crushing strength of concrete rings was determined according to EN 1917:2002. Nine C25/30 concrete rings were subjected to the crushing strength test. Three components comprising the first batch were marked as control samples and were not polyurea-coated (Fig. 9). Three components of the second batch were coated with polyurea on their outer surface (Fig. 10). Three components of the third batch were coated with a membrane on their inner and outer surface (Fig. 11).

Fig. 9. Concrete ring after failure: type I.

Fig. 10. Concrete ring after failure: type II.

Fig. 11. Concrete ring after failure: type III.

During the tests of the concrete rings, cracked cross-sections were observed. Cracks appeared on tension surfaces of the shell, i.e. according to the deformation of the cross-section under load (Fig. 12). For concrete rings without the polyurea coating (type I), for the maximum load exerted on the components, the largest cracks measured about 0.4 mm in width. When the maximum load was exceeded, the cracks virtually did not develop in the components up to the point of final failure of the components. Observing cracks in polyurea-coated concrete rings (type II and III) was practically impossible. Polyurea effectively bridged the cracks to the extent that only those about 2 to 5 mm in width were visible. Since the polyurea coating covered the cracks, their widths could not be reliably measured. The application of the polyurea coating on the concrete rings had no impact on the mechanism of crack occurrence and development in the cross-section of the test objects.

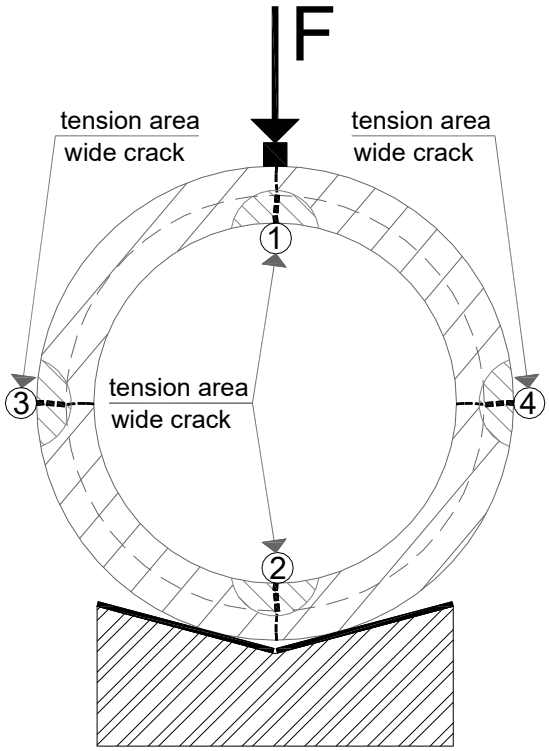

Fig. 12. Cracks occurring in concrete rings during the test.

The control samples (type I), i.e. the concrete rings without any coating, failed dynamically upon exceeding their crushing strength. In line with the classical theory of a failure mechanism, these components broke up into four smaller separate pieces (Fig. 9). The concrete rings with polyurea coatings on their surfaces (type II and III) failed when they were largely deformed and the concrete cracked in tension areas (Fig. 10, Fig. 11). The samples finally lost their load-carrying capacity with the largest deformations. Despite very large straining, the polyurea coating remained continuous on surfaces of the shell.

Tab. 3. Results of the crushing strength tests of concrete rings.

Sample	Crushing strength [kN]	Average crushing strength [kN]	Load-carrying capacity gain over control samples
C-1	58.8		
C-2	66.2	**60.5**	- / -
C-3	56.4		
E-1	52.7		**- 3.5 kN**
E-2	58.9	**57.0**	**- 5.8 %**
E-3	59.4		(no effect)
A-1	78.0		
A-2	70.6	**72.8**	**+ 12.3 kN** **+ 20.3 %**
A-3	69.8		

Table 3 summarizes the relation between the crushing strength and the limit load of each type of concrete rings. Average values of the crushing strength out of three tests of each type of samples were also calculated and are given in Table 3.

The analysis of the results showed that the crushing strength of the components coated on both surfaces was higher by 20%, and polyurea helped the rings maintain their integrity after their crushing strength was exceeded (Szafran and Matusiak 2020).

7. CONCLUSIONS

The main goal of the considerations and tests described in the paper was to present polyurea coatings as a product that improves functional properties of structural components. Based on the results of the experimental research and their analysis, the following conclusions can be drawn:

- polyurea has unique functional properties and can be used in a number of modern industries,
- due to its extraordinary elasticity and adherence to the substrate, the product considered in the paper can efficiently bridge cracks in concrete elements and thus help protect them from corrosion and aging,
- the application of the coating on elements made of brittle materials, such as cellular concrete, has a positive impact on their ability to maintain integrity after their compressive strength was exceeded,
- the polyurea provides additional reinforcement improving the crushing strength of concrete rings,
- the application of the coating on concrete rings makes them maintain their integrity after their crushing strength was exceeded.

REFERENCES

Badowska, H., Danilecki, W. & Mączyński, M. 1974. *Protection of structures against corrosion (in Polish).* Warszawa: Arkady.

Banera, J., Maj, M. & Ubysz A. 2017. *Polyurea coatings in construction (in Polish).* Poznań: DTP: D-CONCEPT, Grupa MD.

Baszkiewicz, J. & Kamiński, M. 2006. *Materials corrosion (in Polish).* Warszawa: Oficyna Wydawnicza Politechniki Warszawskiej.

Bródka, J. 1995. *Reconstruction and maintenance of steel structures (in Polish).* Łódź: Centralny Ośrodek Badawczo-Projektowy Konstrukcji Metalowych "Mostostal", Politechnika Łódzka.

EN 1917:2002. *Concrete manholes and inspection chambers, unreinforced, steel fibre and reinforced.* 2002.

EN ISO 527:2012. *Plastics. Determination of tensile properties.* 2012.

EN 772-1:2015. *Methods of test for masonry units. Part 1: Determination of compressive strength.* 2015.

Gruener, M. 1983. *Corrosion and protection of concrete (in Polish).* Warszawa: Arkady.

Szafran, J. & Matusiak, A. 2020. *Crushing strength of concrete rings with a polyurea reinforce system.* Tunnelling and Underground Space Technology 101 (2020) 103407.

Szafran, J. & Matusiak, A. 2017. *Modern spray insulations in construction on the example of PUR foam and polyurea (in Polish).* III Konferencja Naukowo-Techniczna TECH-BUD'2017, Kraków, 15-17 Listopad 2017. Kraków: Dział Poligrafii Politechniki Krakowskiej.

Szafran, J. & Matusiak, A. 2016. *Polyurea coating systems: definition, research, applications.* In L. Małyszko & R. Tarczewski (eds), Lightweight Structures in Civil Engineering – Contemporary Problems – Monograph from Scientific Conference of IASS Polish Chapters, Publisher: University of Warmia and Mazury in Olsztyn: 103-110.

Szczepanik, M.; Stabik, J.; Wróbel, G. & Wierzbicki, Ł. *The application of thermovision systems to study of polymeric materials (in Polish).* Modelowanie inżynierskie 36, Gliwice 2008, ISSN 1896-771X.

LIGHTWEIGHT STRUCTURES in CIVIL ENGINEERING
CONTEMPORARY PROBLEMS
Monograph from Scientific Seminar
Organized by Polish Chapters of
International Association for Shell and Spatial Structures
Łódź University of Technology
Faculty of Civil Engineering, Architecture
and Environmental Engineering
XXVII LSCE
Łódź, 2nd – 3rd of December 2021

STRUCTURAL BIONIC SYSTEMS: DESIGN AND NUMERICAL ANALYSIS

R. Szmit [1)]
[1)] Faculty of Geoengineering, University of Warmia and Mazury in Olsztyn., POLAND, *robbo@uwm.edu.pl*

ABSTRACT: The chapter concerns an aspect of the bioinspiration, where flora or fauna are emulated as a basis for design, it is a growing area of research in the fields of architecture and structural engineering. Presents issues related to organic, bionic and biomimetic architecture and show how well-integrated are they with modern methods of construction. Throughout the centuries man driven by curiosity and imagination learned how to harvest and use many of nature's perfect solutions. The reason for such actions is both searching for new solutions, as well as the improvement of current methods in engineering design. The search for efficient structural forms covered in the article is an attempt to discuss the optimization of structures in the field of bionic morphology and geometry. The chapter also includes a simplified numerical analysis of selected static models and their design possibilities of applying natures solutions.

Keywords: bionic design, bio-inspired design, biomimetics, lightweight, structural efficiency.

1. INTRODUCTION

Inspiration in the process of architectural and structural design often comes from nature. Throughout the ages man driven by curiosity and imagination learned how to harvest and use many of nature's perfect solutions. Constructions of modern times not only astonish us by their form and functionality, but also promote harmony between human habitation and the natural world. In the past, humans often consciously or intuitively looked for the inspiration in wildlife for their architectural activities and construction solutions. When we talk about the structural design, we have to start with the structural characteristics of the surrounding world. One look around will show us that nature knows no right angle, nor does it use straight lines. Although there are lots of similarities between species of different life forms, they use no repetition of basic structural elements for the sake of production costs. Actually every structural part of natural systems is unique, no matter how big or small it is (Dimcic 2011).

After thousands of years of testing the effects of different loads and their combinations, as well as the use, natural forms are perfectly adapted to their environment (Benyus 2012). Probably this is the reason why ancient human dwellings resembled to beavers, termites, or bird nests. For example, Brunelleschi based his construction of the dome of Santa Maria del Fiore temple on the shape of egg shell, which is interesting not only because of its geometry but also because of its internal structure. By its shape it is a two-focus of a parabola (Acharya 2012, Bogusz 2012, Samek 2010). Structural bionics is the division of technical bionics devoted to discovery of laws of nature objects shapes and forms and application of these laws in

construction. This is a brand new approach in theory and practice of architecture. Structural bionics examines principles of construction of nature objects and applies these results in engineering tasks. Such approach is fully justified, as in the nature there are no strict barriers between the living and inanimate. The world is integrated into one single unit by laws of nature, creating the possibility of unification in natural sciences and technical sciences (Mattheck 2004, Maciejko 2016).

2. GEOMETRY CONCEPTS IN STRUCTURAL DESIGN

2.1. Basic mechanisms in structural bionics

It is useful to express the relationship between the shape of the projected artificial structure and nature shape in form of their analogy and homology. The analogy means that the same function is fulfilled by originally different structural features. We can draw analogies between the elements of architectural structures and forms in nature and we can also find related shapes: cable roof structure and spider web, dome on the building and anthills, etc. Homology is a different way of expression of natural laws. In biology it means that similar forms with the same origin and construction fulfil different functions (Sumec 2010, Vahedi 2009).
In terms of technical bionics, homology is a manifestation of similarities, based on the common relationship. In search of homology we focus on establishing links between human activity and activity of living organisms. We can make an example of ropes, whether used as a load-bearing structure roofing systems, bridges, structural elements or aerial high-voltage wires. Their origin can be traced to the spider webs, lianas or processed flax fiber. Thus, these and alike structures created different, homologous, functions. As said above, fin of the whale and bat wings are homologous to the human hand. They originate from the same structures on the skeleton, but their functions diversified so much that there is virtually no remaining similarity between them (Lebiediev 1983).

2.2. Creation of forms

The engineering wisdom of nature lies not only in the design of structural solutions that provide maximum load capacity and extraordinary functionality, but also takes into account the economics of managing the means to achieve such excellent results. Nature saves materials by means of "prefabrication" - in organisms and plants very often there are elements with the same form as exemplified by the hexagons in the structure of the fly eye or turtle armor. An excellent example of regularity and cost-effectiveness of materials is also the construction of bee honeycombs made up of a hexagonal prismatic group that is very much used by modern engineers (Tofil 2007). The same applies to the distribution of lines between water bubbles (Voronoi diagrams). The use of such a form allows to significantly reduce the consumption of materials intended to cover the surface or the construction of stiffening partition walls. By using structures based on honeycomb or bone structure, krill eye, diatom frustules or Voronoi diagram, we obtain, with all functional qualities, a reduction in volume and area (Kasim & Hussaini 2005, Konopka 2011, Sadri et al. 2014).

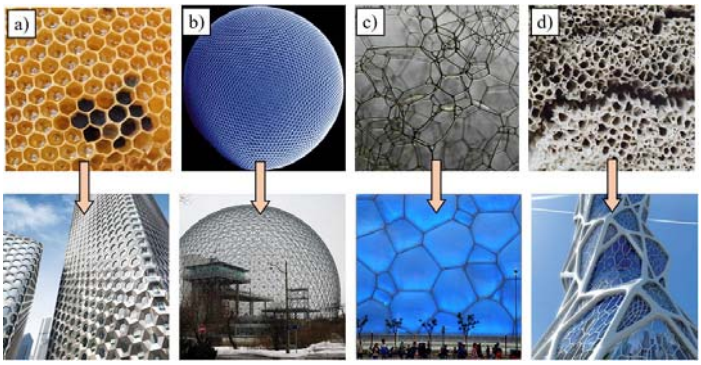

Fig. 1. Bionical facets: a) honeycomb; b) krill eye; c) water foam (Voronoi); d) bone structure.

2.3. Voronoi diagram

Voronoi tessellation can help model the shape of various architectural forms inspired by nature, e.g. from a flat bar structure (bone structure, foam bubbles, etc.) (Fig.2). The Voronoi diagram is a tiling of a surface, often a plane, into regions (cells) based on distances to points (seeds) in a specific subset of the surface. Each point located within a given cell of the diagram lies closer to the seed located in this cell than to any other seeds in the network.

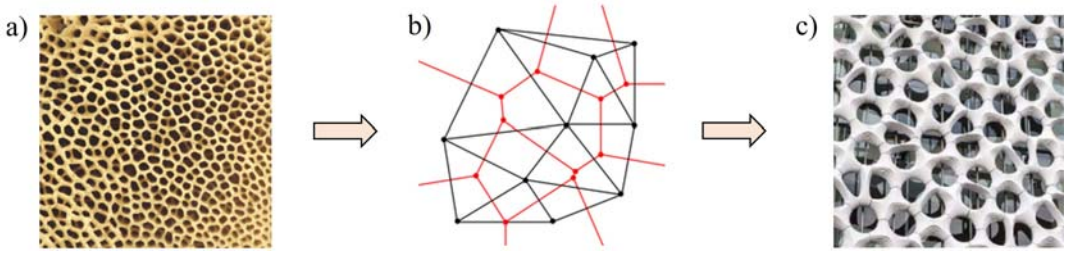

Fig. 2. Application of the diagram Voronoi: a) bone structure; b) diagram Voronoi and triangulations; c) modern façade.

In the analyzes of the observation towers (see point 3.1.), a random distribution of the base points of the Voronoi diagram with different densities was used. The chapter presents a tessellation in which the bar stresses are similar to the distribution of bars on the honeycomb division tower under the action of the same loads.

3. EXAMPLES OF NUMERICAL ANALYSIS

3.1. Observation towers variants

The analysis involved two types of observation towers with different distribution of rods on the side surface. Both towers have a cylindrical shape with a diameter of 4m and a height of 20m (Fig. 3). One of them is forming according to structure of honeycomb (variant I) and the second one is inspired by the Voronoi diagram (variant II). The following are selected values of stress, cross – sectional forces, displacements and efforts in individual bars. The calculation was made in Robot Structural Analysis Professional 2020 (finite element type used for analysis: 3D beam – six nodal degrees of freedom). Visualizations of observation towers in natural environment had been made in SketchUp program.

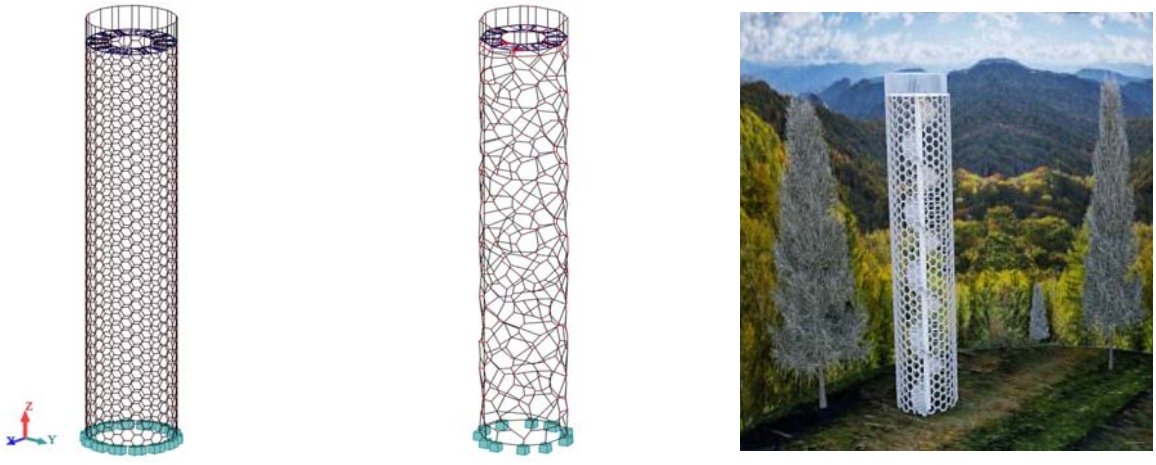

a) b) c)

Fig. 3. Models of bionically inspired observation towers: a) variant I, b) variant II, c) visualisation.

Figs 4÷6 present maps of axial forces F_x, normal stresses S_{max} and deformations of towers under load combinations.

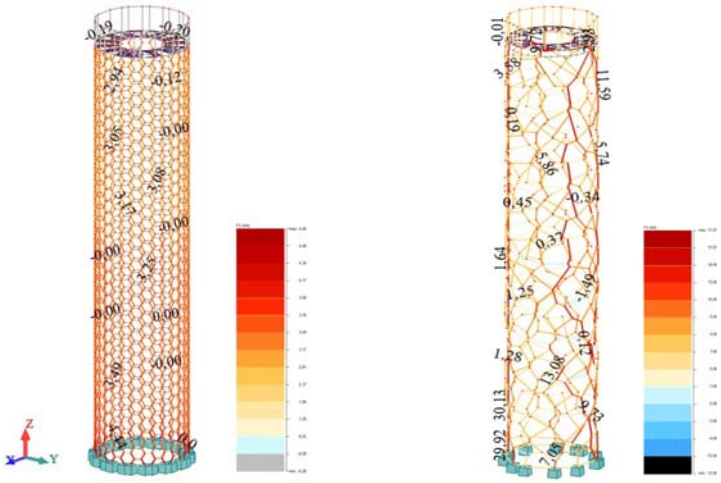

a) b)

Fig. 4. Map of axial forces F_x - load combination: a) variant I, b) variant II.

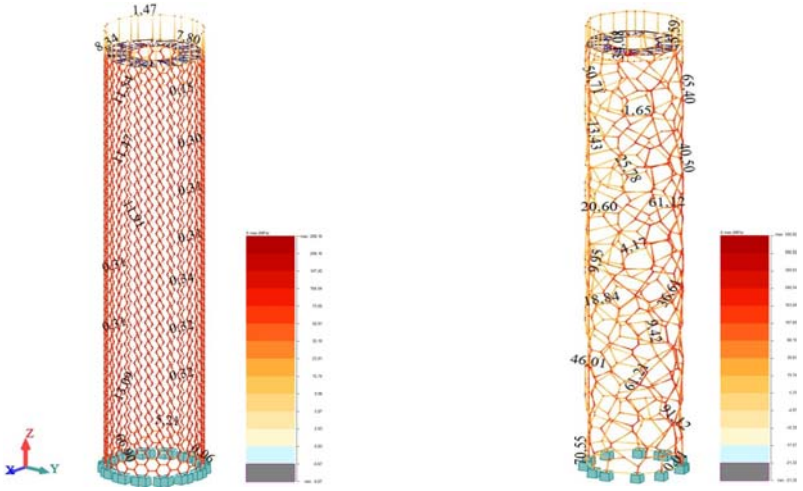

a) b)

Fig. 5. Map of normal stresses S_{max} - load combination: a) variant I, b) variant II.

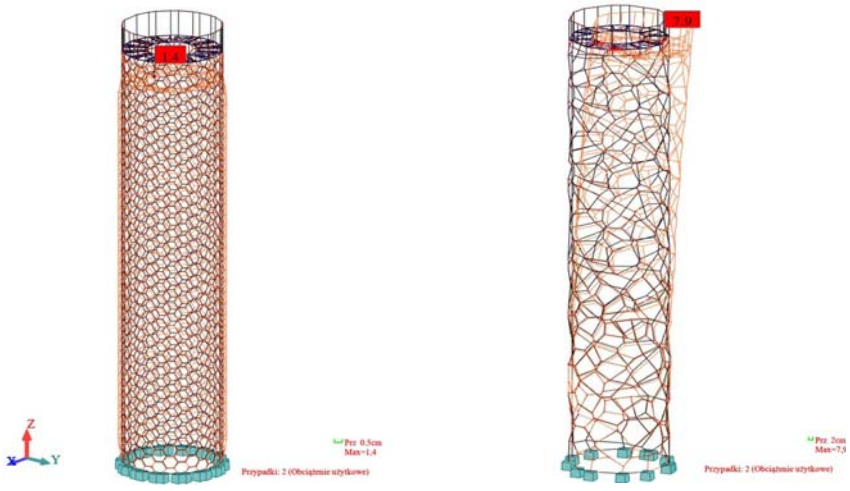

a) b)

Fig. 6. Deformations - load combination: a) variant I, b) variant II.

The models were generated assuming a similar total mass of bars, which resulted in the assumption of different cross-sections of bars, but at a similar cost of construction material (structural pipes: 30x3,2mm in variant, 54x3,2mm in variant II). The Figure 7 show the relationship between the displacement values of the nodes in the X and Z directions, respectively. The orange curves determine the behavior of the honeycomb structure, and the blue one - the Voronoi tower.

In variant I, the displacements of U_x nodes at a height of about 4 - 16 meters are equal to each other. They grow from 0-2 meters, and decrease from 16-20 meters. The plot curve resembles the shape of the tower deformation from the displacement values. In variant II, the displacements in the X direction increase with the height of the tower. This is due to the lack of symmetry in the arrangement of the bars. In both cases, in the Z direction, the value of the nodes displacement increases with the height.

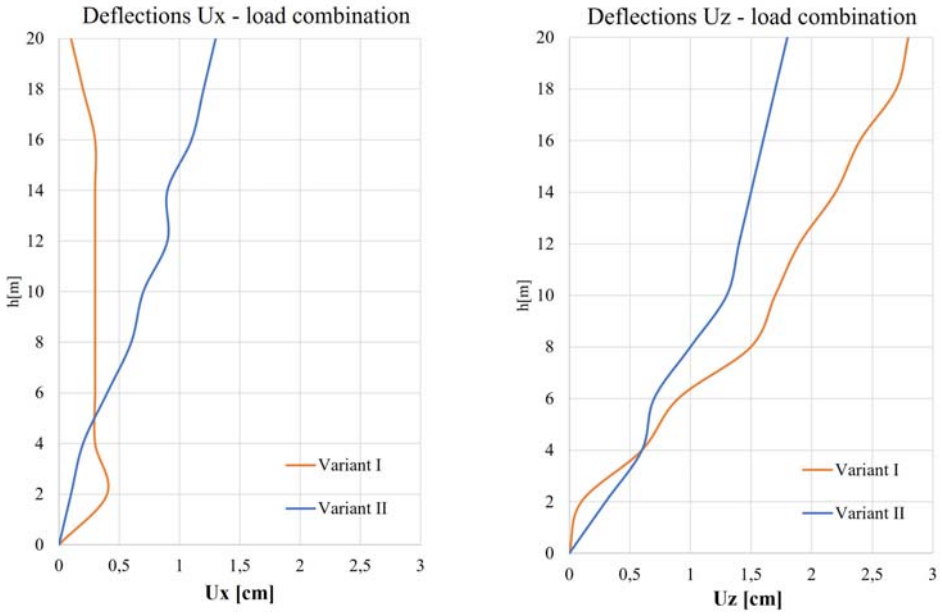

a) b)

Fig. 7. Comparisons of U_x and U_z deflection - load combination: a) variant I, b) variant II.

The presented variants of the observation towers are characterized by similar values of stresses, internal forces and displacements, but the tower modeled on the Voronoi diagram achieved higher values of these parameters. The reason for such results may be primarily the fact that the tower number two is based on irregular geometric grid, without symmetry of the bars arrangement. The bars in this structure do not have the same length and are arranged randomly. In the first variant, the structure of the geometric mesh is based on regular rod lengths, which, compared to the Voronoi tower, has greater rigidity. It is worth paying attention to the architectural qualities of these unusual bar structures. These structures fit well with the landscape.

3.2. Three walls variants

The analysis (using Autodesk Robot Structural Analysis Professional 2020) involved three walls variants with different mass distributions in their volume (Fig. 8). The calculations were designed to present the changes in behaviour of the wall variable distribution of weight of the material, aiming at distribution observed in nature. The analysed structures were modeled from the same material (concrete) with parameters: E = 30000 MPa, ν = 0.18 and ρ = 2300 kg/m^3. In addition to the material, they also have the same external dimensions - length and width - 36.17 x 23.86 m and a thickness of 0.30 m. These are the

walls fixed on the lower edge with a linear pivot support. This work focuses only on cases of plane stresses and plane deformations (Szmit and Chrząszcz 2018).

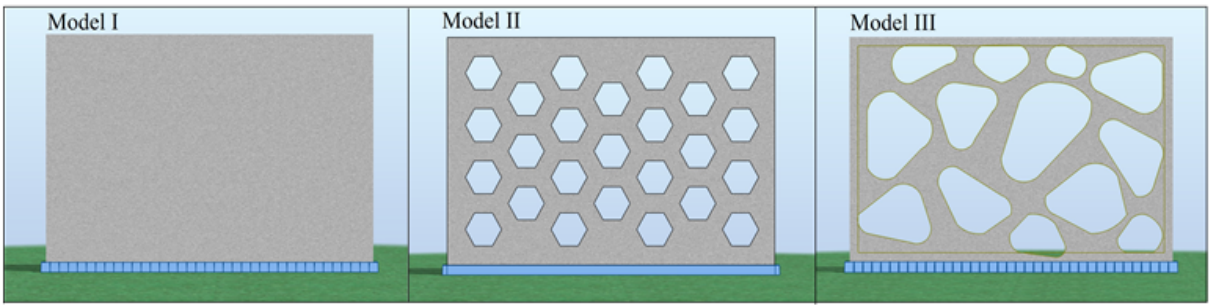

Fig. 8. Views of the analysed walls.

Model I - "filled" wall: The first example is the "filled" wall with dimensions as stated above 36.17 x 23.86 m and thickness 0.30 m. It provides a reference point for analysis and the results obtained. Applied meshing method: simple mesh generation (Coons) with 925 nodes.
Model II - "honeycomb" wall: The second example analysed this wall has in its structure the 25 holes which are imitation of the honeycomb system. Grid computing - 4038 nodes (complex mesh generation: Delaunay + Kang).
Model III - "bone structure" wall: The third example is a wall with holes, as in variant II, however, differing in shape - these are the holes imitating primarily the internal structure of the bone, but can also be partially compared to the "pattern" of the giraffe's coat that was used in the construction of the Warmian Gallery in Olsztyn. The wall has 13 holes and 2713 nodes (complex mesh generation method: Delaunay + Kang).

The type of finite elements used in the numerical analysis is shell (2D planar) elements. In all three variants that includes self-weight load and imposed load of 100 kN/m applied to the top edge of the facing down. Of the three analysed walls, the highest values of displacement were obtained for variant II - "honeycomb". For the "filled" and "honeycomb" walls approximate absolute values of the maximum and minimum displacement were obtained, whereas in the case of the III wall they differ considerably - this is due to lack of symmetry in the III variant of the analysed structure (Tab. 1).

Tab. 1. Extreme deformations U_x and U_y.

		Walls		
		"filled"	**"honeycomb"**	**"bone structure"**
U_x [m]	**max**	1.2658 E-04	4.9563 E-04	2.3927 E-03
	min	-1.2658 E-04	-4.8341 E-04	-1.6294 E-03
U_y [m]	**max**	0.0000 E+00	0.0000 E+00	-1.6294 E-03
	min	-1.1883 E-03	-2.2843 E-03	-6.2242 E-03

The character of the deformations of all three analysed structures is the same - the wall surface under load is moved down. Analysing the displacement fields (Figs 9÷11) we can see that in the case of a "filled" wall, the character of the displacements is parabolic line/ rounded. In the next two variants, the existence of the holes in the panel results in a belt of the same value (same color) arranged in lateral bands.

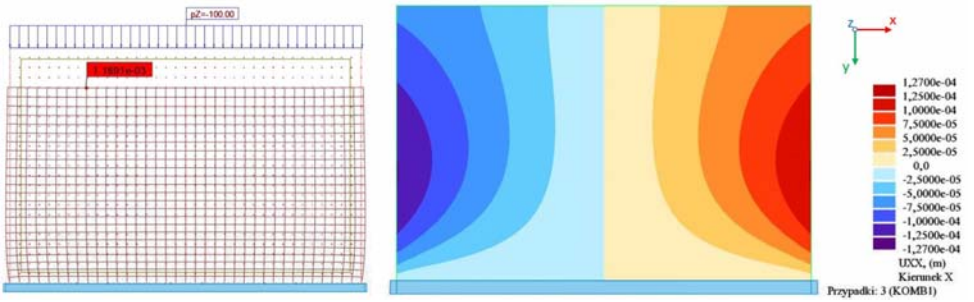

Fig. 9. “Filled” wall - deformation and the displacement field U_x.

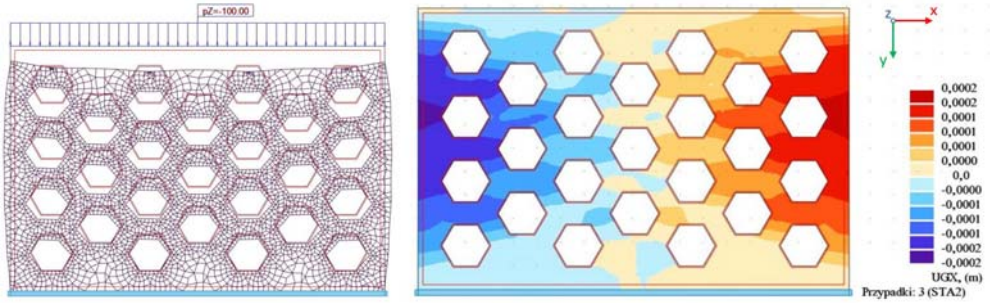

Fig. 10. “Honeycomb” wall - deformation and the displacement field U_x.

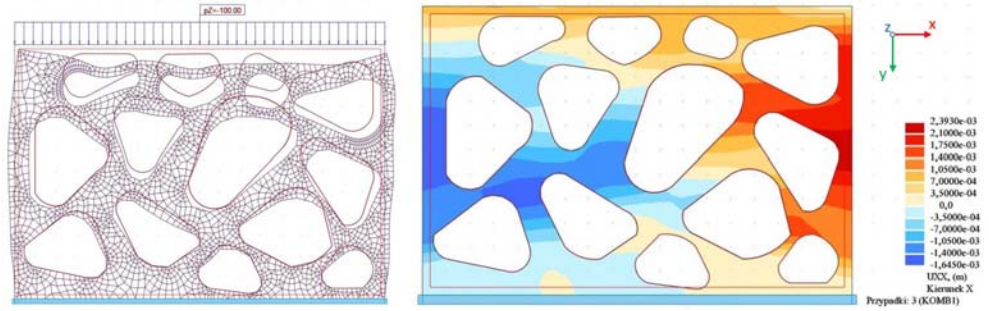

Fig. 11. “Bone structure” wall - deformation and the displacement field U_x.

In the variant of "honeycomb" and "bone structure" on the upper edge there are more unified displacement values than in the case of a standard wall.

As in previous analyzes, the xx - σ_{xx} field for the comparison case - the "filled" wall, we obtain one-time graph characteristics - the stresses are parabolic form. There are two independent objects, but in the "honeycomb" you can capture symmetry and delicacy with parabolic outlines. In the variant "bone structure" there is considerable variation in the obtained results, which is characteristic for such irregular shapes. The concentration of the extreme stresses at the edge of the holes is also characteristic (Figs 12÷17).

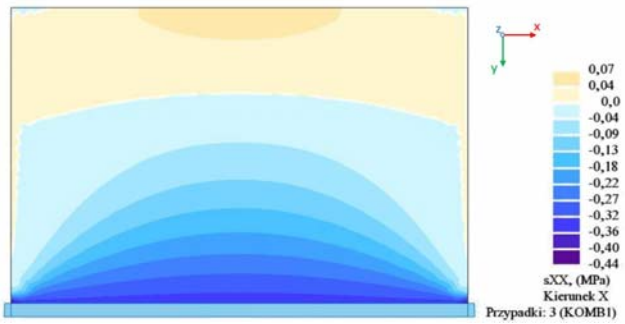

Fig. 12. Normal stresses σ_{xx} – “filled” wall.

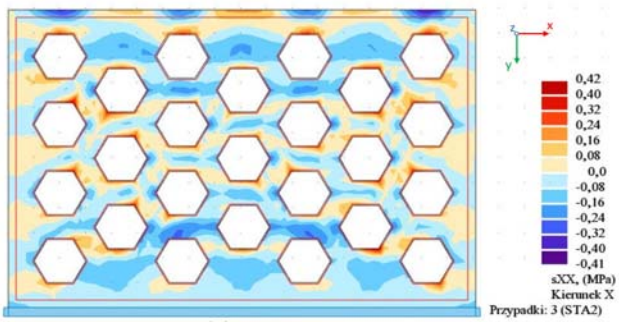

Fig. 13. Normal stresses σ_{xx} – “honeycomb” wall.

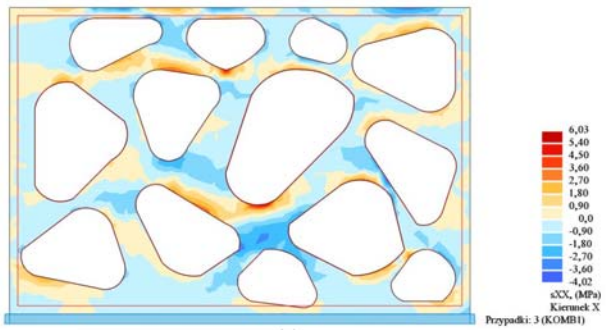

Fig. 14. Normal stresses σ_{xx} – "honeycomb" wall.

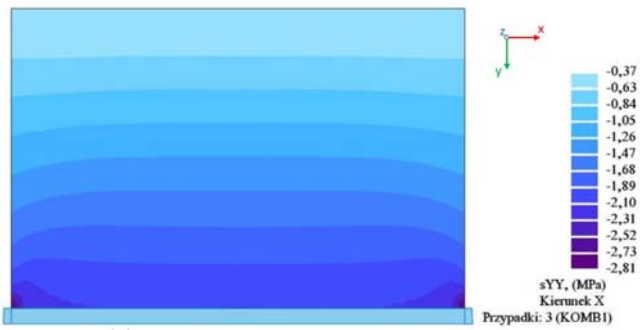

Fig. 15. Normal stresses σ_{yy} – "filled" wall.

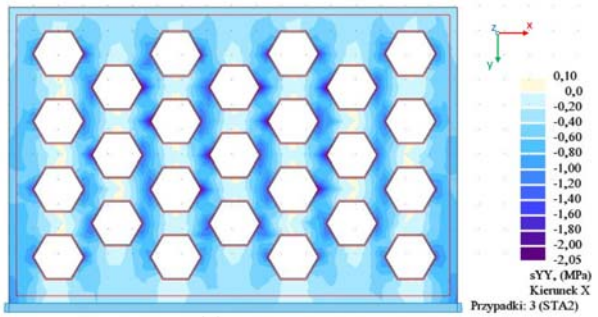

Fig. 16. Normal stresses σ_{yy} – "honeycomb" wall.

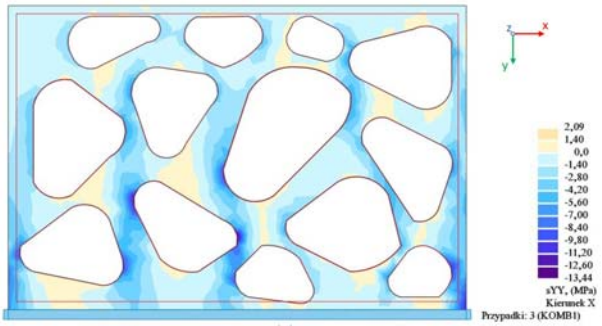

Fig. 17. Normal stresses σ_{yy} – "bone structure" wall.

The analysed structures, as mentioned at the beginning, have the same external dimensions of 36.17 x 23.86 m and the same thickness of 0.30 m. However, owing to having the holes wall II – "honeycomb" and wall III – "bone structure" have a different value for the filled surface and hence a different volume of material used for their construction (Tab. 2).

Tab. 2. Comparison of the filled area and volume of the analysed walls.

	Walls		
	"filled"	***"honeycomb"***	***"bone structure"***
Filled area [m^2]	863,03	603,12	440,70
Volume [m^3]	258,91	180,94	132,22

It can be noted that the area and volume of the "filled" wall is 1.4 times greater than the "honeycomb" and about twice (1.95) larger than the "bone structure".

Keeping the surface area and the volume of used material for wall II - "honeycomb" and wall III - "bone structure" and while building full walls we would get adequate wall, for example: 20 x 30,16 m and 20 x 22.04 m.

Based on received and analysed above results can be inferred from the general conclusion - the best and most transparent results were obtained for "filled" statics model, which is a comparative point (Table 3). The findings "honeycomb" and "bone structure" static model are from 1.09 to 18.82 times greater than "filled" statics model. However not all results of the "filled" statics model wall are better, for example maximum membrane power (von Mises hypothesis) is the best for "honeycomb" - its value is 0.86 of the comparative statics model.

Tab. 3. Comparison of selected parameters of the analysed walls.

		The multiplicity of the results obtained in relation to the "full" wall	
	Analysed parameter	**"honeycomb"**	**"bone structure"**
1.	Max. directional deformation u_x	3.93	**18.82**
2.	Min. directional deformation u_y	1.93	5.27
3.	Extreme equivalent stress (von Mises)	**0.86**	5.65
4.	Max. normal stress (x-x)	14.60	16.00
5.	Total deformation (x-x)	3.60	1.09
6.	Max. normal stress (y-y)	8.43	21.00
7.	Total deformation (y-y)	1.88	5.17

Other results for II and III statics models aren't blatantly excessive or understated than results "filled" statics model. Most are comparable, the difference in values is the result of another geometry.
To conclude the statics model usually leads to changes in the parameters obtained. In some cases this is a more or less significant change in value, other position of maximum value or changed chart.
From the point of view of constructor get results other than for "filled" statics model may be beneficial.
The most important is a fact that models which refer to the world of nature have worse results but require less material consumption - financial considerations and they are distinguished by aesthetics and interesting form (Ruszaj 2016, Szmit and Chrząszcz 2018, Tselas 2013).

4. CONCLUSIONS

The aim of this chapter was to show the influence of bionics and organics on the achievements, capabilities of contemporary civil engineering and presentation of example of their use in building structures. In the collected study material attempts were made to make the reader aware of the wide range of influence of the mechanisms of nature on objects erected.
The collected material for drawing inspiration from nature and transferring its mechanisms to the world of construction shows the reader that man is an integral part of nature, which is an inexhaustible source of knowledge and engineering wisdom.
The second part of the chapter - two simplified numerical analysis's of static models of observation towers and three simplified numerical analysis's of bionic shells - is confirmation of the thesis that through appropriate modifications of geometry and use of nature observation we can achieve constructions who have not much worse parameters, sometimes even better and can use less material what is unfortunately so important from a point of view financial considerations. In addition, we can achieve an interesting, compatible with the environment of the structure space. Regardless of the approach, grid shell design, or any kind of design, is a process of optimization. Every decision making begins with a creation and selection of some solutions that are picked and altered according to some set of objectives. In nature-inspired structural engineering it basically comes down to optical and statical conditions that, as it is already emphasized, should always be considered together.
To wrap up the work realizes the goals set out in showing the essence of the influence of fascination and the use of thousands of years of economic solutions of nature in modern civil engineering. It provides a source of knowledge and examples of implementation based on the phenomena and mechanisms of the world of bionics and organics. This work is confirms that the adaptation of living organisms to the world of construction constitutes the basis for the level of knowledge and skills acquired and provides further opportunities for development.

REFERENCES

Acharya, L. 2013. *Flexible Architecture the Dynamic Societies. Reflection on a Journey from the 20th Century into the Future*. University of Tromso.

Benyus, J.M. 2012. *Biomimicry: Inovation inspired by Nature.* New York Times Book Review.

Bogusz, M. 2012. *Naśladowanie natury w architekturze*. Krakowski rynek nieruchomości 23/2012.

Dimcic, M. 2011. *Structural optimization of grid shell based on genetic algorithms.* Universität Stuttgart.

Kasim, D. & Hussaini, A. 2005. *Design in Nature and Architecture*. Carleton University Ottawa.

Konopka, K. 2011. *Wzorce z natury w technice i inżynierii materiałowej*. Warszawa: Oficyna Wydawnicza Politechniki Warszawskiej..

Lebiediev, J.S. 1983. *Architektura i bionika*. Warszawa: Arkady.

Maciejko, A. 2016. *Inspiracje w architekturze*. Builder 44/2016.

Mattheck, C. 2004. *Design in Nature: Learning from trees*. Springer Verlag.

Ruszaj, A. 2016. *Bio-inspiracja w projektowaniu konstrukcji lekkich*. Mechanik nr 2/2016

Sadri, M. & Kavandi, M. & Jozepiri, A. & Teimouri, S. Abbasi, F. 2014. *Bionic Architecture, Forms and Constructions.* Research Journal of Recent Sciences.

Samek, A. 2010. *Bionika - wiedza przyrodnicza dla inżynierów.* Kraków: Wydawnictwo AGH.

Sumec, J., & Jendzelovsky, N. & Kormanikova, E. & Kotrasova, K. 2010. *Architectural Bionics in civil engineering.* International Scientific Journal "Machines. Technologies. Materials" vol. 6 (2010).

Szmit, R. & Chrząszcz, J. 2018. *Structural Bionic Systems in Civil Engineering.* 2018 Baltic Geodetic Congress (BGC Geomatics), New York: IEEE.

Tofil, J. 2007. *Forma aorganiczna konstrukcji cięgnowej mostów i przekryć - piękno struktury naturalnej*. Kraków: Wydawnictwo Politechniki Krakowskiej.

Tselas, E. 2013. *Architectural design and form inspired by nature.* University of Huddersfield.

Vahedi, A. 2009. *Nature as a Source of Inspiration of Architectural Conceptual Design.* Famagusta: Eastern Mediterranean University.

LIGHTWEIGHT STRUCTURES in CIVIL ENGINEERING
CONTEMPORARY PROBLEMS
Monograph from Scientific Seminar
Organized by Polish Chapters of
International Association for Shell and Spatial Structures
Łódź University of Technology
Faculty of Civil Engineering, Architecture
and Environmental Engineering
XXVII LSCE
Łódź, 2nd – 3rd of December 2021

CATENOIDAL COOLING TOWER – INTRODUCTORY STRUCTURAL ANALYSIS

R. Walentyński [1] **M. Wiśniowski** [2] **D. Cornik** [3]
[1] PhD DSc, Faculty of Civil Engineering, Silesian University of Technology, POLAND, *rwalentynski@polsl.pl*
[2] MSc, Faculty of Civil Engineering, Silesian University of Technology, POLAND, *mwwisniowski@polsl.pl*
[3] MSc, Faculty of Civil Engineering, Silesian University of Technology, POLAND, *dcornik@polsl.pl*

ABSTRACT: Optimisation plays a major role in scientific and engineering research. This paper presents the effects of using the catenoidal shape to design the structure of the chimney cooling tower. This paper compares some geometrical variations of the catenoid in comparison to the reference real hyperboloidal structure. This work compares the internal forces, deformation, and stability of the catenoidal structure. The comparison shows some predominance of catenoid over the popular hyperboloid structure of the shell. This paper attempts to find an optimal shape of the cooling tower to reduce the amount of material and labour. It focuses on optimisation of geometry and also precise load values.

Keywords: optimisation, catenoid, shell, cooling tower, Finite Element Method.

1. INTRODUCTION

The main objective of this work is to optimise the structural shell of the chimney cooling towers. It has already been proposed to use a catenoidal shape of the shell instead of the frequently used hyperboloidal one (Bielak and Walentyński 1993). The work focuses on theoretical considerations on static calculation and wind load acting on the concrete surface.
Hyperboloid is a ruled surface, so it contains straight lines. It creates the possibility of bending and buckling along those lines. The catenoid does not contain any straight lines, so there is an expectation that it will be more stable. The catenoid is also a minimal surface, so it has the lowest possible area between two boundary rings. It gives opportunity to optimise the geometry of chimney cooling towers using a catenoidal shape, and reduce the mass of structure or strength it.

2. METHODS

The analysis focuses on an existing chimney cooling tower at the Opole Power Plant. The parameters of that structure (size, material property, technical parameters, local environmental load) have been used as boundary conditions for further consideration. The hyperboloidal shape has been replaced by a catenoid, saving boundary conditions (heights, key radiuses).
The following paper concentrates on numerical calculation. The finite element method (FEM) and computational fluid dynamics (CFD) have been used for static calculation and numerical estimation of the

wind load acting on the concrete surface consequently. For both analyses ANSYS software has been applied. Ansys Mechanical for FEM calculation and Ansys Fluent for CFD. Both modules have been combined, so the pressure obtained from the CFD has been applied as the load acting on the concrete surface in the FEM model.

2.1. Geometry

The catenoid is obtained by Equation (1) or by the revolution of the curve given by Equation (2).
The parameters given in the equation refer to the values marked in Figure 1. Using Equation (3) it is possible to modify the parameters of the shell geometry. This paper compares a few cases of catenoid given by equation (3) that vary by parameters h, which refer to the level of the narrowest section of the shell. The radius of the bottom (at altitude z = 0, which refers to the level of the bottom of the columns) is constant for each case analysed and equal to 54 m. Similarly, the narrowest radius is constant and equal to 32,5m. Each value of radius is measured in the middle of the surface.

$$x^2 + y^2 = a^2 \cdot \cosh(z'/c)^2, \tag{1}$$

$$R(z') = a \cdot \cosh(z'/c), \tag{2}$$

$$R(z) = \mathrm{R}_{\min} \cdot \cosh\left[\frac{z-h}{h} \cdot \operatorname{arccosh}(\mathrm{R}_{\max} / \mathrm{R}_{\min})\right], \tag{3}$$

$$R_{hyperboloid}(z) = \mathrm{R}_{\min}\sqrt{1+\frac{(z-h)^2}{h^2}\cdot\left(\frac{\mathrm{R}_{\max}^2}{\mathrm{R}_{\min}^2}-1\right)}. \tag{4}$$

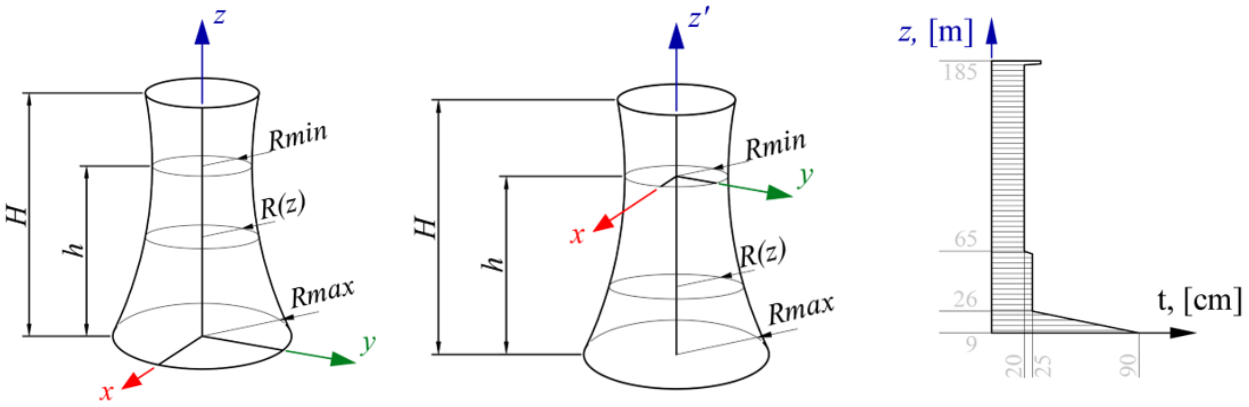

a) b) c)

Fig. 1. a), b) Cooling tower shell. Coordinate systems, variables, and parameters. c) The thickening of the shell varies with altitude.

Another parameter that varies for the models is the surface thickness. The smallest thickness of the concrete is approximately 20 cm. The thickness t of the shell varies as shown in Figure 1 and does not change throughout the study.

2.2. Loads cases and comboination

According to Eurocode, there are a few possible, independent typical load cases acting on structures of cooling towers: self-load (gravity) (G), wind load (W), concrete contraction (Shrink) (S), environmental temperature (T_{env}), technological temperature (T_{tech}), uneven ground settlements (B), dynamical response (Dyn). Combinations of loads required to determine utility of structure can be obtained using Eurocode 0 (equation 6.10 Ultimate Limit State). It generates few situations to analyse, however, the VGB standard points just two load combinations as reliable for determining internal forces in shell and member substructure. They are:

$$\gamma_G \cdot \mathbf{G} + 1.5 \cdot \mathbf{W} + \gamma_Q \cdot \mathbf{B} + \gamma_Q \cdot \mathbf{S}, \tag{5}$$

$$\gamma_G \cdot \mathbf{G} + 0.9 \cdot \mathbf{W} + \gamma_Q \cdot \mathbf{T} + \gamma_Q \cdot \mathbf{B} + \gamma_Q \cdot \mathbf{S}. \tag{6}$$

For this analysis, the following loads have been taken into account: deadload and wind load as the most influential load cases:

$$1.1 \cdot [1.35 \cdot \mathbf{G} + 1.5 \cdot \mathbf{W}]. \tag{7}$$

Deadload contains the load of concrete structure weight, which is equal to 25kN/m^3. Wind load has been determined according to Eurocode for typical conditions in Poland, with a base wind speed v = 22 m / s, a base pressure wind q = 0,3kPa and a flat area with low vegetation and isolated obstacles. The other loads indicated by the German standard (VGB, 2019) or literature (Ledwoń, 1967) will be considered in further work.

2.3. Wind load

As the self-load of the structure is quite easy to estimate, it is difficult to determine the load of the wind acting on the structure. Wind load may act as dynamic load, but widely used methods in civil engineering calculation (FEM, implicit, static) allows to apply only static loads. Norms (Eurocode 1, VGB Standard) and literature - Flaga (2008) recommends applying equivalent static load, which substitutes dynamic character of wind load by increasing value of static pressure by Turbulence factor. Wind load distribution, are given in Eurocode 1- 4, past regional standards and many scientific studies: Flaga, (2008) Padewska (2015) for cylindrical cross-section of structure. Pressure is given as a function of altitude (z) and angular direction (α). However, the previous author's consideration shows that the pressure distribution in the hyperboloidal or catenoidal tower differs from the distribution in the cylindrical cross section. That difference indicates a noticeable difference in static calculation. To increase accuracy for each analysed case, the wind load was estimated numerically (using CFD). Fig. 2 presents the difference between the pressure obtained using the VGB standard and numerical calculation (CFD). For estimation, a normative wind profile was used.

2.4. FE model

Calculation model consist of curved shells, divided in planar finite elements. The model assumes division of curved panels on flat finite elements. The support zone contains member elements – 72 inclined columns and a foundation member with elastic Winkler support. The size of the finite element mesh has been chosen to obtain satisfactory results. Quality of the finite element mesh has already been tested by Wiśniowski (2020) or Rakowski (2005).
Globally, mesh was set to size 2m, which divides cooling tower into 408 FE along the radial direction.

The local mesh had been refined, in the bottom area, to a size of 0,5m (between columns) to determine the distribution of forces in the shell between concrete columns, and 1 m in the zone where the thickness of the shell varies.

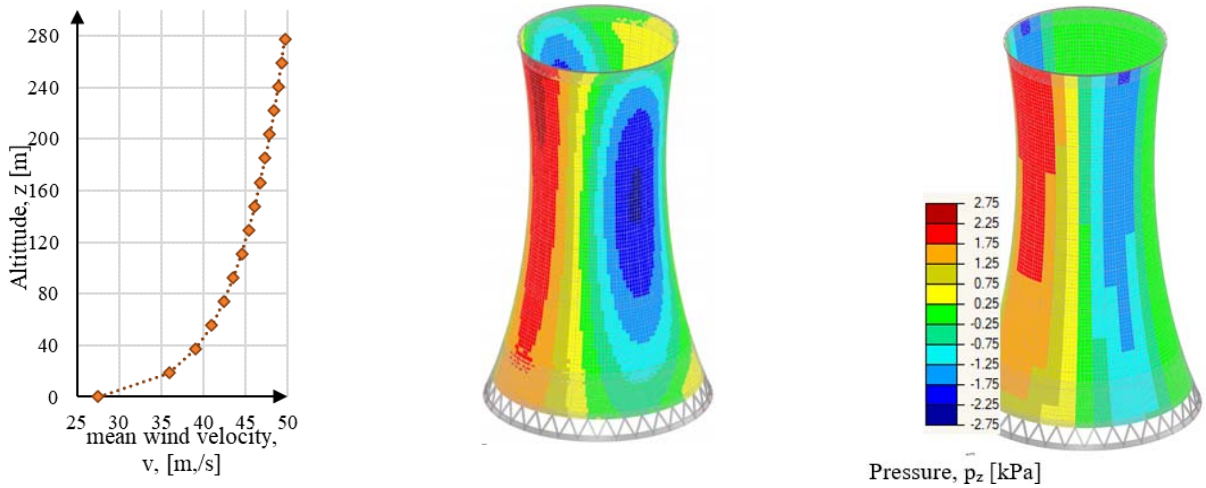

a) b) c)

Fig. 2. a), b) Wind load over chimney cooling tower. a) wind profile for terrain category II and wind zone (1) according to the Polish national annex in Eurocode, b) wind load obtained using CFD, c) wind load obtained using the VGB-S610e equations, given in the VGB standard, presented in units [kPa].

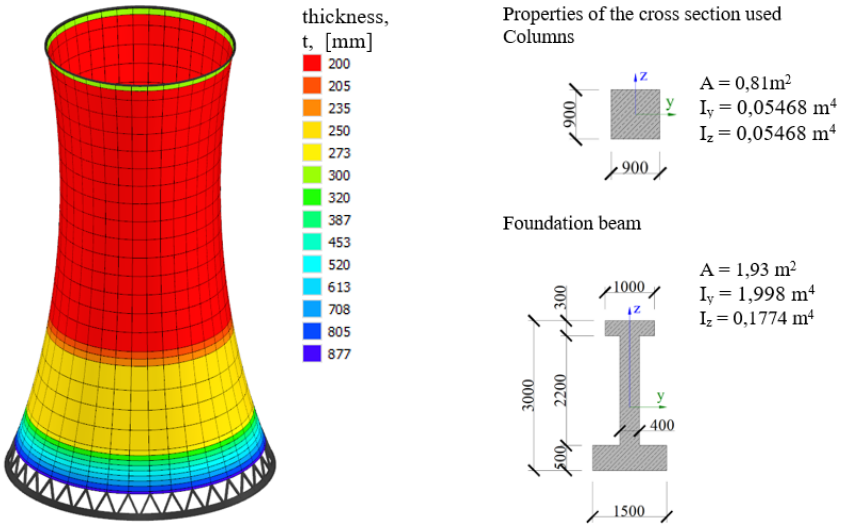

Fig. 3. Numerical model geometry – cross sections and thickness

Each tested model contains the same number of plates. To avoid errors caused by building the model for each geometry, each sample is a copy of the template model, where the node coordinates were adjusted to a suitable function (3) or (4). A table of node coordinates was generated on radial coordinates.

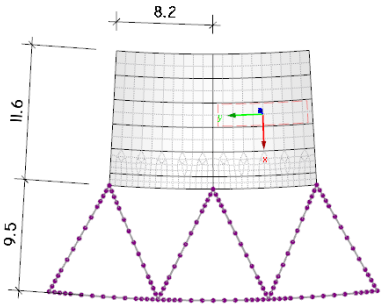

Fig. 1. Numerical model: mesh size, mesh refinement on member elements and orientation of local coordinates for shell (axis X – vertically, axis Y – horizontal/ radial)

3. RESULTS

The result of the calculation is the distribution of all internal forces, so the interpretation of the results can be ambiguous. Because it is difficult to compare the distributions of internal forces, only the highest values of internal forces and displacements were taken into account in the comparison.

3.1. Mesh convergence

The mesh convergency was provided on the maximal displacement and stress in one selected point for catenoid, with altitude h equal to 122m. First step of mesh convergency changes the global mesh size (10÷0,5m). In the second step the size of mesh refinement was checked in the lowest layer of FE on the shell.

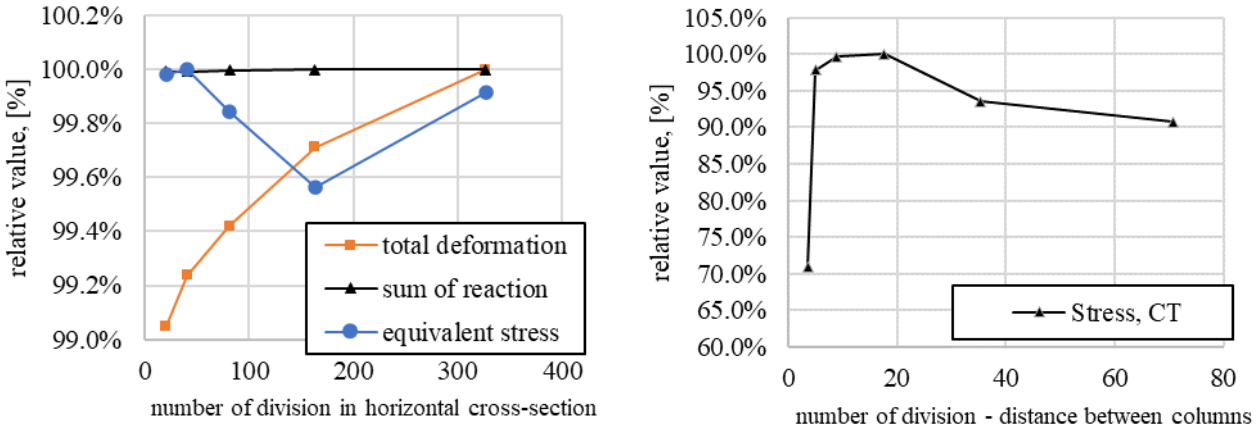

a) b)

Fig. 5. Mesh convergence: a) influence of global mesh size on results, b) influence of mesh refinement on results in distance between columns

The additional mesh convergence was provided on maximal displacement and stress in one selected point for the catenoid, with parameter h set to 122m. First step of mesh convergence tests the global mesh size (for range 10÷0,5m). In the second step, the size of mesh refinement was checked in the lowest layer of FE on the shell. In the bottom area, mesh divides distance between columns in 18 elements, and mesh size is approx. 0,5m

3.2. Internal forces

The shell changes its thickness with altitude, so a comparison of internal forces is presented separately for each sector. The structure has been divided into parts where the thickness of shell is uniform or does not very much. The separation of results shows the results in a clearer way. Picture below presents the division of the model into parts.

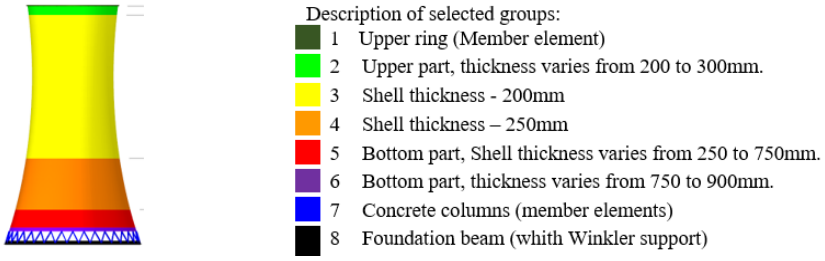

Fig. 2 – selected sectors to compare results

The example results – bending moments and normal forces in horizontal direction are presented in the Fig. 7. To show better results, ending layers of finite elements (where internal forces are disturbed) were hidden for normal forces and bending moments graph. In the lowest region, the concrete shell meets supporting columns and the thickness is 4 times greater, so there occurs greater internal forces locally.

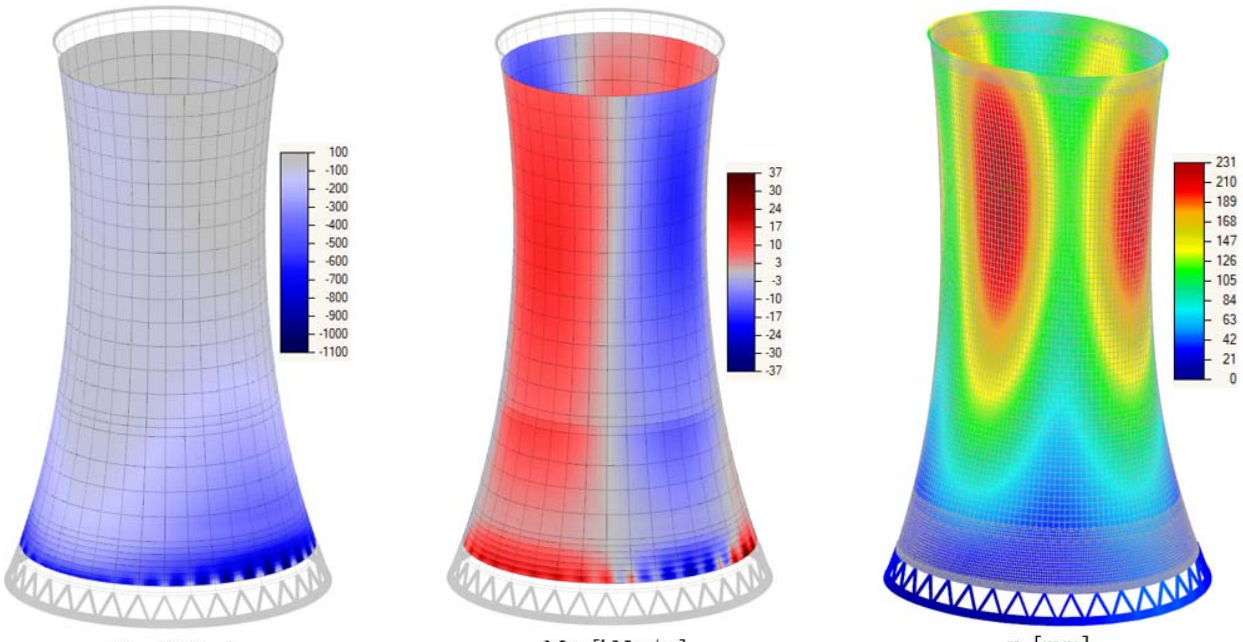

Fig. 7. a) Normal forces in the radial direction, b) bending moments in the radial direction, and c) total deformation of the structure.

The internal forces distribution in the lowest region is irregular due to supporting the shell on 36 pair of columns. This indicates a local increase of each component internal force.

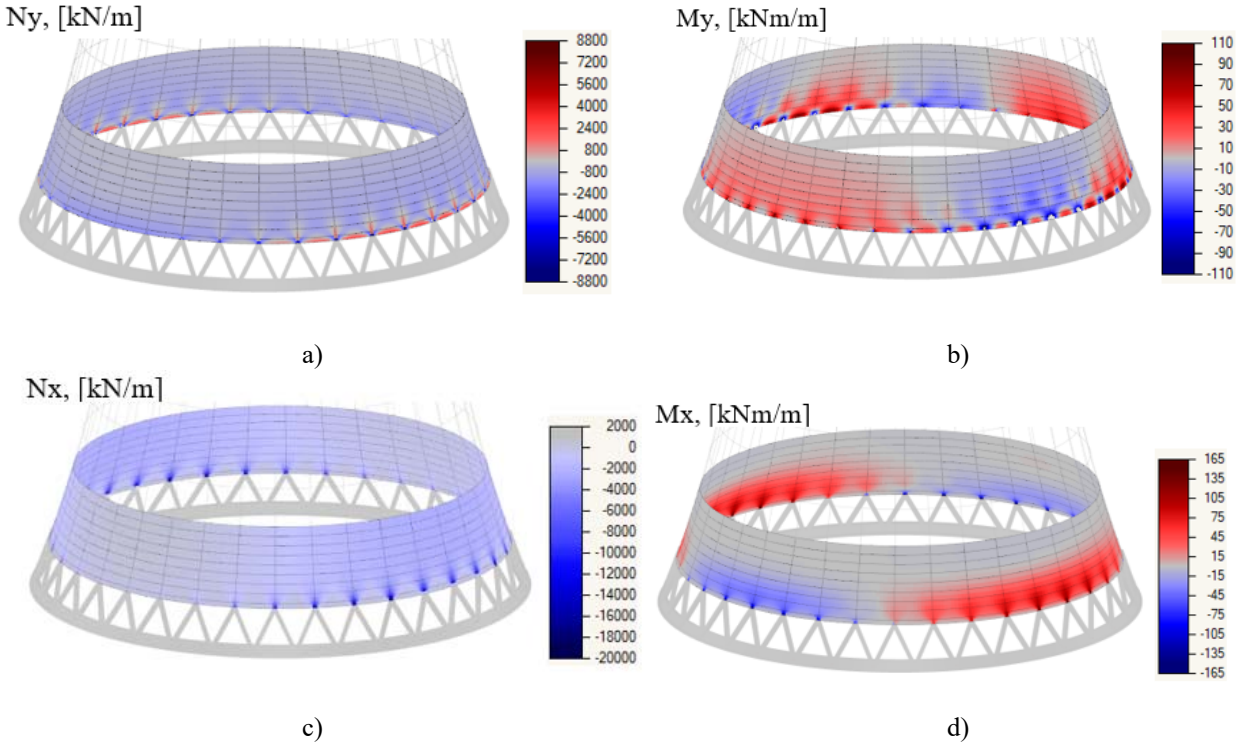

Fig. 8. Forces in the shell in the support region. a), c) Normal forces; b), d) bending moments.

3.3. Geometry influence on the magnitude of internal forces

The graphs below compare the relative change of internal forces for each region presented in Fig. 6. For each component and region, the relative change refers to the template model, the hyperboloidal chimney cooling tower in Opole Power Plant. The graphs shows the variation of force components with the parameter h in equation (3).

Axial forces – group 3

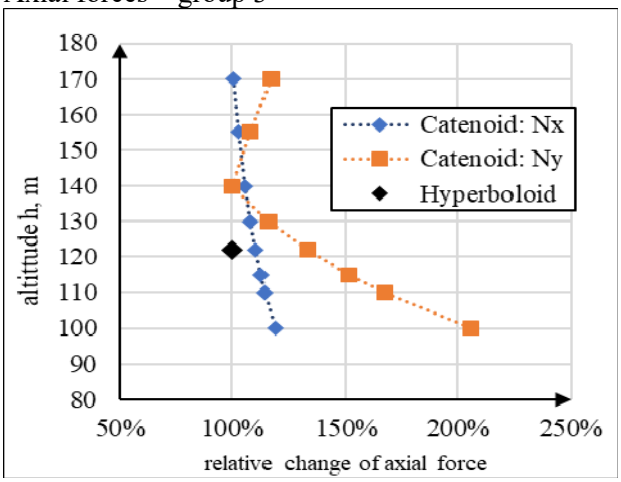

Bending moments – group 3

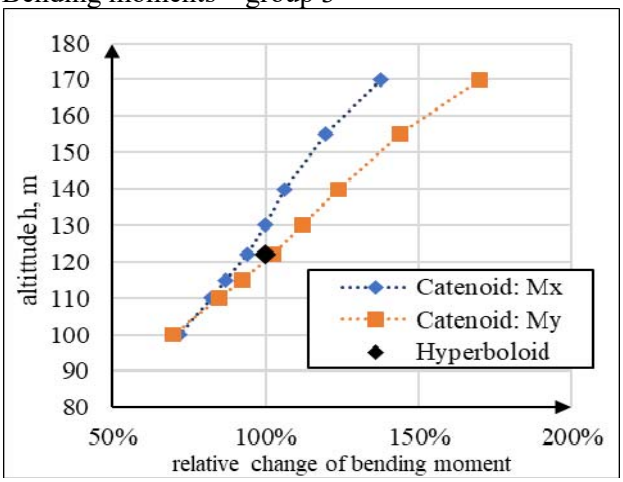

Axial forces – group 4

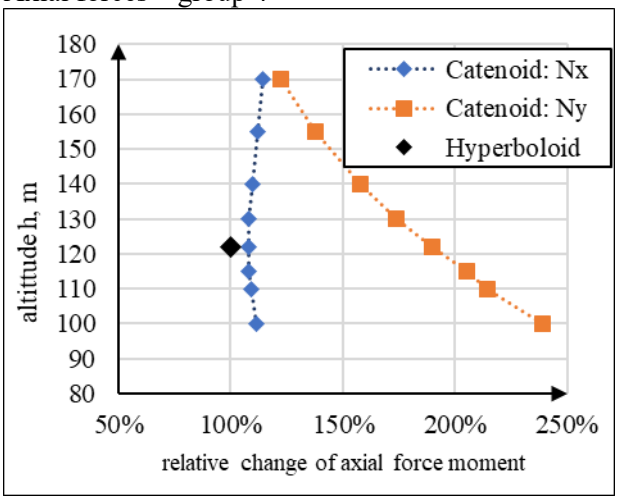

Bending moments – group 4

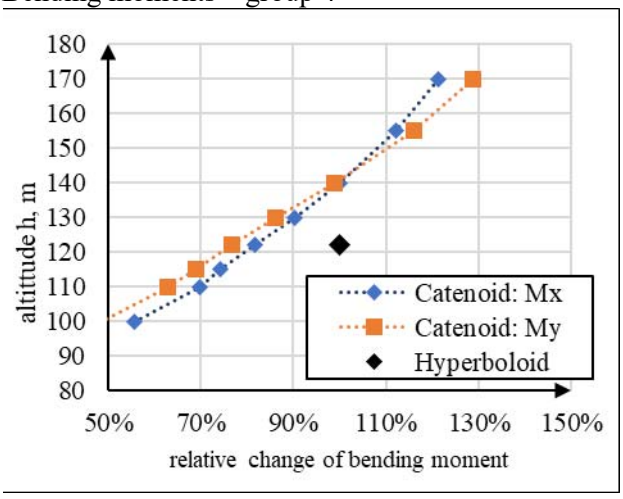

Axial forces – group 5

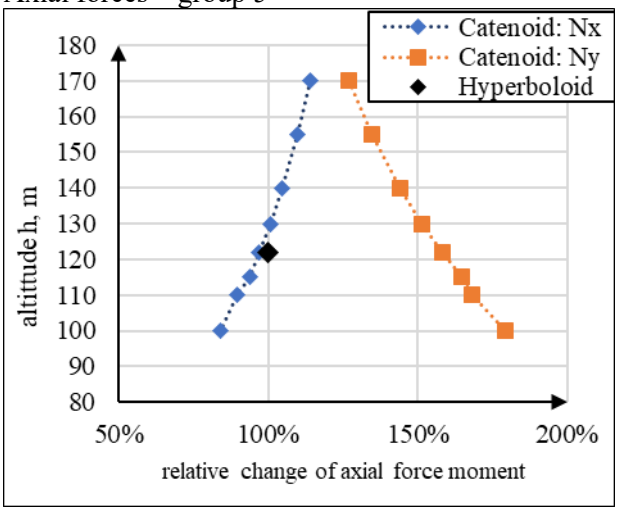

Bending moments – group 5

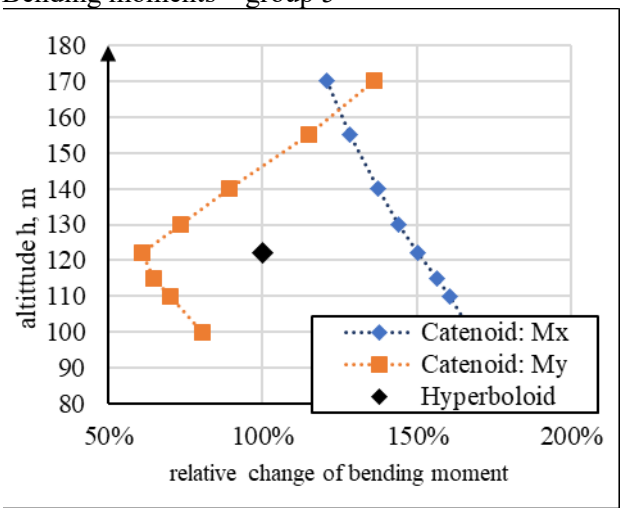

Fig. 3. Axial forces and bending moments in regions 2, 3 and 4.

It is not possible to find one common rule to determine which geometry generates the lowest internal forces. For example, in groups 3 and 4 the bending moments increase almost in direct proportion to the variable h, although in group 5 the radial moments achieve the local minimum for the parameter h≈120m. In the case of a thin concrete shell, high compressive forces are not a problem; however, it increases the risk of buckling. It

was also observed that catenoid (h≈120m) generates the smallest sum of reactions in the analysed load combination. Another observation is that the total deformation increases with parameter h.

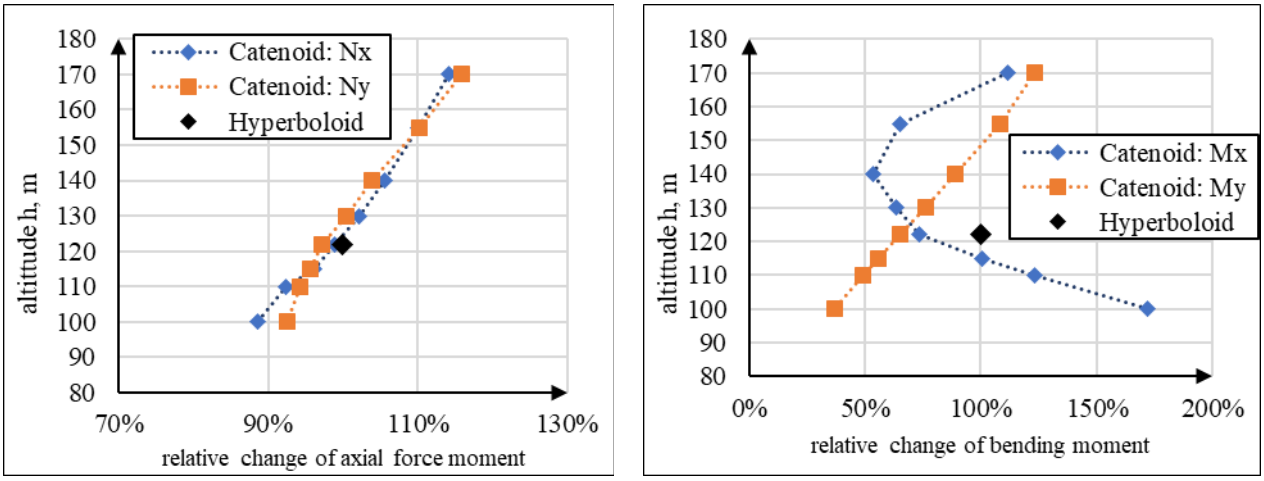

Fig. 4. Axial forces and bending moments in the lowst area - region 5.

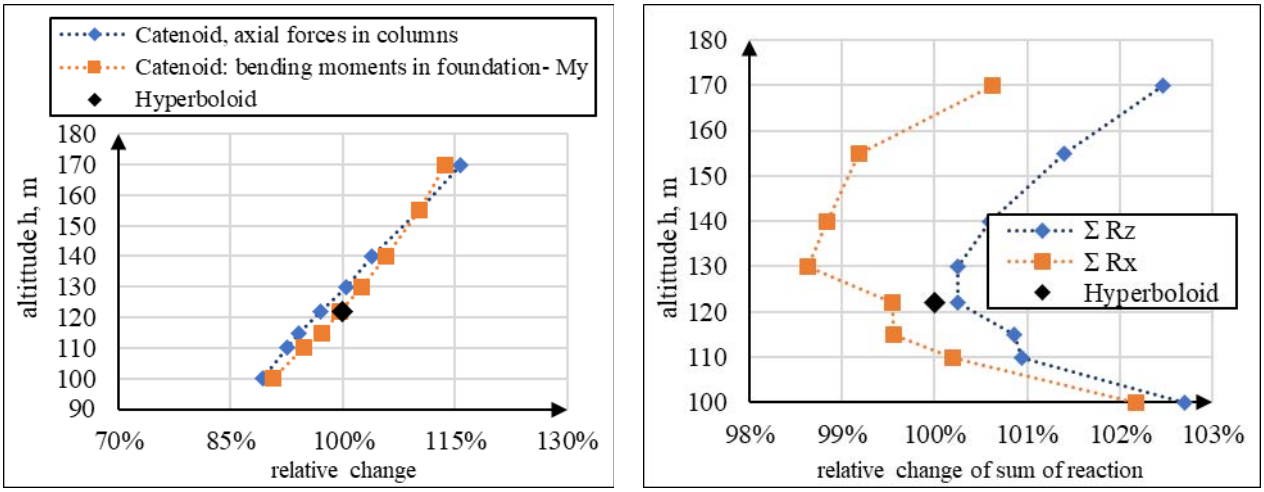

Fig. 5. a) axial forces in columns and bending moments in foundation beams,
b) sum of reaction: Z- vertical; X – along wind flow.

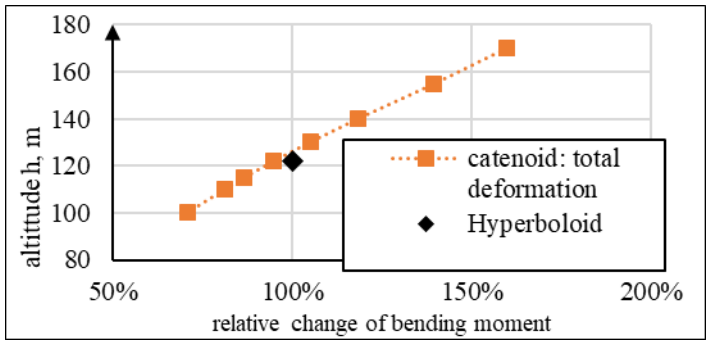

Fig. 6. Total deformation of the structure.

3.4. Stability

For thin structures, stability is often the most important limit state, which must be checked. For this reason, this paper also includes stability analysis using the eigenvector method. The values obtained from the critical load factor are presented in the graph below.

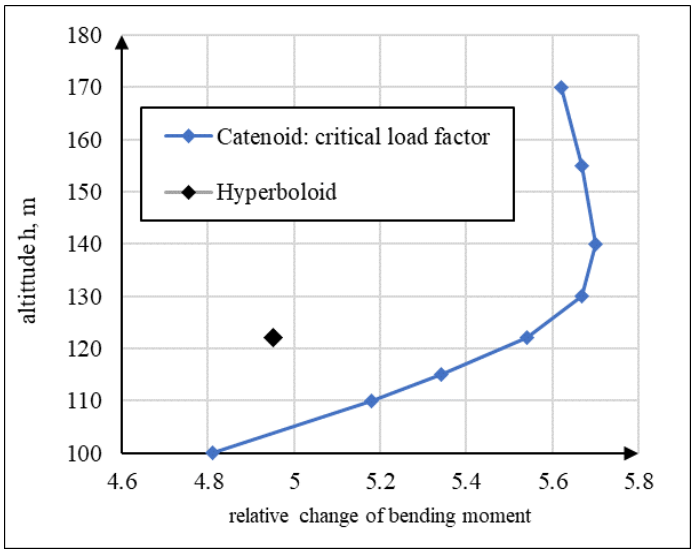

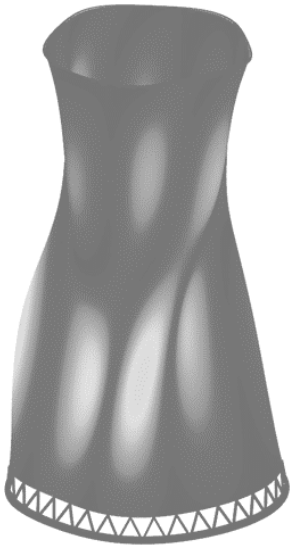

a) b)

Fig. 13. a) Total deformation and critical load factor ration, b) modal vector shape.

It should be mentioned that a higher value of factor f means that the structure is more stable. Values less than 1,0 mean that the structure is unstable. If the factor o critical load is greater than 10, the influence of buckling can be neglected according to Eurocode. The values obtained are between 4,8 and 5,7 for both – catenoid and hyperboloid. The observed change is slight, but stability is one of the most important factors in the design of thin-wall structures.

– For each analysis case, the critical load factor was at the safe level, but the influence of buckling should be considered in the design process.
– There is no huge difference between the hyperboloidal and catenoid structure.
– The highest value of the critical load factor has been obtained for the structure that had the thinnest point at altitude at 3/4 of the total height of the structure (h=3/4 H).

The results presented in the previous analysis showed that the highest critical load factor is obtained for a value h equal to 2/3H. However, in the previous analysis the wind load was obtained by analytical equations.

3.5. Natural vibration

The following study also compares natural vibrations. For each model, the first natural frequency of vibration (fn) was used for comparison. Natural frequencies do not depend on the load (Gromysz 2017), so absolute values are given in Table 1. Profound phenomenon analysis were performed in the thesis (Cornik 2020). Cooling towers are not exposed on dynamic technological loads; however, there may occur some dynamic wind action (Flaga, 2008). The potential vortex shedding for wind velocity 40m/s and diameter of tower 65m will oscillate with frequency approx. fo = 0,12Hz, which is much less than the frequency of natural vibration. However, more fn is different than fo, the dynamic amplification of wind load decreases. Catenoid has higher natural frequencies, so it seems to be more insusceptible on dynamic amplification of wind load than hyperboloid.

Table 2 – Natural vibration frequencies for chimney cooling towers.

Parameter	Frequency	
'h'	Catenoid	Hyperboloid
170	0.556	
155	0.625	
140	0.698	
130	0.699	
122	0.701	0,4951
115	0.693	
110	0.692	
100	0.714	
[m]	[Hz]	

Fig. 7 – First modal shape of natural vibration

4. CONCLUSION

The whole comparison shows some differences between the hyperboloid and catenoid structure. The catenoidal shell is stiffer than the hyperboloidal one. Thus, it has smaller deformations and better stability parameters; this indicates the possibility of creating larger cooling towers, which would also improve cooling performance. Calculation also showed the problem of huge sensitivity of result on assumed wind load distribution. It is very difficult to predict real wind load, because of the character of phenomena, so it should be analysed further. The authors will concentrate on the influence of other load cases that must be taken into account in the design of chimney cooling towers.

REFERENCES

Bielak, S., Walentyński R. 1993. *Powłoka katenoidalna - opis geometryczny, rozwiązanie ogólne umownego stanu błonowego i przykład dla osiowo-symetrycznego obciążenia ciężarem własnym*, Zesz. Nauk. WSI Opole, Bud., z. 36: 39-52.

Cornik, D. 2020. *Porównanie charakterystyk dynamicznych chłodni kominowych hiperboloidalnej i katenoidalnej.*

Eurocode 0: Basis of structural design. EN 1990:2002+A1 (2005)

Eurocode 1, Part 1-4: General actions - Wind actions. PN-EN 1991-1-4 (2005).

Flaga, A. 2008. *Inżynieria Wiatrowa. Podstawy i Zastosowania*. Arkady.

Gromysz, K. 2017. *Dynamika Budowli. Obliczanie układów prętowych o masach skupionych.* PWN.

Huihan, M., Zongyu, L., Shaozhen, L., Bingbing, S., Feng, F. 2018. *Stability analysis and performance comparison of large-scale hyperbolic steel cooling towers with different latticed shell systems*, Journal of Constructional Steel Research.

Ledwoń, J. 1967. *Chłodnie kominowe i wentylatorowe*. Arkady.

Padewska, A. 2015. *Determination of the interference coefficients of cylinders in rows arrangement*. Współczesny stan wiedzy w inżynierii lądowej.

Rahm, H. 2002. Fachgebiet Baustatik, Modellierung und Berechnung von Alterungsprozessen bei Stahlbeton-Flächentragwerken.

Rakowski, G., Kacprzyk, Z. 2005. *Metoda Elementów Skończonych w mechanice konstrukcji*. Warszawa: Oficyna Wydawcza Politechniki Warszawskiej.

VGB Standard, *Structural Design of Cooling Towers*, VGB-S610-00-2019-10-EN.

Wiśniowski, M. 2020. *Proposal application of catenoidal chimney cooling tower shell*.

Pokorska-Silva, I., Gromysz, K. *Współczesne Zagadnienia z Inżynierii Lądowej*: 347-35.

LIGHTWEIGHT STRUCTURES in CIVIL ENGINEERING
CONTEMPORARY PROBLEMS
Monograph from Scientific Seminar
Organized by Polish Chapters of
International Association for Shell and Spatial Structures
Łódź University of Technology
Faculty of Civil Engineering, Architecture
and Environmental Engineering
XXVII LSCE
Łódź, 2nd – 3rd of December 2021

INFLUENCE OF STEEL ROOF STRUCTURE RIGIDITY ON THE DISTRIBUTION OF INTERNAL FORCES IN LOAD-BEARING MULTI-SPAN TRAPEZOIDAL SHEET

M. Wiśniowski [1] **K. Kozieł** [2] **L. Rogoziński** [3]
[1] MSc, Faculty of Civil Engineering, Silesian University of Technology, POLAND, *mwwisniowski@polsl.pl*
[2] Optimal Design of Structures, POLAND, *krzysztof.koziel@ods-projekt.pl*
[3] Optimal Design of Structures, POLAND, *leszek.rogozinski@ods-projekt.pl*

ABSTRACT: In this paper results of the structural calculations of typical warehouse purlinless steel roof structure were presented. The objective of this research was to compare, currently most popular, approach to designing trapezoidal sheet based on 2D beam model on rigid supports with 3D modelling one, which takes into account stiffness of whole structural system. It was concluded that stiffness relations between roofing sheet and main structure may significantly influence the distribution of internal forces. This effect is usually omitted by structural designers.

Keywords: trapezoidal sheet, roofing sheet design, purlinless roof.

1. INTRODUCTION

There has been an outstanding increase in the newly built warehouse space in Poland in recent years; over 2 million m^2 in 2020 alone. Large warehouses are usually designed with similar column grid (12x24m). Girder trusses (12m long) are supported by reinforced concrete columns. Those girders support purlin trusses, oriented perpendicularly. Purlins are typically 22.5 or 24 meters long. On top of purlins a trapezoidal sheet is placed, most often multi-span. Roofing sheet acts as a roof bracing and provide out-of-plane buckling stability of top chord of the purlin truss.

Fig. 1. Typical warehouse – construction site.

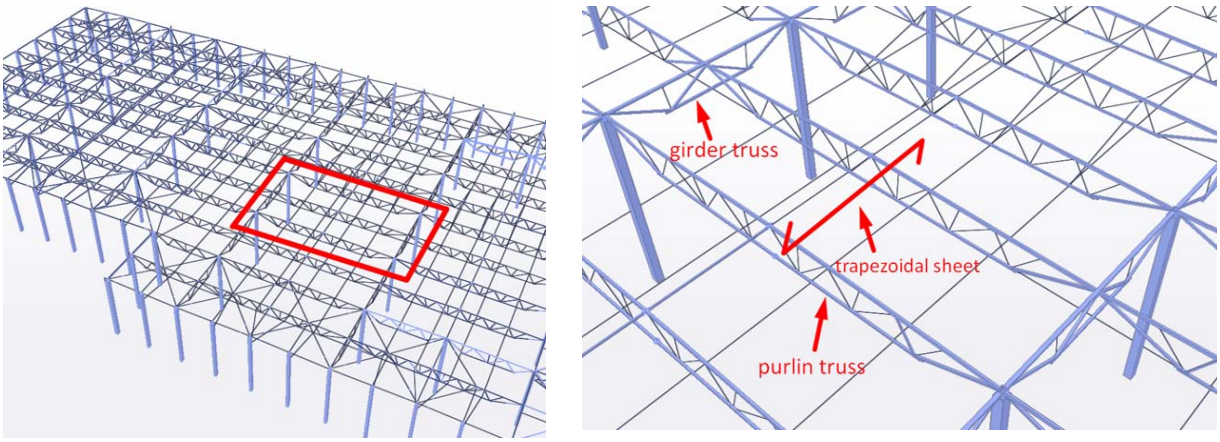

Fig. 2. Typical warehouse structural module.

Steel roofing sheet is usually designed using software programs provided by manufacturer, e.g. Blachy Pruszyński or Ruukki (Fig. 3). Static calculations are based on a simple model: a multi-span beam on rigid hinged supports. After determining internal forces distribution, critical span and support sections are verified via comparison with the sheet resistance, including interaction formulas for bending moment and shear force (at supports). This simplification is generally accepted in the industry. However, in case of structural layout of a warehouse show in Figure 2, stiffness of sheet support differs noticeably across the roof. It raises a question, whether the influence of this variable stiffness is negligible and may be safely omitted in calculations. In the following chapters this method is compared with a more advanced approach employing 3D modelling, thus taking into account stiffness of whole structural system. Resultant differences in internal forces distribution will be used to evaluate the severity of this phenomenon.

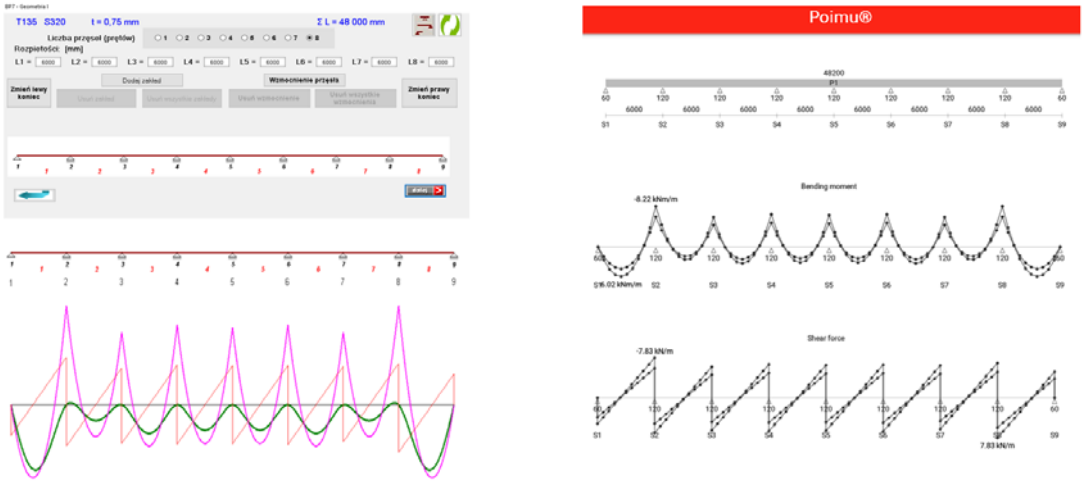

Fig. 3. Pruszyński and Ruukki Poimu design tools.

2. METHODOLOGY

2.1. FE model

Autodesk Robot Structural Analysis software was used to perform static calculations. Main structure was modelled with beam elements (reinforced concrete columns, girder trusses, purlin trusses). Orthotropic shell with parameters corresponding to sheet T135Px0.75mm (Fig. 6) was used in order to take into account stiffness of trapezoidal sheet. Trapezoidal sheet was connected to top chords of trusses using short beam elements. This approach allows to consider stiffness of fasteners and may be helpful in their design as well.

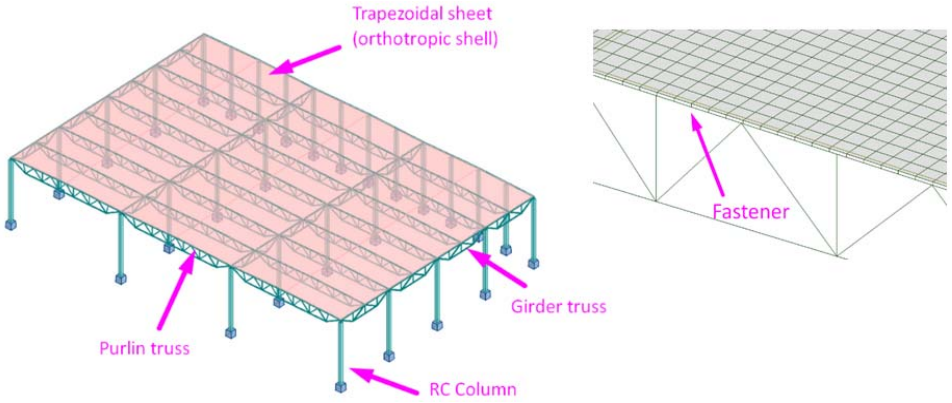

Fig. 4. FE model view.

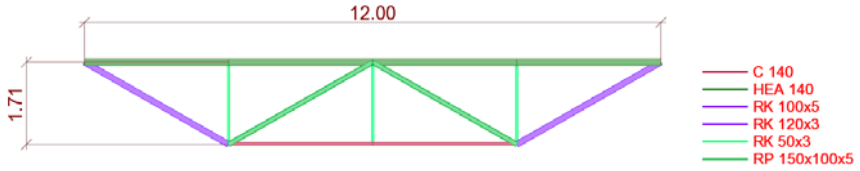

Fig. 5. Girder truss view.

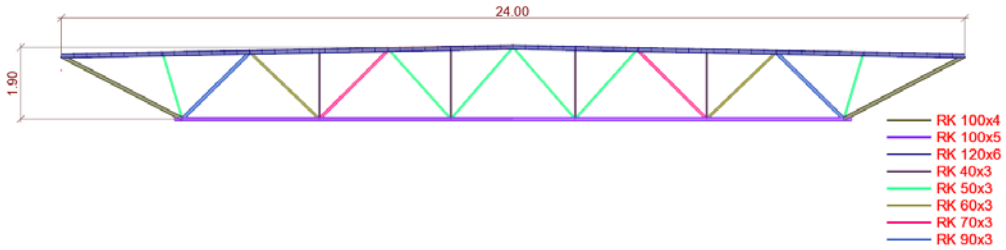

Fig. 6. Purin truss view.

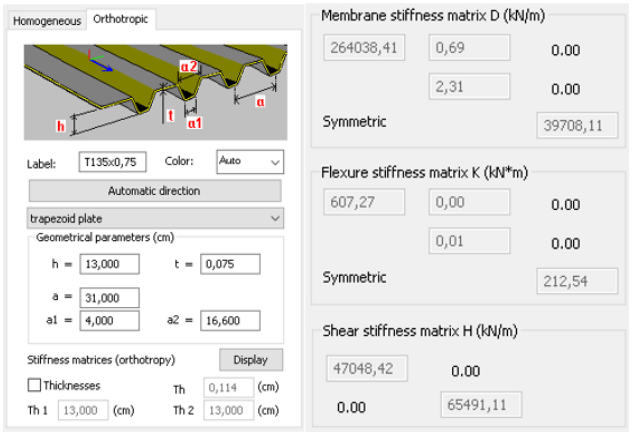

Fig. 6. Orthotropic shell parameters.

2.2. Trapezoidal sheet stiffness

Though it is known that as a Class 4 section trapezoidal sheet is subject to local instabilities and stiffness vary depending on stress state, the stiffness was assumed to be constant for the entire sheet for the sake of analysis. This simplification is based on literature (Bródka 1999). It is also supported by experimental and numerical tests performed by Szumigała (2021) showing force-displacement relationship for second generation trapezoidal sheet (Fig. 7). For the most part up to sheet bearing capacity the relationship is almost linear.

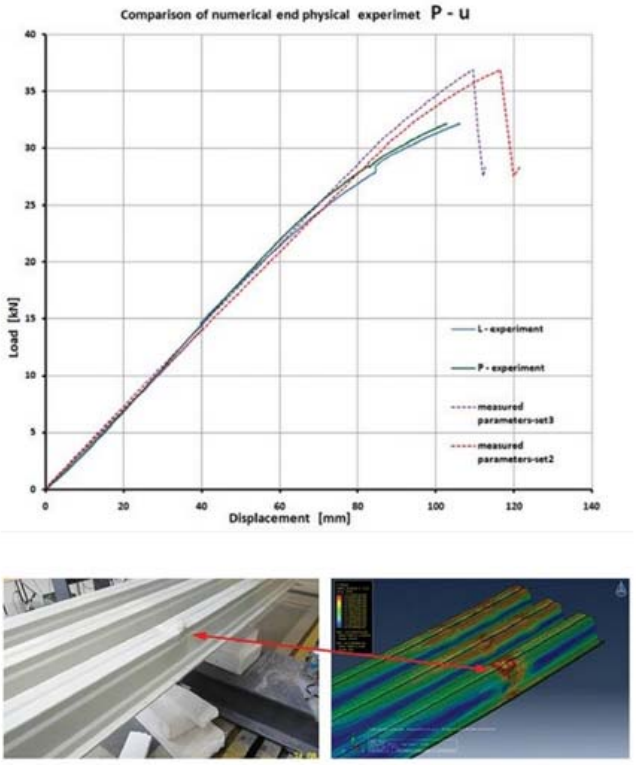

Fig. 7. Force-displacement relationship 2nd gen. sheet (Szumigała 2021).

However, to gain better understanding, additional numerical analysis was carried out. Equivalent moment of inertia of T135Px0.75mm sheet was determined using the geometrically and materially nonlinear analysis with imperfections analysis in Midas NFX software. Figure 8 shows the relation between applied bending moment and equivalent moment of inertia determined numerically. Bending stiffness of this profile turned out to be very stable within load range required for further analysis, thus results should not be affected by mentioned simplification.

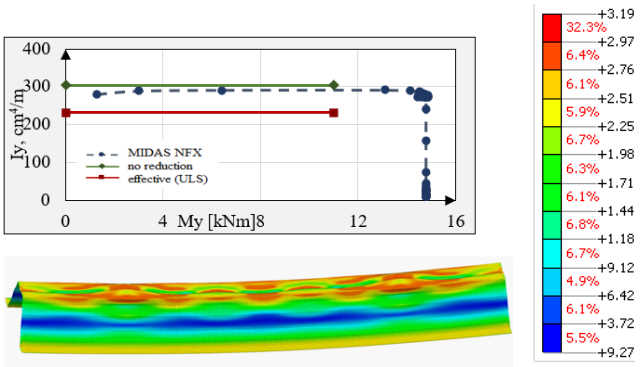

Fig. 8. Equivalent moment of inertia of the T135P profile.

2.3. Loads

Structure was loaded with a set of actions most common in Poland: snow load (zone II), wind load (zone I), self-weight, basic imposed loads.

It was decided that for the sake of analysis, to draw proper conclusions, it is enough to consider just one load combination: Ultimate Limit State (ULS) combination consisting of all loads acting downwards. In such scenario those loads sum up to 2.3 kN/m^2 of uniformly distributed load. Weight of the main structure was not

taken into account for comparison of deflections and internal forces in trapezoidal sheet, as roofing sheet is mounted to the main structure already deformed due to its self-weight.

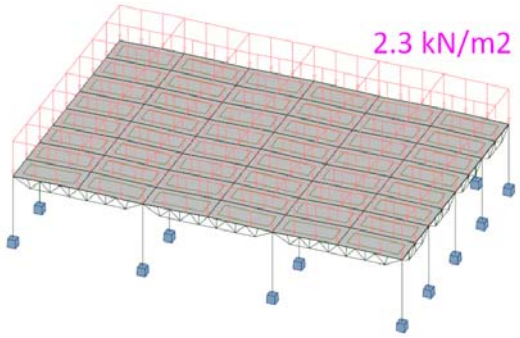

Fig. 9. Load combination.

3. RESULTS

Looking at the deformation of the structure (Fig. 10) it is clear that roofing sheet support stiffness varies significantly. As one may expect, the deflection is close to zero near columns and reaches its maximum in the middle of purlin truss (one that is supported by girder truss). It is caused by the fact that both girder and purlin deflect when loaded. It results in additional vertical displacement of about 3cm at every second support (in ULS), which is equal to the deflection of girders (Fig. 13). It should be also noted that one external wall (on the right hand side of Figure 10) provides much stiffer support due to smaller column spacing.

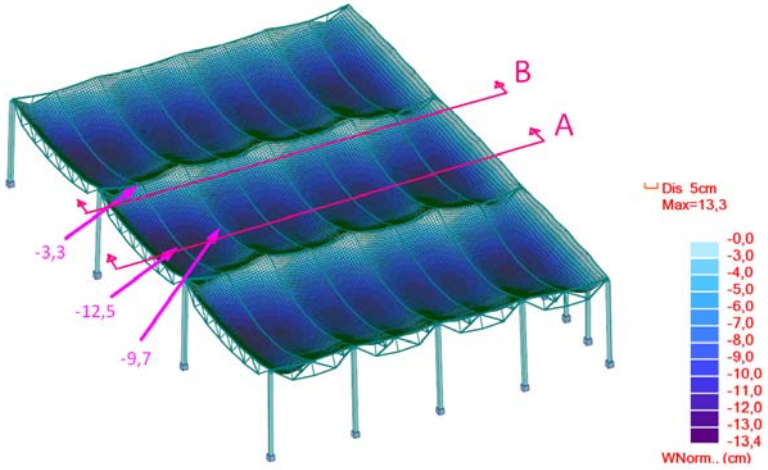

Fig. 10. Roofing sheet deflections [cm].

As a result, the differences in trapezoidal sheet deflection at supports can reach up to 13 cm globally. This leads to a distribution of internal forces in roofing sheet that is vastly different from the one obtained on rigid supports. Figure 11 and Figure 12 present the distribution of bending moments and shear forces. Internal forces, especially bending moment, concentrates at stiffer supports. Naturally, maximal value of support bending moment occurs where the columns are located.

The most interesting and quite unexpected observation is that according to continuous beam on rigid supports maximal bending moment should occur at second support, while this is not the case in 3D model. Much bigger values may be found at third support. It is caused by the fact that the purlin supported by girder deflects more easily and sheets naturally finds other ways to transfer the load, resting more on the stiffer supports, directly following stiffness distribution.

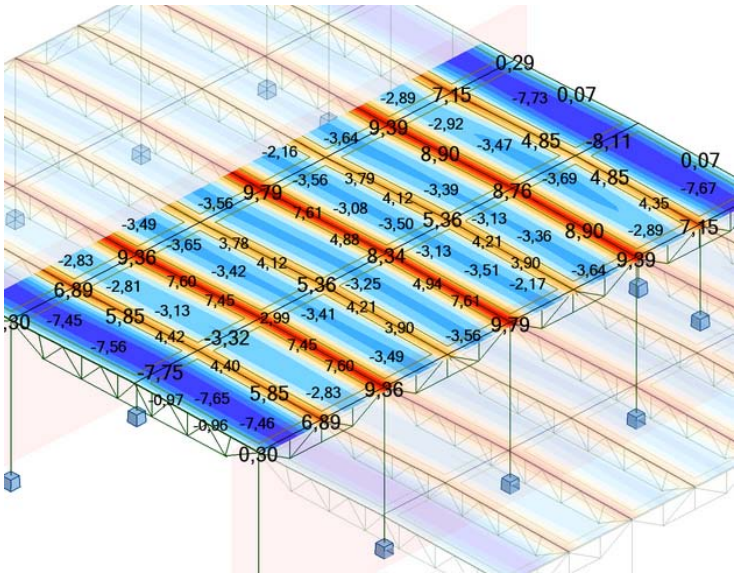

Fig. 11. Bending moments [kNm/m].

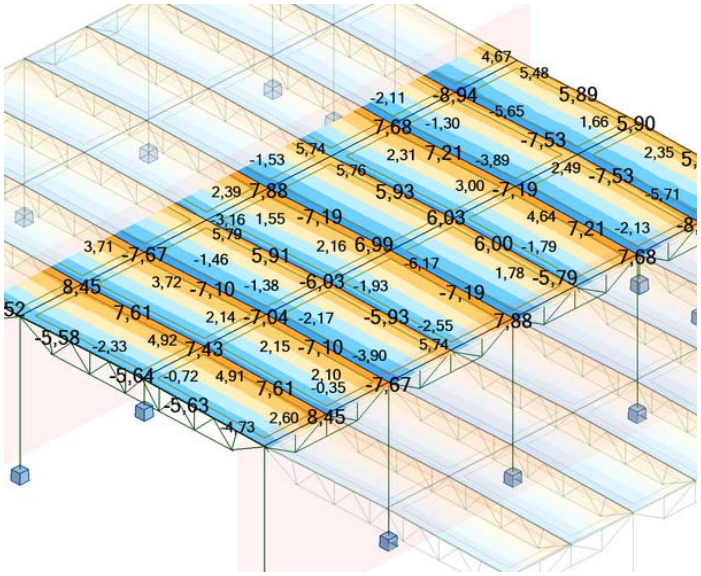

Fig. 12. Shear forces [kN/m].

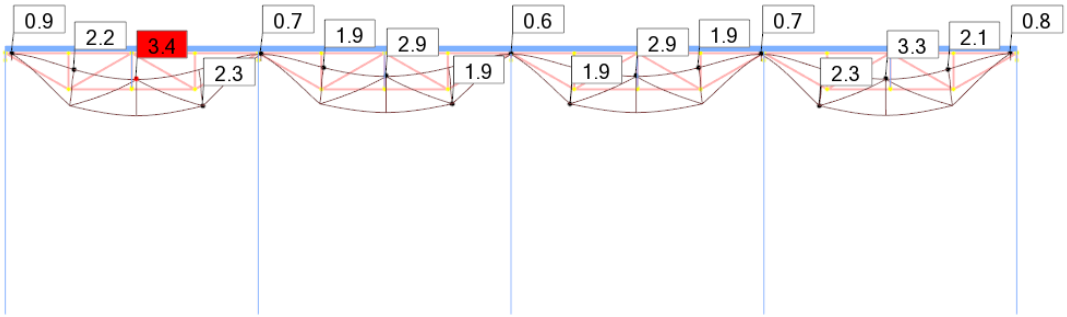

Fig. 13. Girder deflections (section A) [cm].

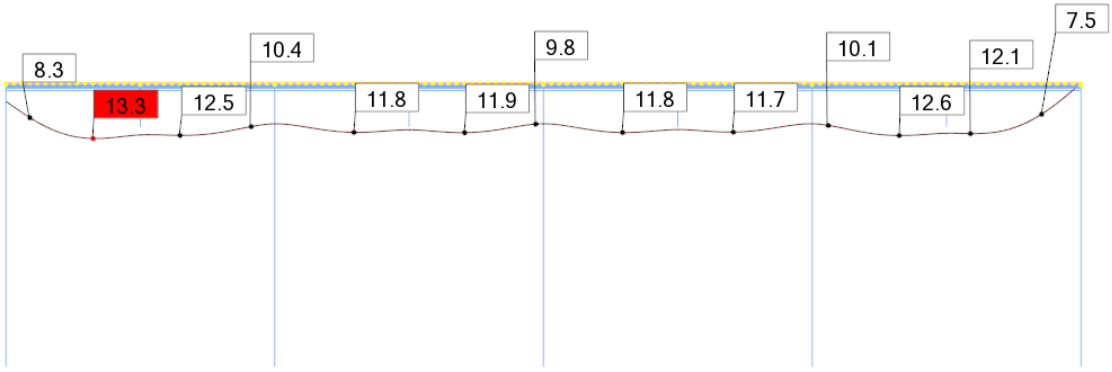

Fig. 14. Sheet deflection (section B) [cm].

3.1. Influence on trapezoidal sheet design

A section corresponding to maximal bending moment was selected in 3D model (Fig. 15 and 16). Internal forces were then compared with results obtained from 2D beam model. Differences in bending moment and shear force are presented in Tables 1- 2.

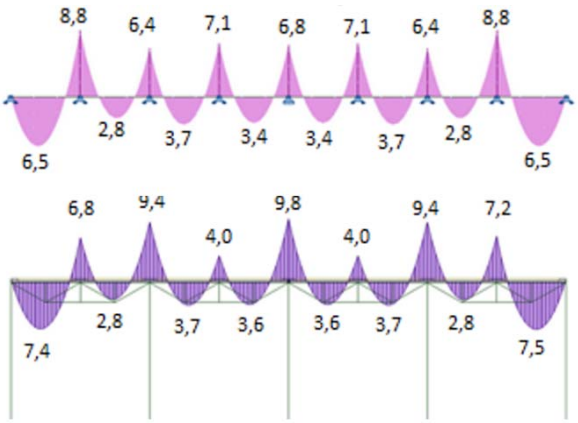

Fig. 15. Bending moments diagrams [kNm/m].

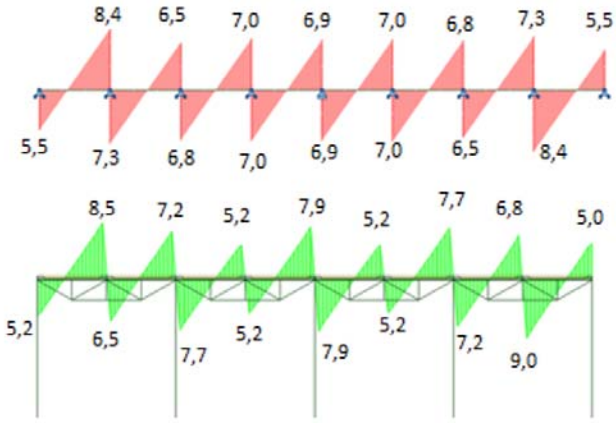

Fig. 16. Shear forces diagrams [kN/m].

Tab. 1. Bending moment comparison

Bending moment comparison [kNm/m]

Support/span No.	1-2	2	2-3	3	3-4	4	4-5	5	5-6	6	6-7	7	7-8	8	8-9
2D beam	6.5	8.8	2.8	6.4	3.7	7.1	3.4	6.8	3.4	7.1	3.7	6.4	2.8	8.8	6.5
3D model	7.4	6.8	2.8	9.4	3.7	4.0	3.6	9.8	3.6	4.0	3.7	9.4	2.8	7.2	7.5
difference [%]	14	-23	0	47	0	-44	6	44	6	-44	0	47	0	-18	15

Tab. 2. Shear forces comparison

Shear force comparison [kN/m]

	1	2	3	4	5	6	7	8	9
2D beam	5.5	15.7	13.3	14.0	13.8	14.0	13.3	15.7	5.5
3D model	5.2	15.0	14.9	10.4	15.8	10.4	14.9	15.8	5.0
difference [%]	-5	-4	12	-26	14	-26	12	1	-9

3.2. Influence on rest of the structure

Trapezoidal sheet is the main focus of this paper, but it should be mentioned that analysed phenomenon affects other structural elements as well. Traditionally cladding objects are used to distribute loading acting on the roof in 3D models. They distribute load equally on every purlin. In fact, girders supported directly by columns take up more load as they provide stiffer support for the trapezoidal sheet. As an example a comparison of axial forces in purling and girder are show in tables 3 and 4 when actual sheet stiffness is taken into account.

Tab. 3. Purlin axial force comparison

Axial force at mid-span [kN]

	Bottom chord	Top chord
Cladding	507.0	504.0
Orthotropic panel	558.0	517.0
difference [%]	+10.0	+2.5

Tab. 4. Girder axial force comparison

Axial force, midspan [kN]

	Bottom chord	Top chord
Cladding	575.0	284.0
Orthotropic panel	596.0	267.0
difference [%]	+3.7	+6.3

4. DISCUSSION

Presented results suggest, that designing load-bearing trapezoidal sheet as independent structural element based on traditional simple model: a multi-span beam on rigid hinged supports, may not be fully correct. The biggest differences can be noticed comparing values of bending moment. Taking into consideration maximal moments in analyzed approaches the difference may reach up to 11% (9.8 kNm/m against 8.8 kNm/m) at supports and 15% (7.5 kNm/m against 6.5 kNm/m) in the midspan. Therefore it is the traditional approach that poses a risk of underestimating design values.

What one may find a bit counterintuitive, maximal bending moment does not necessarily occur at second support. Typically strengthening overlap joint is made at second support, while there can be other place that should be strengthened instead.

In general, the more variety in rigidity of the supporting structure, the bigger differences in internal forces distribution should be expected compared to traditional approach. Obtained differences seem to be significant enough to conclude that current calculation method should be verified. What is more, it would be interesting to evaluate most popular warehouse structural layouts in terms of stiffness distribution and its influence on corrugated sheet and rest of the main structure as well.

REFERENCES

Bródka, J. 1999. *Blachy fałdowe w budownictwie stalowym*. Warszawa: Arkady

Czepiżak, D. 2006. *Nośność graniczna lokalnie wzmocnionych wieloprzęsłowych blach trapezowych.* Politechnika Wrocławska Instytut Budownictwa

Szumigała, T. 2021. *Experimental tests of second generation trapezoidal sheets.*

LIGHTWEIGHT STRUCTURES in CIVIL ENGINEERING
CONTEMPORARY PROBLEMS
Monograph from Scientific Seminar
Organized by Polish Chapters of
International Association for Shell and Spatial Structures
Łódź University of Technology
Faculty of Civil Engineering, Architecture
and Environmental Engineering
XXVII LSCE
Łódź, 2nd – 3rd of December 2021

OPTIMAL CABLE NET AS AN INITIAL STAGE OF DESIGN – FORCE DENSITY METHOD APPROACH

I. Wójcik-Grząba [1)]
[1)] Phd., Eng., Faculty of Civil Engineering, Warsaw University of Technology, POLAND,
izabela.grzaba@pw.edu.pl

ABSTRACT: The initial stage of design of cable nets is presented. Form-finding process is based on the Force Density Meth-od with some extensions. An optimal structure with minimal sum of cable lengths is regarded as a good starting point for adding self-weight and obtaining a real geometry and force distribution. On this basis cable sections can be proposed for the next stages of design. Iterative procedures for reaching optimal cable net and adding self-weight are presented. A few examples show how the optimal or partially optimal structure can be used to improve a cable net and achieve configuration under self-weight which is close to the optimal one.
A Scilab program called UC-Form developed by the author is used for this purpose.

Keywords: form-finding, force density method, cable net.

1. INTRODUCTION

Cable structures and especially cable nets are widely used for large span roofs since 1952 when Paraboleum (or Dorton Arena) by Maciej Nowicki was completed in Raleigh. Due to particular features these structures are considered as lightweight, economical, efficient and visually attractive. As cable elements work only in tension their cross-sections are fully utilized. High tensile strength of steel cables enables achieving large span of the structures without intermediate supports. Cable structures are characterized by low self-weight compared with traditional "rigid" structures and due to low material usage they can be considered as sustainable.
Many research have been done in the subject of form-finding, design, optimization, detailing and erecting cable structures since their behavior is much different from the "rigid" (beam-columns) ones. Particularly a form-finding stage is necessary because of the geometrical nonlinearity of cable structures (see e.g. Lewis 2003, Topping and Iványi 2007). It is impossible to impose the initial geometry which fulfills all the mechanical and architectural requirements due to the initial geometric instability and large displacements under different loads. Form-finding is usually performed in order to establish pretension forces in cables and also corresponding geometry of the structure. This configuration is then used in typical static and dynamic analyses. Properly pretensioned cable net ensures sufficient spatial stiffness and in such case adding self-weight should have negligibly small influence on the configuration (see Otto 1973). However using real cable sections, especially when they are quite large, can cause changes in tensile forces distribution. Therefore in this paper it is proposed to include cables self-weight in order to better estimate target sections on the basis of real force values. Moreover, for economical material use, it is suggested to find optimal

configuration in the first step. Such configuration of minimum weight can be subsequently used for adjusting initial lengths of cables to achieve geometry under prestress and self-weight which is possibly close to the optimal one.

2. THE BASICS OF THE FORCE DENSITY METHOD

The Force Density Method (FDM) proposed by Schek (1974) for form-finding of cable nets is the basis for calculation procedure presented in this paper. Due to his concept a cable net is a system consisting of straight, weightless truss elements connected with nodes. Selected nodes with coordinates $\bar{\boldsymbol{x}},\bar{\boldsymbol{y}},\bar{\boldsymbol{z}}$ can be fixed (anchored) and selected free nodes can be loaded with nodal forces $\boldsymbol{p}_{\mathrm{x}},\boldsymbol{p}_{\mathrm{y}},\boldsymbol{p}_{\boldsymbol{z}}$. A simple example of a cable net and its definition due to FDM is shown in Figure 1. The incidence matrix $\tilde{\boldsymbol{C}}=[\boldsymbol{C}\,\bar{\boldsymbol{C}}]$ defines the connections between elements as each column corresponds to one node and each row corresponds to one element. The numbers 1 and -1 indicate starting and ending node of a particular element. First part of incidence matrix $\boldsymbol{C}$ concerns free nodes and the rest of the columns forms submatrix $\bar{\boldsymbol{C}}$ regarding fixed nodes. Notation rule assumed for corresponding vectors and matrices is that the same letter in small version means a vertical vector and in capital version means a square matrix with the vector elements on a diagonal. For example element lengths can be defined as vector $\boldsymbol{l}$ or square matrix $\boldsymbol{L}$.

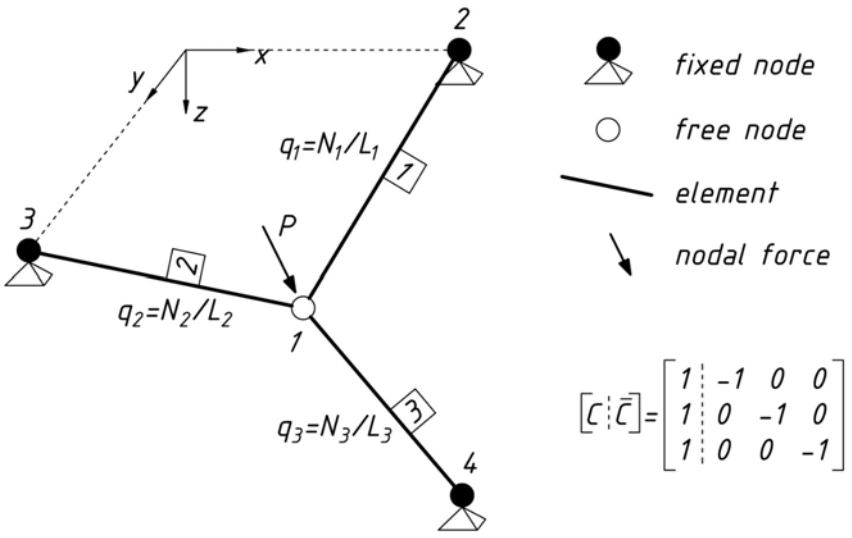

Fig. 1. Example of a cable net definition.

Free nodes coordinates $\boldsymbol{x}$, $\boldsymbol{y}$, $\boldsymbol{z}$ which are unknown can be found with the use of a system of nonlinear nodal equilibrium equations (1):

$$\begin{cases} \boldsymbol{C}^T\boldsymbol{X}_\Delta\boldsymbol{L}^{-1}n=\boldsymbol{p}_{\mathrm{x}} \\ \boldsymbol{C}^T\boldsymbol{Y}_\Delta\boldsymbol{L}^{-1}n=\boldsymbol{p}_{\mathrm{y}} \\ \boldsymbol{C}^T\boldsymbol{Z}_\Delta\boldsymbol{L}^{-1}n=\boldsymbol{p}_{\mathrm{z}} \end{cases}, \tag{1}$$

where $\boldsymbol{X}_\Delta,\boldsymbol{Y}_\Delta,\boldsymbol{Z}_\Delta$ are element length projections in *x*, *y* and *z* direction. In order to linearize the equations with regard to free nodes coordinates a concept of force density is introduced, which is a ratio between the element force and length:

$$\boldsymbol{q}=\boldsymbol{L}^{-1}\boldsymbol{n}. \tag{2}$$

By defining values of force density in each element it is possible to find the configuration and tensile force distribution of the whole cable structure. It means that each set of force densities corresponds to unique geometrical form which can be chosen as the initial one for design process. The FDM solution can be eventually written as:

$$\boldsymbol{x} = \boldsymbol{D}^{-1}\left(\boldsymbol{p}_{\mathrm{x}} - \bar{\boldsymbol{D}}\bar{\boldsymbol{x}}\right),\ \boldsymbol{y} = \boldsymbol{D}^{-1}\left(\boldsymbol{p}_{\mathrm{y}} - \bar{\boldsymbol{D}}\bar{\boldsymbol{y}}\right),\ \boldsymbol{z} = \boldsymbol{D}^{-1}\left(\boldsymbol{p}_{\mathrm{z}} - \bar{\boldsymbol{D}}\bar{\boldsymbol{z}}\right), \tag{3}$$

where auxiliary matrices are introduced: $\boldsymbol{D} = \boldsymbol{C}^T\boldsymbol{Q}\boldsymbol{C},\ \bar{\boldsymbol{D}} = \boldsymbol{C}^T\boldsymbol{Q}\bar{\boldsymbol{C}}$.

3. THE EXTENDED FORCE DENSITY METHOD

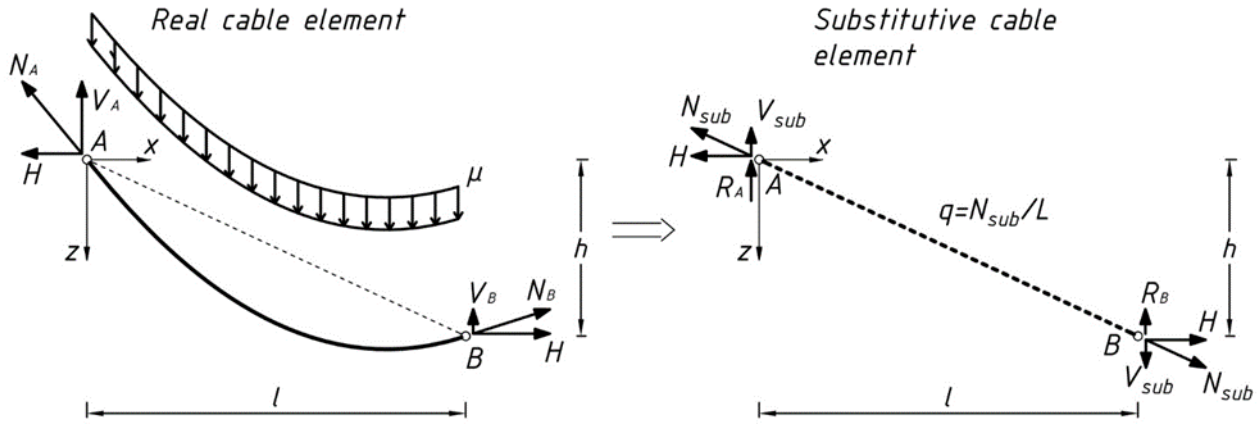

Fig. 2. The model of catenary cable element used in EFDM.

In the Extended Force Density Method (EFDM) Wójcik-Grząba (2021) enabled finding form and forces in cable nets under self-weight. As a result structures consisting of taut and slack elements can be modelled. Because the catenary cable element is introduced the results are close to real behavior and unlike the parabolic formulation, there are no limits regarding geometry. The main idea is to substitute a real catenary cable by statically equivalent straight element as it is demonstrated in Figure 2. It is loaded with constant N_{sub} tensile force which horizontal and vertical components are H and V_{sub} and with reaction forces from self-weight R_{A} and R_{B}. The proposed method modifies the original FDM in two steps. First of all nodal reactions from self-weight shown in Figure 2 as R_{A} and R_{B} and collected in vector $\boldsymbol{p}_{\mathrm{r}}$ are added to the external vertical loads:

$$\begin{cases} \boldsymbol{D}\boldsymbol{x} = \boldsymbol{p}_{\mathrm{x}} - \bar{\boldsymbol{D}}\bar{\boldsymbol{x}} \\ \boldsymbol{D}\boldsymbol{y} = \boldsymbol{p}_{\mathrm{y}} - \bar{\boldsymbol{D}}\bar{\boldsymbol{y}} \\ \boldsymbol{D}\boldsymbol{z} = \left(\boldsymbol{p}_{\mathrm{z}} + \boldsymbol{p}_{\mathrm{r}}\right) - \bar{\boldsymbol{D}}\bar{\boldsymbol{z}} \end{cases}. \tag{4}$$

Second part of modification requires iterative procedure of finding force densities corresponding to the final configuration. This can be achieved with the aid of equation (5) describing the catenary, linearly elastic cable element under self-weight (see Wójcik-Grząba 2021 for details):

$$g_{\mathrm{w}}(q) = -\frac{HL_0}{EA} - \frac{H}{\mu}\left[\operatorname{arsinh}\left(\frac{V_{\mathrm{A}}}{H}\right) + \operatorname{arsinh}\left(\frac{\mu L_0 - V_A}{H}\right)\right] + l = 0. \tag{5}$$

Here L_0 denotes for the initial cable length, EA is a longitudinal stiffness, μ is self-weight per meter and the rest of symbols are shown in Figure 1. The equation (5) contains a function of the force density because tensile force components V_A and H can be defined as it is shown below:

$$V_A(q) = qh + \mu L_0 - \frac{q^2 l}{\mu}[2\eta \sinh(2\eta - \zeta) - \cosh(2\eta - \zeta) + \cosh\zeta], \qquad H(q) = ql.$$

For the whole cable net we get the additional, nonlinear system of equations (6) which can be solved with the use of iterative Newton procedure.

$$\boldsymbol{g}_w(\boldsymbol{q}) = \boldsymbol{g}_w(\boldsymbol{x}(\boldsymbol{q}), \boldsymbol{y}(\boldsymbol{q}), \boldsymbol{z}(\boldsymbol{q}), \boldsymbol{q}) = 0. \tag{6}$$

Calculated force densities are then used to find the current nodal coordinates from the system of equations (4).

4. OPTIMIZATION PROBLEM

In order to find the optimal starting configuration of a cable net three basic problems of minimization were presented by Schek (1974). One of them which is minimization of the sum of cable lengths was also expanded by Dzierżanowski and Wójcik-Grząba (2020). It can be proved that solution of this problem with some additional assumptions is equivalent to the state of uniform stretch in the cable net.

The basic optimization problem is to find the minimum weight configuration which is equivalent to minimum volume problem. After assuming limit tensile stress σ_T and constant cross-section A_S along the S-th element we get a formula for overall volume of a cable net consisting of s elements:

$$N_S = A_S \sigma_T, \qquad V = \frac{1}{\sigma_T} \sum_{S=1,\ldots,s} N_S l_S. \tag{7}$$

Now making the supposition that a cable net of minimal weight (volume) is uniformly prestressed to the limit tensile stress σ_T the vector of tensile forces is defined as $\boldsymbol{n} = A_0 \sigma_T \mathbf{1}$, where A_0 is a cross-section area assumed for the specific level of tension. In such case the solution of minimization problem is shown below:

$$\hat{V} = A_0 \min \left\{ \sum_{S=1,\ldots,s} l_S(\boldsymbol{x}, \boldsymbol{y}, \boldsymbol{z}) \;\middle|\; \begin{array}{c} \boldsymbol{x}, \boldsymbol{y}, \boldsymbol{z} \in R^m \\ \text{and satisfies} \\ \text{equilibrium equations} \end{array} \right\}. \tag{8}$$

To prove this supposition a new, auxiliary functional is defined. It is a sum of square lengths with force densities as weights:

$$\wp(\boldsymbol{q}, \boldsymbol{x}, \boldsymbol{y}, \boldsymbol{z}) = \boldsymbol{l}^T \boldsymbol{Q} \boldsymbol{l}. \tag{9}$$

After defining the force density vector corresponding with uniform prestress state as $\hat{\boldsymbol{q}} = A_0 \sigma_T \boldsymbol{L}^{-1} \mathbf{1}$ we get a new form of the functional (9) shown below:

$$\frac{1}{\sigma_T} \wp(\hat{\boldsymbol{q}}, \boldsymbol{x}, \boldsymbol{y}, \boldsymbol{z}) = A_0 \boldsymbol{l}^T \boldsymbol{L}^{-1} \boldsymbol{l} = A_0 \sum_{S=1,\ldots,s} l_S(\boldsymbol{x}, \boldsymbol{y}, \boldsymbol{z}). \tag{10}$$

By minimizing (10) we get the same solution as in (8), what confirms our conjecture of uniform prestress state in minimum volume cable net. Some similarities can be found with minimal surfaces in which the uniform stress state is present. This is emphasized by Lewis (2003) who claims that tensile structures during exploitation would always tend to reach minimal surface shapes, therefore it is beneficial to assume their initial geometry possibly close to them. It is impossible to achieve the optimal shape under each load combination but it can be assumed in the state of pretension. A different kind of a cable net optimization is to find optimal shape under particular load case which was performed with the use of genetic algorithm by Thai et al. (2017) or by topology optimization by Sanders et al. (2020).
As it was proved in this chapter, finding the cable net with minimal sum of cable lengths can be achieved by imposing uniform tensile force distribution with no external loads. This can be done with the additional system of equations defining force values:

$$\boldsymbol{g}\left(\boldsymbol{q}^{*}\right)=\boldsymbol{n}^{*}-A_0\sigma_T\mathbf{1}=\boldsymbol{L}^{*}\boldsymbol{q}^{*}-A_0\sigma_T\mathbf{1}=0\,. \tag{11}$$

The asterisks are for the elements taking part in the optimization process as a cable net can be in particular case only partially optimized. The force density vector, which is a solution of this system, defines a new configuration of the optimal structure. It can be found by the iterative Newton procedure with the use of least square approximation for the case of partial optimization (underdetermined system of equations):

$$\boldsymbol{\Delta q}=\boldsymbol{G}^{+}\,\boldsymbol{b},\qquad \text{where: } \boldsymbol{G}^{+}=\boldsymbol{G}^{\boldsymbol{T}}\left(\boldsymbol{G}\boldsymbol{G}^{\boldsymbol{T}}\right)^{-1},\qquad \boldsymbol{G}=\left.\frac{\partial \boldsymbol{g}}{\partial \boldsymbol{q}}\right|_{\boldsymbol{q}=\boldsymbol{q}_{(\boldsymbol{n}-1)}},\qquad \boldsymbol{b}=-\boldsymbol{g}\left(\boldsymbol{q}_{(\boldsymbol{n}-1)}\right).. \tag{12}$$

5. CALCULATION PROCEDURE

In order to find a cable net configuration under self-weight close to the optimal one the Extended Force Density Method is used. For verification, accuracy tests and recommended values of initial parameters of the method see Wójcik-Grząba (2021) and also PhD thesis of the author (2019).
Configuration of a cable net under self-weight is usually slightly different from the optimal one but assuming proper initial lengths of elastic elements is crucial in finding good agreement between them. Different options of calculations available in the Extended Force Density Method are utilized sequentially in the procedure pointed below:
(0. find a starting configuration);
1. assume tensile forces in the part or in the whole structure;
2. find optimal configuration in uniform prestress state;
3. read the current element lengths;
4. calculate the initial element lengths assuming linearly elastic material;
5. assume cable sections which design value of tension resistance exceeds the tensile force with a margin for live loads;
6. find a new configuration of a cable net under self-weight with initial element lengths and cable sections as assumed above.

Usually the initial step of calculations is needed when the optimal solution cannot be achieved (step 0). In order to find a starting configuration a basic form-finding procedure without additional conditions can be performed. Usually force density values from 0,1 to 1 kN/m in all the elements are proper to get the initial solution which can be a basis for subsequent analyses.
The calculations are executed with the use of the self-developed program UC-Form written in Scilab package. For more information concerning the program algorithm and simple instruction manual see PhD thesis of the author (2019). Geometrical input data is defined in the MS Excel auxiliary file. This approach is

very convenient for editing and in the case of using coordinates from other programs or analyses. The calculations can be performed according to three different paths:
1. form-finding without self-weight;
2. form-finding without self-weight and with additional constraints (here: imposing tensile force values);
3. form-finding with self-weight.

After obtaining a new configuration of a cable net the program creates and displays an interactive window with the current view which can be shifted, rotated and zoomed. All the information about current configuration of the cable net can be displayed in Scilab console and some of them can be switched on or off in the figure when needed.

6. EXAMPLES

6.1. Introduction

A few examples of open and closed cable nets are analyzed with the use of Extended Force Density Method. First the analysis with the uniform tensile force distribution is performed to check if there exists an optimal solution for the whole structure. For some particular forms of cable nets it is not always possible to find it or the achieved form is unsuitable from the esthetic point of view. In other cases the optimal solution can be achieved for the whole structure or for the chosen part of it. In the latter situation such analysis can be helpful to improve the geometry by refining the net. A simple form-finding analysis with assumed force density values can give the auxiliary information about the forces distribution. It can be used to identify areas of similar force values and then perform partial optimization. In such case different cable sections should be assumed in different areas.
After achieving optimal or partially optimal configuration of the structure calculated lengths l_{opt} of elements are used in the stage of adding self-weight. For this purpose elastic elongation should be obtained and subtracted from the calculated lengths l_{opt} as it is shown below:

$$l_0 = l_{opt} - \frac{N l_{opt}}{EA}. \tag{13}$$

It is crucial to define proper initial (unstretched) lengths in order to achieve the pretension level close to the optimal one. Along with the assumed section data the lengths are the input for the analysis with self-weight. As a result we achieve the real configuration and force distribution in the prestressed cable net under self-weight which is a good starting point for adding live loads and performing remaining phases of design process. Then cable sections can be verified in order to guarantee a proper margin of tension resistance.

6.2. Closed cable net outspread on two parabolic arches

In the first example a closed cable net outspread on two parabolic arches with rectangular cables layout is analyzed. After assuming forces equal to 100 kN in each cable we get the optimal configuration shown from two different angles in Figure 3:

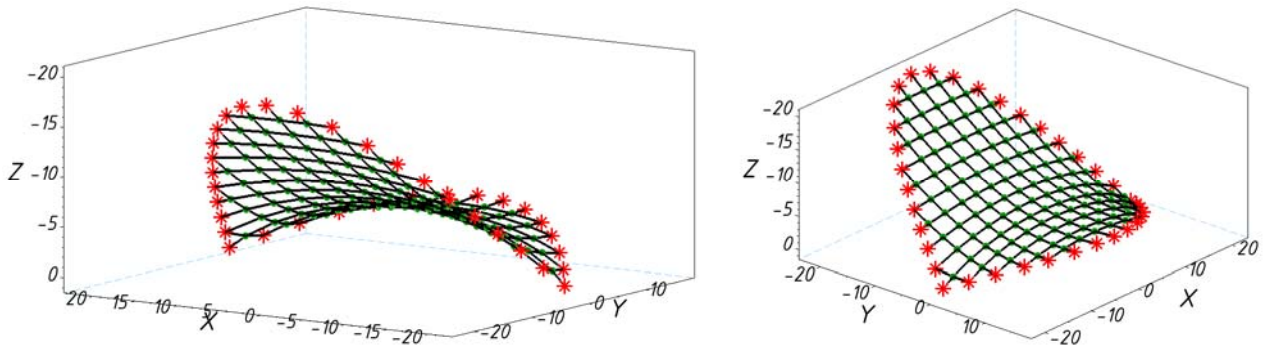

Fig. 3. Optimal configuration of a closed cable net from two different angles.

In order to find a configuration under self-weight close to optimal one the initial lengths of elements are calculated from the optimal ones according to formula (13). A spiral strand wire rope of 16mm diameter is assumed with design tensile load 154 kN, tensile stiffness EA = 27000 kN and self-weight μ = 1,26 kg/m. Achieved configuration is close to the optimal one which can be seen in Figure 4 where the central axis profiles are shown.

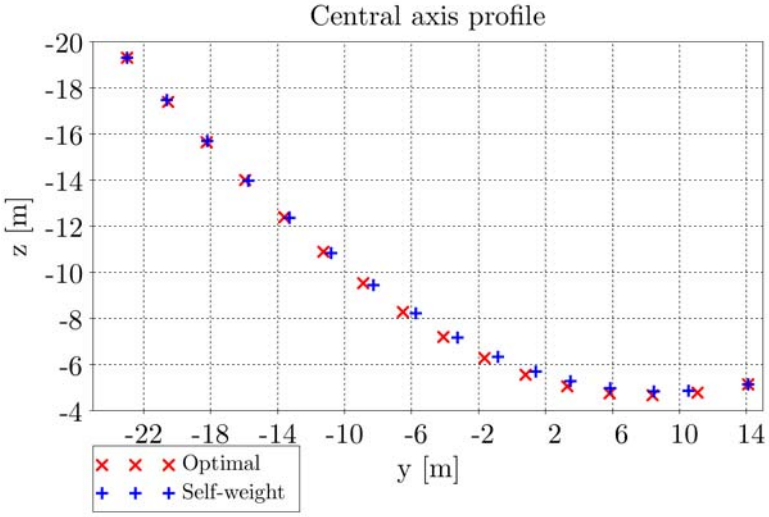

Fig. 4. Central axis profiles of optimal and under self-weight cable net.

The values of forces, force densities and sums of lengths are summarized in the Table 1 and are very close in both versions. It means that achieved configuration under self-weight can be considered as the optimal initial configuration for subsequent analyses.

Tab. 1. Comparison of optimal and under self-weight versions of closed cable net

Configuration	N_{min}	N_{max}	q_{min}	q_{max}	Σl_S
	kN	kN	kN/m	kN/m	m
Optimal	99,999	100,001	23,018	66,116	753,767
Self-weight	99,562	101,570	22,956	65,825	753,767

6.3. Open cable net outspread on two parabolic arches

In this example a similar cable net is analyzed but some of the supports were removed and substituted by the new edge cables. This type of a cable net is called open. Here only inner cables will be optimized because edge cables usually have to be highly prestressed in order to achieve possibly large area covered by the roof. It is assumed that forces in the inner cables are equal to 100 kN. Three different versions of edge cables prestress are compared. In the first case shown in Figure 5 initial force density values are the same in the whole cable net and equals to 35 kN/m. Force distribution is shown with the use of colormap.

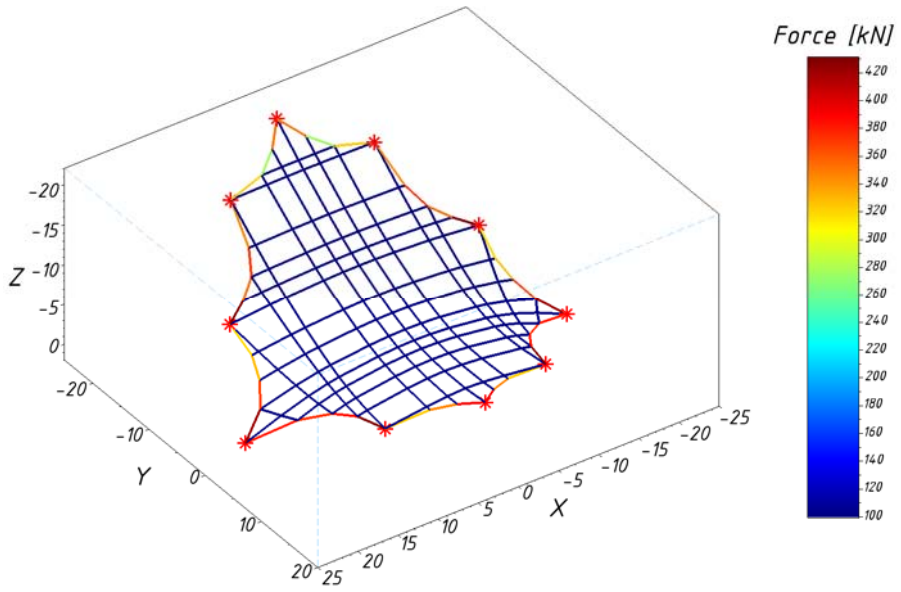

Fig. 5. Optimal configuration and force distribution in the first prestress version.

In the second version initial force densities in the edge cables are 350 kN/m and in inner cables 35 kN/m. The optimal configuration is shown in Figure 6 along with tensile force distribution.

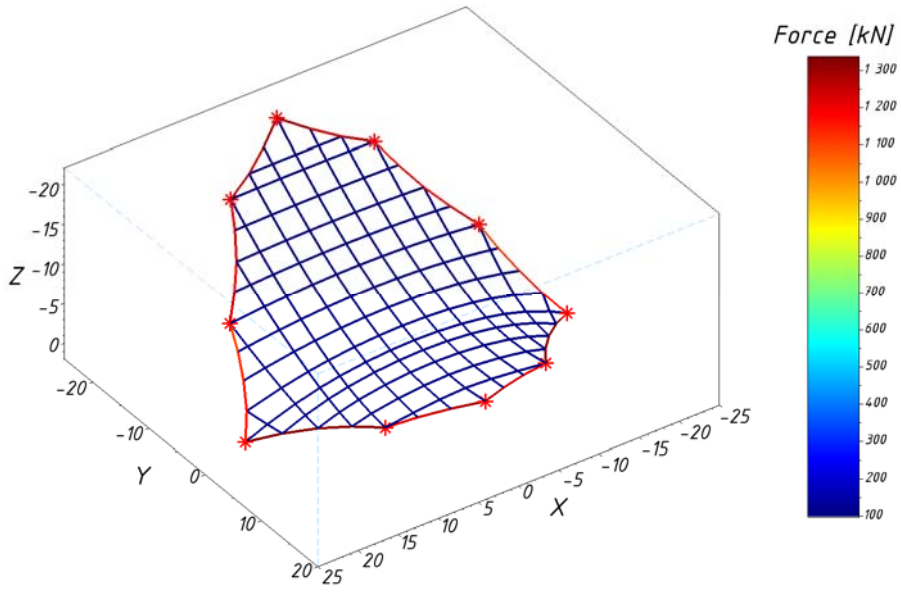

Fig. 6. Optimal configuration and force distribution in the second prestress version.

The last version of optimal open cable net is calculated for 3500 kN/m initial force densities in the edge cables and 35 kN/m in the inner cables. Figure 7 clearly shows the highest prestress in edge cables and also the largest area covered by the net.

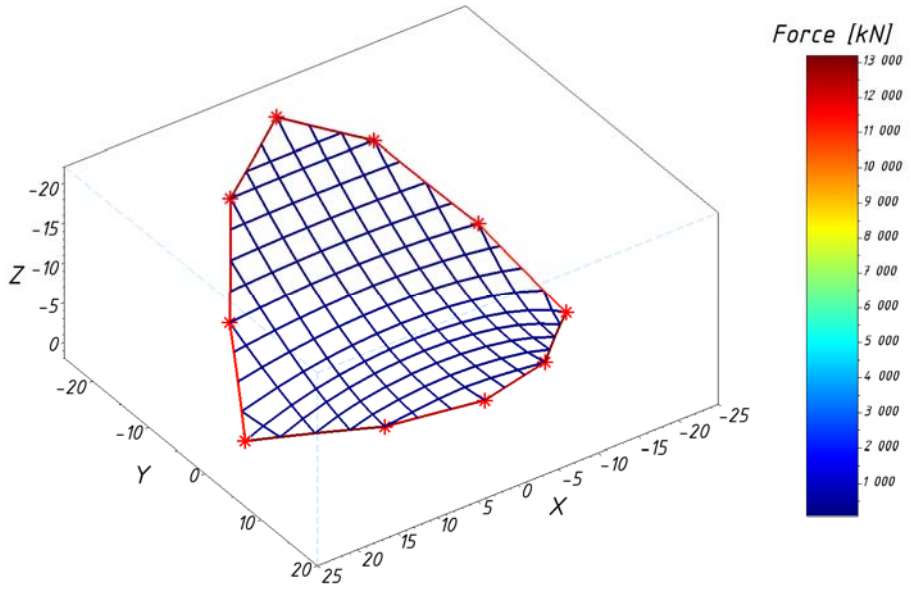

Fig. 7. Optimal configuration and force distribution in the third prestress version.

In this example it is clear that comparing sums of element lengths is inappropriate because the boundary conditions for inner cables change with different prestress of edge cables. The main advantage here is achieving uniform tensile forces distribution in inner cables.

Because of the moderate prestress values in edge cables the second version was chosen as a basis for the analysis under self-weight. The optimal element lengths were used to calculate initial lengths with the use of the formula (13). A spiral strand wire rope of 16 mm diameter is assumed for inner cables and 50 mm diameter with design tensile load 1460 kN, tensile stiffness EA = 242000 kN and self-weight μ = 11,90 kg/m for edge cables. Figure 8 shows the comparison of symmetry axis profile in all versions which are very similar.

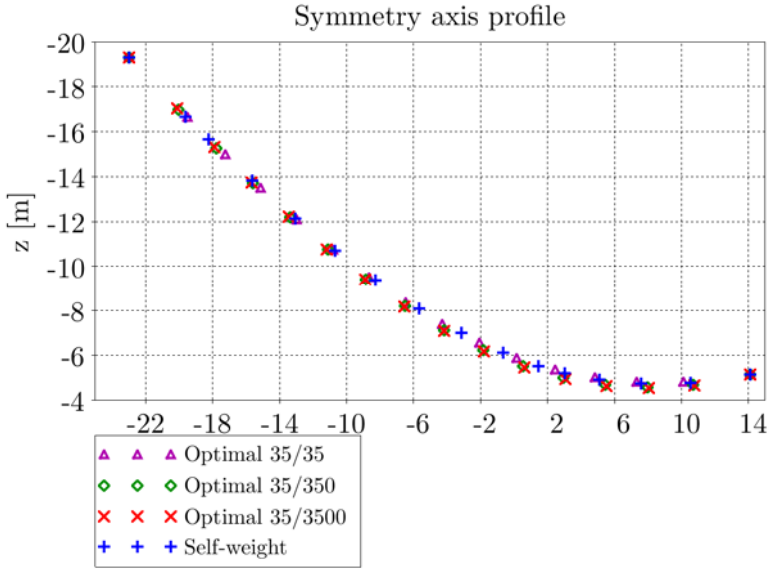

Fig. 8. Central axis profiles of three optimal and under self-weight cable nets.

Additionally Table 2 summarizes values of forces, force densities and sums of lengths in all versions. Values achieved in the second optimal version and under self-weight are very close to each other so this configuration can be considered as initial for subsequent stages of design process.

Tab. 2. Comparison of three optimal and under self-weight versions of open cable net

Configuration	Inner		Edge		Inner		Edge		Inner
	N_{min}	N_{max}	N_{min}	N_{max}	q_{min}	q_{max}	q_{min}	q_{max}	Σl_S
	kN	kN	kN	kN	kN/m	kN/m	kN/m	kN/m	m
Opt 35/35	99,996	100,002	277,773	430,997	18,630	126,817	62,007	142,365	687,434
Opt 35/350	100,000	100,000	1089,258	1336,808	23,390	107,608	338,541	357,608	723,504
Opt 35/3500	99,994	100,001	11172,842	13180,027	22,676	85,758	3499,379	3500,382	737,423
Self-weight	99,052	102,038	1092,973	1341,191	23,277	108,479	339,643	359,370	723,507

6.4. Hexagonal open cable net

The last example concerns the open, hexagonal cable net with supports on different ordinates. In this case only inner elements will be optimized. Figure 9 shows the auxiliary initial configuration and Figure 10 tensile force distribution in this configuration.

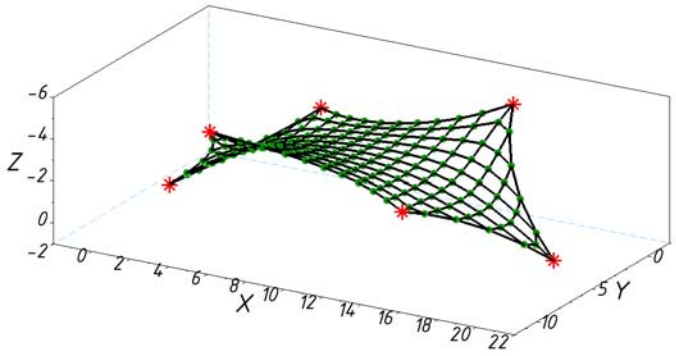

Fig. 9. Initial, auxiliary configuration of the hexagonal cable net.

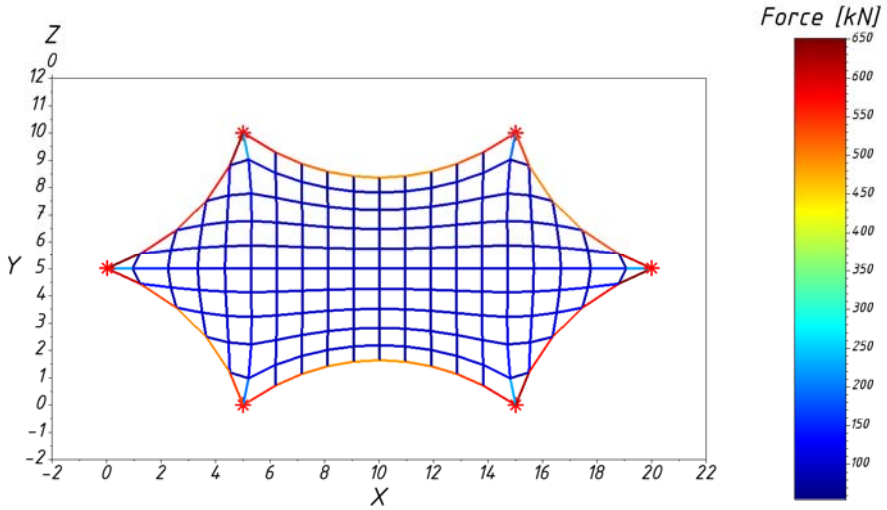

Fig. 10. Tensile force distribution in auxiliary configuration of the hexagonal cable net.

After assuming tensile forces equal to 50 kN in all the inner elements the partially optimal configuration is achieved – edge cables are not optimized. Tensile force distribution is shown in Figure 11 and extreme values of forces in inner and edge cables are compared in Table 3 for both analyzed configurations.

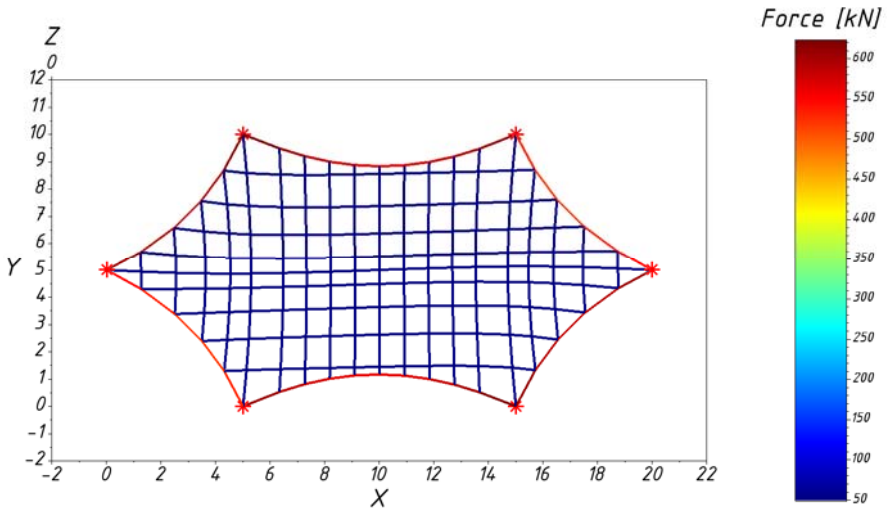

Fig. 11. Tensile force distribution in partially optimal configuration of the hexagonal cable net.

Tab. 3. Comparison of initial and optimal versions of hexagonal cable net

Configuration	Inner		Edge	
	N_{min}	N_{max}	N_{min}	N_{max}
	kN	kN	kN	kN
Initial	55,560	231,451	482,645	650,315
Optimal	50,000	50,000	515,892	622,450

In the initial configuration difference between minimum and maximum value of tensile forces in inner cables is significant. After optimization it is possible to choose only one cross-section for the whole inner part. Also differences in force values in edge cables are slightly lower than in the initial version.

7. CONCLUSIONS

In this paper the algorithm for the initial stage of cable nets design is proposed. It allows for finding close to optimal configuration under self-weight which is a good starting point for subsequent static and dynamic analyses. Exact geometry and tensile force distribution are obtained thanks to the catenary element formulation. Imposing uniform prestress in the whole cable net leads to the minimum volume configuration. In the case of partial optimization (e.g. in open cable nets) the minimum volume is not always desirable condition because the area covered by the roof can be also minimized. In such situation proper prestress level in edge cables and optimization performed for only inner cables can yield the best solution from the usable and economical point of view. Initial cable lengths for analysis under self-weight can be defined on the basis of optimal configuration. It was proved by the results from three different examples that this approach leads to obtaining the solution close enough to the optimal one. Solution presented here enriches purely geometrical approach of the Force Density Method with the elastic properties of cables, uniform force distribution and self-weight of real cable cross-sections.

ACKNOWLEDGEMENT

The author acknowledges the financial support for this research provided by the Dean's Grant for postgraduate students and young scientists at the Faculty of Civil Engineering, Warsaw University of Technology.

REFERENCES

Dzierżanowski, G. & Wójcik-Grząba, I. 2020. *Optimal form-finding of cable systems.* Archives of Civil Engineering LXVI(3): 305-321.

Lewis, W. 2003. *Tension structures. Form and behaviour.* London: Thomas Telford.

Otto, F. 1973. *Tensile structures.* Cambridge: MIT Press.

Sanders, E. D., Ramos Jr., A. S., Paulino G. H. 2020. *Topology optimization of tension-only cable nets under finite deformations.* Structural and Multidisciplinary Optimization 62: 559-579.

Schek, H.-J. 1974. *The Force Density Method for form finding and computation of general networks.* Computer Methods in Applied Mechanics and Engineering 3: 115-134.

Thai, S., Kim, N.-I., Lee, J., Kang, J.-W. 2017. *Optimum design of cable nets by using genetic algorithm.* International Journal of Steel Structures 17(3): 1183-1198.

Topping B. H. V., Iványi P.: *Computer Aided Design of Cable Membrane Structures*. Saxe-Coburg Publications, Glasgow, 2007.

Wójcik-Grząba, I. 2021. *Extended Force Density Method for cable nets under self-weight. Part I – Theory and verification.* Archives of Civil Engineering LXVII(4): 139-157.

Wójcik-Grząba, I. 2019: *Numeryczne kształtowanie konstrukcji przekryć cięgnowych*. PhD thesis, Faculty of Civil Engineering, Warsaw University of Technology, 2019.

LIGHTWEIGHT STRUCTURES in CIVIL ENGINEERING
CONTEMPORARY PROBLEMS
Monograph from Scientific Seminar
Organized by Polish Chapters of
International Association for Shell and Spatial Structures
Łódź University of Technology
Faculty of Civil Engineering, Architecture
and Environmental Engineering
XXVII LSCE
Łódź, 2nd – 3rd of December 2021

THE IMPACT OF FOOTING CONDITIONS OF A VERTICAL-AXIS FLOATING-ROOF TANK ON STRUCTURAL SHELL DEFORMATION

K. Żyliński [1] **J. Górski** [2]
[1] Faculty of Civil and Environmental Engineering, Gdańsk University of Technology, POLAND
zylinskikamil@gmail.com
[2] Faculty of Civil and Environmental Engineering, Gdańsk University of Technology, POLAND,
jgorski@pg.edu.pl

ABSTRACT: Structural shells of fuel tanks are often subjected to geometric imperfections which may lead to exceeding the ultimate and serviceability limit states. One of the means triggering shell deformation is non-uniform settlement caused by incoherent soil conditions. Analysis carried out in the work concerns of vertical-axis, floating-roof cylindrical shell which volume is 50.000 m^3, founded on a complex multi-layered soil. The sensitivity analysis was conducted of a tank settlement due to variation of material soil parameters and the strata layout. It reads that even in the case of extremely disadvantageous material data the structure is not bound to exceed the serviceability limit states.

Keywords: storage tanks, foundation settlement, subsoil parameters, sensitivity analysis.

1. INTRODUCTION

Fuel tank design should be considered as a highest-standard task due to possible environmental pollution in case of possible structural failure. The FE models are bound to exceed the standards of deterministic analysis of perfect structures, to consider the issues of geometric and material imperfections, post-welding stresses (Rasiulis et al. 2006) etc. Reliability analysis may be employed to assess structural degradation due to corrosion (Geary and Hobbs 2013). In selected cases footing conditions should be regarded while they may lead to limit state exceedance (Grget et al. 2018, Gunerathne et al. 2018, Ignatowicz and Hotala 2020, Nassernia and Showkati 2020). The attempts of structural optimization are denoted too (Magnucki et al. 2006). Basics of structural sensitivity analysis are based i.e.: on (Kleiber and Hisada 1993, Kowalczyk and Kleiber, 1999).

The paper analyses the fuel tank of a vertical axis, with a floating roof. Scope of calculation is restricted to the estimation of the impact of diverse soil conditions to the tank shell deformation. The impact of geometric and material imperfections is neglected, the interaction of tank footing is investigated only. Non-uniform settlement may produce excessive tank deformation and stress increase, subsequently, operational obstacles e.g. by floating roof locking (Kaczor and Sygulski 2006). The in-situ experimental results make it possible to realistically reflect complex soil conditions. The computations are limited to sensitivity analysis of the tank shell to the variation of foundation conditions. The work incorporates the procedures addressed in (Żyliński et al. 2021, 2020).

2. OUTLOOK ON A FUEL TANK WITH A FLOATING ROOF

The work analyses a vertical-axis cylindrical fuel tank (Fig. 1) of a 50000 m^3 volume, designed according to the EN 14015 standard (hoop stress criterion). The shell stability due to extreme wind pressure according to the standard EN 1993-4-1 and considering local action was checked numerically in the light of EN 1993-1-6. Wind cover shell was also designed in the case of failure and leakage of the stored medium. This additional structural element was not considered in the computations. The design assumes the S355J2 steel for the structure. The tank diameter is 60.5 m, its height is 22.0 m. Fig. 1 presents the tank model and the information on sheet thicknesses in meters. All the computations were performed in the ZSoil environment [Commend et. al] combined with Python aided modules.

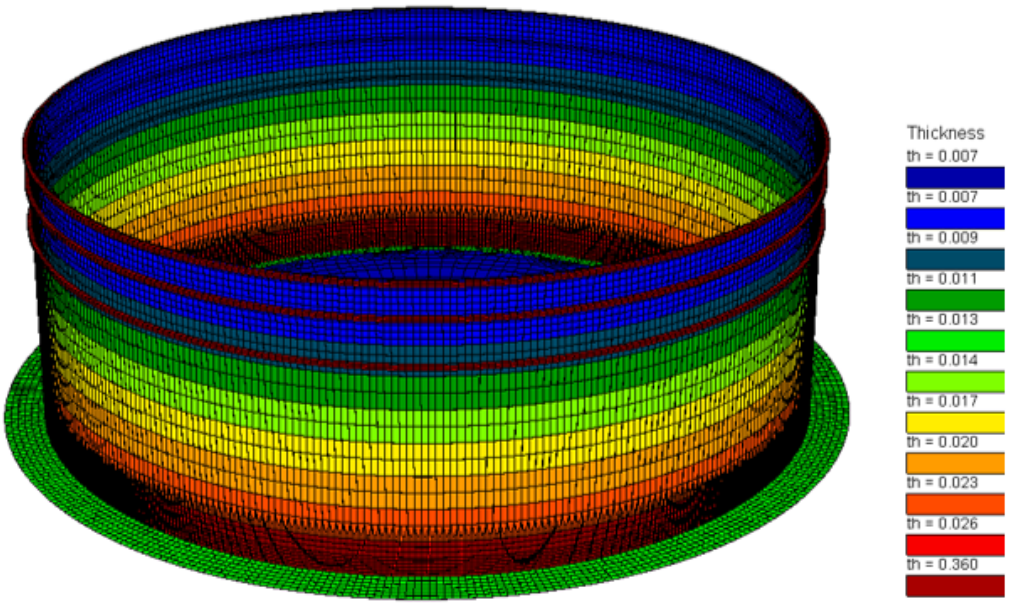

Fig. 1. The tank overview, regarding variable shell thickness (ZSoil).

In addition, Table 1 shows the sheet thicknesses due to standards, t_{ini}, and the effective ones, reduced by corrosion, t_{efect}. Table 1 also presents the data on heights of distinct courses and their location.

Tab. 1. The heights and thicknesses of distinct sections of the tank

No.	t_{init} [mm]	t_{efect} [mm]	h [m]	$h_{overall}$ [m]
9	11	7,5	2,25	2,25
8	11	7,5	2,25	4,50
7	12	8,5	2,25	6,75
6	15	11,4	2,50	9,25
5	18	14,4	2,50	11,75
4	21	17,4	2,50	14,25
3	24	20,4	2,50	16,75
2	27	23,2	2,50	19,25
1	30	26,2	2,75	22,00

The numerical model incorporates the reduced sheet thicknesses t_{efect}, hence the computations reflect the structure in its occupation. Moreover, reducing the structural stiffness made an indirect impact of some means: initial imperfections, sheet fabrication tolerances, post-welding stresses and other means which are hard to detect. The wind cover plates thicknesses were not included in Table 1. while this structural part was

not analyzed. Second shell weight was assumed in the form of a nodal load of 12.04 kN. The mean Young's modulus E = 210 GPa and the mean Poisson's ratio ν = 0.3 were taken for the analysis. The corner ring was designed in the form of a panel 0.36 m thick to reflect the minimum stiffness required by the standard EN 14015, it was fixed 0.25 m below the shell top edge.

The sub-foundation region was discretized by eight-node 3D elements whose parameters represent the structural parts, i.e.: ring foundation, sand ballast and relevant soil strata. The foundation strip was modelled as a RC element whose dimensions are 4.05×3.0 m (Fig. 2).

The transfer of friction forces between the sheet, the soil and the concrete foundation strip was considered by the so-called contact introduced to the model. The functions are applied corresponding to the friction coefficients based on the PN-82/B-02003 standard, i.e.: $\mu = 0.3$.

The soil regions of the footing subjected to sensitivity analysis are presented in Fig. 2b in orange, green and pink. The elements marked in yellow between the strip and the external area correspond to the soil parameters in the tank vicinity E = 128 MPa. The stiffness modulus of concrete mixed with sand (marked in greenish) is denoted by a value E = 130 MPa, because this is not the concrete made on the building site by mixing cement with aggregate.

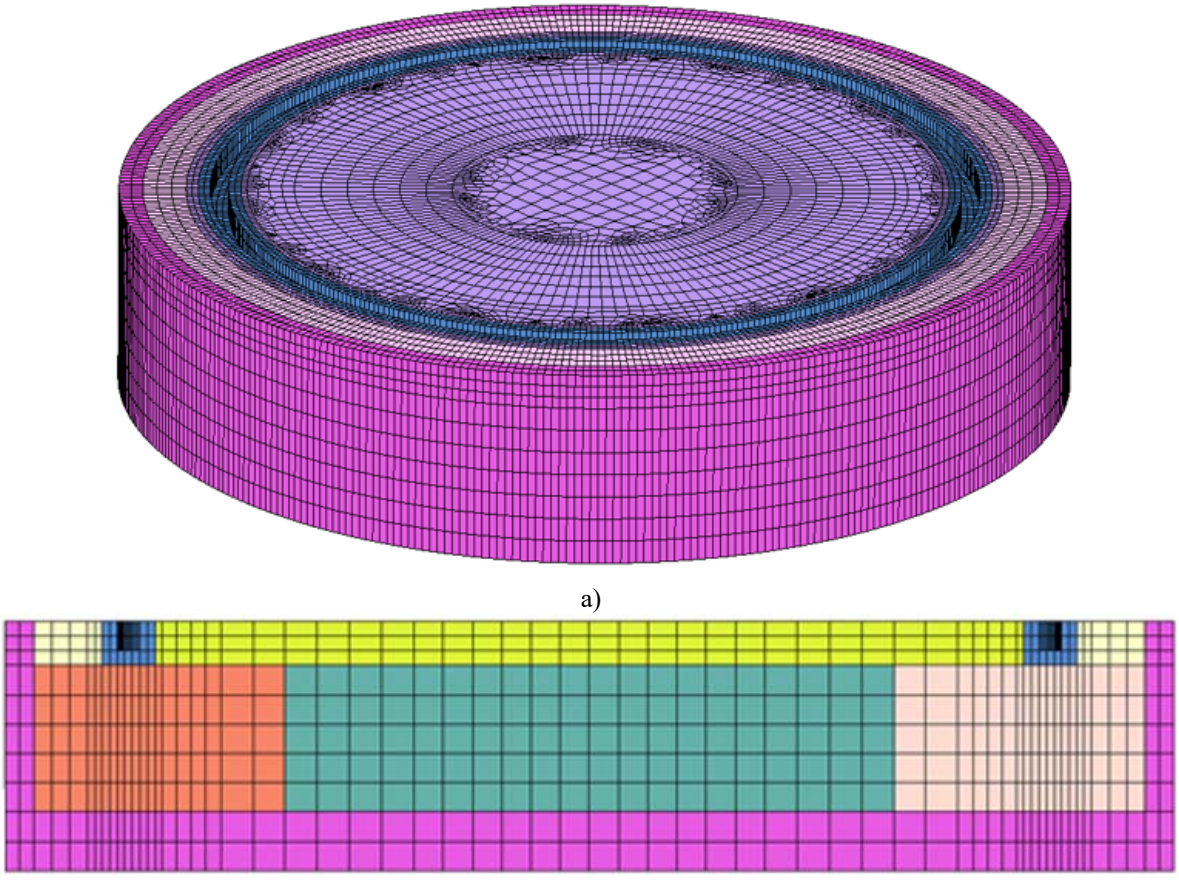

a)

b)

Fig. 2. Three-dimensional overview of a tank a) foundation section, b) subsoil section.

The boundary elements of the subsoil (marked in violet, Fig. 2) form a layer whose effective Young's modulus is E = 50 MPa. The numerical values are bound to consider the deformation impact of an infinite zone. The reduced stiffness of the elements surrounding the computational domain allows to minimize the boundary conditions effect by non-controlled vertical deformation caused by fixed horizontal edges of adjacent elements.

The soil strata layout based on the drillings are displayed in Fig. 3, their parameters are collected in Table 2. Due to Young's moduli diversity the area beneath the tank is divided into five regions of variable stiffness, marked *KZ*. The sensitivity analysis incorporates elastic subsoil model employing mean Young's moduli of each region, included in Table 2.

According to the design the tank is filled in with a liquid up to the level of 19.6 m from the bottom, yielding operational hydrostatic pressure. The computations also consider uniform pressure on the tank bottom corresponding to the liquid pressure of the height 19.6 m. The medium density equals 1000 kg/m3. With regard to the roof structure the variable load (snow) does not occur in this case. The analysis also neglects the wind load because its interaction with the liquid pressure on the walls is remote, not resulting in considerable actions on the foundation.

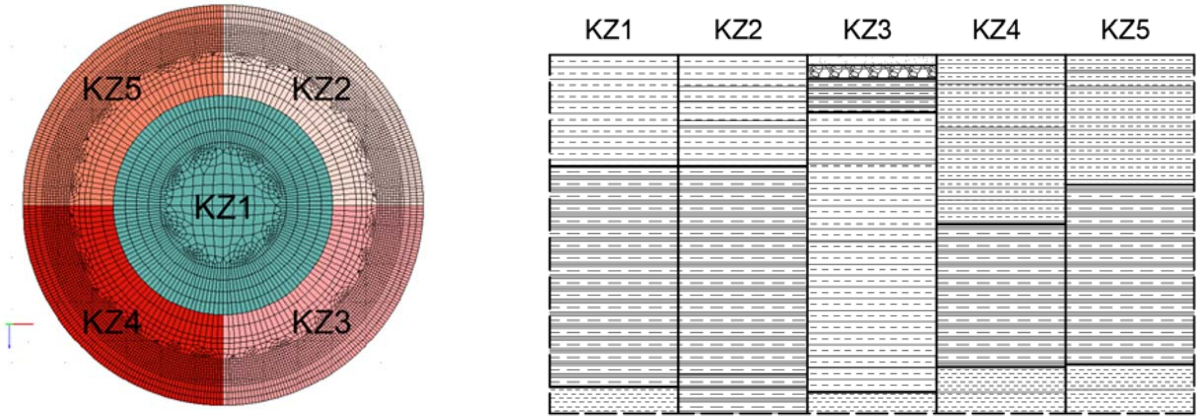

a) b)

Fig. 3. Distributions: a) subsoil strata, b) five distinct material parameters.

Tab. 2. Material parameters of subsoil strata (measurement results at selected boreholes)

*KZ*1		*KZ*2		*KZ*3		*KZ*4		*KZ*5	
t [m]	*E* [kPa]	*T* [m]	*E* [kPa]	*t*[m]	*E* [kPa]	*t* [m]	*E* [kPa]	*t* [m]	*E* [kPa]
4.3	30.88	1.2	14.6	0.4	62.97	1.1	14.59	0.6	14.59
8.5	46.31	0.6	30.7	0.5	144.59	1.7	24.28	0.6	24.28
1	24.47	0.7	19.6	0.4	14.59	2.8	30.88	3.8	30.88
0	24.47	0.3	24.3	0.3	30.65	0.9	39.91	6.9	46.31
-	-	1.5	30.7	0.6	39.91	5.5	46.31	1	24.47
-	-	8	46.3	2.0	30.65	1	24.47	0	24.47
-	-	0.5	39.9	3.0	39.91	0	24.47	-	-
-	-	0	39.9	4.8	46.31	-	-	-	-
-	-	-	-	1.0	24.47	-	-	-	-
-	-	-	-	0.0	24.47	-	-	-	-
E_{mean} [kPa]	39.92	38.54		43.40		35.30		37.57	
σ_{KZ} [kPa]	10.30	10.94		37.22		10.74		10.59	
μ_{KZi} [-]	0.26	0.28		0.86		0.30		0.28	

3. SENSITIVITY ANALYSIS

Analysis of the settlement impact on the shape deformation and the tank effort requires appropriate computational models. It is a highly important task while the impact of various footing conditions is compared. The comparative analysis employs two means, i.e.: extreme vertical deformations of the bottom and vertical bending moments causing additional shell deformation.

Variation of mechanical response of a structure is investigated to the variation of foundation parameters. The subsoil is modelled in two variants.

The first approach distinguishes five subregions *KZ*1-*KZ*5 on the basis of the Table 2, these regions are marked with appropriate Young's moduli. The model in Fig. 3a yields deformation of the bottom central node equal $u_5 = 0.066$ m (5 is a number of distinctly assumed material parameters). While the parameters *KZ* of all regions are averaged to a single value *KZ* = 38.95 kPa the maximum settlement of the bottom raises up to $u1 = 0.069$ m. This difference is slight because all the material parameters *KZ*1-*KZ*5 are close to their mean value KZ = 38.95 kPa. Tab. 3 presents the deformation of the annular plate. They yield a conclusion that no threat of limit state exceedance occurs here.

Tab. 3. The results - perimeter sheet of a tank

	u_y [m]	σ_{ya} [m]	min(u_y) [m]	max(u_y) [m]
5 *KZ*	-0.01891	0.00428	-0.02809	-0.01353
1 *KZ*	-0.01877	0.00428	-0.02731	-0.01398

The next step addresses the impact of stiffness modulus *KZ* variation of selected regions according to Tab. 4. The test is aimed at determining the relationship type between the stiffness variation and the anticipated mechanical response of the tank.

Tab. 4 The input data - sensitivity analysis - model II

No.	E_{mean} [MPa]	Sensitivity analysis [MPa]			
		E_{mean} (1+0.1σ)	E_{mean} (1+0.4 σ)	E_{mean} (1-0.1 σ)	E_{mean} (1-0.4 σ)
*KZ*1	42,71	46,99	59,80	38,44	25,63
*KZ*2	37,19	40,91	52,07	33,47	22,32
*KZ*3	41,23	45,36	57,73	37,11	24,74
*KZ*4	38,12	41,93	53,37	34,31	22,87
*KZ*5	39,98	43,97	55,97	35,98	23,99

The relation between the assumed moduli and the results is presented in Table 5 and Fig. 4. The results regarding perimeter sheet deformation may be approximated linearly while variation of bottom stiffness is non-linear (Fig. 4).

Tab. 5. The results - settlements, variable Young's modulus of the input data - model II

		Annular plate				Bottom
		u_y [m]	σ_{ya} [m]	min(u_y) [m]	max(u_y) [m]	u_{yd} [m]
II	KZ(n) +0,1v	-0,0176	0,0041	-0,0263	-0,0126	-0,0619
	KZ(n) +0,4v	-0,0148	0,0036	-0,0226	-0,0100	-0,0532
	KZ(n) -0,1v	-0,0205	0,0045	-0,0302	-0,0147	-0,0710
	KZ(n) -0,4v	-0,0286	0,0057	-0,0407	-0,0207	-0,0958

The last analytical step of structural response to variable subsoil conditions assumes each KZ parameter change independent (Fig. 3), according to Fig. 5.

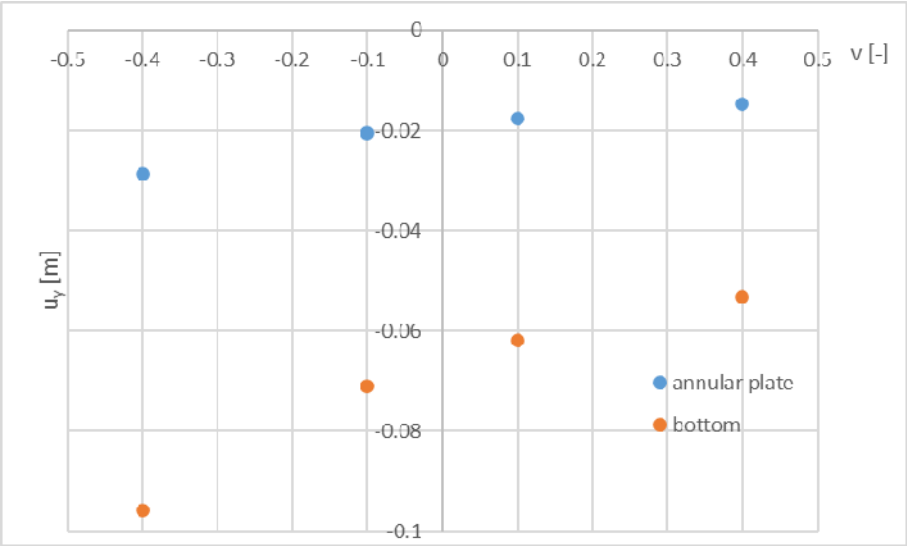

Fig. 4. The relationship - deflections vs variable subsoil stiffness

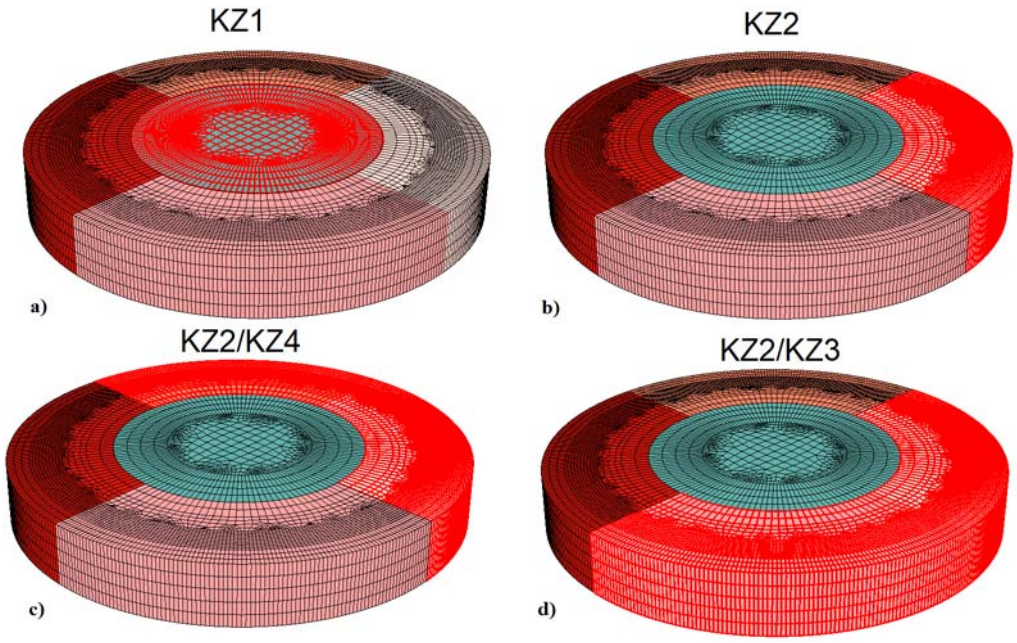

Fig. 5. Distinction of subregions in the models of sensitivity analysis.

While the parameter KZ1 varies (Fig. 5a) the stiffness is reduced to reach the extreme bottom settlement. The second regarded model (Fig. 5b) concerns the variations in structural strains due to overstiffening or weakening of KZ2. Such a configuration of subsoil parameters may trigger local foundation ring settlement, subsequently, irregular deformations of a boundary sheet and the bottom part. Two latter cases are aimed at selective reduction of subsoil stiffness, bringing irregular and extreme variations in sheet stresses and deflections. A featured important parameter in tank operation is the variation of radial deflection of the stiffening ring, at the elevation of the tank head. The results are included in Table 6. Most cases are grouped in pairs (Tab. 6)

Tab. 6. The input data - sensitivity analysis - model III

No.	KZ1 [MPa]	KZ2 [MPa]	KZ3 [MPa]	KZ4 [MPa]
KZ1 -0.3 E_{mean}	29.90	-	-	-
KZ2 -0.3 E_{mean}	-	26.03	-	-
KZ2 -0.5 E_{mean}	-	18.60	-	-
KZ2/4 +0.3 E_{mean}	-	48.35	-	49.56
KZ2/4 -0.3 E_{mean}	-	26.03	-	26.69
KZ2/4 -0.5 E_{mean}	-	18.60	-	19.06
KZ2/4 -0.8 E_{mean}	-	7.44	-	7.76
KZ2/3 -0.3 E_{mean}	-	26.03	28.86	-
KZ2/3 -0.5 E_{mean}	-	18.60	20.62	-
KZ2/3 -0.8 E_{mean}	-	7.44	8.25	-

Global deformation of the shell and the subsoil is presented in Fig. 6, the results are collected in Table 7. The analysis of bottom and boundary (perimeter) sheet deflections (Fig. 6) yields that the extreme reduction of the central region stiffness a local, point deflection difference occurs, up to u = 0.224 m. Such a point difference is irrational hence the form of subsoil parameter introduction should be verified. Other differences in average deflections remain constant at the level of u = 0.07 m in the case of parameter variation of boundary layers.

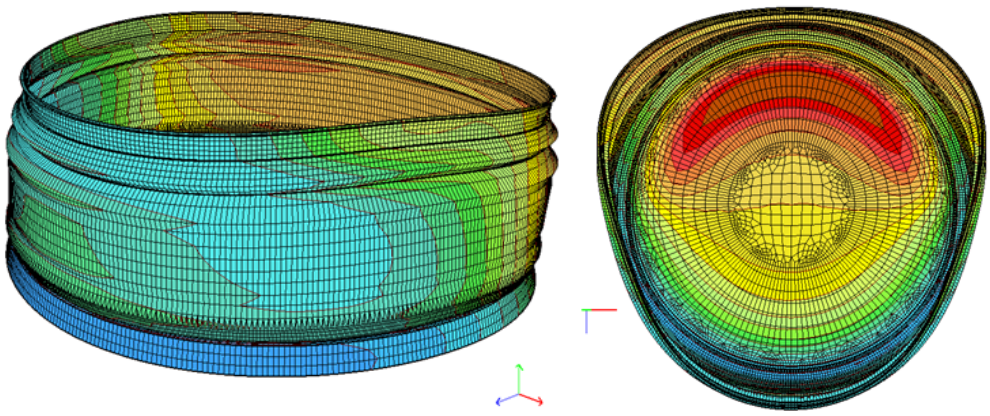

Fig. 6. The map of nodal deflections due to weakening of KZ2 and KZ3 regions, 80% with regard to the averaged subsoil stiffness modulus

Tab. 7. The results - settlements, variable Young's modulus of the input data - model III

No.	Annular plate				Bottom
	u_y [m]	σ_{ya} [m]	min(u_a)	max(u_a)	u_a [m]
KZ1 -0.3	-0,0192	0,0045	-0,0282	-0,0141	-0,0843
KZ1 -0.5	-0,0198	0,0048	-0,0293	-0,0141	-0.1082
KZ1 -0.8	-0,0212	0,0058	-0,0322	-0,0141	-0.2240
KZ2 -0.3	-0,0203	0,0050	-0,0346	-0,0137	-0,0692
KZ2 -0.5	-0,0218	0,0066	-0,0419	-0,0134	-0,0693
KZ2 -0.8	-0,0267	0,0134	-0,0657	-0,0124	-0,0694
KZ2 KZ4 +0.3	-0,0175	0,0043	-0,0274	-0,0118	-0,0689
KZ2 KZ4 -0.3	-0,0219	0,0054	-0,0351	-0,0136	-0,0694

Deformations of boundary courses are substantial (Fig. 6) while the irregular sheet layout affects force and strain distribution on the other side of the tank (tab. 8). Thus, the last analytical stage specifies the impact of footing parameter change on the deflections of the stiffening ring (located at the tank top). The results are collected in Tab. 8, an additional parameter is introduced to reflect the percentage of standard deviation with regard to the mean value of a given variant. The largest variation from the mean value corresponds to weakening of a smaller part along the tank foundation perimeter (the KZ reduced almost by 50%).

Tab. 8. Radial deflections - model III

No.	v(mean)	σ_v [m]	v [%]
KZ1 -0.3	1.094E-05	3.879E-06	35.45%
KZ2 -0.3	4.653E-03	4.036E-03	86.75%
KZ2 -0.5	9.187E-03	8.118E-03	88.35%
KZ2/4_+0.3	1.876E-03	1.152E-03	61.43%
KZ2/4_-0.3	4.593E-03	2.801E-03	60.98%
KZ2/4_-0.5	9.174E-03	5.464E-03	59.56%
KZ2/4_-0.8	2.497E-02	1.375E-02	55.06%
KZ2/3_-0.3	4.779E-03	2.900E-03	60.69%
KZ2/3_-0.5	8.399E-03	4.861E-03	57.88%
KZ2/3_-0.8	2.388E-02	1.320E-02	55.27%

Based on the conducted tests it yields that the structure exhibits deformation due to subsoil stiffness degradation. No analyzed case makes the radial displacement reach its limit value. Thus, the stiffening rings and appropriate sheet thickness required by the standards may prevent the structure from the subsoil settlement effect in this case.

4. CONCLUSIONS

The sensitivity analysis confirms a small stiffness degradation impact of distinct sub-foundation subsoil zones to the deflection variability of the bottom midpoint and the perimeter sheet. The most elevated stiffening ring of relevant (standard) parameters properly resists the circumferential deformations caused by non-uniform settlement, subsequently, by a variate subsoil stiffness. These deformations are numerically correct, checking the deflection from the perfect tank radius curvature. Local deformations are excluded which could possibly cause locking the guides of a floating roof or failure of the measurement equipment. Note that the wind rings are linked with the disadvantageous action of wind pressure. Possible extension of conducted work by impact of non-linear geometry or other in-situ aspects may led to different conclusions. Therefore, such approach may be incorporated by the Authors in the future.

REFERENCES

Commend, S., Kivell, S., Obrzud, R., Podleś, K., Truty, A., Zimmermann T. 2018 *Computational Geomechanics. Getting Started with ZSOIL.PC*; V.; Rossolis Editions, Switzerland: Preverenges.

Geary, W. & Hobbs, J. 2013. *Catastrophic failure of a carbon steel storage tank due to internal corrosion*. Case Studies in Engineering Failure Analysis 1: 257–264.

Grget, G., Ravnjak, K., Szavits-Nossan, A. 2018. *Analysis of results of molasses tanks settlement testing.* Soils and Foundations 58, 1260–1271.

Gunerathne, S., Seo, H., Lawson, W.D., Jayawickrama, P.W. 2018. *Analysis of edge-to-center settlement ratio for circular storage tank foundation on elastic soil.* Computers and Geotechnics 102: 136–147.

Ignatowicz, R., Hotala, E. 2020. *Failure of cylindrical steel storage tank due to foundation settlements*. Engineering Failure Analysis 115.

Kaczor, A., Sygulski, R. 2006. *Free Vibrations of Plate and Fluid in Container*. Symposium Vibrations in Physical Systems 22: 161-166.

Kleiber, M., Hisada, T. 1993. *Design Sensitivity Analysis*. Atlanta Technology Publications.

Kowalczyk, P., Kleiber, M. 1999. *Shape sensitivity in elasto-plastic computations*. Computer Methods in Applied Mechanics and Engineering.

Magnucki, K., Lewiński, J. & Stasiewicz, P. 2004. *Optimal sizes of a ground-based horizontal cylindrical tank under strength and stability constraints*. International Journal of Pressure Vessels and Piping 81: 913–917.

Nassernia, S., Showkati, H. 2020. *Experimental investigation to local settlement of steel cylindrical tanks with constant and variable thickness*. Engineering Failure Analysis 118.

Rasiulis, K., and Šapalas, A., Vadlūga, R. & Samofalov, M. 2006. *Stress/strain state investigations for extreme points of thin wall cylindrical tanks*. Journal of Constructional Steel Research 62: 1232–1237.

Truty, A. 2018. *On consistent nonlinear analysis of soil-structure interaction problems*. Stud. Geotech. Mech..

Zimmermann, T., Sarf, J., Truty, A., Podles, K. 2007. *Numerics for geotechnics and structures*. Recent developments in ZSoil.PC. In *Applications of Computational Mechanics in Geotechnical Engineering V*. Taylor & Francis.

Żyliński, K., Korzec, A., Winkelmann, K., Górski J. *Random field model of foundations at the example of continuous footing.* AIP Conf. Proc. 2239 (2020).

Żyliński, K., Winkelmann, K., Górski, J. 2021. *The effect of the selection of 3-D random numerical soil models on strip foundation settlements*. Appl. Sci. (11).

LIGHTWEIGHT STRUCTURES in CIVIL ENGINEERING
CONTEMPORARY PROBLEMS
Monograph from Scientific Seminar
Organized by Polish Chapters of
International Association for Shell and Spatial Structures
Łódź University of Technology
Faculty of Civil Engineering, Architecture
and Environmental Engineering
XXVII LSCE
Łódź, 2nd – 3rd of December 2021

DYNAMIC ANALYSIS OF STEEL MAST UNDER SOME ENVIRONMENTAL UNCERTAINTIES

R. Bredow [1] **M. Kamiński** [2]
[1] PhD Candidate, Department of Structural Mechanics, Łódź University of Technology, POLAND,
Rafal.Bredow@dokt.p.lodz.pl
[2] Professor, Department of Structural Mechanics, Łódź University of Technology, POLAND,
Marcin.Kaminski@p.lodz.pl

ABSTRACT: A concise and factual abstract is required. The abstract should state briefly the purpose of the research, the principal results and major conclusions. An abstract is often presented separately from the article, so it must be able to stand alone. For this reason, references should be avoided, but if essential, then cite the author(s) and year(s). Also, non-standard or uncommon abbreviations should be avoided, but if essential they must be defined at their first mention in the abstract itself.

Keywords: generalized stochastic perturbation technique, Stochastic Finite Element Method, reliability analysis, structural mechanics.

1. INTRODUCTION

The aim of this work is to analyse behaviour of some steel mast under dynamic excitation of the given wind spectrum including also uncertain temperature load and further to contrast two different Finite Element Method solvers of equations of motion integration.

The exemplary structure taken into account is a steel mast plsced in Zygry. Mast structure features the height equal to 198,0 meters. The mast shaft has been designed with the use of S235J2 steel in form of three-walled lattice with side width equal to 130,0 cm. The leg members have been modelled as round pipes with diameter of 168,3 mm and with the cross-section wall thickness varying along a height of this structure. The mast face lacings have been introduced as the round pipes of diameter 63,5 mm and also varying cross-section wall thicknesses. The mast guys have been attached to the shaft at following heights: 60,0 m, 120,0 m and 180,0 m with the inclination angle equal to about 45°. A spiral strand steel rope 1x37 with the diameter of 32,0 mm has been applied having mean strength of 1960 MPa and elasticity modulus of 150GPa. An initial tension of the guys has been set by pre-shortening equal to 11,0 cm, 22,0 cm and 31,0 cm correspondingly for consecutive attachment levels with ascending order starting from the bottom. A general geometry of this mast has been presented in Figure 1.1a. Geometry of shaft has been presented in Figure 1.1b.

Environmental uncertainty has been expressed by the Gaussian temperature load. Positive and negative temperature loads have been considered dependingly on which of these two contributes more significantly to structural safety reduction regarding some principal state variables. Positive temperature load has been introduce within a range of -10°C to +40°C when negative temperature load has been described within

a range of -50°C to ±0°C. Computations have been performed regarding both types of temperature load and repeated 11 times dividing both ranges of temperature load into ±5°C interval. The assumption has been made that the temperature applied to structure acts equally and no temperature fluctuations regarding height of the structure has been considered.

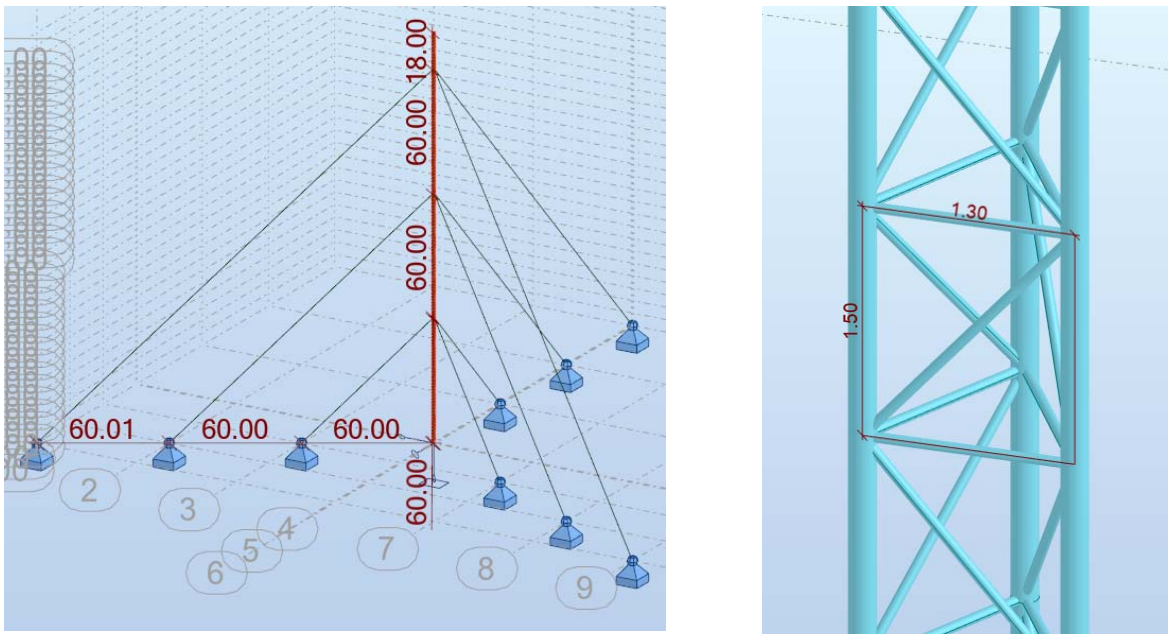

a) b)

Fig. 1.1. Mast geometry: a) general geometry, b) mast shaft geometry.

Computations have been performed regarding both types of temperature load and repeated 11 times dividing both ranges of temperature load into ±5°C temperature interval. The assumption has been made that the temperature applied to structure acts equally and no temperature fluctuations regarding height of the structure has been considered. Principal state variables have been identified as stress of the main legs and of the face lacing referring to single structural elements of the mast. Global horizontal displacement and rotation of the entire structure top have been also considered for this purpose. Several series of numerical simulations with the Finite Element Method system have been performed assuming specific dynamic action of the wind load (see Fig. 1.2). This wind load has been modelled according to the Eurocode 1 guidelines (1) for towers, chimneys and masts including an effect of local wind gusts (2, 3, 4). Dynamic analysis of the wind influence on this structure has been performed in 10 minutes time interval.

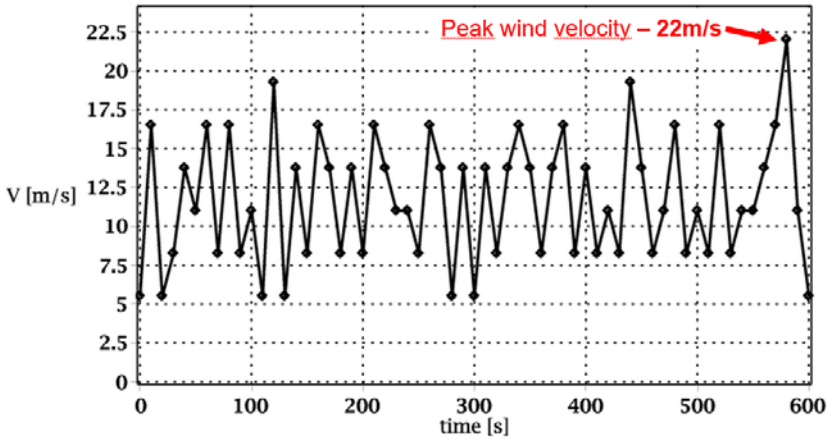

Fig. 1.2. History of wind load introduced into calculations.

This includes some wind action applied to the entire structure (see Fig. 1.3a) and some patch loads describing additional wind gusts along the height of the structure (see Fig. 1.3b).

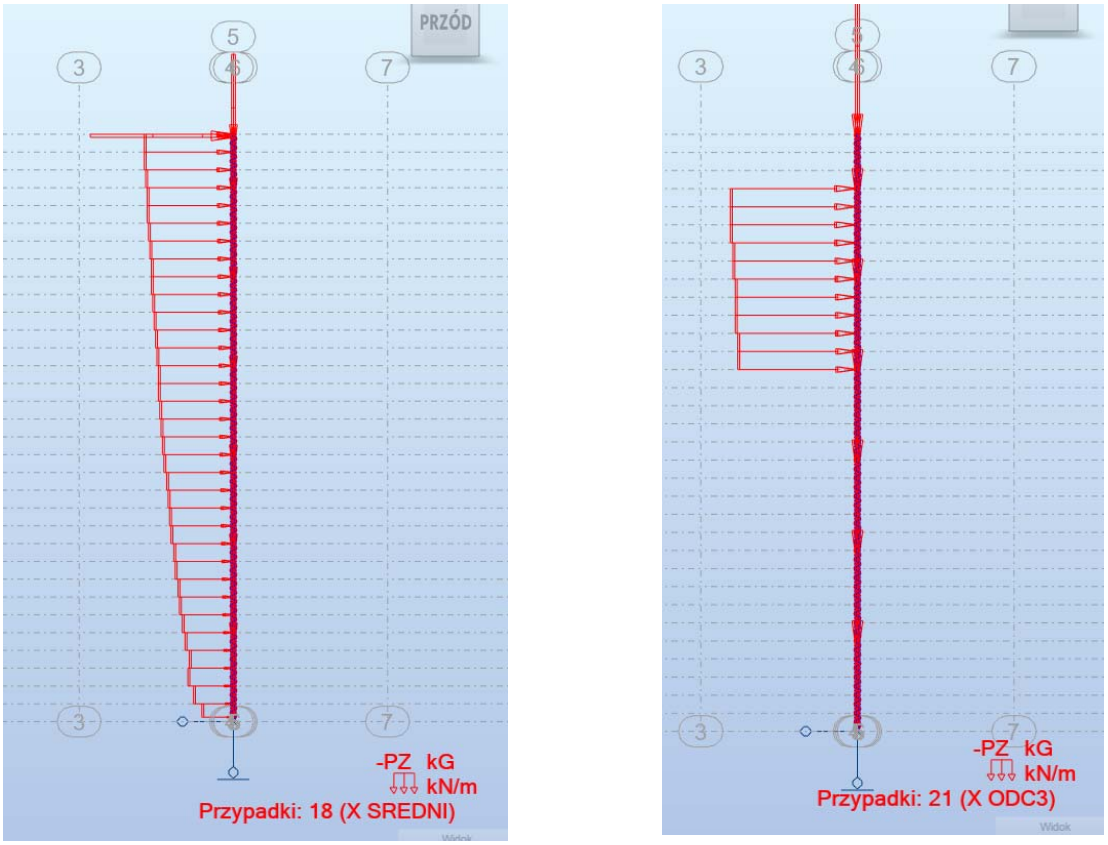

a) b)

Fig. 1.3. Exemplary wind load acting along X-axis of global coordinate system: a) mean load, b) patch load.

2. NUMERICAL SOLUTION

Numerical solution for each computational case study has been performed in Autodesk Robot Structural Analysis (ARSA) using non-linear dynamic analysis option based on the Broyden-Fletcher-Goldfarb-Shanno (BFGS) algorithm. Hilber-Hughes-Taylor (HHT) solver has been applied in order to integrate equations of motion (5). It is based upon the following approximation of the structural displacements and velocities:

$$\begin{cases} x_{i+1} = x_i + \Delta t \cdot \dot{x}_i + \left(1/2 - \beta\right) \cdot \left(\Delta t\right)^2 \cdot \ddot{x}_i, \\ \dot{x}_{i+1} = \dot{x}_i + \left(1 - \gamma\right) \cdot \Delta t \cdot \ddot{x}_i. \end{cases} \tag{2.1}$$

Additionally, the HHT solver has been contrasted with the results achieved by Newmark method (6) and exemplary results have been presented in Figure 2.1.

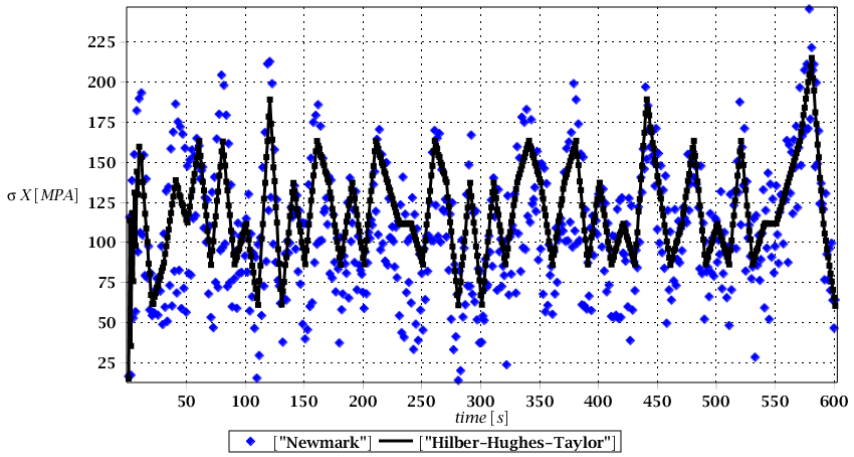

Fig. 2.1. History of normal stresess in main leg under dynamic wind exctitation obtained using the HHT and Newmark method.

This figure documents very well that the Newmark algorithm results in relatively larger variations of the given stress about the value relevant to the static equilibrium, while the HHT series is obtained in a quite regular pattern.

At this point it has to be mentioned that Autodesk Robot Structural Analysis does not calculate effective stress in beam elements. The index of share of normal stress in Huber-Mises effective stress has been investigated in order to check whereas there is a necessity to calculate an effective stress in each time step manually for main legs and face lacing elements. In order to pursue such investigation, author checked the effective stress of elements by finding elements in which normal or shear stress calculated by ROBOT was the greatest among the entire structure and time of analysis. Products of solving equations of motion indicates that those elements are mainly stressed by axial force and some bending moments. Shear forces and torsional moment are of the minor interest as those figures are mainly lesser by three orders of magnitude comparing to normal force. Nevertheless effective stress has been calculated by following Huber-Mises hypothesis of effective stress. Normal stress has been calculated as a product of axial force and bending moments acting on a cross section of element (see Fig 2.2a.). Total shear stress has been calculated as a product of vector aggregation performed on shear stress generated by shear forces and by torsional moment (see Fig 2.2b.). Taking into account abovementioned procedure, effective stress has been calculated for main leg and face lacing truss. This calculations has been performed by a deterministic approach as it is recommened by currently valid engineering guidelines (i.e. Eurocodes). In some future research on the other hand, some probabilistic approach might be worth taking into account regarding such a cross-sectional stress distribution analysis. Exemplary calculations performed for main leg element are being presented below.

Cross sectional properties:

$$
\begin{aligned}
&r = 8.4cm,\\
&A = 58.9cm^2,\\
&J_y = J_z = J_1 = 1810cm^4,\\
&J_0 = \frac{4A_0^{\,2}}{\oint \frac{ds}{\delta}} = \frac{4\cdot\left(\pi\cdot(8.4cm)^2\right)^2}{2\pi\cdot 8.4cm} = 3724.07cm^4.
\end{aligned}
\tag{2.2}
$$

Internal forces have been determined consecutively and they equal in turn:

$$\begin{aligned} &N_{Ed} = -1089.19kN, \\ &T_{Ed} = -0.05kNm, \\ &M_{y.Ed} = 4.84kNm, \\ &M_{z.Ed} = -3.88kNm, \\ &V_{y.Ed} = 0.97kNm, \\ &V_{z.Ed} = -6.47kN. \end{aligned} \tag{2.3}$$

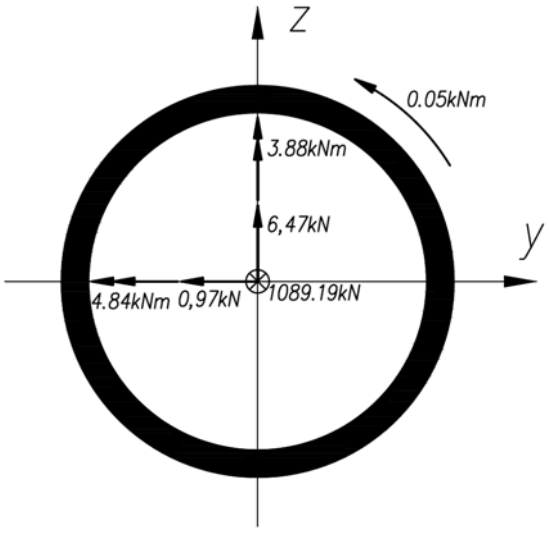

Fig. 2.2. Load acting on cross-section of chosen main leg element.

Utilizing bi-simmetrical properties of cross section, normal stress can be easily calculated in tilted coordinate system. Effective bending moment might be represented as:

$$M_{Ed} = \sqrt{M_{y.Ed}{}^2 + M_{z.Ed}{}^2} = \sqrt{4.84^2 + 3.88^2}\,kNm = 6.20kNm. \tag{2.4}$$

Resulting normal stress is then calculated respectively:

$$\sigma_A = \frac{-N_{Ed}}{A} + \frac{M_{Ed}}{J_1} \cdot \rho = \frac{-1089.19kN}{58.9 \cdot 10^{-4} m^2} + \frac{-6.20kNm}{1810 \cdot 10^{-8} m^4} \cdot 84 \cdot 10^{-3} m = -213.695MPa. \tag{2.5}$$

Shear stress has been calculated in point A, which corresponds to greatest normal stress and considering relatively small shear stress, point A describes greatest effective stress as well.

$$\tau_{mean.Z} = \frac{V_{z.Ed}}{A} = \frac{6.47kN}{58.9 \cdot 10^{-4} m^2} = 1.098MPa. \tag{2.6}$$

$$\tau_{xz}{}^A = \frac{4}{3} \cdot \tau_{mean.Z} \cdot \cos(51.26^\circ) = 0.916MPa. \tag{2.7}$$

$$\tau_{mean.Y} = \frac{V_{y.Ed}}{A} = \frac{0.97kN}{58.9 \cdot 10^{-4} m^2} = 0.165MPa. \tag{2.8}$$

$$\tau_{xy}{}^{A} = \frac{4}{3} \cdot \tau_{mean.Y} \cdot \sin(51.26^{\circ}) = 0.172MPa. \tag{2.9}$$

$$\tau_{T.z}{}^{A} = \tau_{T}{}^{A} = \frac{T_{Ed}}{W_0} \cdot \cos(51.26^{\circ}) = \frac{0.05kNm}{532.01 \cdot 10^{-6} m^3} \cdot \cos(51.26^{\circ}) = 0.0588MPa. \tag{2.10}$$

$$\tau_{T.y}{}^{A} = \tau_{T}{}^{A} = \frac{T_{Ed}}{W_0} \cdot \sin(51.26^{\circ}) = \frac{0.05kNm}{532.01 \cdot 10^{-6} m^3} \cdot \sin(51.26^{\circ}) = 0.0733MPa. \tag{2.11}$$

$$\overline{\tau}_{y}{}^{A} = \overline{\tau}_{xy}{}^{A} + \overline{\tau}_{T.y}{}^{A} = 0.172MPa + 0.0733MPa = 0.2453MPa. \tag{2.12}$$

$$\overline{\tau}_{z}{}^{A} = \overline{\tau}_{xz}{}^{A} + \overline{\tau}_{T.z}{}^{A} = 0.0588MPa + 0.916MPa = 0.9748MPa. \tag{2.13}$$

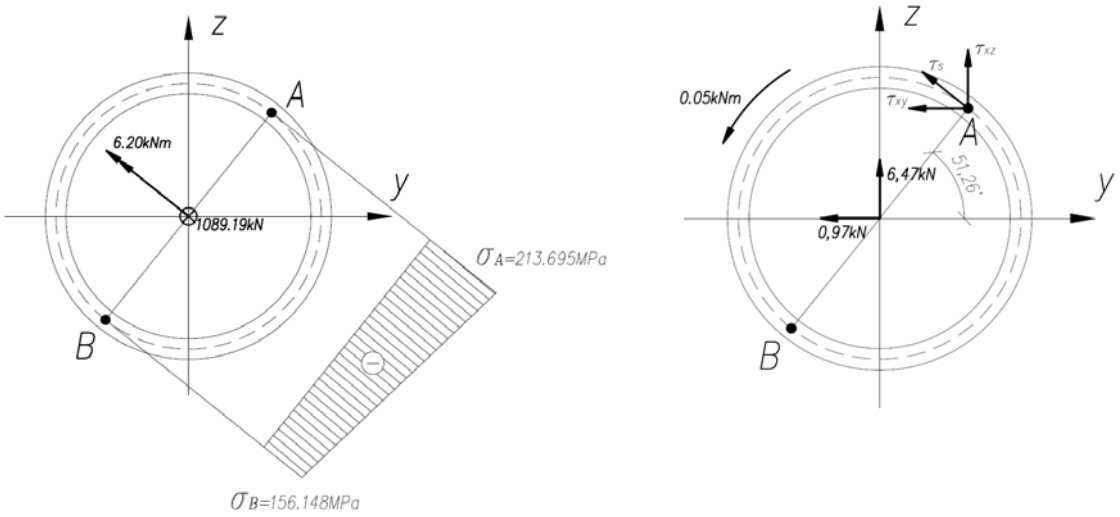

a) b)

Fig. 2.3. Stress generated by internal forces: a) normal stress, b) shear stress as a product of vector-aggregation.

Finally, the Huber-Mises effective stress in point A:

$$\sigma_{red}{}^{HA} = \sqrt{\left(\sigma^{A}\right)^2 + 3\left(\tau^{A}\right)^2} = \sqrt{213.695^2 + 3 \cdot 1.01^2}\, MPa = 213.702MPa. \tag{2.14}$$

Share index of normal stress to effective stress has been described as:

$$\frac{\left|\sigma^{A}\right|}{\sigma_{red}{}^{HA}} = \frac{213.695MPa}{213.702MPa} = 0.99997 = 99.997\%. \tag{2.15}$$

Comparison of a normal stress to effective stress shows that the influence of shear stress might be neglected. Simmilar calculations and conclusions has been drawn from analysis of stress state of face lacing elements. This brings the conclusion that calculating effective stress every time step of calculations can be neglected and normal stress can be taken as a representative instead.

Discrete results of the resulting extreme stresses and displacements have been saved for any second of FEM simulations, where every save step has been subdivided into 10 time steps giving as a result computational time step equal to Δt=0.10 s. This calculus procedure has been repeated for 11 series of uniform temperature

load within a range of -50 °C up to +40 °C. A set of 600 discrete values of stresses and displacements computed for several series of the FEM tests was the basis to carry out Structural Response Function estimation in a form of the 11th order polynomial (or less). Polynomials have been fitted by the Weighted Least Squares Method in which the weighing function has been assumed as a triangular one. Structure Response Function (SRF) accuracy has been adjusted by the mean square root error minimization criterium as well as controlling whether over-fitting problem occurs. The SRF has been recovered for each random state variable separately (leg stress, face lacing stress, horizontal displacement and rotation) at any save step using both solvers (HHT and Newmark) giving as a result 4x600=2400 SRFs. These SRFs are analytical functions of the external temperature, which is assumed to be Gaussian variable. It has to be noted that polynomial order has been established once for all series of the SRFs that describe one of four state variables i.e. horizontal displacement. This means that all 600 SRFs associated with horizontal displacement in subsequent save steps of movement are described by polynomials of the same order.

3. PROBABILISTIC ANALYSIS

The generalized Stochastic Perturbation Technique (SPT) (7) has been introduced in order to compute the basic probabilistic characteristics of the structural response, where Monte Carlo Simulation (MCS) and Semi-Analytical Method (SAM) have been chosen as the reference techniques (8, 9, 10). Time fluctuations of the expected values, variances, skewness, kurtosis and coefficient of variation for the extreme values of normal stresses in the main legs have been presented in Figures (3.1-3.16), correspondingly.

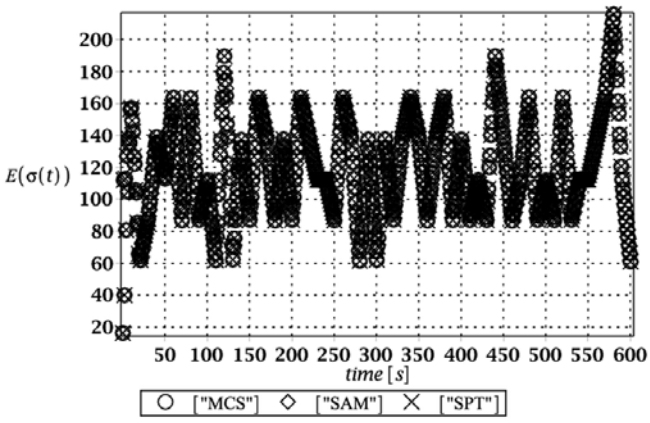

Fig. 3.1. History of expected value for normal stress in main legs.

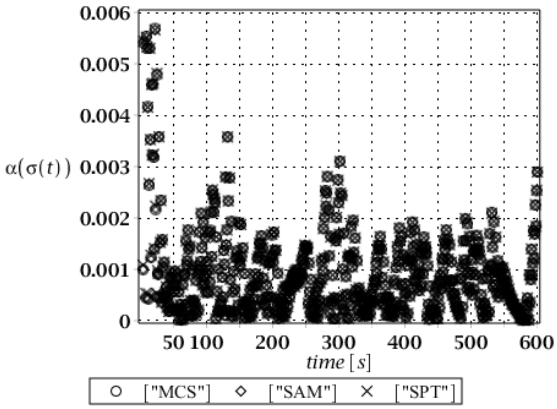

Fig. 3.2. History of the coefficient of variation for normal stress in main legs.

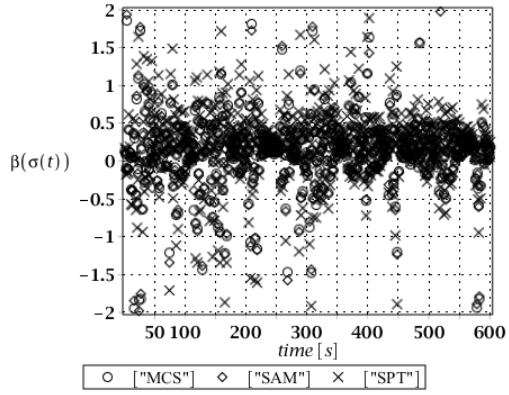

Fig. 3.3. History of the skewness for normal stress in main legs.

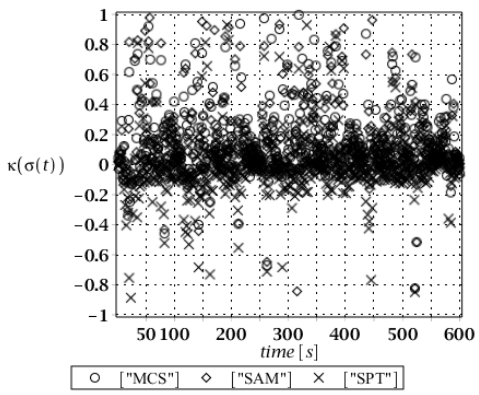

Fig. 3.4. History of the kurtosis for normal stress in main legs.

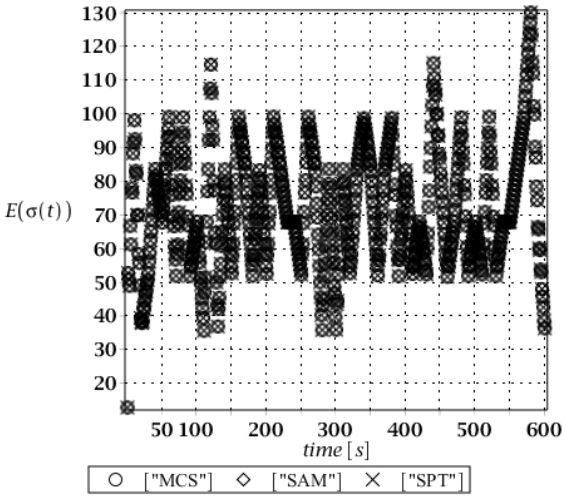

Fig. 3.5. History of the expected values of stress in face lacing.

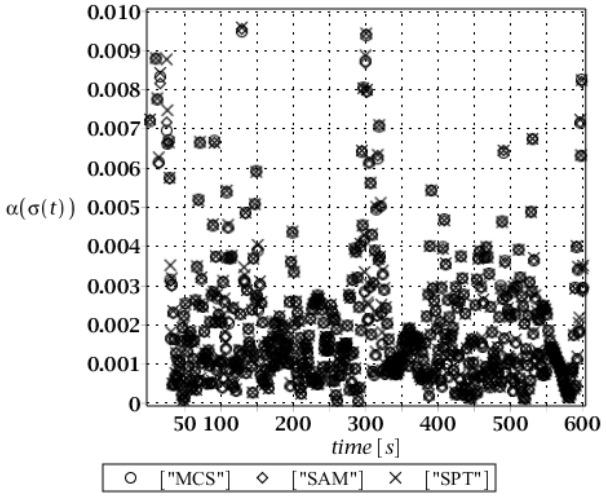

Fig. 3.6. History of coefficient of variation of stress in face lacing.

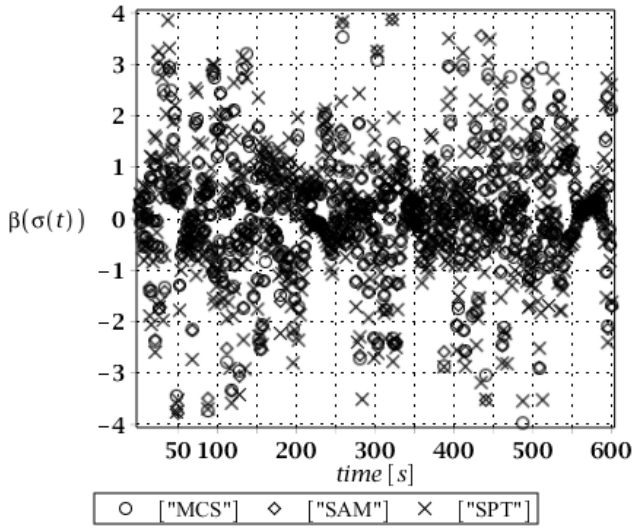

Fig. 3.7. History of skewness of stress in face lacing.

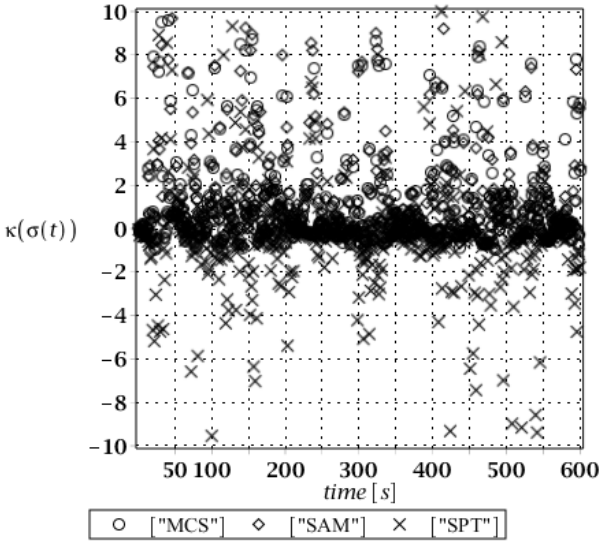

Fig. 3.8. History of skewness of stress in face lacing.

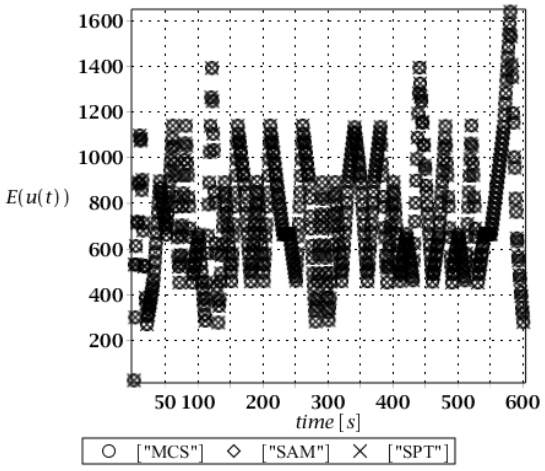

Fig. 3.9. History of expected values of horizontal displacement.

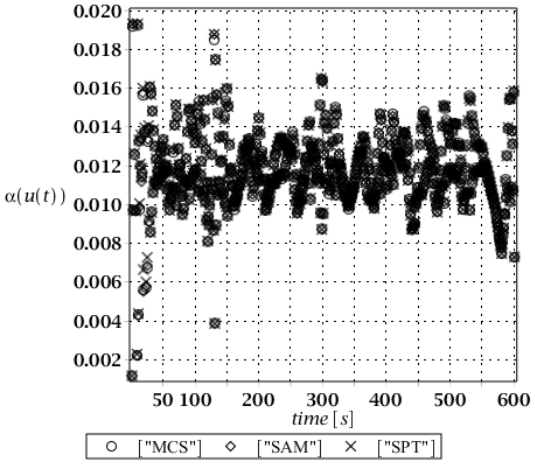

Fig. 3.10. History of coefficient of variation of horizontal displacement.

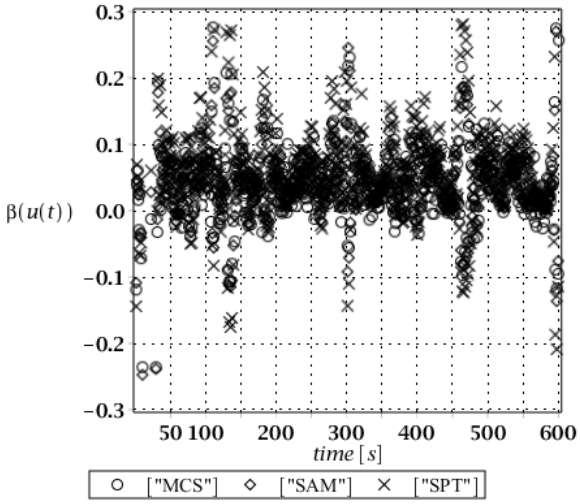

Fig. 3.11. History of skewness of horizontal displacement.

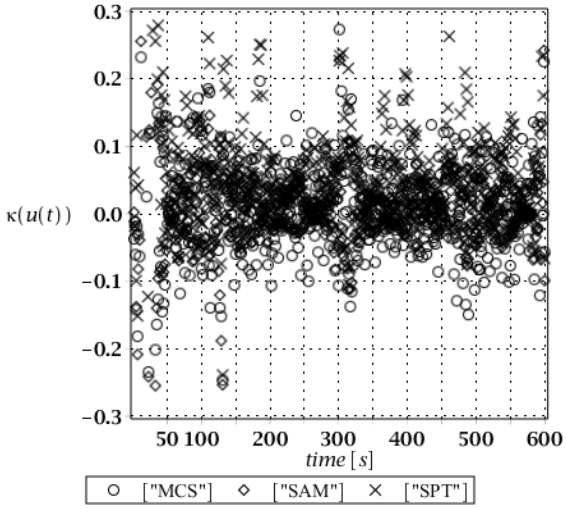

Fig. 3.12. History of kurtosis of horizontal displacement.

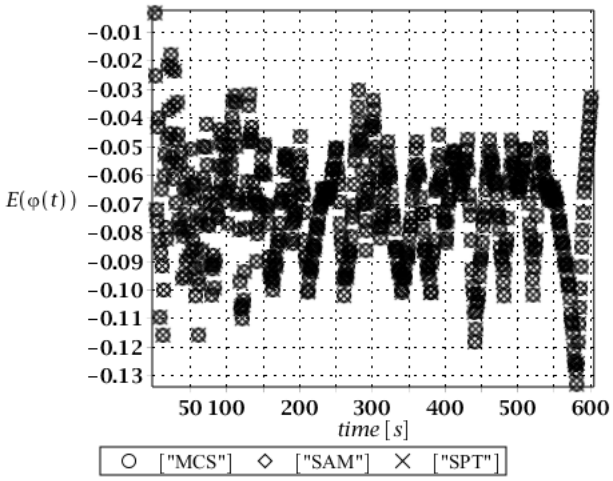

Fig. 3.13. History of expected values of rotation.

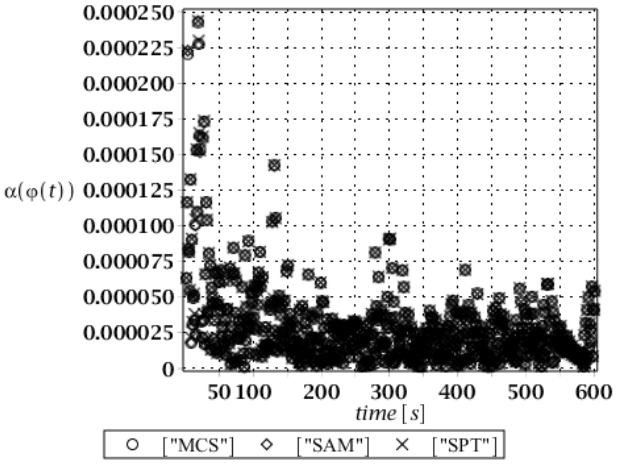

Fig. 3.14. History of coefficient of variation of rotation.

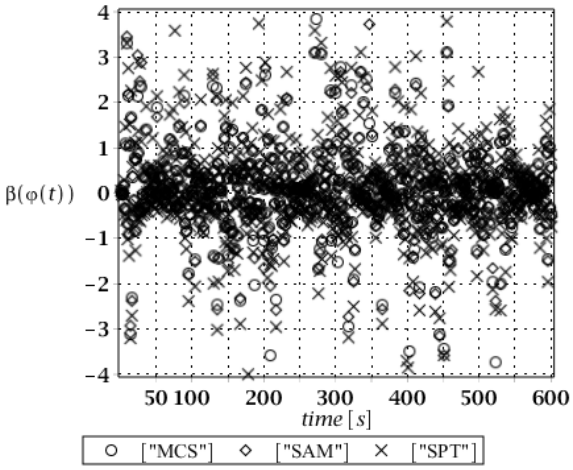

Fig. 3.15. History of skewness of rotation.

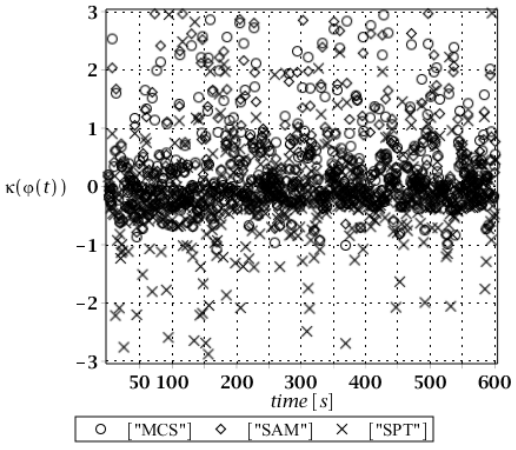

Fig. 3.16. History of kurtosis of rotation.

4. CONCLUDING REMARKS

A very general conclusion, which can be drawn from these results is a good coincidence of all three probabilistic numerical methods, which taking into account nonlinear problem with large deformations including dynamic excitation is not trivial. Numerical results obtained here, and especially the first two probabilistic moments, may be directly used in stochastic reliability assessment according to the statements proposed in Eurocode 0. Finally, one can conclude that external temperature uncertainty has rather limited importance while dynamic stresses fluctuations are under consideration and cannot affect remarkably the resulting reliability index.

REFERENCES

Eurocode 1: Actions on structures – Part 1-4: General actions – Wind actions – European Committee for Standardization, Brussels, 2010.

Eurocode 3: Design of steel structures – Part 3-1: Towers, masts and chimneys – Towers and masts – European committee for Standardization, Brussels, 2006.

Spak, K.S., Agnes, G.S., Inman, D.J. 2015. *Modeling vibration response and damping of cables and cables structures*. Journal of Sound & Vibration 336: 240-256.

Wang, L., Rega, G. 2010. *Modelling and transient planar dynamics of suspended cables with moving mass*. International Journal of Solids & Structures 47: 2733-2744.

Hilber, H.M., Hughes, T.J.R. & Taylor, R.L. 1997. *Improved Numerical Dissipation for Time Integration Algorithms in Structural Dynamics*. Earthquake Engineering & Structural Dynamics 5: 282-292.

Newmark, N.M. 1959. *A method of computation for structural dynamics*. Journal of the Engineering Mechanics Division 85 (EM3): 67-94.

Kamiński, M. The Stochastic Perturbation Method for Computational Mechanics. Chichester: Wiley.

Bredow, R. & Kamiński, M. 2021. *Computer analysis of dynamic reliability of some concrete beam structure exhibiting random damping*. International Journal of Applied Mechanics and Engineering 26(1): 45-64.

Kamiński, M. & Bredow, R. *On uncertainty analysis for overhead powerlines by the generalized stochastic perturbation technique*. Journal of Aerospace Engineering (in press).

Carassale L, Solari G. 2006. *Monte Carlo simulations of wind velocity fields on complex structures*. Journal of Wind Engineering and Industrial Aerodynamics 94: 323–339.

LIGHTWEIGHT STRUCTURES in CIVIL ENGINEERING
CONTEMPORARY PROBLEMS
Monograph from Scientific Seminar
Organized by Polish Chapters of
International Association for Shell and Spatial Structures
Łódź University of Technology
Faculty of Civil Engineering, Architecture
and Environmental Engineering
XXVII LSCE
Łódź, 2nd – 3rd of December 2021

RESPONSE OF STEEL SPIRE WITH IMPERFECT JOINTS AT DYNAMIC WIND LOADING

M.D. Gajewski [1] **R.B. Szczerba** [2] **D. Trinh Duc** [3] **B.A. Gajewska** [4] **M.A. Giżejowski** [5]
[1)] BEng, PhD, DSc, Warsaw University of Technology, Faculty of Civil Engineering, POLAND,
m.gajewski@il.pw.edu.pl
[2)] BEng, MSc, Warsaw University of Technology, Faculty of Civil Engineering, POLAND,
r.szczerba@il.pw.edu.pl
[3)] BEng, MSc, Warsaw University of Technology, Faculty of Civil Engineering, POLAND,
duyen.trinh_duc.dokt@pw.edu.pl
[4)] BEng, MSc, Warsaw University of Life Sciences – SGGW, POLAND,
beata_gajewska@sggw.edu.pl
[5)] Professor, Warsaw University of Technology, Faculty of Civil Engineering, POLAND,
m.gizejowski@il.pw.edu.pl

ABSTRACT: A concise and factual abstract is required. The abstract should state briefly the purpose of the research, the principal results and major conclusions. An abstract is often presented separately from the article, so it must be able to stand alone. For this reason, references should be avoided, but if essential, then cite the author(s) and year(s). Also, non-standard or uncommon abbreviations should be avoided, but if essential they must be defined at their first mention in the abstract itself.

Keywords: dynamic response, steel, spire, FEM, resonance.

1. INTRODUCTION

In recent decades, in the race for the tallest building in a city, country or the world, engineers have to resort to certain "tricks", to be competitive. Such solutions include additional truss structures, towers, spires or masts. Very often a reinforced concrete building is supplemented with a light steel structure, which may be susceptible to influence of wind or dynamic excitations, e.g. from an earthquake. This chapter presents the boundary problem solutions of vibrations of this type of selected structure excited by wind whose loading have a frequency close to the first natural frequency.

Analyzing examples of high buildings, it turns out that in many situations only a part of the building can fulfill its standard functions, while the rest only serves to make the building original or attractive from the architectural point of view, or simply taller. This problem has been noticed, but there is no indication that anything will change (Campbell-Dollaghan 2018, English 2020). Tab. 1.1. presents information on selected high-rise buildings from recent years, in which the non-occupied part of the building in extreme situations approaches 40%, and in most cases exceeds 20%. This list includes two buildings located in Warsaw (one completed and the other under construction), which also follow this trend. These buildings are certainly spectacular and architecturally stand out from the surrounding buildings but is this sufficient justification for their construction in the light of the global trend of saving raw materials and energy from non-renewable

sources. As a partial justification for these solutions, it can be indicated that cellular network transmitters or TV antennas are often mounted on structures of this type, but this is not a common solution. The section presents examples of analyzes carried out for the historic masonry chimney, which may be useful for the engineering applications and needs of SHM, especially if the monitoring of that structures will be necessary tor the future. Such analysis may be carried out for various structures or structural elements, e.g., light steel structures (lattice, plate, etc.), various types of wooden structures, concrete objects, or masonry structures which are discussed here.

The paper describes numerical simulations with the 3D laser scanning process which was used for recognizing structural problems such as damage or geometric irregularities of the masonry chimney (Ogden 1984). The scanning data was analyzed for cracking at higher levels of the chimney, where the direct inspection was difficult to achieve. Next, a real numerical model of the structure was created based on scanning data and the simulations of it were carried out in Finite Element (FE) software.

Table 1.1. Basic information about chosen highest buildings.

Building	**A**	**B**	**C**	**D**	**E**	**F**	**G**	**H**	**I**	**J**	**K**	**L**
Overall height [m]	828	450	366	360	355	333	331	321	319	310	309	220
Non-occupied height [m]	244	133	131	95	113	96	94	124	99	80	97	40
Non-occupied height as a percent of overall height [%]	29	30	36	27	32	29	28	39	31	26	31	18

A: Burj Khalifa, Dubai, UAE, 2010, **B**: Zifeng Tower, Nanjing, China, 2010, **C**: Bank of America Tower, New York City, USA, 2009, **D**: The Pinnacle, Guangzhou, China, 2012, **E**: Emirates Tower One, Dubai, UAE, 2000, **F**: Rose Rayhaan by Rotana, Dubai, UAE, 2007, **G**: Minsheng Bank Building, Wuhan, China, 2008, **H**: Burj Al Arab, Dubai, UAE, 1999, **I**: New York Times Tower, New York City, USA, 2007, **J**: Varso, Warsaw, Poland, planning 2021, **K**: Emirates Tower Two, Dubai, UAE, 2000, **L**: Warsaw Spire, Warsaw, Poland, 2016.

2. ANALYZED STRUCTURE AND PROBLEM DESCRIPTION

The chapter deals with the dynamic analysis of steel spire in the form shown in Fig. 2.1., being an additional element placed on the highest ceiling of a skyscraper, only to make it the tallest building in the city for some time. The original structure was not designed for this type of solution, and the spire itself was erected from segments prepared in the factory and assembled in quite difficult conditions. As was to be expected, this led to some unforeseen problems with the dynamic response of the element to typical wind loads. The problem was at first solved by applying lashings and finally by installing properly tuned vibration dampers on the top of the element, but the dynamic analysis of the structure without dampers, taking into account its flaws and imperfections, can lead to interesting observations. An additional element significantly influencing the obtained solutions are the consequences of the numerical formulation of the initial boundary-value problem. This chapter is a continuation of the work presented at the SEMC 2019 conference (Gajewski et. al. 2019).

The results presented there are supplemented and expanded. The first of the new elements is taking into account the influence of the accuracy of the determination of the natural frequency on the amplitude of the tower vibrations caused by gusts of wind of this frequency. Another element extending the scope of the analysis is the application to the dynamic analysis of the structure the large deformation theory implemented in the ABAQUS program under the NLGEOM option. It turns out that this affects not only the vibration amplitude of the structure, but also the nature of these vibrations. Technical drawing of the analyzed structure, consisting of 12 factory-made elements, which are connected by bolted flange connections,

is presented in Fig. 2.1. Additionally, the technical solution of connecting the lowest segment with the ceiling slab of the highest storey of the building is shown in the drawing.

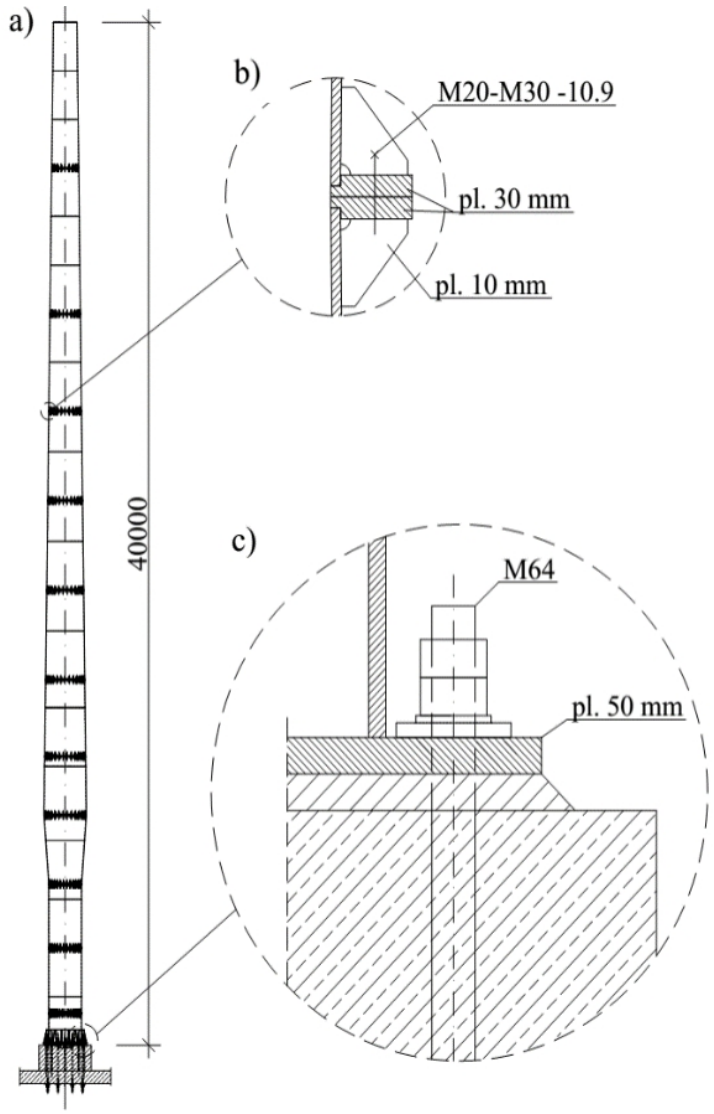

Fig. 2.1. Details of the spire's structure; a) geometry (in mm), b) segment's flange connection, c) the connection of the lowest segment with the base plate.

3. MODELLING OF THE STRUCTURE

In paper (Gajewski et. al. 2019) the analysis was carried out in two ways, i.e. using the analytical approach according to the so-called Procedures 1 and 2 of EC1-1-4 and using the results of the FEM simulation (ABAQUS/Standard User's manual 2011, ABAQUS Theory manual 2011). The results of this analysis are essentially based on conclusion that the standard approach does not lead to a rational prediction of structural behavior including determining the maximum amplitude of wind induced vibration. There are actually two main reasons why such approach will not lead to rational predictions, i.e. the inability to take into account the compliance of the connections made between the segments of the structure and inability to take into account the overall compliance of the reinforced concrete slab on which the structure is founded. Therefore, it is necessary to prepare a FEM calculation model including the above-mentioned elements. Due to the size of the structure (mainly the proportion of wall thickness compared to characteristic structure dimensions), an assumption was made to create a three-dimensional computational model using shell elements with linear

shape functions (four-node in the case of the structure and three- and four-node in the case of the slab on which the structure is mounted), see Fig. 3.1.

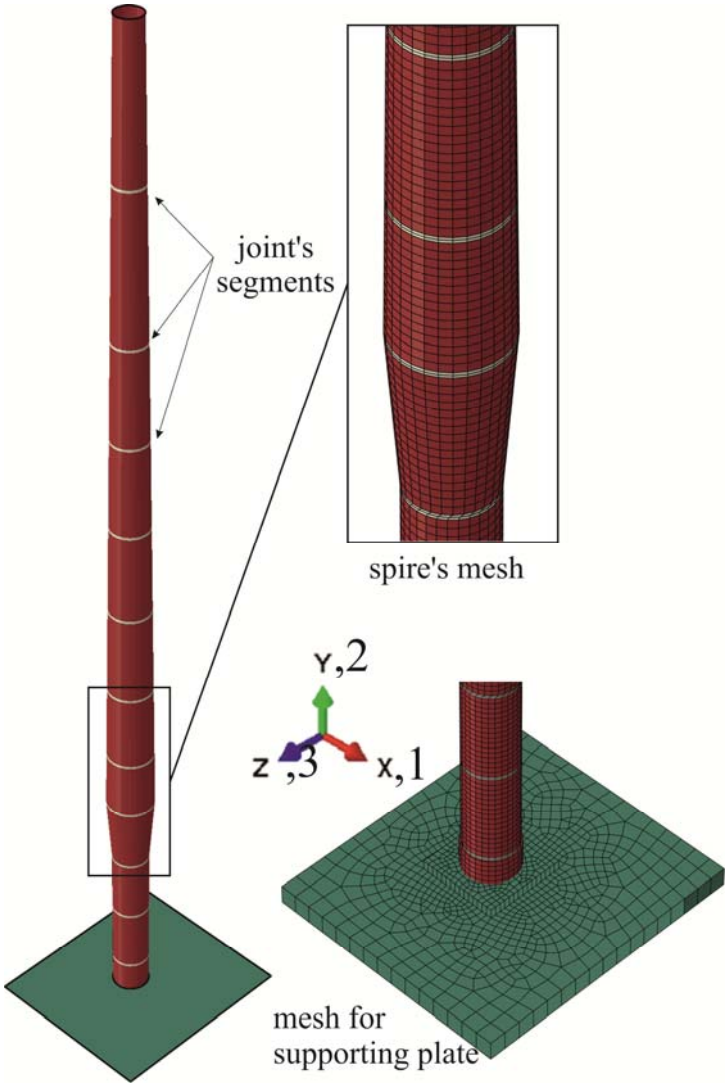

Fig. 3.1. FEM model of the spire (variant with reinforced concrete slab and indication of the joints).

The mesh density was established based on convergence analysis, but the limitation on number of elements is also important having in mind that we want to observe dynamical behavior of the structure in a long-time interval. As a result, the choice of a mesh with average element side dimension equal to 100 mm was a compromise between accuracy and numerical robustness.

3.1. Joints modelling

The calculation model preparation was preceded by the analysis of a representative connection element in order to determine the decrease in its stiffness as a result of its faulty execution (opening of the bolted flanges, most likely as a result of residual post-welding stresses). In Fig. 3.2. the technical drawing of the symmetrical element of the joint is shown altogether with specific dimensions and information about the bolt joint. It was assumed according to measurements that initial flanges opening distance is equal to 3 mm – see Fig. 3.3a.

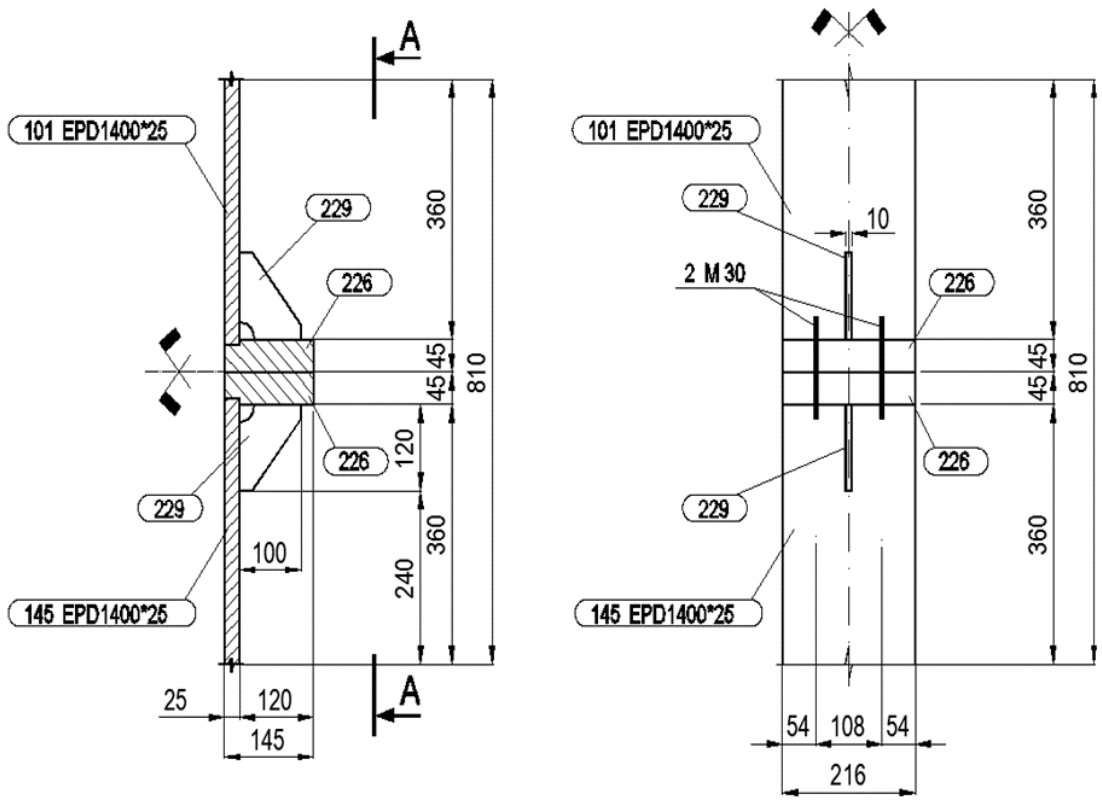

Fig. 3.2. Details of symmetrical part of the bolted flange joint.

A fragment of the imperfect flange joint was modeled using shell finite elements as a static contact task. The FEM model consists of 3862 eight-node shell elements with square shape functions (S8R). In the places of seating of the bolted connectors, rigid joints of the nodes belonging to the adjacent horizontal sheets (No. 226, as shown in Fig. 3.2.) were used, using the MPC option. Moreover, at the junction of the horizontal sheets No. 226, the contact conditions with parameters typical for the steel material were applied, i.e. the friction coefficient was assumed to be 0.3. The joint element was subjected to elastic static analysis under tensile conditions (displacement control). The boundary conditions together with the loading method and the appropriate symmetry conditions are shown in Fig. 3.3b. The visualization of the FEM model with a visible uniform FEM mesh is shown in Fig. 3.3c. (the dimension of one finite element is approximately 10x10 [mm]). For the calculations, it was assumed that the steel elements of the connection are made of a linear-elastic material with isotropic material parameters: E = 210 [GPa], ν = 0.3.

The compliance of a fragment of a flange connection was determined under tensile conditions, as shown in Fig. 3.3b. Under load, the displacement of the upper edge of the shell was controlled. The displacement along the y axis was assumed, i.e. $u_y = \delta$ with a value of 1.5 [mm]. The calculations were carried out in the case of analyzed joint, assuming the wedge opening of s = 3 [mm], and in the case of a perfect joint, when its load capacity is not less than that of the connected segments. Calculation results in the form of a reaction force F_y as a function of u_y are shown in Fig. 3.4. In the case of a perfect joint the reaction force F_y for displacement u_y =1.5 [mm] is equal to 2450.63 [kN], while in case of imperfect joint (with wedge opening) the reaction force was only F_y = 402.386 [kN].

The contour graph of horizontal displacement $u_1 = u_x$ (perpendicular to the tension direction) for joint with wedge opening is shown in Fig. 3.5. The values were read in the case of $u_y = \delta$ = 1.5 [mm]. Horizontal displacements reach a value almost twice as high (2.9 [mm]) as the displacement in the tension direction.

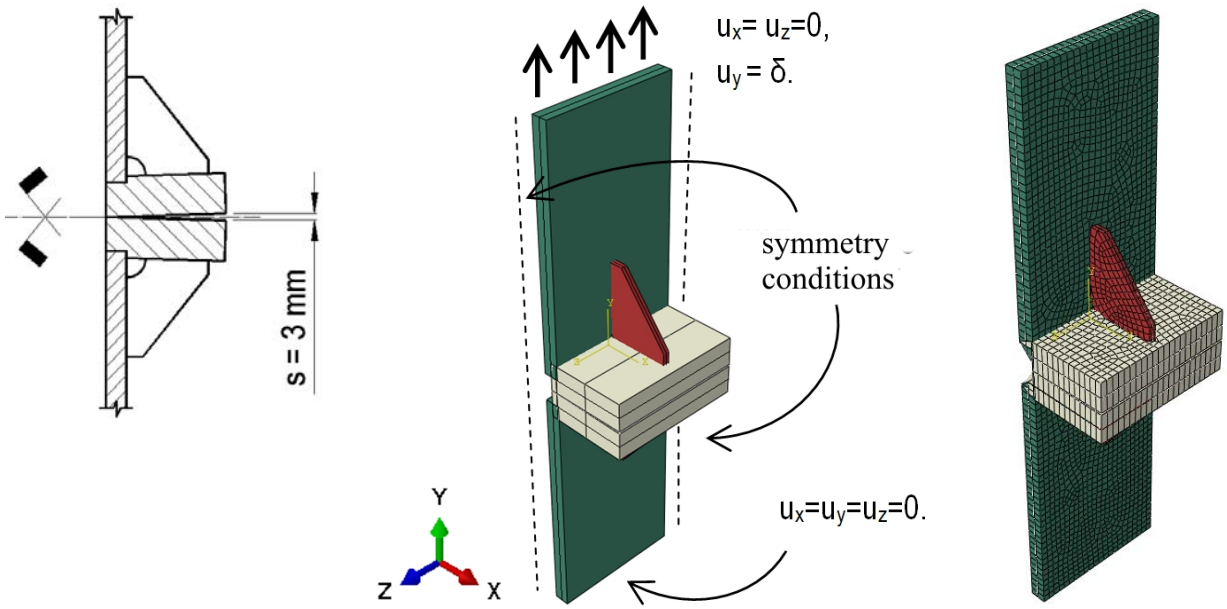

a) b) c)

Fig. 3.3. a) Typical imperfections of joints, b) FEM model of the joint (with boundary conditions), c) FEM mesh for the analyzed problem.

On the basis of performed calculations, the effective properties of the elastically modelled imperfect joint were determined. At first the equivalent stiffness modulus was determined on the basis of the following equation $E_{eq} = F_y / A / \varepsilon \approx 38$ [GPa] where: spire's shell cross-sectional area - $A = 216 \cdot 25 = 5400$ [mm^2], the summary length of the joint - $l = 2 \cdot (2 \cdot 120 + 120 + 45/2) = 765$ [mm] and average strain - $\varepsilon_y = 1.5 / 765$. As it was assumed that the height of the joint modeling zone with increased compliance will be r = 100 [mm], according to Fig. 3.6., it was still necessary to scale the stiffness modulus proportional to the length. Value was finally obtained as equal to $E_{red} = 5.894$ [GPa], and the method of adopting material properties is presented on the example of the first joint from the bottom of the spire, in Fig. 3.6.

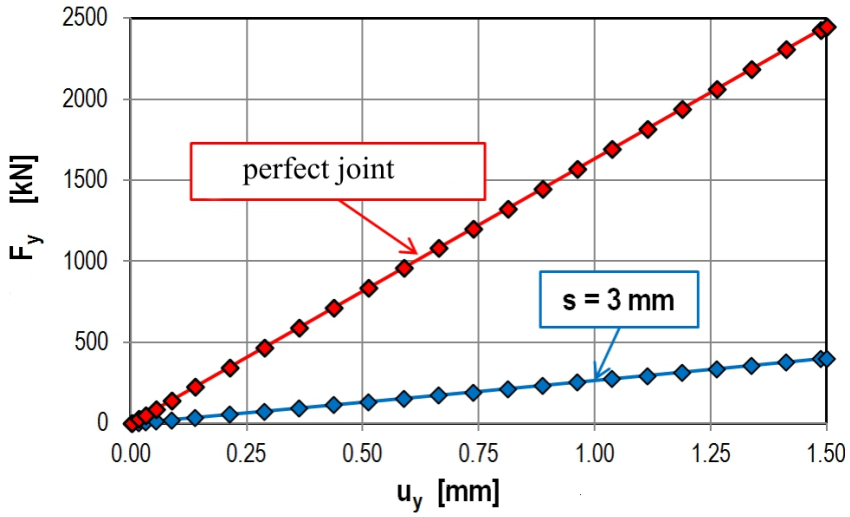

Fig. 3.4. a) The relationship between and displacement in case of perfect and imperfect type of analyzed joints.

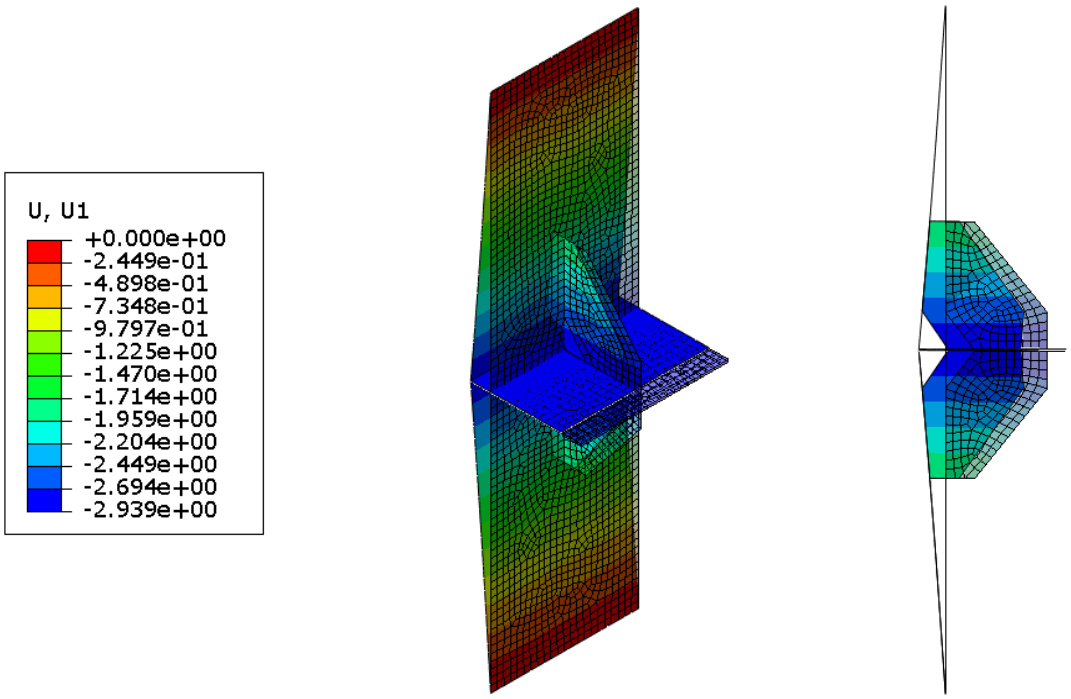

Fig. 3.5. The contour graph of horizontal displacements ($u_1 = u_x$) in the shell model of the joint; the results are given in [mm], the deformation scale factor in the direction of $u_1 = u_x$ is equal to 10.

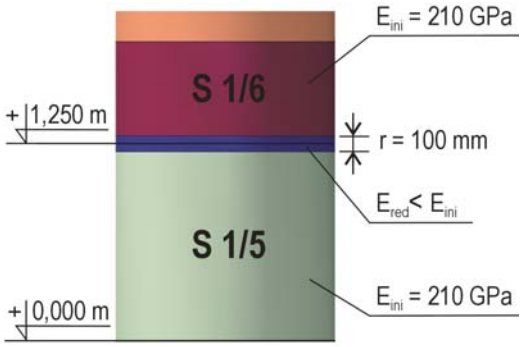

Fig. 3.6 Assuming a reduced value of the steel longitudinal elasticity modulus in the places where individual segments of the spire's shank are joined.

4. ANALYSIS OF THE FEM RESULTS

Four basic variants were adopted in the FEM modelling, i.e. spire with perfect joints supported on rigid slab (v1), spire with imperfect joints supported on rigid slab (v2), spire with perfect joints supported on elastic slab (v3) and spire with imperfect joints supported on elastic slab (v4).

4.1. Determination of natural frequencies

For the analyzed problem, the values and modes of free vibrations of the spire structure were determined, see Tab. 4.1. It is visible that in case of the first (and second) natural frequency considering imperfection of the joint leads to almost 50% reduction of frequency value. This reduction is not so substantial in the following natural frequencies. Also, the fact that spire is positioned on elastic concrete slab influence the results, but in more limited manner.

Table 4.1. Natural frequencies of the spire taking into account imperfection of joints.

Variant	Joints	f_1	f_2	f_3	f_4	f_5	f_6	f_7
v1	Perfect	1.5863	1.5863	6.5217	6.5217	16.183	16.183	16.510
v2	Imperfect	1.0446	1.0446	4.6154	4.6154	11.523	11.523	15.830
v3	Perfect	1.5037	1.5091	6.2549	6.2704	15.424	15.458	16.857
v4	Imperfect	1.0173	1.0190	4.5184	4.5236	11.244	11.259	16.172

When comparing the obtained results presented in Tab. 4.1. in case of spire positioned on rigid slab $f_1 = f_2$ (in some sense that is the same natural frequency value), but in case of the spire mounted on concrete plate $f_1 \neq f_2$ what is the consequence of the fact that dimensions of concrete plate are not symmetrical with respect to spire support middle point (the dimension of the plate were determined on the basis of the building technical documentations as distances to the closest vertical walls). Similar situation may be also observed for higher natural frequency values.
Summarizing, after the evaluation of the obtained results in view of natural frequencies of the structure, only the model for the v4 variant was used for further analyses.

4.2. Wind induced vibrations

After determination of the spire's natural frequencies, the wind induced vibrations may be analyzed. In that case, according to standard's requirements, the spire was loaded on 10 m length (measured from the top) side area of the spire. The uniformly distributed wind load equal to 0.8 kN/m was represented by statically equivalent constant loading q_0. It was assumed that this loading is changing according to the sinusoidal function: $q(t) = q_0 \sin(2\pi f t)$, where f is the loading frequency. Each initial boundary value problem was solved in three steps. In the first step, the self-weight of the structure was statically applied. Then, in the second step, the spire was loaded with sinusoidally changing pressure for $t \in (0, 240)$ s. After this structure excitation phase, there was 120 s free vibration phase. In that phase $q(t) = 0$, for $t \in (240, 360)$ s.
Dynamic problems of step two and three were solved taking into account the structural damping or neglecting this phenomenon (it will be referred to further as "D" - damping or "ND" - no damping cases). Structural damping parameter β used in FEM model was estimated according to procedure given in (Kawecki and Zuranski 2007, Kawecki and Kowalska 2010) as equal to 0.00111777 (see also Mrozek 2010). Mass damping in the solutions naturally results from proper dynamic formulation of the problem.
The first two natural frequencies in case of analyzed variant are very close to each other and this is a certain interpretation problem. Therefore, an analysis of the structure's sensitivity to the load acting on it with frequencies close to the first and second of the previously determined natural frequencies (and values close to them) was carried out leading to results given in Tab. 4.2. The responses of the spire to loading program described with frequencies like in Tab. 4.2. top row is shown in Fig. 4.1. In that graphs the displacement of the top node of the spire is presented as a function of time in case of structures modelled considering damping and without such assumption. For both cases in the analyzed period amplitudes are limited, and in case of "D" are fading very quickly. In the whole analysis the only case without amplitude stabilization (in observation period) was the one with excitation frequency equal to 1.0100 Hz, cf. Fig. 4.1c.

Table 4.2. Extreme values of spire's vibration amplitude for frequencies close to first natural frequency [in cm].

f [Hz]		0.9800	1.0000	1.0100	1.0170	1.0173	1.0190
u_1 ND	max	47	144	850	171	165	137
	min	-44	-141	-849	-167	-161	-134
u_1 D	max	39	83	149	92	90	81
	min	36	-80	-146	-88	-87	-78

ND – no damping, D – damping

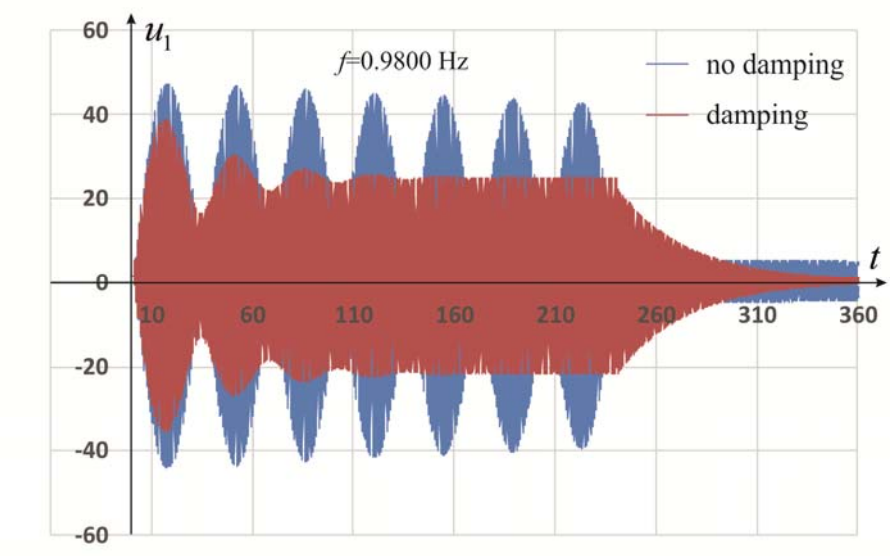
60
40
20
0
-20
-40
-60
u_1
f=0.9800 Hz
no damping
damping
t
10
60
110
160
210
260
310
360

a)

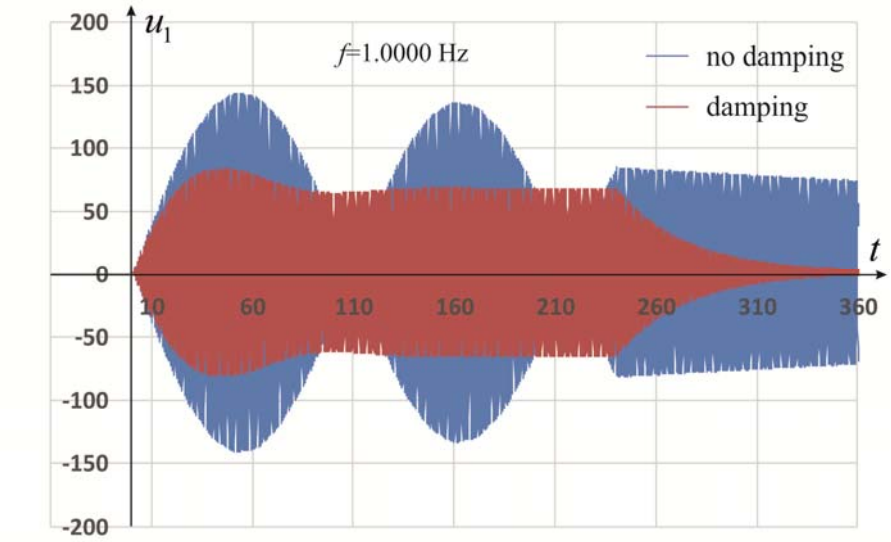
200
150
100
50
0
-50
-100
-150
-200
u_1
f=1.0000 Hz
no damping
damping
t
10
60
110
160
210
260
310
360

b)

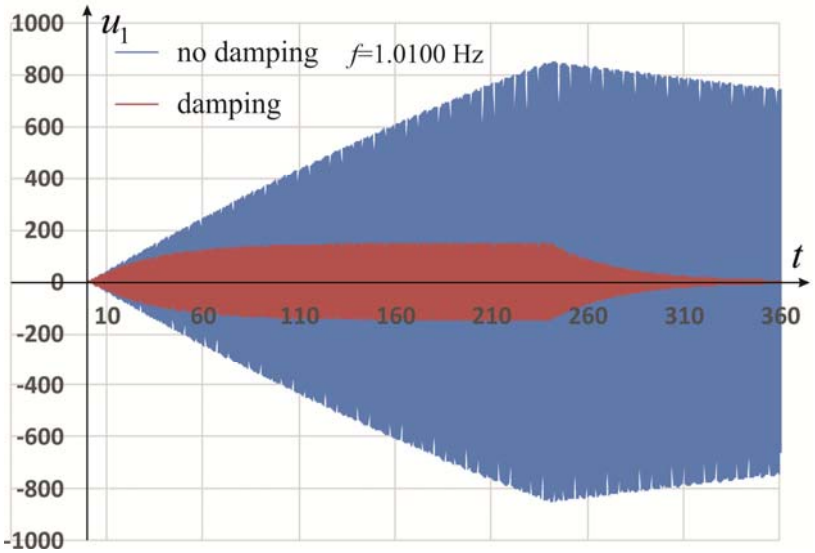
1000
800
600
400
200
0
-200
-400
-600
-800
-1000
u_1
no damping
f=1.0100 Hz
damping
t
10
60
110
160
210
260
310
360

c)

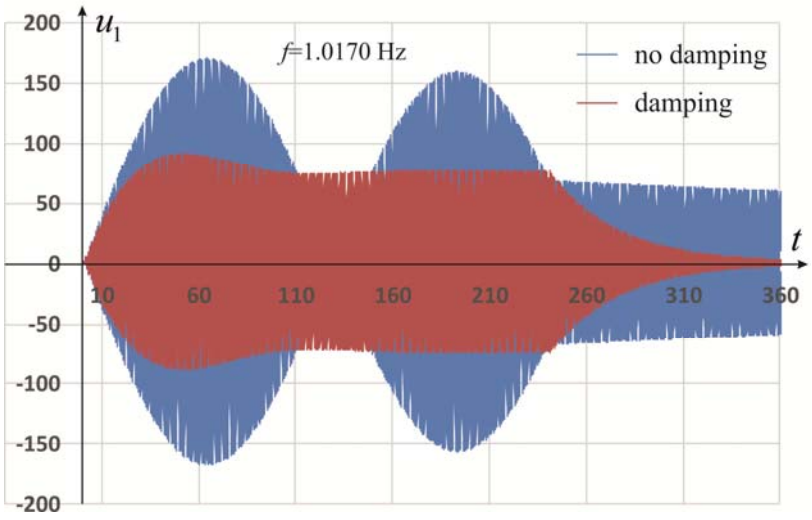

d)

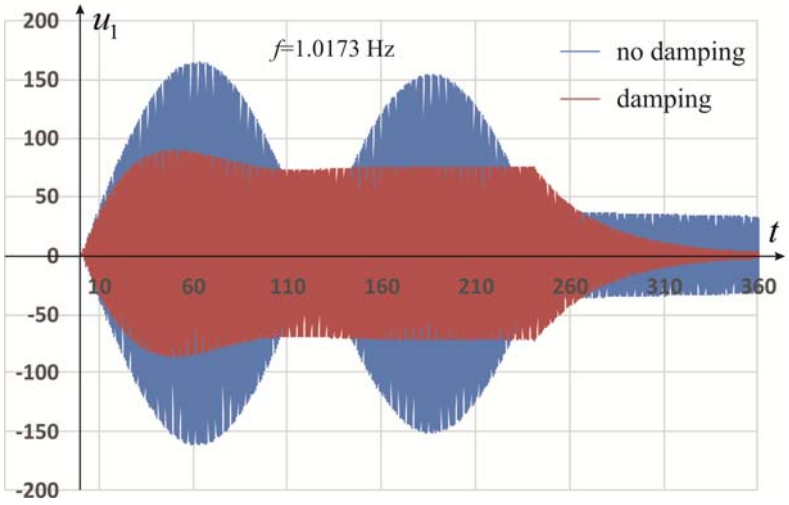

e)

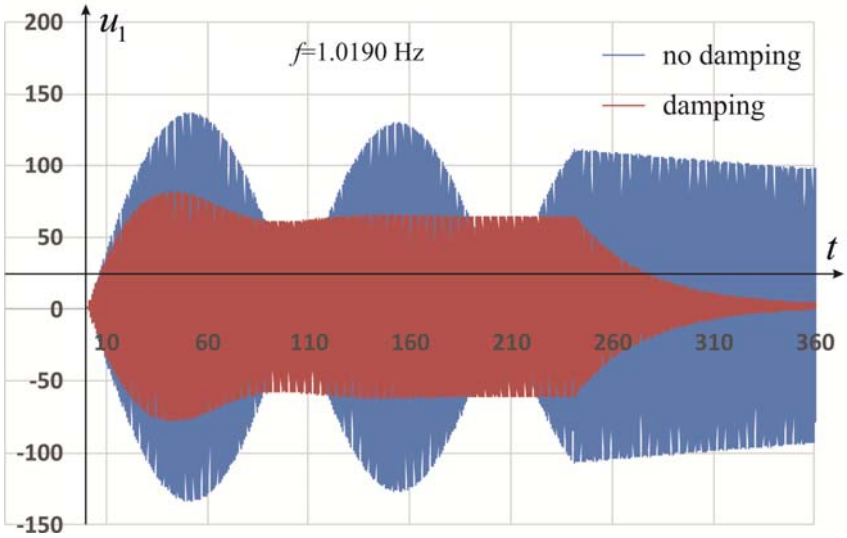

f)

Figure 4.1. Displacement u_1 of the top spire's node in function of time during first and second step of FEM analysis for excitation frequency equal to: a) 0.9800 Hz, b) 1.0000 Hz, c) 1.0100 Hz, d) 1.0170 Hz, e) 1.0173 Hz, f) 1.0190 Hz.

4.3. Solutions for large deformation theory

In this section, the solutions of the vibrating spire obtained within the framework of the theory of large deformations, which is implemented in the ABAQUS program under the NLGEOM option (ABAQUS Theory manual 2011, Jemioło and Gajewski 2014, Ogden 1984), are presented. A distinction can often be seen in the literature between physically and geometrically non-linear theories. It should be emphasized, however, that taking into account the NLGEOM option leads not only to the formal distinction of the deformable body configuration, but also to the constitutive relations between the Kirchhoff stress tensor and the logarithm of the left Cauchy-Green stretch tensor with the material tensor as in the case of the small displacement theory. Formally, the application of this relationship leads to non-linear relationships between the classical stress and strain tensors used in the theory of small displacements and rotations. The application of the large deformation theory is presented on the example marked as variant 4 (v4), assuming the excitation frequency is equal to the first natural frequency for the model, taking into account the compliancy of the concrete supporting plate and the degradation of joints between the components of the tower (i.e. 1.0173 Hz). The obtained results are shown in Fig. 4.2. presenting solutions with and without structural damping.

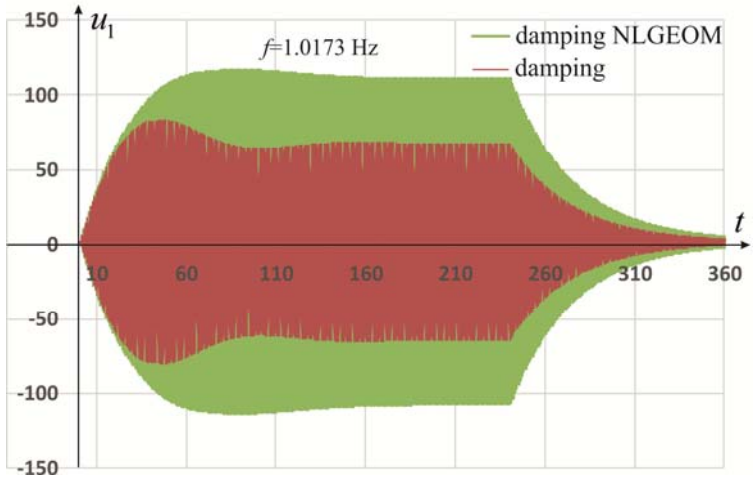

a)

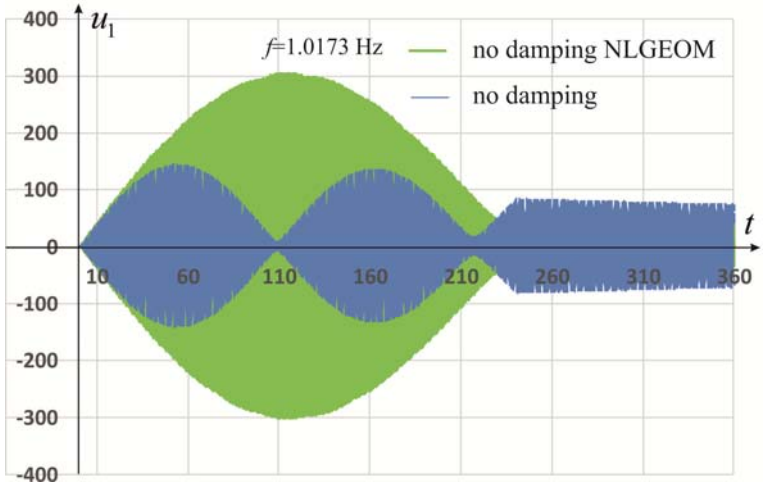

b)

Figure 4.2. Displacement of the top spire's node in function of time during first and second step of FEM analysis for excitation frequency equal to 1.0173 Hz – comparison of results obtained for linear and non-linear theory with and without damping (a) and b) respectively).

5. CONCLUSIONS AND FINAL REMARKS

The amplitude results collected in Tab. 4.2., prove that in real engineering problems it is very important to be careful in estimation of some characteristic designing values (like maximum vibration amplitude). We have substantial differences between the values there, but what is more important the values obtained from finite element analysis are in all cases higher than the value obtained using Eurocode rules (Eurocode 3), (in case of analysed spire maximum amplitude is equal to 66.7 cm).

Based on the FEM analyzes, the following conclusions can be formulated:

1) Considering some imperfections of real structures (e.g. imperfect connections) significantly influences the nature of its dynamic response. Each action of this type, leading to the consideration of real phenomena, leads to a qualitative improvement in the dynamic response of the structure.
2) The values of natural vibration frequencies should be determined with high accuracy.
3) Even in the case of a very precise determination of the natural frequency values and the analysis of near-resonance behavior (i.e. with excitations with a frequency equal to the natural frequencies), it is worth checking the sensitivity of the structure to the excitation frequency values close to the natural frequencies, cf. Fig. 4.1c.
4) Taking into account the structural damping at the same level changes not only the extreme displacement values (amplitude) of vibrations but also their nature (elimination of rumbling). In the case shown in Fig. 4.1c., it changes the resonance behavior to a stable response with a vibration of limited amplitude.
5) Modeling of the structure in the framework of the theory of large deformations leads to a significant increase in the vibration amplitudes of the excited structure (in the case of no damping, see Fig. 4.2b., the increase is more than double).

REFERENCES

Campbell-Dollaghan, K. 2018. *Spire Shame: Why Today's Tallest Buildings Are Mostly Just Spire* [online]. Available: https://gizmodo.com/spire-shame-why-todays-tallest-buildings-are-mostly-j-1264286446 [accessed: 21-Apr-2018].

English, T. 2020. *The World's Tallest Skyscrapers are Actually Made Up of Vanity Height* [online]. Available: https://interestingengineering.com/the-worlds-tallest-skyscrapers-are-actually-made-up-of-vanity-height [accessed: 07-Mar-2021].

Gajewski, M.D., Szczerba, R.B., Giżejowski, M.A., Siennicki M., Wierzbicki S. 2019. *FEM modeling of different factors affecting the cross wind direction vibrations of a tall building steel spire*. Adv. Eng. Mater. Struct. Syst. Innov. Mech. Appl. - Proc. 7th Int. Conf. Struct. Eng. Mech. Comput.: 67-74.

EN 1991-1-4. *Eurocode 1: Actions on structures -Part 1-4: General actions -Wind actions* 2005.

ABAQUS/Standard User's manual. Version 6.11, Dassault Systèmes, 2011.

ABAQUS Theory manual. Version 6.11, Dassault Systèmes, 2011.

Kawecki, J., Zuranski, J.A. 2007. *Cross-wind vibrations of steel chimneys--A new case history: The Fourth European and African Conference on Wind Engineering*. J. Wind Eng. Ind. Aerodyn.

Kawecki, J., Kowalska, A. 2010. *Tłumienie drgań w opisie sztywnościowo-bezwładnościowym.* Czas. Tech. Bud. 107(11): 43–50.

Mrozek, D. 2010. *Nieliniowa analiza numeryczna dynamicznej odpowiedzi uszkodzonych budynków*. Gliwice: Politechnika Śląska w Gliwicach.

Jemioło, S., Gajewski, M. 2014. *Hipersprężystoplastyczność*. Warszawa: Oficyna Wydawnicza Politechniki Warszawskiej.

Ogden, R.W. 1984. *Non-linear elastic deformations*. Chichester: Ellis Horwood.

Eurocode 3 - Design of steel structures - Part 3-2: Towers, masts and chimneys - Chimneys," *Eurocode 3*, 1993.

LIGHTWEIGHT STRUCTURES in CIVIL ENGINEERING
CONTEMPORARY PROBLEMS
Monograph from Scientific Seminar
Organized by Polish Chapters of
International Association for Shell and Spatial Structures
Łódź University of Technology
Faculty of Civil Engineering, Architecture
and Environmental Engineering
XXVII LSCE
Łódź, 2nd – 3rd of December 2021

INFLATION OF HYPERELASTIC INCOMPRESSIBLE CYLINDER

S. Jemioło [1] **A. Franus** [2]
[1] Professor, Faculty of Civil Engineering, Warsaw University of Technology, POLAND,
s.jemiolo@il.pw.edu.pl
[2] MSc, Faculty of Civil Engineering, Warsaw University of Technology, POLAND,
aleksander.franus.dokt@pw.edu.pl

ABSTRACT: The paper presents a study on mathematical modelling an inflation of rubber, cylindrical tube. It begins with a definition of the stored energy function of the hyperelastic models under consideration. The main part of the paper concerns the axially symmetric stress formulation of the inflation problem, which may accurately approximate a sufficiently long tube. The boundary value problem is formulated base on polynomial and non-polynomial constitutive models. It can considered as a benchmark problem for hybrid formulation of the finite element method.

Keywords: hyperelasticity, cylindrical tube, inflation, incompressibility, rubber.

1. INTRODUCTION

In this chapter, we consider axisymmetric deformations of an infinitely long cylindrical tube modelled with a hyperelastic, incompressible rubber-like material, cf. (Bharatha 1967, Ogden 1984). Our main goal is to determine the stress state that refers to the phenomenon of the so-called cylinder inflation. We consider the class of constitutive models discussed and proposed in the work of the first author (Jemioło 2002) and some selected models of hyperelasticity used in the biomechanics of soft tissues (Jemioło and Telega 2001, Jemioło 2016). We analyse in detail material models for which we obtain analytical solutions to the associated boundary value problems.

In the literature, a large number of constitutive relations are proposed to describe the nonlinear, elastic properties of a given material, with their similar agreement with the results of basic experimental data (Jemioło 2016). In the case of rubber-like materials, the volumetric compressibility modulus is a few orders of magnitude larger than the shear modulus $K_0 >> \mu_0$ (Alexander 1968, Treloar 1944).

Therefore, when interpreting typical experimental results of uniaxial and biaxial stretching and simple shear, universal relationships concerning incompressible material models are used (Adkins 1961). These tests describe homogeneous deformations of the tested material samples.

Based on the comparison of the results of these tests with the theoretical formulas resulting from the constitutive relation, material parameters are determined (Franus and Jemioło 2019).

Therefore, the validation of hyperelasticity models also requires the interpretation of the results of experiments where non-uniform deformations occur.

Analytical solutions are known to very few problems, e.g. symmetrical deformations of the cylindrical tube and the hollow ball (Jemioło 2002). In the work, we follow the standard tensor notation of the mechanics of continuous media and the theory of hyperelasticity (Bonet et al. 2016, Holzapfel 2010).

2. BASIC RELATIONSHIPS OF HYPERELASTIC INCOMPRESSIBLE ISOTROPIC MATERIALS

2.1.The boundary value problem of hyperelasticity

In the case of an incompressible material model, the stored energy function W is not a potential of elasticity, because the volumetric part of the Cauchy stress tensor is not determined (Jemioło 2002, Holzapfel 2010). The material may be subjected only to isochoric deformations, i.e. deformations without changing the volume of the body. Mathematically, deformation of the incompressible body is constrained by the condition

$$J-1=0, \tag{2.1}$$

where $J=\det\mathbf{F}$ is the determinant of so-called the deformation gradient $\mathbf{F}$ (Ciarlet 1998):

$$\mathbf{F}=\frac{\partial\mathbf{x}}{\partial\mathbf{X}}. \tag{2.2}$$

$\mathbf{X}$ is the vector of the position of a body particle in the initial configuration, and $\mathbf{x}$ is the vector of the position of the body particle in its current configuration.
In quasi-static hyperelasticity problems without inertial forces, the following equilibrium equations in the initial body configuration hold:

$$\mathrm{Div}\,\mathbf{S}=\mathbf{0},\ \ \mathbf{S}\mathbf{F}^{T}=\mathbf{F}\mathbf{S}^{T}, \tag{2.3}$$

which in the current configuration are equivalent to the equations:

$$\mathrm{div}\boldsymbol{\sigma}+\mathbf{f}=\mathbf{0},\ \ \boldsymbol{\sigma}=\boldsymbol{\sigma}^{T}, \tag{2.4}$$

where $\mathbf{S}$ and $\boldsymbol{\sigma}$ are called the first Pioli-Kirchoff stress tensor and the Cauchy stress tensor, respectively. These tensors are related such that

$$\mathbf{S}=J\boldsymbol{\sigma}\mathbf{F}^{-T}. \tag{2.5}$$

For the incompressible material model, the elastic potential must incorporate the constraint (2.1) with the Lagrange multiplier p, which should be interpreted as hydrostatic pressure. From the basic relationships of continuum mechanics and the principle of the conservation of mechanical energy together with (2.1) it follows the constitutive relation

$$\mathbf{S}=\frac{\partial W}{\partial\mathbf{F}}-p\left(\mathbf{F}^{T}\right)^{-1}. \tag{2.6}$$

A formulation of the quasi-static boundary value problem of hyperelasticity also requires kinematic equations and boundary conditions to be specified (Ogden 1984).

2.2. Constitutive relations

The stored energy function (SEF) W depends on a deformation tensor, which results from the principle of objectivity, but is not dependent on their determinants.
Therefore, the tensor $\mathbf{F}$ is decomposed into the isochoric and volumetric part as follows:

$$\mathbf{F} = J^{1/3}\overline{\mathbf{F}}, \quad \det\overline{\mathbf{F}} = 1. \tag{2.7}$$

Further, we introduce

$$\overline{\mathbf{B}} = \overline{\mathbf{F}}\overline{\mathbf{F}}^{T}, \quad \overline{\mathbf{C}} = \overline{\mathbf{F}}^{T}\overline{\mathbf{F}}, \tag{2.8}$$

where $\overline{\mathbf{B}}$ and $\overline{\mathbf{C}}$ denote the modified left and the right Cauchy-Green deformation tensors, cf. (Holzapfel 2010).
In the case of incompressible isotropic materials, SEF is a function of only two modified invariants such that (Bonet et al. 2016)

$$W = W\left(\overline{\mathbf{C}}\right) = W\left(\overline{\mathbf{B}}\right) = \overline{W}\left(\overline{I}_1, \overline{I}_2\right), \tag{2.9}$$

where

$$\overline{I}_1 = \mathrm{tr}\overline{\mathbf{B}} = \mathrm{tr}\overline{\mathbf{C}}, \quad \overline{I}_2 = \mathrm{tr}\overline{\mathbf{B}}^{-1} = \mathrm{tr}\overline{\mathbf{C}}^{-1}. \tag{2.10}$$

These can be written as

$$\overline{I}_1 = J^{-\frac{2}{3}} I_1, \quad \overline{I}_2 = J^{-\frac{4}{3}} I_2, \tag{2.11}$$

where

$$I_1 = \mathrm{tr}\,\mathbf{B} = \mathrm{tr}\,\mathbf{C}, \quad I_2 = \mathrm{tr}\left(\mathrm{cof}\,\mathbf{B}\right) = \mathrm{tr}\left(\mathrm{cof}\,\mathbf{C}\right), \quad J = \sqrt{\det\mathbf{B}} = \sqrt{\det\mathbf{C}}. \tag{2.12}$$

Then, the constitutive relationship in the current configuration yields

$$\boldsymbol{\sigma} = -p\mathbf{I} + 2\frac{\partial\overline{W}\left(\overline{I}_1, \overline{I}_2\right)}{\partial\overline{I}_1}\overline{\mathbf{B}} - 2\frac{\partial\overline{W}\left(\overline{I}_1, \overline{I}_2\right)}{\partial\overline{I}_2}\overline{\mathbf{B}}^{-1} \equiv -p\mathbf{I} + \overline{\beta}_1\overline{\mathbf{B}} + \overline{\beta}_{-1}\overline{\mathbf{B}}^{-1}. \tag{2.13}$$

3. MODELS OF INCOMPRESSIBLE ISOTROPIC HYPERELASTIC MATERIALS

3.1. Model MV and its special cases

In this chapter we consider the MV model proposed in the monograph (Jemioło 2002) with the following SEF:

$$\overline{W}\left(\overline{I}_1,\overline{I}_2\right)=\frac{1}{2}\Big[a_1\left(\overline{I}_1-3\right)+\frac{1}{2}a_2\left(\overline{I}_1^2-9\right)+\frac{1}{3}a_3\left(\overline{I}_1^3-27\right)+a_4\left(\overline{I}_2-3\right)+a_5\left(\overline{I}_1\overline{I}_2-9\right)\Big], \tag{3.1}$$

where $a_k\ (k=1,\ldots,5)$ are the parameters of the model. The functions in constitutive relation (2.13) are given by

$$\overline{\beta}_1=2\frac{\partial\overline{W}}{\partial\overline{I}_1}=a_1+a_2\overline{I}_1+a_3\overline{I}_1^2+a_5\overline{I}_2,\quad \overline{\beta}_{-1}=-2\frac{\partial\overline{W}}{\partial\overline{I}_2}=-a_4-a_5\overline{I}_1. \tag{3.2}$$

Basic invariants $\overline{I}_1$ and $\overline{I}_2$, due to the constraints of incompressibility (2.1), can be considered as functions of only two independent eigenvalues $\overline{\lambda}_1$ and $\overline{\lambda}_2$ of the stretch tensors $\overline{\mathbf{U}}=\sqrt{\overline{\mathbf{C}}}$ and $\overline{\mathbf{V}}=\sqrt{\overline{\mathbf{B}}}$, i.e.:

$$\overline{I}_1=\overline{\lambda}_1^2+\overline{\lambda}_2^2+\left(\overline{\lambda}_1\overline{\lambda}_2\right)^{-2},\ \overline{I}_2=\overline{\lambda}_1^{-2}+\overline{\lambda}_2^{-2}+\left(\overline{\lambda}_1\overline{\lambda}_2\right)^{2}. \tag{3.3}$$

The constrains of incompressibility implie that $\overline{\lambda}_3=\left(\overline{\lambda}_1\overline{\lambda}_2\right)^{-1}$. Principal stretches $\overline{\lambda}_1$ and $\overline{\lambda}_2$ are independent but they are unordered eigenvalues of stretch tensors. It is easy to check that the function $\overline{I}_1$ is a convex function with respect to $\overline{\lambda}_1$ and $\overline{\lambda}_2$ while the function $\overline{I}_2$ is not a convex function with respect to $\overline{\lambda}_1$ and $\overline{\lambda}_2$, for sufficiently large deformations (Jemioło 2002).

The stored energy function of the MV model (2.11) can be written in the equivalent form

$$\overline{W}=U\left(\overline{I}_1,\overline{I}_2\right)=C_{10}\left(\overline{I}_1-3\right)+C_{20}\left(\overline{I}_1-3\right)^2+C_{30}\left(\overline{I}_1-3\right)^3+C_{01}\left(\overline{I}_2-3\right)+C_{11}\left(\overline{I}_1-3\right)\left(\overline{I}_2-3\right), \tag{3.4}$$

where

$$\begin{aligned}&C_{10}=\frac{1}{2}\left(a_1+3a_2+9a_3+3a_5\right),\ C_{20}=\frac{1}{4}\left(a_2+6a_3\right),\\ &C_{30}=\frac{1}{6}a_3,\ C_{01}=\frac{1}{2}\left(a_4+3a_5\right),\quad C_{11}=\frac{1}{2}a_5.\end{aligned} \tag{3.5}$$

The function (3.1) is a special case of the Rivlin SEF (3.4) with constants:

$$\begin{aligned}&a_1=2\left(C_{10}-3C_{11}-6C_{20}+27C_{30}\right),\quad a_2=4\left(C_{20}-9C_{30}\right),\quad a_3=6C_{30},\\ &a_4=2\left(C_{01}-3C_{11}\right),\quad a_5=2C_{11}.\end{aligned} \tag{3.6}$$

The material functions in constitutive relation (2.13) are of the form

$$\bar{\alpha}_1 = \frac{1}{2}\bar{\beta}_1, \quad \bar{\alpha}_2 = -\frac{1}{2}\bar{\beta}_2,$$
$$\bar{\beta}_1 = 2\frac{\partial U}{\partial \bar{I}_1} = a_1 + a_2\bar{I}_1 + a_3\bar{I}_1^2 + a_5\bar{I}_2, \quad \bar{\beta}_{-1} = -2\frac{\partial U}{\partial \bar{I}_2} = -a_4 - a_5\bar{I}_1. \tag{3.7}$$

Moreover, the initial shear modulus is given by

$$\mu_0 = a_1 + 3a_2 + 9a_3 + a_4 + 6a_5 = 2\left(C_{10} + C_{01}\right). \tag{3.8}$$

From (3.1) other well-known stored energy functions of incompressible hyperelastic material models may be obtained.

By neglecting the factor with the coupling of the first and second invariant of isochoric deformation we have the SEF equivalent to the Biderman model (MB) from 1958, cf. (Jemioło and Suchocki 2019). If we additionally omit the factor referring to the second invariant an equivalent form of the Yeoh model (MY) is recovered (Jemioło 2002).

On the order hand, taking $a_2 = a_3 = 0$ yields the Mooney model (MR). The simplest SEF of incompressible yields the neo-Hookean (NH) model, where there is only one non-zero constant of the interpretation of the initial shear modulus, i.e. $a_1 = \mu_0$.

Setting $a_3 = 0$, $a_5 = 0$ Ishihara-Zahorski model is recovered (MIZ), cf. (Zahorski 1959). The stored energy function can be expressed in the form:

$$\bar{W}\left(\bar{I}_1, \bar{I}_2\right) = \frac{1}{2}\mu_0\left[f\left(\bar{I}_1 - 3\right) + \left(1 - f\right)\left(\bar{I}_2 - 3\right) + \frac{1}{2}\bar{c}\left(\bar{I}_1 - 3\right)^2\right], \tag{3.9}$$

with the initial shear modulus $\mu_0 > 0$ and two material parameters such that $f \in (0,1)$, $\bar{c} > 0$.

We emphasize that functions (3.1) and (3.9) are respectively consistent third and second-order approximation of existing stored energy function in term of $\|\bar{\mathbf{C}}\|$, cf. (Jemioło and Franus 2019). In the case of rubber-like materials, typical experimental tests of homogeneous deformations from which material parameters are determined are uniaxial and biaxial stretching tests (interpreted as plane stress state tests) and uniaxial compression/tension tests, assuming a plane deformation state (PDS).

In the above-mentioned tests, principal stretches and nominal stresses are measured. In the case of the rubber material models analysed here, the material parameters are determined by simultaneous approximation of Treloar's (Treloar 1944) and Alexander's (Alexander 1968) experimental data, see Table 3.1.

Table 3.1. Parameters for Alexander's data (Alexander 1968) (neoprene).

Model	a_1 [MPa]	a_2 [MPa]	a_3 [MPa]	a_4 [MPa]	a_5 [MPa]
MR	3.513×10^{-1}	-	-	1.364×10^{-2}	-
MV	3.152×10^{-1}	-6.469×10^{-3}	1.173×10^{-4}	1.899×10^{-2}	-3.011×10^{-4}

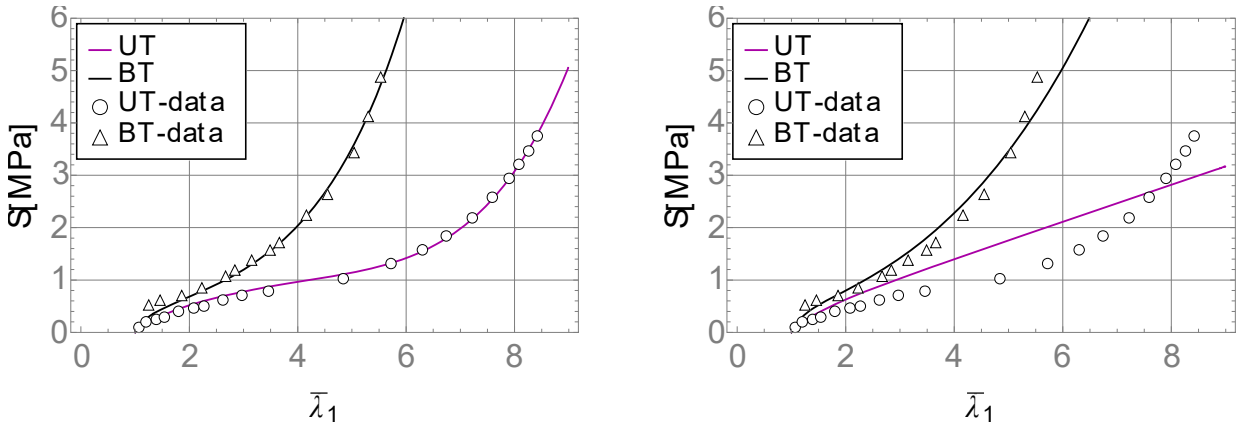

Fig. 3.1. Nominal stress vs principal stretch plots for uniaxial (UT) and biaxial (BT) tension modes in the case of Alexander's data – a) MV model, b) MR model. Parameters are presented in Tab. 3.1.

3.2. Non-polynomial material models

An extensive review of the constitutive models of isotropic incompressible materials is provided in the monograph (Jemioło 2002).

In this chapter, we will consider only two classes of non-polynomial models that are generalizations of the Gent's (Gent 1996) and Demiray's (Demiray 1972) models. The SEF of the Gent's model is given by

$$W = \bar{W}_G\left(\bar{I}_1\right) = -\frac{\mu_0}{2} g \ln\left(1 - \frac{\bar{I}_1 - 3}{g}\right), \tag{3.10}$$

where $\mu_0 > 0$ and $\bar{I}_1 < 3 + g$. If $\bar{I}_1 \to 3 + g$, then $\bar{W}_G \to +\infty$. It yields

$$\lim_{g \to +\infty} \bar{W}_G = \frac{\mu_0}{2}\left(\bar{I}_1 - 3\right) \equiv \bar{W}_{NH}\left(\bar{I}_1\right), \tag{3.11}$$

where $\bar{W}_{NH}\left(\bar{I}_1\right)$ is the SEF of an incompressible neo-Hooke material (NH).

The function (3.10), around the natural state ($\bar{I}_1 \cong 3$), can be approximated such that

$$\bar{W}_{NH}\left(\bar{I}_1\right) + \frac{\mu_0}{2} \sum_{n=2}^{N} \frac{\left(\bar{I}_1 - 3\right)^n}{n g^{n-1}} + O\left(\bar{I}_1 - 3\right)^{N+1}, \tag{3.12}$$

It should be emphasized that μ_0 is an initial shear modulus with the same value as in the Hooke relation of incompressible materials in the linear theory of elasticity.

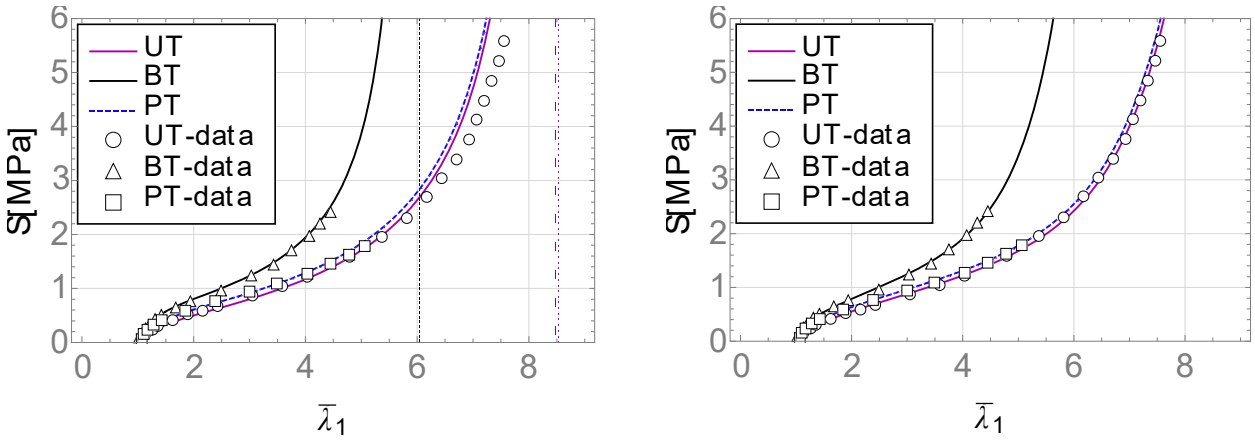

Fig. 3.2. Nominal stress vs principal stretch plots for uniaxial (UT) tension, biaxial (BT) tension and planar tension (PT) modes in the case of Treloar's data – a) UMG model, b) HMG model.

In the work of the first author (Jemioło 2016), the following generalization of the SEF of Gent's model was proposed:

$$W = \bar{W}_{UG}\left(\bar{I}_1,\bar{I}_2\right) = -\frac{\mu}{2} g \ln\left(1-\frac{\bar{I}_1-3}{g}\right) + b\left(\bar{I}_1^{\alpha}-3^{\alpha}\right) + c\left(\bar{I}_2^{\beta}-3^{\beta}\right), \tag{3.13}$$

where, $\mu > 0$, $g > 0$, $\bar{I}_1 < 3+g$ and b, c, α, β are material parameters. It holds

$$\mu_0 = \mu + \frac{2}{3}\left(\alpha b 3^{\alpha} + \beta c 3^{\beta}\right). \tag{3.14}$$

Fig. 3.2a shows the results of Treloar's experiments (rubber, 8% sulfur) and the theoretical curves predicted by the UMG model (3.13). Currently, the material parameters of UMG are as follows: $\mu \cong 0.255$ MPa, $g \cong 78.344$, $b \cong -1.482\,10^{-5}$ MPa, $\alpha \cong 2.702$, $c \cong 2.496\,10^{-1}$ MPa, $\beta \cong 0.386$, i.e. $\mu_0 \cong 0.352$ MPa.
The SEF of Demiray's model is given by

$$\bar{W}_B\left(\bar{I}_1\right) = \frac{\mu_0}{2} g\left[\mathrm{Exp}\left(\frac{\bar{I}_1-3}{g}\right)-1\right], \tag{3.15}$$

where $\mu_0 > 0$ and $g > 0$. Similar to the Gent model, we have

$$\lim_{g\to+\infty} \bar{W}_B = \bar{W}_{NH}\left(\bar{I}_1\right), \tag{3.16}$$

A generalization of the SEF of Demiray's model may be stated as (Jemioło 2016)

$$W = \bar{W}_{HG}\left(\bar{I}_1,\bar{I}_2\right) = \frac{\mu}{2} a\left[\mathrm{Exp}\left[a\left(\bar{I}_1-3\right)\right]-1\right] + \frac{b}{2\alpha}\left(\bar{I}_1^{\alpha}-3^{\alpha}\right) + \frac{c}{2\beta}\left(\bar{I}_2^{\beta}-3^{\beta}\right), \tag{3.17}$$

where b, c, α, β and μ are material parameters. Figure 3.2b shows the results of Treloar's experiments and the theoretical curves predicted by the HMG model (3.17). HMG material parameters are as follows: $\mu \cong 2.590\,10^{-2}$ MPa, $g \cong 18.127$, $b \cong 0.528$ MPa, $\alpha \cong 0.958$, $c \cong 0.116$ MPa, $\beta \cong 0.482$, $\mu_0 \cong 0.357$ MPa.

4. INFLATION OF A CYLINDRICAL TUBE

We consider axisymmetric deformations of an infinitely long cylindrical tube modelled with an incompressible material model, cf. (Bharatha 1967, Ogden 1984, Jemioło 2002). The problem is set in cylindrical coordinates (R,Φ,Z) and (r,ϕ,z), respectively, in the initial configuration and the current configuration. Boundary conditions are given as prescribed displacements with parameters: inner radius R_i and outer radius R_o in a reference configuration, see Figure 4.1. The geometry of the problem shows that the eigenvalues of the stretch tensors are as follows:

$$\lambda_r = \frac{\mathrm{d}r}{\mathrm{d}R}, \quad \lambda_\phi = \frac{r}{R}, \quad \lambda_z = 1, \tag{4.1}$$

where $r = r(R)$. In each cross-section of the tube perpendicular to $z = Z$, we have the plain strain state (PDS) and deformations independent of the coordinates $\phi = \Phi$. From the incompressibility constraints (2.1) and (4.1) we have

$$\lambda_\phi = \lambda_r^{-1}, \quad \frac{\mathrm{d}r}{\mathrm{d}R} = \frac{R}{r}. \tag{4.2}$$

Hence, it holds

$$R(r) = \sqrt{r^2 + a}\,. \tag{4.3}$$

where $a = const$. If $a < 0$, then the radius of the cylinder increases, and if $a > 0$, then the radius of the cylinder decreases. Eq. (4.1) – (4.3) describe the "inflation" of the cylinder such that its length does not change and the incompressibility condition is met.

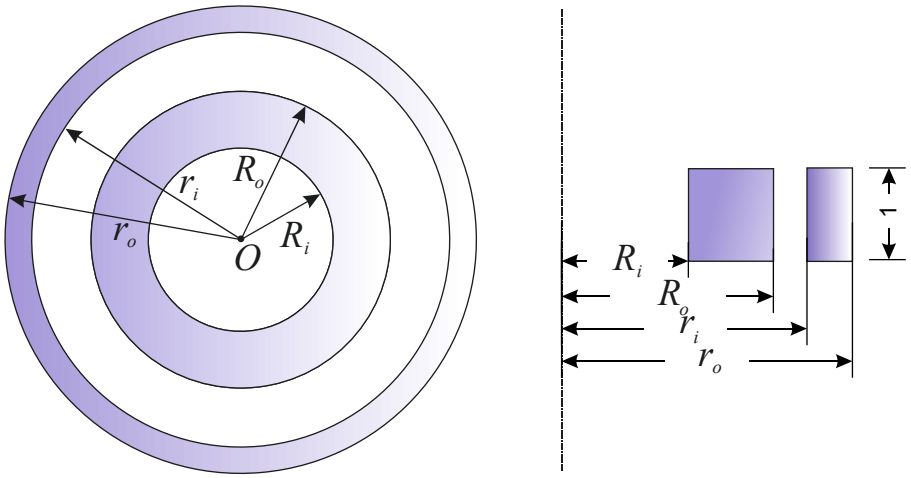

Fig. 4.1. Reference and current configuration of the cross-section of the cylindrical tube.

We consider two specific cases of cylindrical tube deformation:
a) the displacement of the inner surface of the cylinder is set,

$$a = R_i^2 - r_i^2, \tag{4.4}$$

$$\sigma_r\left(r_o\right) = 0, \quad r_o = \sqrt{R_o^2 - a}\,, \tag{4.5}$$

b) the displacement of the outer surface of the cylinder is prescribed,

$$a = R_o^2 - r_o^2, \tag{4.6}$$

$$\sigma_r\left(r_i\right) = 0, \quad r_i = \sqrt{R_i^2 - a}\,, \tag{4.7}$$

where r_i denotes the inner radius and r_o is the outer radius in the deformed configuration. Substituting (4.3) to (4.1) we obtain eigenvalues of the left Cauchy-Green tensor in the current configuration

$$\lambda_r^2 = \frac{r^2 + a}{r^2}, \quad \lambda_\phi^2 = \lambda_r^{-2} = \frac{r^2}{r^2 + a}\,. \tag{4.8}$$

Next, substituting

$$\begin{aligned} &\overline{\mathbf{B}} = \lambda_r^2 \mathbf{e}_r \otimes \mathbf{e}_r + \lambda_r^{-2} \mathbf{e}_\varphi \otimes \mathbf{e}_\varphi + \mathbf{e}_z \otimes \mathbf{e}_z, \quad \overline{\mathbf{B}}^{-1} = \lambda_r^{-2} \mathbf{e}_r \otimes \mathbf{e}_r + \lambda_r^2 \mathbf{e}_\varphi \otimes \mathbf{e}_\varphi + \mathbf{e}_z \otimes \mathbf{e}_z, \\ &\overline{I}_1 = \overline{I}_2 = \lambda_r^2 + \lambda_r^{-2} + 1, \end{aligned} \tag{4.9}$$

into (2.13), we obtain the physical components of the Cauchy stress tensor

$$\begin{aligned} \sigma_r &= -p\left(r\right) + \overline{\beta}_1 \lambda_r^2 + \overline{\beta}_{-1} \lambda_r^{-2}, \\ \sigma_\phi &= -p\left(r\right) + \overline{\beta}_1 \lambda_r^{-2} + \overline{\beta}_{-1} \lambda_r^2, \\ \sigma_z &= -p\left(r\right) + \overline{\beta}_1 + \overline{\beta}_{-1}. \end{aligned} \tag{4.10}$$

The unknown hydrostatic pressure (Lagrange multiplier) is established from the equilibrium equation

$$\frac{\mathrm{d}\sigma_r}{\mathrm{d}r} + \frac{\sigma_r - \sigma_\phi}{r} = 0\,, \tag{4.11}$$

and boundary conditions (4.9) or (4.10).
In the case of the MV, we obtain

$$\begin{aligned} \overline{\beta}_1\left(r\right) &= a_1 + \left(a_2 + a_5\right)\left(2 + \frac{a}{r^2} + \frac{r^2}{r^2 + a}\right) + a_3\left(2 + \frac{a}{r^2} + \frac{r^2}{r^2 + a}\right)^2, \\ \overline{\beta}_{-1}\left(r\right) &= -a_4 - a_5\left(2 + \frac{a}{r^2} + \frac{r^2}{r^2 + a}\right). \end{aligned} \tag{4.12}$$

The differential equation (4.11) yields

$$p(r)=\frac{1}{2}(a_1+3a_2+11a_3-a_4)\frac{a}{r^2}+\frac{1}{4}(3a_2+15a_3+2a_5)\frac{a^2}{r^4}+\frac{5}{6}a_3\frac{a^3}{r^6}+$$
$$-\frac{1}{2}(a_2+6a_3-2a_4-4a_5)\frac{a}{r^2+a}+\frac{1}{4}(a_3-4a_5)\frac{a^2}{(r^2+a)^2}+ \tag{4.13}$$
$$+\frac{1}{2}(a_1+2a_2+5a_3+a_4+4a_5)\ln\frac{r^2}{r^2+a}+C,$$

where

$$C=a_1+3a_2+9a_3-a_4+\frac{1}{2}(a_2+4a_3+2a_5)\frac{a}{R_o^2}-\frac{1}{4}a_3\frac{a^2}{R_o^4}+$$
$$+\frac{1}{2}(a_1+3a_2+9a_3+a_4+6a_5)\frac{a}{R_o^2-a}+\frac{1}{4}(a_2+5a_3+2a_5)\frac{a^2}{(R_o^2-a)^2}+ \tag{4.14}$$
$$+\frac{1}{6}a_3\frac{a^3}{(R_o^2-a)^3}+\frac{1}{2}(a_1+2a_2+5a_3+a_4+4a_5)\ln\frac{R_o^2}{R_o^2-a}.$$

Substituting (4.12) into (4.10), we obtain the physical components of the Cauchy stress state in the configuration of the current cylinder in the case of deformation a) and b). The constant occurring in (4.11) needs to be determined from boundary condition We do not give the final formulas for the MV as they are quite lengthy. Components of the first Piola-Kirchhoff stress tensor are given by

$$S_r=\lambda_r^{-1}\sigma_r,\quad S_\phi=\lambda_r^{-1}\sigma_\phi,\quad S_z=\sigma_z. \tag{4.15}$$

Simple formulas for the components of the stress state are obtained in the case of MR and NH models. Then, we consider the following set of material parameters:

$$a_1=\mu_0 f,\quad a_4=\mu_0(1-f),\quad a_2=a_3=a_5=0. \tag{4.16}$$

5. SOLUTION TO THE BOUNDARY VALUE PROBLEM

5.1. NH and MR material models

Relatively simple formulas for the components of the stress state are obtained in the case of the MR and NH models. It holds

$$\overline{\beta}_1=\mu_0 f,\quad \overline{\beta}_{-1}=-\mu_0(1-f) \tag{5.1}$$

The NH and MR models in the case of PDS lead to an identical form of the SEF. Hence, the stress states σ_r and σ_ϕ are the same for the models, respectively.
From (3.10) and (5.1) in the case of the NH material, it follows that

$$\begin{aligned}
\sigma_r &= -p(r) + \mu_0 \lambda_r^2 = -p(r) + \mu_0 \frac{r^2 + a}{r^2}, \\
\sigma_\phi &= -p(r) + \mu_0 \lambda_r^{-2} = -p(r) + \mu_0 \frac{r^2}{r^2 + a}, \\
\sigma_z &= -p(r) + \mu_0.
\end{aligned} \tag{5.2}$$

After substituting (5.2) into (3.11) we have

$$\frac{\mathrm{d}p(\mathrm{r})}{\mathrm{d}r} = -\mu_0 \frac{a^2}{\left(r^2 + a\right) r^3} \quad \Rightarrow \quad p(\mathrm{r}) = \frac{\mu_0}{2}\left(\frac{a}{r^2} + \ln \frac{r^2}{r^2 + a} \right) + C, \tag{5.3}$$

where $C = const$. We determine the constant from the boundary conditions of the problem a) or b). In the case of a) $\sigma_r(r_o) = 0, \quad r_o = \sqrt{R_o^2 - a}$, it holds

$$C = \frac{\mu_0}{2}\left(1 + \frac{R_o^2}{r_o^2} + \ln \frac{R_o^2}{r_o^2} \right). \tag{5.4}$$

However, for the other case, the integration constant is of the form

$$C = \frac{\mu_0}{2}\left(2 + \frac{R_o^2 - r_o^2}{r_i^2} + \ln \frac{R_i^2}{r_i^2} \right). \tag{5.5}$$

On the other hand, for the MR model we obtain

$$\begin{aligned}
\sigma_r &= \frac{1}{2}\mu_0 \left[1 - \frac{R_o^2}{R_o^2 + r_i^2 - R_i^2} + \frac{R_i^2 - r_i^2}{r^2} + \ln \frac{\left(r^2 - r_i^2 + R_i^2\right)\left(R_o^2 + r_i^2 - R_i^2\right)}{R_o^2 r^2} \right], \\
\sigma_\phi &= \frac{1}{2}\mu_0 \left[-1 - \frac{R_o^2}{R_o^2 + r_i^2 - R_i^2} + \frac{R_i^2 - r_i^2}{r^2} + \frac{2r^2}{r^2 + R_i^2 - r_i^2} + \right. \\
&\quad \left. + \ln \frac{\left(r^2 - r_i^2 + R_i^2\right)\left(R_o^2 + r_i^2 - R_i^2\right)}{R_o^2 r^2} \right], \\
\sigma_z &= \frac{1}{2}\mu_0 \left[-1 + 2f - \frac{R_o^2}{R_o^2 + r_i^2 - R_i^2} + (1 - 2f)\frac{R_i^2 - r_i^2}{r^2} - 2(1 - f)\frac{2r^2}{r^2 + R_i^2 - r_i^2} + \right. \\
&\quad \left. + \ln \frac{\left(r^2 - r_i^2 + R_i^2\right)\left(R_o^2 + r_i^2 - R_i^2\right)}{R_o^2 r^2} \right].
\end{aligned} \tag{5.6}$$

Note that the components of the stress state σ_r and σ_ϕ are independent of the material parameter *f*. The formula for the component σ_z for the NH model can be obtained by substituting $f = 1$. The expressions may be rewritten with dimensionless variables such that

$$\sigma_r = \frac{1}{2}\mu_0 c\left[\frac{1-c-\rho^2}{(1-c)\rho^2} - \frac{1}{c}\ln\frac{\rho^2}{(1-c)\left(\rho^2+c\right)}\right],$$
$$\sigma_\phi = \frac{1}{2}\mu_0 c\left[\frac{3(1-c)+\rho^2+c}{(1-c)\left(\rho^2+c\right)} + \frac{c}{\left(\rho^2+c\right)\rho^2} - \frac{1}{c}\ln\frac{\rho^2}{(1-c)\left(\rho^2+c\right)}\right], \quad (5.7)$$

where

$$c = \eta^2 - \tilde{\chi}^2 \,.\; \rho = \frac{r}{R_o}, \quad \eta = \frac{R_i}{R_o}, \quad \tilde{\chi} = \frac{r_i}{R_o} = \eta + \chi \quad (5.8)$$

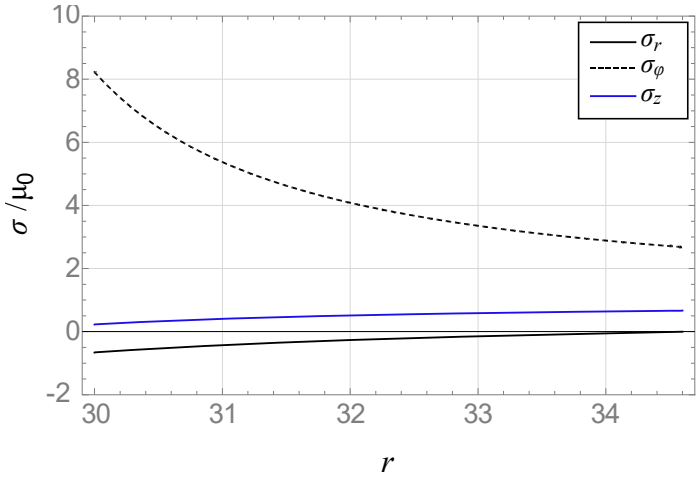

Fig. 5.1. Stress state components in the final configuration for the NH model. Stresses and are the same for the NH and MR models.

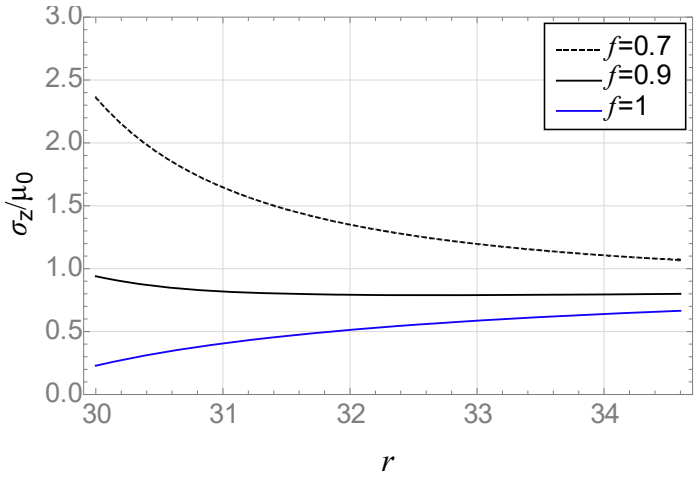

Fig. 5.2. Stress state component in the final configuration for the MR model for different values of the parameter *f*.

The stress component in the direction of the cylinder axis is as follows:

$$\sigma_z = \frac{1}{2}\left[\mu_0 - 1 + 2f - \frac{1}{1-c} + (1-2f)\frac{c}{\rho^2} - 2(1-f)\frac{2\rho^2}{\rho^2+c} - \ln\frac{\rho^2}{(1-c)(\rho^2+c)}\right]. \quad (5.9)$$

Fig. 5.1 shows the plots of the Cauchy stress components normalised by the shear modulus μ_0 for the NH model. It should be noted that the stress σ_z value strongly depends on *f*, see Figure 5.2.

5.2. The linearised problem

From the solution (5.7) for an incompressible hyperelastic material, we obtain the solution of the small strain theory problem. We calculate the limit for $c \to 0$ which means that the body configurations are indistinguishable

$$\begin{aligned}
&\lim_{c\to 0}\left[\frac{1-c-\rho^2}{(1-c)\rho^2}-\frac{1}{c}\ln\frac{\rho^2}{(1-c)\left(\rho^2+c\right)}\right]=2\left[\frac{1}{\rho^2}-1\right],\\
&\lim_{c\to 0}\left[\frac{3(1-c)+\rho^2+c}{(1-c)\left(\rho^2+c\right)}+\frac{c}{\left(\rho^2+c\right)\rho^2}-\frac{1}{c}\ln\frac{\rho^2}{(1-c)\left(\rho^2+c\right)}\right]=-2\left[\frac{1}{\rho^2}+1\right],
\end{aligned} \tag{5.10}$$

and assuming that

$$\chi^2 \ll 2\chi\eta\,, \tag{5.11}$$

which states small strains, we have

$$\sigma_r=-2\mu_0\eta\chi\left[\frac{1}{\rho^2}-1\right],\quad \sigma_\phi=2\mu_0\eta\chi\left[\frac{1}{\rho^2}+1\right],\quad \sigma_z=2\mu_0\eta\chi\,. \tag{5.12}$$

In the formulas (5.12), the product χR_o is the displacement of the inner edge of the cylinder given according to the radius increase. This is equivalent to prescribed traction in the inner surface of the cylinder cross-section

$$p=2\mu_0\chi\frac{\left(1-\eta^2\right)}{\eta}. \tag{5.13}$$

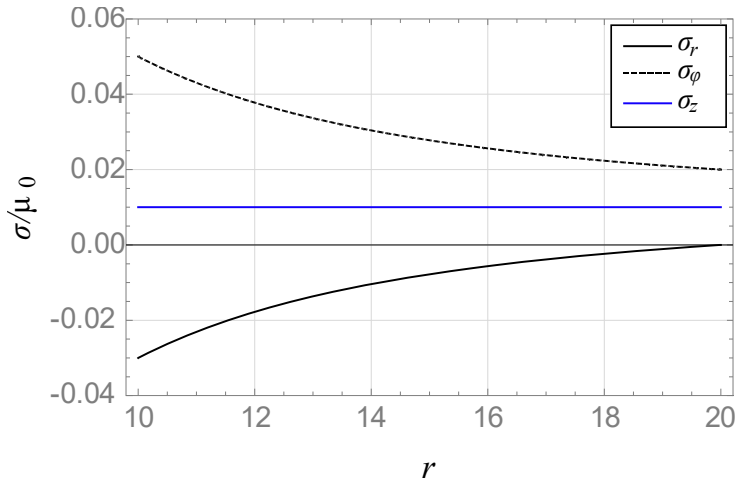

Fig. 5.3. Stress state components in the final configuration for the NH model for small strains. The results obtained according to the NH model or formulas (5.12) are indistinguishable on the scale of the drawing.

5.3. The UMG and HMG material models

The solution to the problem for the other constitutive models can be obtained in a similar way (Jemioło 2002). In this section, we present two solutions for (3.10) and (3.15), which describe the NH model as $g \to \infty$.

The constitutive relation corresponding to SEF (3.10) yields

$$\boldsymbol{\sigma} = -p\mathbf{I} + \frac{\mu_0 g}{3 + g - \bar{I}_1}\bar{\mathbf{B}}. \tag{5.14}$$

From the relations (5.14) and (4.10) we obtain the components of the stress state

$$\begin{aligned}
\sigma_r &= -p(r) + \mu_0 \frac{g\lambda_r^2}{2 + g - \lambda_r^2 - \lambda_r^{-2}}, \\
\sigma_\phi &= -p(r) + \mu_0 \frac{g\lambda_r^{-2}}{2 + g - \lambda_r^2 - \lambda_r^{-2}}, \\
\sigma_z &= -p(r) + \mu_0 \frac{g}{2 + g - \lambda_r^2 - \lambda_r^{-2}}, \qquad \text{where} \quad \lambda_r^2 = \frac{r^2 + a}{r^2}.
\end{aligned} \tag{5.15}$$

The formulas are fairly complicated, therefore we do not present them. It is easy to check that if $g \to \infty$, the relation for the NH model is recovered

$$\boldsymbol{\sigma} = -p\mathbf{I} + \mu_0\bar{\mathbf{B}}. \tag{5.16}$$

In Figure 5.4 we present examples of results for the stress state components normalised by the shear modulus for two parameter values g. For $g = 100$, we obtain a solution that numerically (Wolfram 2018) slightly differs from the solution obtained for the NH material model, see Figures 5.2, 5.4.

In the case of Demiry's model, the constitutive relationship is given by

$$\boldsymbol{\sigma} = -p\mathbf{I} + \mu_0 \mathrm{Exp}\left(\frac{\bar{I}_1 - 3}{g}\right)\bar{\mathbf{B}}. \tag{5.17}$$

As in the case of the Gent model, for $g \to \infty$ we obtain from (5.17) the constitutive relation of the NH model (5.16).

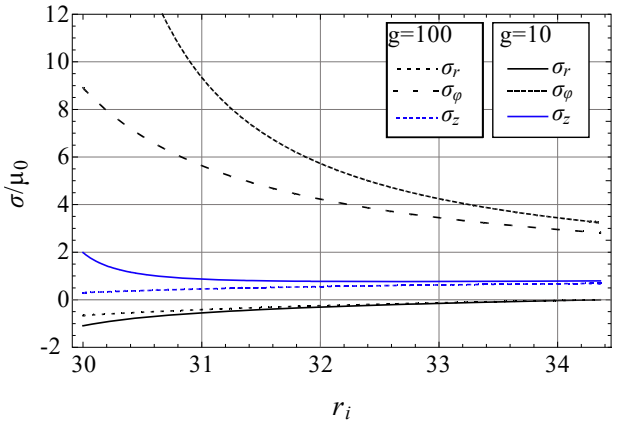

Fig. 5.4. Stress state components in the final configuration for Gent models for different values of the parameter g=10, g=100.

From the relations (5.17) and (4.10) we obtain the components of the stress state in the cylinder:

$$\sigma_r = -p(r) + \mu_0 \mathrm{Exp}\left(\frac{\lambda_r^2 + \lambda_r^{-2} - 2}{g}\right)\lambda_r^2,$$
$$\sigma_\phi = -p(r) + \mu_0 \mathrm{Exp}\left(\frac{\lambda_r^2 + \lambda_r^{-2} - 2}{g}\right)\lambda_r^{-2}, \qquad (5.18)$$
$$\sigma_z = -p(r) + \mu_0 \mathrm{Exp}\left(\frac{\lambda_r^2 + \lambda_r^{-2} - 2}{g}\right), \qquad \text{where} \quad \lambda_r^2 = \frac{r^2 + a}{r^2}.$$

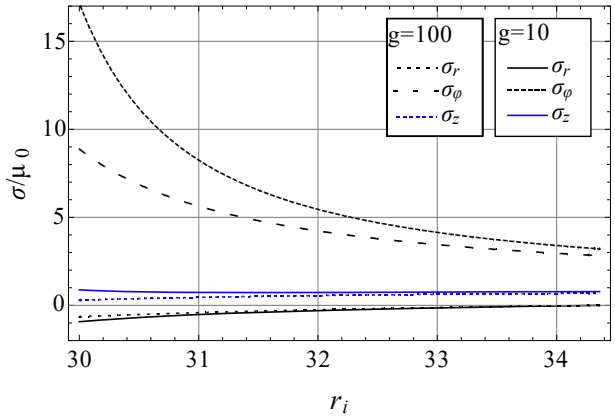

Fig. 5.5. Stress state components in the final configuration for Demiray's model for different values of the parameter g=10, g=100.

Substituting (5.18) into (4.11), we obtain a differential equation for $p(r)$. The solution can be presented in the form of an integral - the result of the integration is not in the form of elementary functions. Therefore, the corresponding equations are solved numerically. Plots of the results are shown in Figure 5.5. The curves are qualitatively similar to those presented in Figure. 5.4.

6. INTERPRETATION OF THE SOLUTIONS

In the section, we compare the obtained results for NH and MV models. We remind that according to (3.9) the NH and MR models in the case of PDS lead to the same form of SEF. As a consequence, the stress states σ_r and σ_ϕ are the same for the models, respectively.

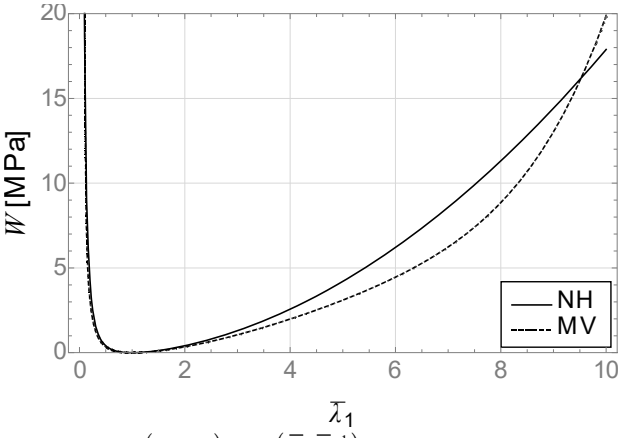

Fig. 6.1. Comparison of SEF $W(\lambda_r, \lambda_\phi) = W(\bar{\lambda}, \bar{\lambda}^{-1})$ graphs for the NH and MV models (dotted line), the Yeoh model (dashed line) and the V model (solid line).

Figure 6.2 presents plots of the stress state components for NH and MV in the case of Alexander's data. We notice a significant qualitative and quantitative influence of the second isochoric deformation invariant on values of σ_z.

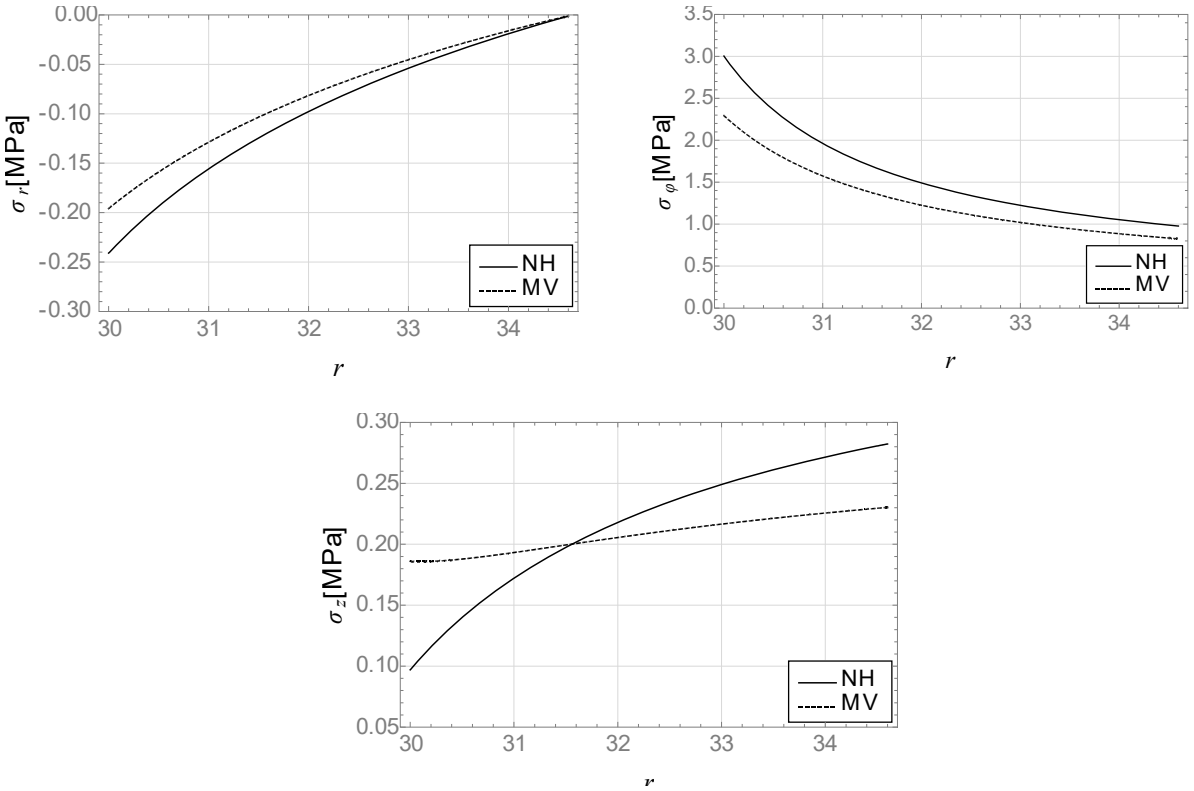

Fig. 6.2. Components of the stress state in the final configuration for the NH, MV models.

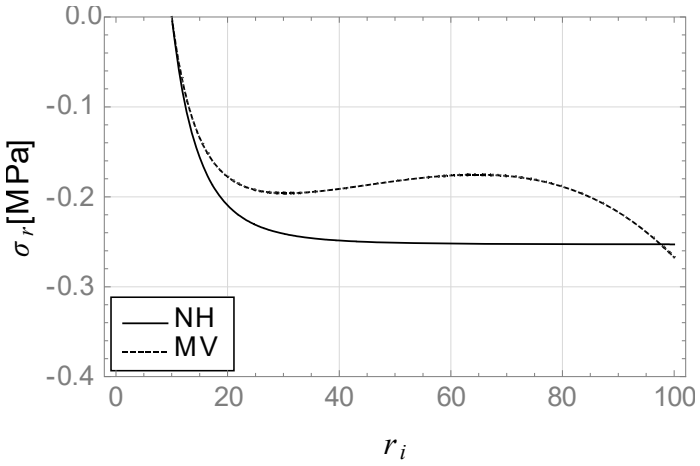

Fig. 6.3. Stress σ_r vs the actual inner radius r_i - NH and MV models comparison.

The NH and MR models provide a qualitatively different solution in comparison to the MV model for large cylinder deformations. This is especially noticeable when we analyse the relationship between the pressure inside the cylinder and the actual inner radius r_i, see Figure 6.3. The boundary conditions of the problem show that the pressure inside the cylinder is equal $-\sigma_r(r_i)$. In the case of the NH and MR models, the function $\sigma_r(r_i)$ tends asymptotically to a constant value. We notice that the MV model does not produce a monotonic increasing stress value, i.e., the curve shows a local maximum followed by a local minimum, cf. Figure 6.3. In the case of cylinder inflation, the qualitative differences between the solutions predicted by MR and MV models are much more noticeable than in the case of balloon inflation (Jemioło 2002).

7. CONCLUSIONS

The inflation of a cylindrical tube presented in this chapter can be a benchmark problem of a formulation of the hybrid FEM algorithm (Han et al. 2020).

The solution of the boundary problem of hyperelasticity discussed in the paper allows revealing unstable states of cylinder deformation, which are related to the phenomenon of its inflation. This phenomenon depends mostly on constitutive relation. Local pressure extremes heavily depend on the initial thickness of the tube. Apart from the analytical solution, the numerical results obtained with the ABAQUS program (ABAQUS 2015) are also considered. The results are discussed in the next chapter of this monograph, see also (Jemioło 2002).

The NH and MR models in the case of PDS lead to the same form of SEF. Hence, the stress states σ_r and σ_ϕ are the same for the models, respectively. It should be noted that in the case of MR and NH material models a monotonic increase of pressure inside the cylinder occurs as the displacement monotonically increases which is not the case for the MV model.

REFERENCES

ABAQUS 2015. *Abaqus 2016 Theory Guide.* Dassault Systèmes Simulia.

Adkins, J.E. 1961. *Large elastic deformation*. In Snedon & R. Hill (eds), Progress in solid mechanics, vol. II: 1-60. Amsterdam: North-Holland Publishing Company.

Alexander, H. 1968. *A constitutive relation for rubber-like materials*. International Journal of Engineering Science 6(9): 549-563.

Anani, Y., & Rahimi, G. 2018. *On the stability of internally pressurized thick-walled spherical and cylindrical shells made of functionally graded incompressible hyperelastic material.* Latin American Journal of Solids and Structures 15(4): 1-17.

Antman, S.S. 1995. *Nonlinear problems of elasticity*. New York – Budapest: Springer-Verlag.

Bharatha, S. 1967. *Cylindrically symmetrical deformations of Mooney materials*. Archiwum Mechaniki Stosowanej 19(6): 857-866.

Bonet, J., Gil, A. J., & Wood, R. D. 2016. *Nonlinear solid mechanics for finite element analysis: statics*. Cambridge University Press.

Ciarlet, P.G. 1998.: *Mathematical elasticity, vol.1: Three-dimensional elasticity*. *Studies in mathematics and its applications, vol. 20*. Amsterdam-Tokyo: North-Holland.

Demiray, H. 1972. A note on the elasticity of soft biological tissues. Journal of biomechanics 5(3) : 309-311.

Han, Y., Duan, J., & Wang, S. 2020. Benchmark problems of hyper-elasticity analysis in evaluation of FEM. Materials 13(4): 885.

Franus, A. & Jemioło, S. 2019. *Application of least-squares approximation to determine the parameters of polynomial hyperelastic models* [In Polish]. In S. Jemioło (eds), Nonlinear elasticity. Constitutive modelling, stability and waves propagation. Warsaw: Warsaw University of Technology Publishing House.

Holzapfel, G.A. 2010. *Nonlinear solid mechanics*. New York : John Wiley & Sons Ltd.

Gent, A. N. 1996. *A new constitutive relation for rubber*. Rubber chemistry and technology 69(1): 59-61.

Ogden, R.W. 1984. *Non-linear elastic deformations*. Chichester: Ellis Horwood.

Jemioło, S. 2002. *Study of hyperelastic properties of isotropic materials. Modelling and numerical implementation* [In Polish]. Warsaw: Warsaw University of Technology Publishing House.

Jemioło, S. 2016. *Constitutive relationships of hyperelasticity* [In Polish]. Warsaw: PAN, KILiW.

Jemioło, S. & Franus, A. 2019. *Isotropic constitutive models of hyperelasticity. Determination of material parameters and numerical implementation* [In Polish]. Warsaw: Warsaw University of Technology Publishing House.

Jemioło, S. & Suchocki, C. 2019. *Hipersprężystość i jej modyfikacje. Zarys teorii, pseudo-hipersprężystość i quasi liniowa lepko-hipersprężystość*, Warsaw: Warsaw University of Technology Publishing House.

Jemioło, S., & Telega, J. J. 2001. *Modelling Elastic Behaviour of Soft Tissues. Part I. Isotropy*. Engineering Transactions 49(2-3): 213-240.

Ogden, R.W. 1984. *Non-linear elastic deformations*. Chichester: Ellis Horwood.

Treloar, L. R. G. 1944. Stress-strain data for vulcanized rubber under various types of deformation. Rubber Chemistry and Technology 17(4) : 813-825.

Zahorski, S. 1959. *A form of the elastic potential for rubber-like materials*. Arch. Mech. Stos. 5(11): 613–618.

Wolfram Research Inc. 2018. *Mathematica, Version 11.3*. Champaign, IL.

LIGHTWEIGHT STRUCTURES in CIVIL ENGINEERING
CONTEMPORARY PROBLEMS
Monograph from Scientific Seminar
Organized by Polish Chapters of
International Association for Shell and Spatial Structures
Łódź University of Technology
Faculty of Civil Engineering, Architecture
and Environmental Engineering
XXVII LSCE
Łódź, 2nd – 3rd of December 2021

FINITE ELEMENT METHOD MODELLING OF LONG AND SHORT HYPERELASTIC CYLINDRICAL TUBES

S. Jemioło [1] **A. Franus** [2]
[1] Professor, Faculty of Civil Engineering, Warsaw University of Technology, POLAND,
s.jemiolo@il.pw.edu.pl
[2] MSc, Faculty of Civil Engineering, Warsaw University of Technology, POLAND,
aleksander.franus.dokt@pw.edu.pl

ABSTRACT: A concise and factual abstract is required. The abstract should state briefly the purpose of the research, the principal results and major conclusions. An abstract is often presented separately from the article, so it must be able to stand alone. For this reason, references should be avoided, but if essential, then cite the author(s) and year(s). Also, non-standard or uncommon abbreviations should be avoided, but if essential they must be defined at their first mention in the abstract itself.

Keywords: cylindrical tube, hyperelastic, finite element method.

2. INTRODUCTION

In the previous chapter, we discussed some aspects of a solution to the boundary value problem of a cylindrical tube subjected to an internal displacement. Several hyperelastic incompressible rubber-like material models were considered there. In this chapter, we focus on modelling a rubber cylindrical tube in the finite element method software ABAQUS (Abaqus 2016 Theory Guide 2015). This problem is known as an excellent example of a benchmark problem in an evaluation of numerical results (Anani and Rahimi 2018, Dragoni 1996, Han, Duan and Wang 2020, Horgan and Saccomandi 2003).

3. HYPERELASTIC INCOMPRESSIBLE MATERIAL MODELS

Several hyperelastic incompressible rubber-like material models are considered in the previous chapter in the context of a cylindrical tube inflation problem (Jemioło 2016, Jemioło 2011, Ogden 1984). For the sake of clarity, we present relevant stored energy functions here as well. A five-parameter polynomial model (called MV) is given by

$$\breve{W}_{MV}\left(\overline{I}_1,\overline{I}_2\right)=\frac{1}{2}\left[a_1\left(\overline{I}_1-3\right)+\frac{1}{2}a_2\left(\overline{I}_1^2-9\right)+\frac{1}{3}a_3\left(\overline{I}_1^3-27\right)+a_4\left(\overline{I}_2-3\right)+a_5\left(\overline{I}_1\overline{I}_2-9\right)\right], \tag{2.1}$$

where $\overline{I}_1,\overline{I}_2$ denote the invariants of the modified right and left Cauchy-Green deformation tensors. The model states a third-order consistent polynomial expansion of the stored energy function. The Mooney model is a special case of (2.1) such that:

$$\breve{W}_{MR}\left(\bar{I}_1,\bar{I}_2\right)=\frac{1}{2}\left[a_1\left(\bar{I}_1-3\right)+a_4\left(\bar{I}_2-3\right)\right], \tag{2.2}$$

which reduces to the neo-Hookean model if $a_4=0$. Another considered model called EXP-PL one (Jemioło 2016), which is not of polynomial type, reads

$$\breve{W}_{EXP-PL}\left(\bar{I}_1,\bar{I}_2\right)=\frac{\mu}{2a}\left(e^{a\left(\bar{I}_1-3\right)}-1\right)+b\left(\bar{I}_1-3\right)+c\left(\bar{I}_2-3\right). \tag{2.3}$$

The function (2.3) is polyconvex if the parameters are positive. For more details, we refer the reader to (Ciarlet 1988). Fig. 2.1 presents nominal stress vs principal stretch for Alexander's experimental data on neoprene (Alexander 1968). Parameters are shown in Tab. 2.1. It should be noted that MV and EXP-PL models accurately describe the data for large deformations which is not the case for NH or MR material models. However, the range of small deformations is not sufficiently accurate predicted especially in the case of biaxial tension mode. Parameters are presented in Tab. 2.1.

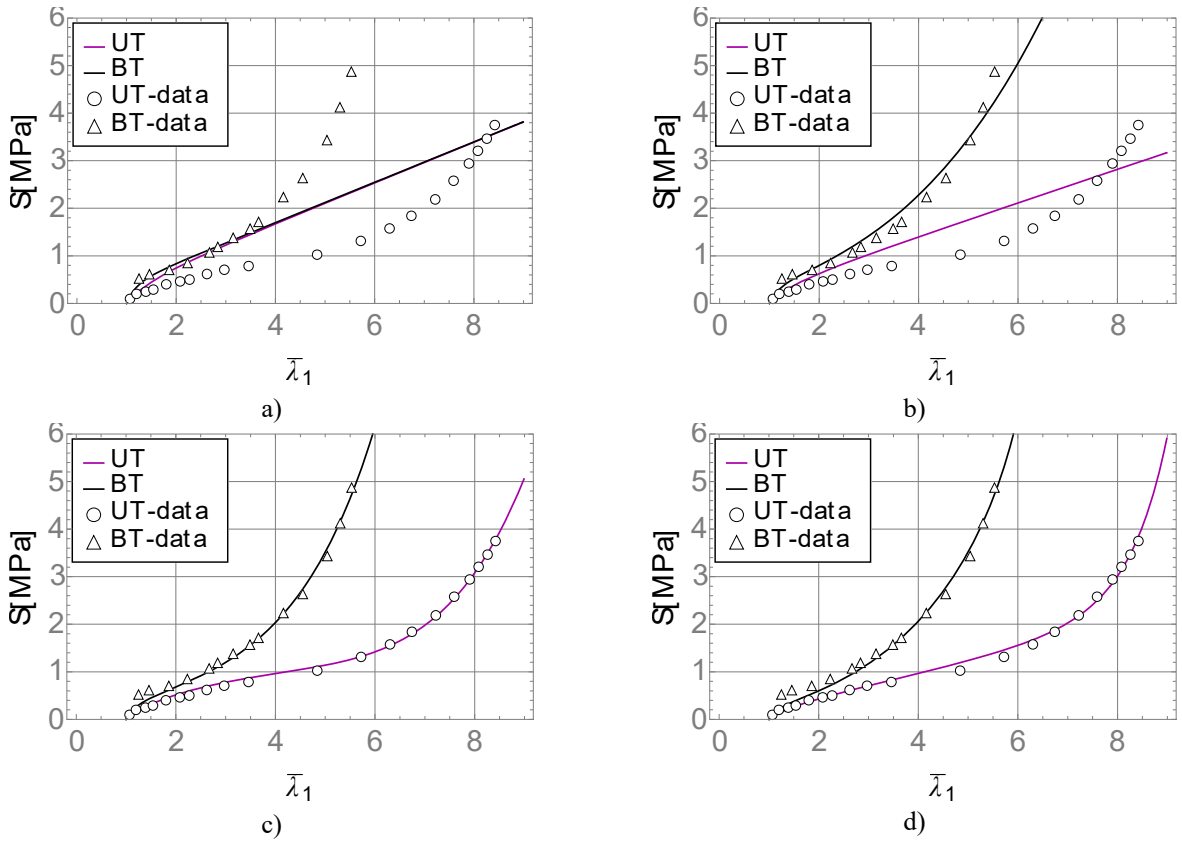

Figure 2.1. Nominal stress vs principal stretch plots for uniaxial (UT) and biaxial (BT) tension modes in the case of Alexander's data [1] – a) Neo-Hooekan model, b) Mooney model, c) MV model, d) EXP-PL model

Table 2.1. Parameters for Alexander's data [1] (neoprene).

Model	a_1 [MPa]	a_2 [MPa]	a_3 [MPa]	a_4 [MPa]	a_5 [MPa]
MR	3.513×10^{-1}	-	-	1.364×10^{-2}	-
MV	3.152×10^{-1}	-6.469×10^{-3}	1.173×10^{-4}	1.899×10^{-2}	-3.011×10^{-4}
Model	μ	a	b	c	-
EXP-PL	2.542×10^{-3}	6.545×10^{-2}	2.351×10^{-1}	1.652×10^{-2}	

4. FEM MODELLING OF THE CYLINDICAL TUBE PROBLEM IN ABAQUS

A cylindrical tube of unit length (plane-strain state) is modelled in ABAQUS using two approaches. The first one consists of a quarter of the cross-section with boundary conditions that impose symmetry, see Fig. 3.2. Finite elements of type CPE4H are applied (seven elements of the tube's thickness). The internal surface is subjected to a prescribed displacement u_i. It is worth to notice that the model does not impose an axially symmetric solution.

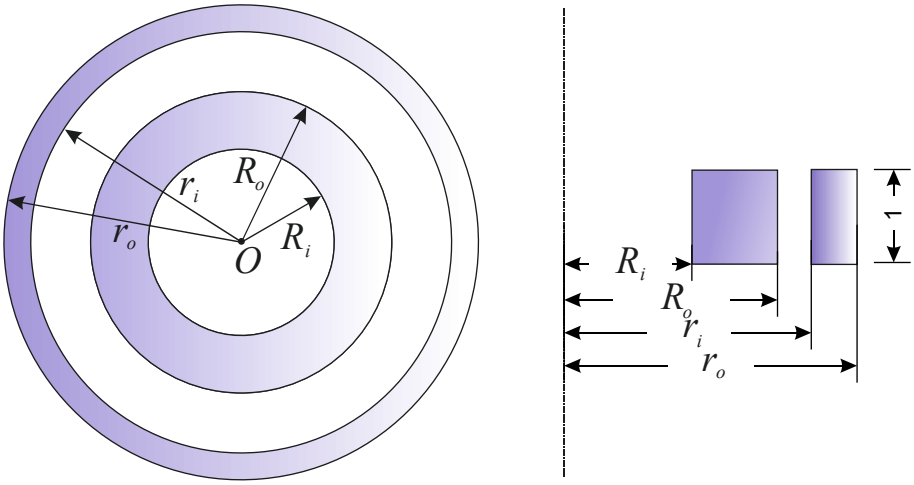

Fig. 3.1. A cylindrical tube of unit length represents a plane stain problem.

The other FEM model involves an axially symmetric stress formulation (Bonet and Wood 2008, Abaqus 2016 Theory Guide 2015). To this end, we use CAX4H elements (seven elements in the section). Similarly to the previous case, the internal surface is subject to a prescribed displacement u_i. Material models are implemented via UHYPER user-subroutines.

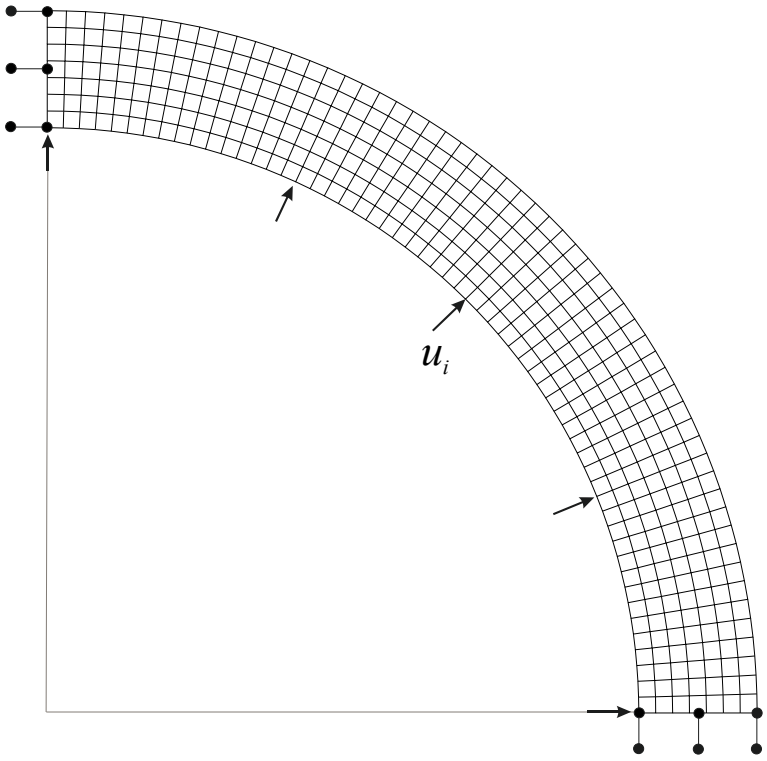

Fig. 3.2. The mesh with boundary conditions – CPE4H elements.

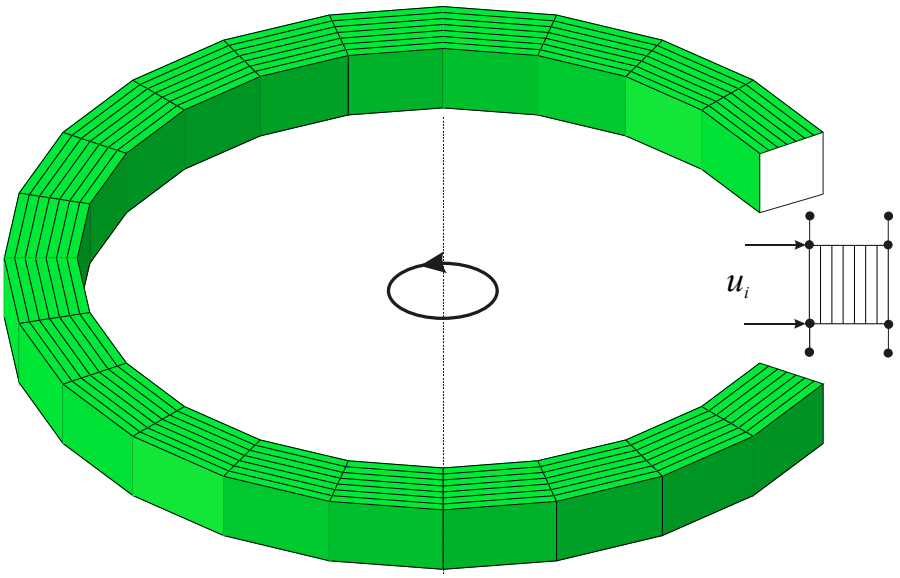

Fig. 3.3. The mesh with the boundary conditions for the axially symmetric model – CAX4H elements.

3.1. The neo-Hookean and the Mooney models

The first test for verification numerical results concerns the neo-Hookean and the Mooney material models with the axially symmetric stress formulation. It is known (see the previous chapter) that these material models produce the same in-plane stresses if the initial shear moduli match (Jemioło 2002).

Fig. 3.1 presents plots of the normalised Cauchy stress tensor components through the thickness of the tube. The values obtained show high accuracy as presented in Tab. 3.1, where the analytical results computed employing MATHEMATICA (Wolfram Research 2020) are collected. Moreover, ABAQUS produce the outer radius $r_o = 50.4381$ which fully coincides with the analytical result.

Similar results in terms of accuracy are reported in (Han, Duan and Wang 2020, Wolfram Research 2020), where ABAQUS is employed as well to solve several benchmark problems.

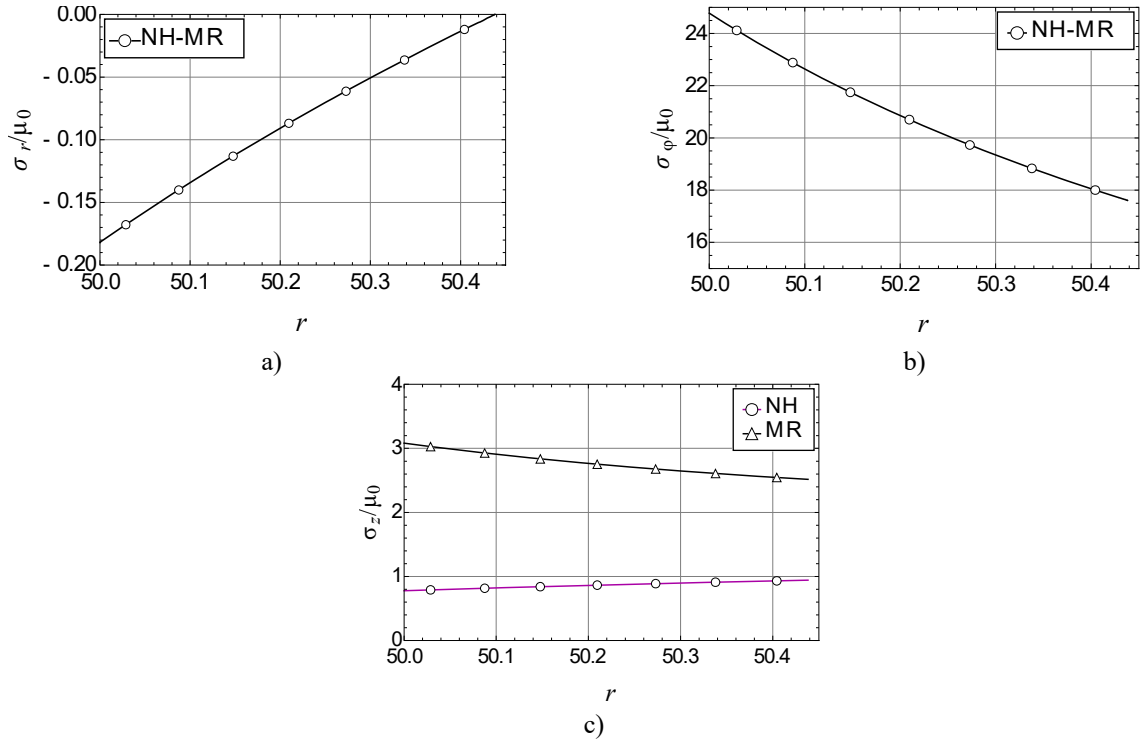

Figure 3.1. Comparison of analytical (solid lines) and ABAQUS's results (markers), R_i=10, R_b=12, r_i=50.

Table 3.1. Results comparison – stress values at the four integration points are equal.

R		10.1429	10.4286	10.7143	11	11.2857	11.5714	11.8771
$\lvert\sigma_r\rvert/\mu_0$	ABQ	0.16782	0.14009	0.11311	0.086846	0.061263	0.036326	0.012003
	M	0.16774	0.14009	0.11303	0.086774	0.061194	0.036259	0.011939
σ_φ/μ_0	ABQ	24.120	22.885	21.748	20.700	19.732	18.835	18.004
	M	24.120	22.885	21.748	20.700	19.732	18.835	18.003
σ_z/μ_0 (NH)	ABQ	0.79108	0.81656	0.84124	0.86516	0.88834	0.91083	0.93266
	M	0.79116	0.81664	0.84131	0.86523	0.88841	0.91090	0.93272
σ_z/μ_0(MR)	ABQ	3.0281	2.9277	2.8365	2.7534	2.6777	2.6085	2.5453
	M	3.0281	2.9278	2.8366	2.7535	2.6778	2.6086	2.5453

3.2. A comparison of FEM models

As it is shown in the previous subsection, the axially symmetric formulation produces results of excellent accuracy. Here we focus on a comparison of the results produced by this model with the results obtained with the model involving the quarter of the cross-section. The latter does not impose the axially symmetric solution.

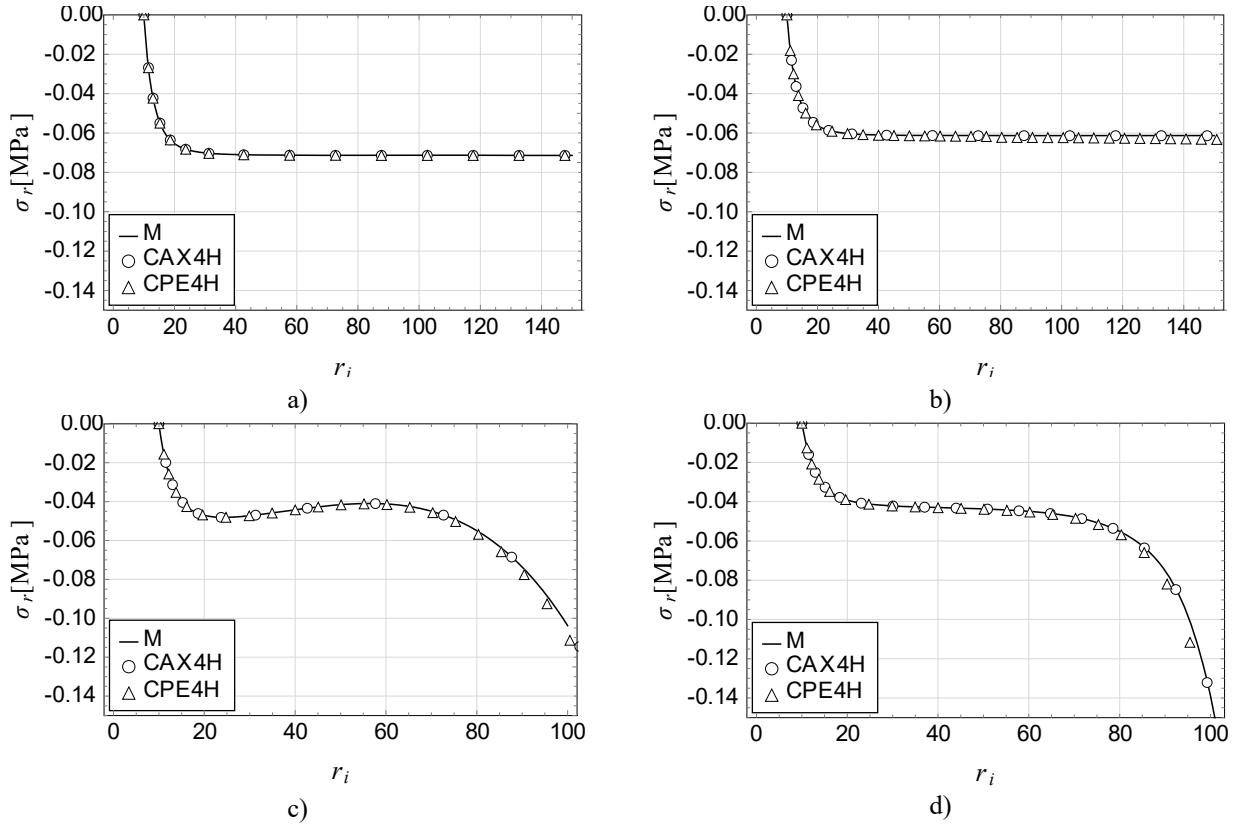

Figure 3.2. Comparison of ABAQUS's results of different FEM models a) the neo-Hooekan model, b) the Mooney model, c) the MV model, d) the EXP-PL model.

For this purpose, we plot the radial stress $\sigma_r(r_i)$ versus the inner radius in the current configuration. First of all, we notice that only the MV model does not produce a monotonic increasing stress value, i.e., the curve shows a local maximum followed by a local minimum, see also (Jemioło 2002, Taghizadeh, Bagheri, and Darijani 2015). Similarly to the previous case, the model involving the axially symmetric formulation produces highly accurate results. The other one gives the same accuracy only for the neo-Hookean material

model. Comparing the results of other material models, a deviation from the analytical values is notable as the inner radius increases, see Fig. 3.2. However, the error is significant for very large deformations.
Very similar problems are considered in the monograph (Wolfram Research 2020). It is reported that besides the MV models, the Yeoh model produces a non-monotonic increase of the stress value. Besides very large stretches and displacements, a significant rotation takes place in the final configuration of the body. Thus, it is another aspect of the problem that makes it an excellent benchmark problem.

5. A SHORT CYLINDRICAL TUBE

The previous sections concern a cylindrical tube problem under the plane deformation assumption, which physically may accurately approximate a sufficiently long tube. To show the behaviour of a pressurized short cylindrical tube (Soleimani and Funnell 2016), the problem illustrated in Fig. 4.1 is solved by employing ABAQUS (CAX4H elements). We use the MV material model.
The equilibrium path concerning the centre of the tube appears to be qualitatively similar to the one shown in Fig. 3.2. The different boundary conditions lead to a significantly higher value of limit point stress in comparison to the plane deformation problem. Deformations obtained characterize a typical bulging in the middle of the tube (Pamplona, Gonc-Alves and Lopes 2006, Taghizadeh, Bagheri and Darijani 2015), which has been confirmed experimentally (Ogden 1984). As the solution does not produce a monotonic increasing stress value, the Riks procedure is employed to obtain the path.

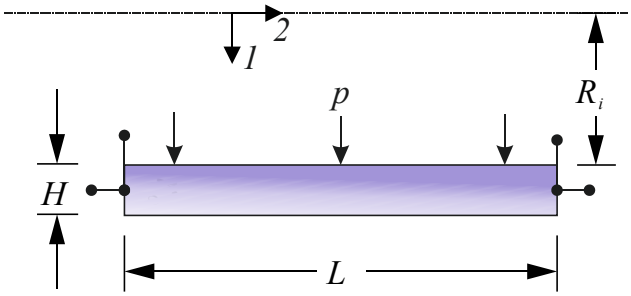

Fig. 4.1. A short cylindrical tube problem illustration, R_i=19, H=2, L=20.

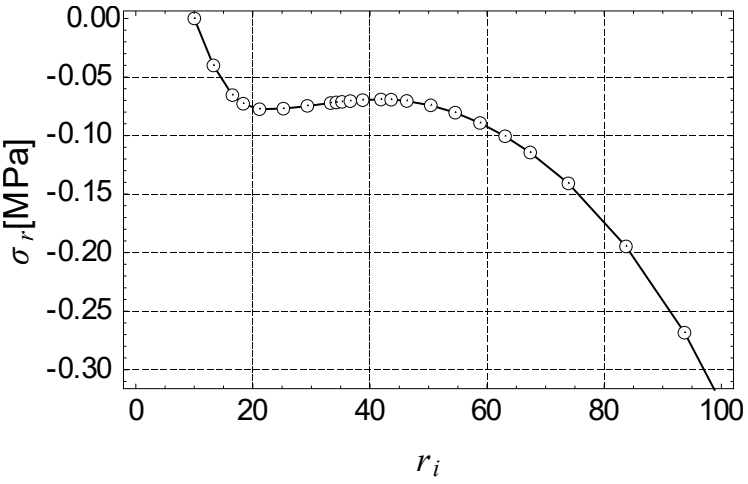

Fig. 4.2. The radial stress $\sigma_r(r_i)$ versus the inner radius in the current configuration – the centre of the tube.

Figs. 4.3, 4.4 and 4.5 present intermediate and final configurations of the considered short cylinder inflation. It should be noted that besides very large stretches and displacements, a significant rotation takes place in the final configuration of the body. Thus, the problem should be considered in a regime of large deformations and arbitrary large rotations.

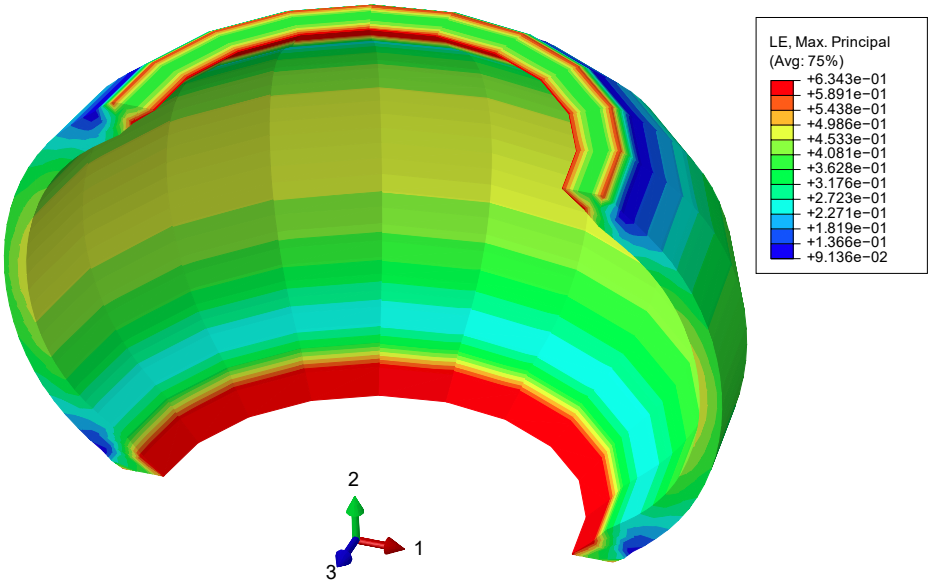

Fig. 4.3. An intermediate configuration of the short cylinder.

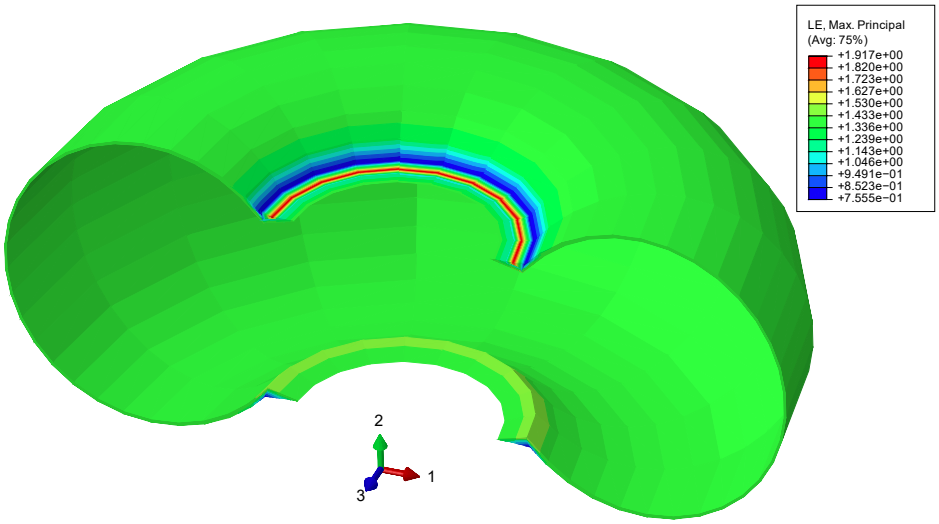

Fig. 4.4. An intermediate configuration of the short cylinder.

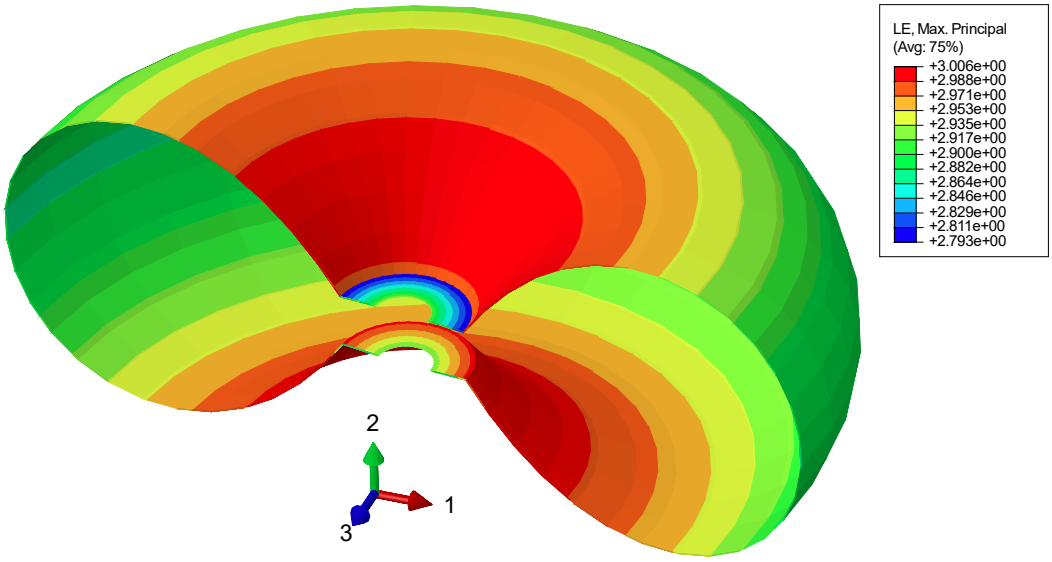

Fig. 4.5. The final configuration of the short cylinder.

6. CONCLUSION

The cylindrical tube problem is an excellent benchmark problem in an evaluation of a numerical method. The results obtained show that the axially symmetric stress formulation in the finite element method software ABAQUS provides high accuracy for the hyperelastic material models considered. The FEM model involving CPE4H elements produces results that do not fully coincide with the analytical ones, but the formulation does not impose the axially symmetric solution. In the case of the short cylinder problem, the equilibrium path concerning the centre of the tube appears to be qualitatively similar to the one produced by the plane deformation problem's solution. However, applied boundary conditions lead to a significantly higher value of limit point stress in comparison to the previous cases.

REFERENCES

Alexander, H. 1968. *A constitutive relation for rubber-like materials*, International Journal of Engineering Science 9(6): 549–563.

Anani, Y., Rahimi, G.H. 2018. *On the stability of internally pressurized thick-walled spherical and cylindrical shells made of functionally graded incompressible hyperelastic material* Latin American Journal of Solids and Structures 15(4): 1–17.

Bonet, J., Wood, R.D. 2008. *Nonlinear Continuum Mechanics for Finite Element Analysis*, Cambridge: Cambridge University Press.

Ciarlet, P.G. 1988. *Mathematical elasticity*. *Three-dimensional elasticity*. Amsterdam: North-Holland.

Dassault Systèmes 2015. *Abaqus 2016 Theory Guide.*

Dragoni, E. 1996. *The radial compaction of hyperelastic tube as a benchmark in compressible finite elasticity*. Int. J. Non-Linear Mechanics 31(4): 483–493.

Han, Y., Duan, J., Wang, S. 2020. *Benchmark Problems of Hyper-Elasticity Analysis in Evaluation of FEM*. Materials 13(4): 885.

Horgan, C.O., Saccomandi, G. 2003. *A description of arterial wall mechanics using limiting chain extensibility constitutive models*. Biomechanics and Modeling in Mechanobiology 1(4): 251–266.

Jemioło, S. 2016. *Relacje konstytutywne hipersprężystości*. PAN Komitet Inżynierii Lądowej i Wodnej.

Jemioło, S. 2002. *Studium hipersprężystych własności materiałów izotropowych, Modelowanie i implementacja numeryczna*. Prace Naukowe, Budownictwo, z. 140, OWPW, Warszawa.

Ogden, R.W. 1984. *Non-linear elastic deformations*. Chichester: Ellis Horwood.

Pamplona, D.C., Gonc-Alves, P.B., Lopes, S.R.X. 2006. *Finite deformations of cylindrical membrane under internal pressure*. International Journal of Mechanical Sciences 48: 683–696.

Soleimani, M., Funnell, W.R.J. 2016. *Deformation and stability of short cylindrical membranes*. International Journal of Mechanical Sciences 119: 266–272.

Taghizadeh, D.M., Bagheri, A., Darijani, H 2015. *On the hyperelastic pressurized thick-walled spherical shells and cylindrical tubes using the analytical closed-form solutions*. International Journal of Applied Mechanics 7(2): 1150027.

Ye, Y., Liu, Y., Fu, Y. 2020. *Weakly nonlinear analysis of localized bulging of an inflated hyperelastic tube of arbitrary wall thickness.* Journal of the Mechanics and Physics of Solids 135: 103804.

Wolfram Research, Inc., System Modeler, Version 12.2, Champaign, IL 2020.

LIGHTWEIGHT STRUCTURES in CIVIL ENGINEERING
CONTEMPORARY PROBLEMS
Monograph from Scientific Seminar
Organized by Polish Chapters of
International Association for Shell and Spatial Structures
Łódź University of Technology
Faculty of Civil Engineering, Architecture
and Environmental Engineering
XXVII LSCE
Łódź, 2nd – 3rd of December 2021

NUMERICAL ANALYSIS OF THE MASONRY CHIMNEY WITH THE TLS METHOD AS A POSSIBILITY OF APPLICATION IN SHM

E. Kowalska [1)]
[1)] MSc. Eng., Faculty of Geoengineering, University of Warmia and Mazury in Olsztyn, POLAND,
edyta.kowalska@uwm.edu.pl

ABSTRACT: The paper presents a dynamic behaviour structural model of masonry chimney using the finite element analysis. The geometry of the chimney is prepared using the 3D laser scanner and the documentation of in situ survey to simulate the dynamic response of the structure. The case study of the masonry chimney and the 3D laser scanning with the application are described. Next part includes the dynamic behaviour a finite element model of the real masonry structure. The dynamic analysis started from determining eigenfrequencies and the corresponding eigenmodes of a spatial model. Then the response of the model to a base kinematic excitation via a modal response analysis is determined. At the end an earthquake spectral analysis of the chimney model is demonstrated.

Keywords: masonry chimney, laser scanning, monitoring, dynamics, finite element method.

1. INTRODUCTION

There are many historic masonry structures around us, which often still have useful functions or if do not, they cannot threaten the surroundings. Because of the safety of the structures, it becomes necessary to periodically check the technical condition. The process of determination of the technical condition and potential damages detection in civil engineering structures is important mainly for the protection of human health and life as well as for the preservation of architectural heritage. These issues are taken under Structural Health Monitoring (SHM) (see more information in Farrar and Worden 2010, Kołakowski 2007, Kralovec and Schagerl 2020). Many SHM methods based on the Non-Destructive Testing (NDT) like the most basic Visual Testing (VT), Ultrasonic Testing (UT), thermography, the Vibration-Based Damage Identification Method (VBA DIMs) and others. Within SHM, numerical simulations as nondestructive testing of the real models of the structures are also carried out. The use of SHM is slowly becoming a standard in modern infrastructure. Therefore, the possibility of application should be considered and included in research works.

It must be mentioned that in connection to historic structures there are problematic issues e.g., related to documentation (sometimes even lack of it), proper conservation, or restoration of this type of facility, which will not be discussed here. Overall, the structural analysis of historic objects requires comprehensive knowledge of the structure that can be obtained by taking measurements in-situ and conducting complicated numerical analyzes.

The section presents examples of analyzes carried out for the historic masonry chimney, which may be useful for the engineering applications and needs of SHM, especially if the monitoring of that structures will be necessary tor the future. Such analysis may be carried out for various structures or structural elements, e.g., light steel structures (lattice, plate, etc.), various types of wooden structures, concrete objects, or masonry structures which are discussed here. The paper describes numerical simulations with the 3D laser scanning process which was used for recognizing structural problems such as damage or geometric irregularities of the masonry chimney (Małyszko, Jemioło, Bilko and Gajewski 2015). The scanning data was analyzed for cracking at higher levels of the chimney, where the direct inspection was difficult to achieve. Next, a real numerical model of the structure was created based on scanning data and the simulations of it were carried out in Finite Element (FE) software.

2. DESCRIPTION OF THE CASE STUDY

The masonry historic chimney which is discussed here is located in Olsztyn, Poland. The chimney was built in the years 1884-1889 from ceramic bricks as a part of The Old Boiler House located in Kortowo - one of the districts of Olsztyn (Figure 2.1a). The total height of the chimney is equal to 40.45 meters. The bottom part is built from a square section, with edges having a length of 4.30 m up to the height of 10.35 m. Higher parts, with a length of 30.1 m, are built as circular sections with the outside diameter diminishing from 2.90 m on the bottom to 2.00 m on the top. The cap of the chimney has an enlarged section. Iron rings, securing from fracture, are located with 0.86 m intervals, and are created from 80×6 mm^2 bar.

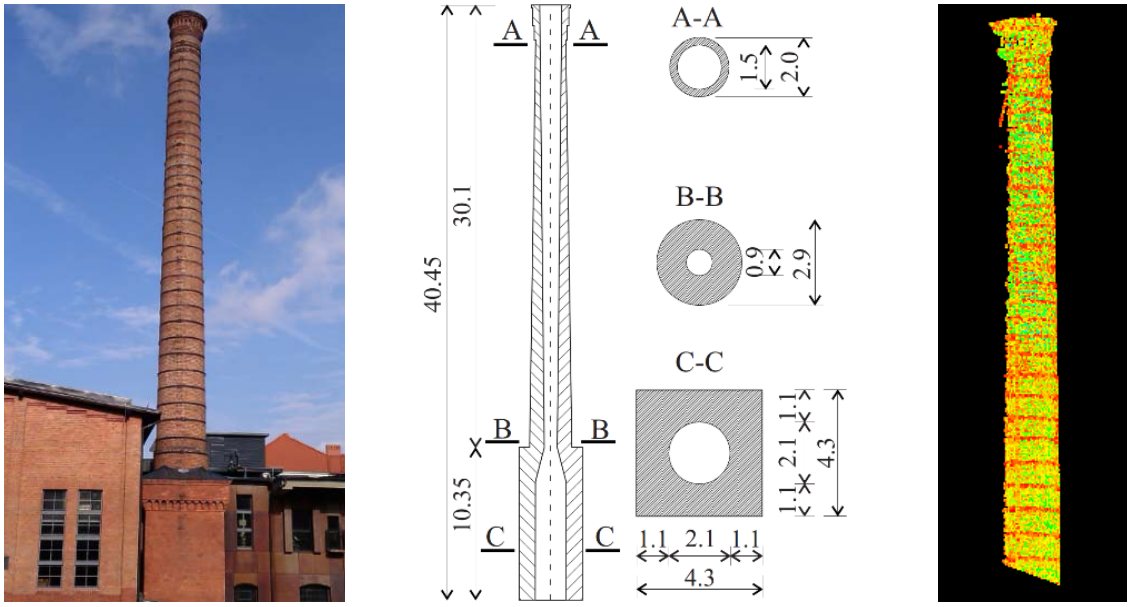

a) b)

Fig. 2.1. The masonry chimney in Olsztyn: a) the real view and the dimensions; b) the point cloud.

A redrawing of the chimney scheme, taken from the University's archives, is presented in Figure 2.1a. In the years 2011-2013, the boiler house with the chimney was renovated and modernized so the technical condition currently is considered as good.

3. USAGE OF LASER SCANNING

The real geometry of the structures can be obtained using non-contact and non-destructive Terrestrial Laser Scanning (TLS). The technology of the TLS allows the creation of a high-accuracy real model, as well as the

detection and localization of defects of the structures especially in hard-to-reach places. The three-dimensional coordinate information of the geometry of the structures, can be also useful for comparison of the changing condition of the construction in subsequent years to assess the needs of SHM. This is especially important in historical structures which must be constantly monitored. In the case of SHM of object deformations, the laser scanning can quickly give the general notion about the displacement tendency of the structure. This is in contrast to traditional geodetic measurements, when results can only give observations of a rare point set, usually restricted to the critical zones, which have to be earlier appointed. Such measurement will provide the precise measure of the deformation and the point cloud will show global trend and possible critical zones (Antón, Pineda, Medjdoub and Iranzo 2019, Riveiro, Morer, Arias and Arteaga 2011).

TLS 3D technology belongs to the modern field-of-view method of a distance measurement, which allows contact-free determination of space coordinates of different complex structures. It allows to gather several thousand points of the point cloud per second and still experiences continuous progress (Riveiro, Morer, Arias and Arteaga 2011). The spatial coordinates of point cloud are defined basing on the measured distance as the time needed to traverse the distance from the laser to the object and back or as the phase shifting. The point data (x, y, z) also includes a reflection intensity value (Fig. 2.1b) and if the scanner has a built-in camera then realistic color information can be mapped to the point cloud data. More complex structures must be scanned from several places. Then these multiple scans from different positions should be transposed into the same reference system. After all the sub-scans are registered, the global point cloud still needs extensive processing to obtain useful information in the special software application (Cyclone 2011). The processing may include noise reduction, resampling, surface modeling, and filling empty holes. The main technical parameters which characterize the scanner are the resolution diameter of the spot scan, the scan rate, the field of view, and the minimum size of the measured increment. The resolution diameter of the spot scan decides the accuracy of the distance measure and precision of the whole 3D model. One ought also to consider attention to the minimum and maximum range scanning, the precision of measured horizontal and vertical angle which influences the accuracy of the measurement. The form of the measuring signal is as well of prime importance. The phase form gives quick and exact instruments with a limited range of the measurement, on the contrary, the impulse form gives slower instruments but with large distant possibilities. Table 3.1. shows technical specifications of the laser scanner used in the measurements.

Table 3.1. Technical specifications of laser scanner used in analysis.

Laser scanning system	
Type	Pulsed; proprietary microchip
Color	Green, wavelength = 532 nm visible
Laser Class	3R (IEC 60825-1)
Range	300 m @ 90%; 134 m @ 18% albedo (min. range 0.1 m)
Scan rate	up to 50 000 points/sec, max. instantaneous rate
Scan resolution: spot size, point spacing	from 0 – 50m: 4.5 m (FWHH); 7 mm (Gaussian) fully selectable horizontal and vertical; 1< mm min. spacing, through full range; single point dwell capacity
Field-of-View: horizontal/vertical aiming/sighting	360° (maximum)/270° (maximum) parallax-free, integrated zoom video

System performance	
Accuracy of single measurement: position/distance, angle (horizontal /vertical)	6 mm/4 mm 60 μrad / 60 μrad (12”/12“)
Modeled surface precision/noise	2 mm

Laser scanning has practical application in many industries (Głowacki, Grzempowski, Sudoł, Wajs and Zając 2017, González-Aguilera, Gomez and Sánchez 2008), mostly in architecture, art preservation, transport infrastructure, gathering dimensions of real, deformed structures for further structural computation (Castellazzi, D'Altri, Miranda and Ubertini 2017, Fekete, Diederichs and Lato 2010) and landslide monitoring (Ossowski, Przyborski and Tysiac 2019).
The advantages of using laser scanning of numerical modeling of the structure are listed below:

– obtaining the real geometry of the structure to create a numerical model for the actual analysis of the real construction,
– the registration of the technical condition of the structure (the real geometry, detection of damages and cracks especially in difficult to reach areas) also for SHM ,
– the possibility to include damaged areas in a numerical model.

Some important and useful additional information about using TLS 3D technology in modelling of masonry structures, which are not described here, can be found in (Rashidi et.al. 2020, Yang, Xu and Neumann 2014).
In the case of the masonry chimney in Olsztyn, only one scan was performed (Figure 3.1a). The resolution of the chimney scan was equal to 1 cm on a 50 m distance, where the horizontal distance from the edge of the object was equal to 25 m.
This scan did not give the whole geometry of the chimney, but it was sufficient to use it to consider the axiality of it. In the point cloud processing software, the circles were fitted in the point cloud on many levels (Figure 3.1a) and further finding the centers of these circles enabled to find the actual axis of the structure (Figure 3.1b). This information was later applied in the real numerical model.

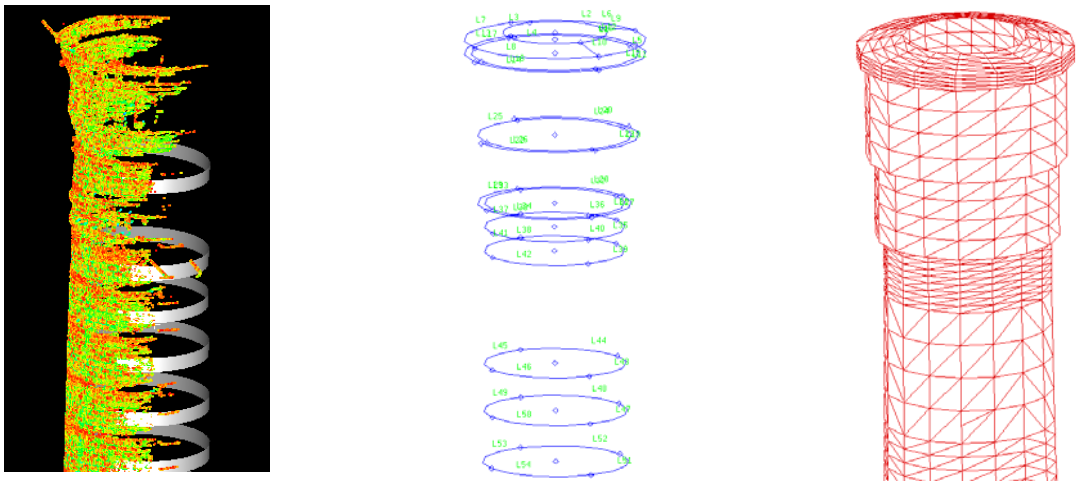

a) b) c)

Fig. 3.1. Geometrical analysis: a) the point cloud; b) geometry preparation; c) the upper part of the FE model.

The point cloud was analyzed for the location of possible cracks. Due to the recent thorough modernization of the chimney, this object has no scratches that were visibly on the registered point cloud. What is more, the scan gave information about external real dimensions and showed geometric irregularities of the chimney. It turned out, that the structure is not vertical, especially in its upper part. The maximum horizontal displacement of the upper part in relation to the base of the chimney trunk was 10 cm, which was included in the preparation of the numerical real model of the structure used in numerical analysis.

4. NUMERICAL ANALYSIS

Numerical simulations of the masonry chimney were performed using the commercial finite element analysis (FEA) software program (DIANA User's manual 2009). The real model is smeared out in a homogeneous continuum and the masonry is considered a homogeneous and isotropic. Material parameters are presented in Table 4.1. The finite element mesh consist of 16 280 eight-node isoparametric solid brick elements with Gaussian integration. Boundary conditions consists of fully pinned nodes creating the bottom, flat surface of the chimney. The upper part of the FE real model of the chimney is presented in Figure 3.1c.

Table 4.1. Technical specifications of laser scanner used in analysis.

Young's modulus [MPa]	Poisson ratio [-]	Mass density [kg/m^3]
7 300	0.18	1 800

Three type of dynamic analyses were performed. First the eigenvalue and eigenfrequency analysis was performed. Secondly, the model was subjected to a base harmonic excitation of acceleration equal to 1m/s^2 in the horizontal direction. The unit base excitation with frequencies from 0 to 10 Hz in steps of 0.1 Hz was applied. The numerical experiment was performed to determine the structural response in the fixed vibration range. The modal superposition analysis was used to solve the equations of motion, assuming the damping at the level of 5% of critical damping. Thirdly, the chimney model was evaluated in the spectral response analysis. The typical earthquake spectrum used in the FEA program was applied (Figure 4.1), where the frequencies f does correspond with load amplification factors SA for the base excitation load. It should be mentioned that this is not a model earthquake spectrum for Olsztyn, but also for the whole country, which is not located in seismic zones.

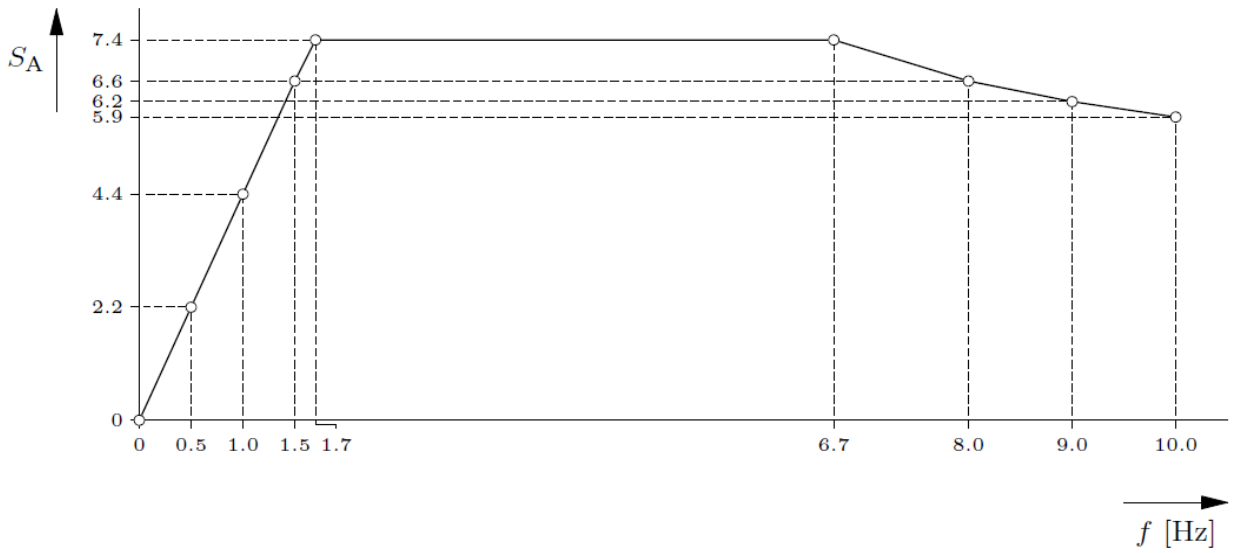

Fig. 4.1. The typical earthquake spectrum used in the selected commercial program.

The first ten eigenfrequencies and eigenmodes were found. The first five ones are presented in Figure 4.2. The presented eigenmodes are of bending type (treating the chimney as cantilever beam), except the fourth one. The maximal frequency, out of the ten found, was equal to 18 Hz, which is typical in this class of objects.

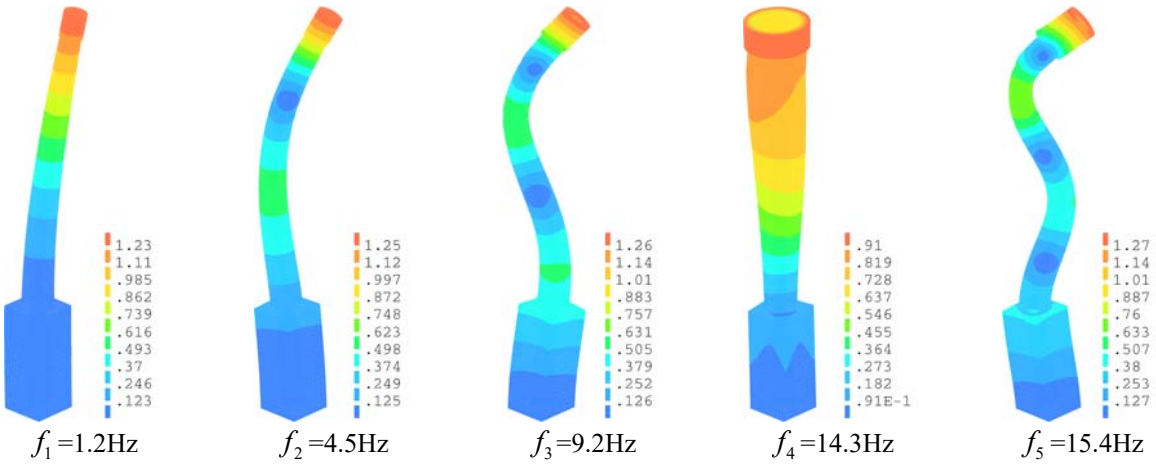

Fig. 4.2. First five numerical eigenfrequencies and eigenmodes of the chimney.

As a result of the harmonic excitation, the amplitudes of displacement, velocity and acceleration of all nodes were determined. Figure 4.3 shows the impact of forcing frequency on horizontal displacement and acceleration of the selected point - node A in the Figure. In the resonance zone of the first vibration frequency, i.e., for an excitation frequency close to 1.2 Hz, a maximum value of the horizontal peak displacement amplitude of 0.35 m was obtained. Other resonance zones are visible, although they are more distinct at the velocity amplitude diagram and in particular at the acceleration amplitude.

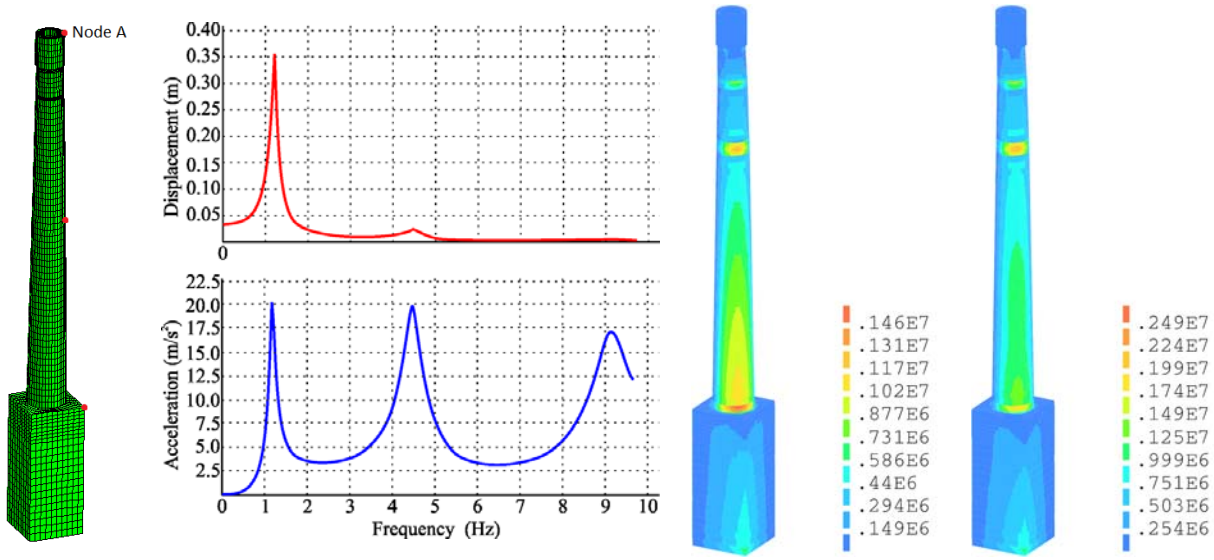

Fig. 4.3. Harmonic excitation results: a) location of selected node A; b) displacement and acceleration of A node in frequency domain; the equivalent stresses response [Pa] according to Huber's strength hypothesis: c) SRSS rule; d) ABS rule.

Figure 4.3c,d shows the equivalent stresses to get an estimate for the damage inflicted by the earthquake on the chimney. The stresses were calculated according to Huber's strength hypothesis using the ABS rule (ABSolute sum) and the SRSS rule (Square Root of the Summed Squares). The maximum peak value of equivalent stress equals 2.0 MPa according to the SRSS method and 5.3 MPa according to the ABS method. The above maps determine the effort of the structure and indicate the places of the possible damage which can be important for structural health monitoring. This enables to perform the numerical simulations of the damage model of the structure to see how the damage affects the dynamic properties, like in paper (Masciotta, Ramos, Lourenco and Vasta 2017). Additionally, it should be mentioned that the determination

of the equivalent stresses response of the masonry chimney according to Huber's strength hypothesis is a very rough estimate, on the grounds that the hypothesis is mainly intended for isotropic materials with the same tensile and compressive strengths. However, a realistic estimate of the effort of the structure was obtained according to the SRSS method.

5. FINAL REMARKS AND CONCLUSIONS

The vibration vulnerability assessment of the masonry chimney was presented as an example of a preliminary solution to a practical technical problem: the assessment of the seismic risk of the real construction based on linear dynamics with isotropic elastic material. As a result of numerical analysis, the areas where stresses are maximum were located. Those areas can be the location for attachment of measuring sensors in case of the necessity to perform periodic or permanent monitoring of the chimney e.g., as a matter of SHM.

Terrestrial laser scanning technique give the possibility to acquire and process data to support 3D geometrical analysis and numerical analysis of any type of structure, in this case masonries, behaviors at different the time span of structures' life-cycle. Laser scanning is a very good complement of sensing techniques like visual inspection which are the primary techniques used for identifying cracks, cavities, or real dimensions and geometric irregularities of the analyzed structures which are recorded in SHM. The collected data as point clouds can be analyzed at any time and what is more, the scans of the inaccessible structure or part of it e.g., because of the height, can be helpful in the analysis of the geometry of this object.

As it was presented in the article, the irregularities in the geometry of the structure, which were recorded on the scan, can be next modeled to create a real numerical model that can be further analyzed. Furthermore due to the accuracy and the possibility of collecting data on the whole geometry of the structure, terrestrial laser scanning can be very helpful especially in periodic monitoring by comparing point clouds recorded at different time epoch. Point clouds related to the same reference system can show changes in the geometry of the analyzed structure, e.g., related to a settlement, an inclination, failures.

REFERENCES

Antón, D. Pineda, P., Medjdoub, B., Iranzo, A. 2019. *As-Built 3D Heritage City Modelling to Support Numerical Structural Analysis: Application to the Assessment of an Archaeological Remain*. Remote Sensing 11:1276.

Castellazzi, G., D'Altri, A.M., de Miranda, S., Ubertini, F. 2017. *An innovative numerical modeling strategy for the structural analysis of historical monumental buildings*. Engineering Structures 132:229-248.

DIANA User's manual, Release 9.3, Published by: TNO DIANA BV, The Netherlands, 2009.

Farrar, C.R., Worden, K. 2010. *An Introduction to Structural Health Monitoring*. In: Deraemaeker A., Worden K. editors, New Trends in Vibration Based Structural Health Monitoring. CISM Courses and Lectures 520. Vienna: Springer.

Fekete, S., Diederichs, M., Lato, M. 2010. *Geotechnical and operational applications for 3-dimensional laser scanning in drill and blast tunnels*. Tunnelling and Underground Space Technology 25: 614-628.

Głowacki, T., Grzempowski, P., Sudoł, E., Wajs, J., Zając, M. 2017. *The assessment of the application of terrestrial laser scanning for measuring the geometrics of cooling towers*. Geomatics, Land management and Landscape 4:49-57.

González-Aguilera, D., Gomez, J., Sánchez, J. 2008. *A New Approach for Structural Monitoring of Large Dams with a Three-Dimensional Laser Scanner*. Sensors 8: 5866-5883.

Kołakowski, P. 2007. *Structural health monitoring - a review with the emphasis on low-frequency methods*. Engineering Transactions 55(3): 239-275.

Kralovec, C., Schagerl, M. 2020. *Review of Structural Health Monitoring Methods Regarding a Multi Sensor Approach for Damage Assessment of Metal and Composite Structures*. Sensors 20(3):826.

Cyclone, L. 7.2 User Guide, Leica Geosystems HDS LLC, 2011.

Małyszko, L., Jemioło, S., Bilko, P., Gajewski, M. 2015. *MES i modelowanie konstytutywne w analizie zniszczenia konstrukcji murowych*. Implementacja i przykłady, tom 2. Olsztyn: Wydawnictwo UWM.

Masciotta, M.G., Ramos, L.F., Lourenco, P.B., Vasta, M. 2017. *Damage identification and seismic vulnerability assessment of a historic masonry chimney*. Annals of geophysics 60(4).

Ossowski, R., Przyborski, M., Tysiac, P. 2019. *Stability Assessment of Coastal Cliffs Incorporating Laser Scanning Technology and a Numerical Analysis*. Remote Sensing 11(16):1951.

Rashidi, M., Mohammadi, M., Kivi, S.S, Abdolvand, M.M, Truong-Hong, L., Samali, B. 2020. *A decade of modern bridge monitoring using Terrestrial Laser Scanning: review and future directions*. Remote Sensing 12(22): 3796.

Riveiro, B., Morer, P., Arias, P., Arteaga, I. 2011. *Terrestrial laser scanning and limit analysis of masonry arch bridge*. Construction and Building Materials 25: 1726-1735.

Yang, H., Xu, X., Neumann, I. 2014. *The benefit of 3D laser scanning technology in the generation and calibration of FEM models for health assessment of concrete structures*. Sensors (Basel) 14(11): 21889-21904.

LIGHTWEIGHT STRUCTURES in CIVIL ENGINEERING
CONTEMPORARY PROBLEMS
Monograph from Scientific Seminar
Organized by Polish Chapters of
International Association for Shell and Spatial Structures
Łódź University of Technology
Faculty of Civil Engineering, Architecture
and Environmental Engineering
XXVII LSCE
Łódź, 2nd – 3rd of December 2021

MODERN SOLUTION OF TUBE TELECOMMUNICATION TOWER – PROBLEMS, ANALYSIS AND PERSPECTIVES

J. Szafran [1] **K. Juszczyk-Andraszyk** [2]
[1] BEng, PhD, DSc, Faculty of Civil Engineering, Architecture and Environmental Engineering,
Lodz University of Technology, POLAND, *jacek.szafran@p.lodz.pl*
[2] PhD, Compact-Project Company, POLAND, *kjuszczyk-andraszyk@compact-project.pl*

ABSTRACT: The paper emphasizes aspects that have to be addressed when analyzing monopole structures, such as vortex excitation occurring due to a repeating pattern of vortex shedding in the flow of air around a tower (von Kármán vortex street). The fatigue analysis is discussed in detail in the paper and it presents solutions that were introduced on the basis of the analysis results in order to reinforce certain areas of the tower (stress concentration in the vicinity of structural details required due to technological reasons).

Keywords: monopol tower, telecommunication tower, vortex excitation, fatigue analysis, 5G network.

1. INTRODUCTION

It is difficult to imagine today's world without high-speed data transmission capabilities at any distance. Billions of Earth's inhabitants use devices designed to make phone calls and send text and graphic messages on a daily basis. As technologies used in mobile devices are advancing, including smartphones and tablets that replace computers in a number of applications, users demand wireless, high-speed and reliable Internet access as standard.

Today we can see the fifth generation networks (5G) grow with increasing number of devices connected to them. Internet of Things (IoT) is a concept of material objects connected with each other and with Internet resources via a powerful computer network, i.e. the Internet. The main goal of the IoT is the creation of smart areas such as smart cities, transport, products, buildings, power systems, health systems or systems related to everyday life. Such a smart area can be developed provided that technologies necessary to implement it have been delivered. Data exchange between all users sets increasingly higher requirements on networks and their operators. The 5G standard is meant to meet these expectations by providing faster Internet connections and enabling many devices to communicate concurrently. One of requirements that have to be satisfied in order for 5G to be properly implemented and operated is building new base stations, and the Polish Ministry of Digital Affairs expects their total number to be 10 to 100 times bigger than in 3G or 4G networks. These new base stations are being built both in open suburban and rural areas and in city centers.

A wide diversity of support structures erected for telecommunications purposes can be found around the world (Smith 2007). The choice of a structure to serve as a support for telecommunications equipment is mostly based on purely technical requirements, but aesthetic reasons are also becoming important particularly for structures located in urban areas. What is essential is that these objects should not stand out

nor require much space and should be relatively fast and simple to build compared to traditional solutions. At the same time the structures need to be safe and durable.
The paper proposes a comprehensive structural solution of a monopole telecommunications tower that ideally meets the above mentioned requirements. Technological solutions and the structural analysis are discussed including issues that were encountered and ways in which these were solved.

2. TOWER STRUCTURE

The structure under consideration is a steel tower solid-wall pole measuring 30.0 m in height (32.53 m including the spire). The structure is made of 4 segments with the three bottom ones having the cross-section in the shape of a regular octadecagon, and the upper one made of a circular hollow section. The middle segments (S-2 and S-3) have a taper and are joined to each other by means of a slip joint connection (a telescopic connection) with an overlap of about 1.5 m. The other segments and the core of the tower with the foundation are joined to each other by means of flanged bolted connections. The entire structure has been designed of S355 steel grade. Table 1 summarizes basic characteristics of the tower segments.

Table 1. Basic characteristics of the tower segments.

Segment	Segment height [m]	Cross sections of core members / wall thickness [mm]	Lower circumcircle/ incircle diameter [m] Upper circumcircle/ incircle diameter [m]	Wall thickness [mm]
S-1 (top)	7.700	RO 245x12	- -	-
S-2	8.044	Regular octadecagon / 5.0	0.971/ 0.956 0.711/ 0.700	5.0
S-3	8.000	Regular octadecagon / 6.0	1.170/ 1.152 0.911/ 0.897	6.0
S-4	7.800	Regular octadecagon / 6.0	1.170/ 1.152 1.170/ 1.152	6.0

Inside the lowest segment of the tower, there is a system of support structures used to mount telecommunication devices serving the BTS. Four ventilated doors are provided to access the equipment in the member. Additional system members (anchoring devices), designed to provide the telescopic connection, are mounted on segments S-2 and S-3.
Support structures (frames and anchoring devices) are mounted on the circular section of segment S-1; by means of these structures, sector antennas (3 pieces) and RRUs are mounted. An antenna beautification cover is provided around the segment along its full height, made of two parts: the lower one 3.74 m in height and the upper one 3.79 m in height, both 1.35 m in their outer diameter.
On the tower top, there is a spire made of circular hollow sections Ø76 mm, Ø60 mm and Ø42 mm, to which a support structure (a frame) for mounting microwave antennas is fixed. The spire is mounted by means of a flanged connection. The view of tower structure is presented on Fig. 1.

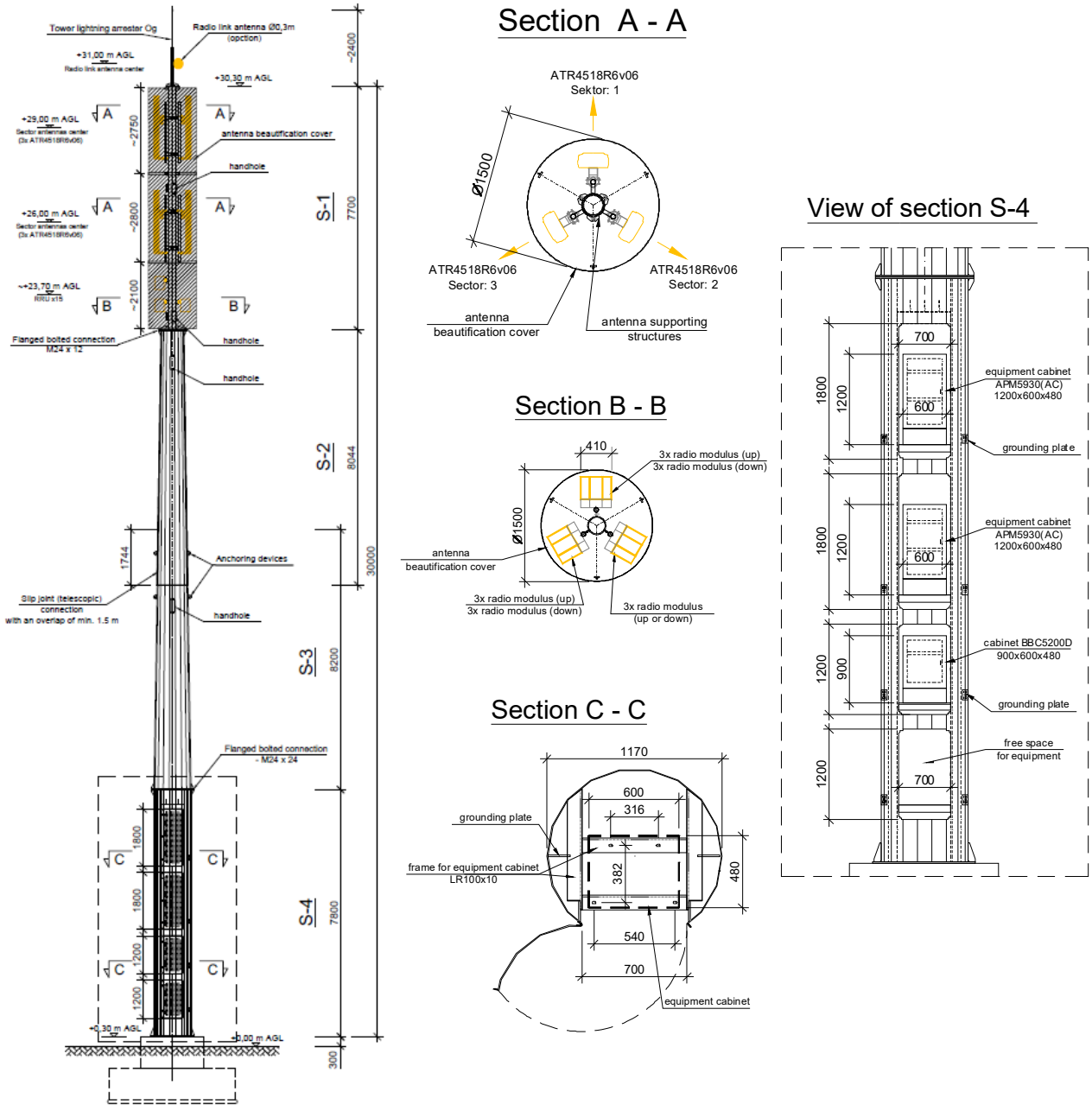

Fig. 1 The view of tower structure, dimensions in mm.

3. STRUCTURAL ANALYSIS

3.1. Alongwind load effects

It was assumed that the structure would be located in wind load zone 1, for which the basic wind velocity pressure is $q_b = 0.3$ kN/m^2, in a terrain corresponding to terrain category II (areas with low vegetation, such as grass, and single obstacles, such as trees and buildings, not less than 20 times their height apart).
Wind load on the tower core was calculated according to PN-EN 1991-1-4. Due to the central symmetry of the core structure cross-section, a single wind load direction was considered in calculations.
The mean wind load on the tower in the wind direction was calculated with the following formula:

$$F_w = c_s c_d \cdot c_f \cdot q_p(z_e) \cdot A_{ref}\,, \tag{3.1}$$

where $c_s c_d$ is structural factor, c_f is total wind force coefficient (for the aerodynamic drag), $q_p(z_e)$ refers to peak velocity pressure and A_{ref} describes reference area.
The aerodynamic drag factor for segments S-2, S-3, and S-4 was determined as for regular polygons (octadecagons) and for segment S-1 as for circular cylinders, whereby geometrical data of a segment cover were taken in calculations.
The structural factor was determined using the following formula:

$$c_s c_d = \frac{1+2\cdot k_p \cdot I_v(z_s)\cdot\sqrt{B^2+R^2}}{1+7\cdot I_v(z_s)}, \tag{3.2}$$

where k_p refers to peak factor defined as the ratio of the maximum value of the fluctuating part of the response to its standard deviation, I_v is turbulence intensity, z_s describes reference height for calculating the structural factor, B^2 is out-of-resonance response factor, allowing for the lack of full correlation of the pressure on the span, and R^2 is resonance response factor, allowing for turbulence in resonance with the vibration mode of the structure.
Wind actions on equipment and support structures were calculated in the same way as the wind force on the tower core, each time considering the height where a given device, or a support structure is mounted.
Aerodynamic drag coefficients for the support structures were calculated as for the core structure dividing structural members into those with sharp edges and those in the shape of a circular cylinder.
The aerodynamic drag coefficient for the telecommunication equipment (the microwave antenna) was taken as $c_f = 1.2$.

3.2. Crosswind action

In addition to the response of the structure to wind loading parallel to wind direction, possible occurrence of vortex excitation, resulting in load fluctuations in the plane perpendicular to wind direction should be considered for structures with a solid-wall circular cross-section. This phenomenon occurs when vortices are shedding in turn from the opposite sides of a structure. Vibrations of the structure can occur if the frequency of vortex shedding matches the eigenfrequency of the structure. This condition is satisfied if wind velocity equals critical wind velocity given by the formula:

$$v_{criti,i} = \frac{b\cdot n_{1,y}}{St}, \tag{3.3}$$

where St is Strouhal number, for circular cross-sections equal to $t = 0.18$, b is a cross-section diameter of a member and $n_{1,y}$ is eigenfrequency of the structure, for towers defined as:

$$n_1 = \frac{46}{h} Hz. \tag{3.4}$$

Vortex excitation should be considered if the ratio of the largest and the smallest measure of a structure in the plane perpendicular to the wind direction is greater than 6; in this case:

$$\frac{h}{b_{\min}} = \frac{30.0m}{0.711m} = 49.2. \tag{3.5}$$

Vortex excitation does not have to be taken into account if:

$$v_{crit,i} > 1.25 \cdot v_m \,. \tag{3.6}$$

In this case:

$$v_{crit,i} = 11.5 \frac{m}{s} \;<\; 1.25 \cdot 26.5 \frac{m}{s} = 33.1 \frac{m}{s}. \tag{3.7}$$

Considering the above, the possible occurrence of vortex excitation should be taken into account for the structure in question.
The effect of vibrations induced by vortex excitation should be calculated based on inertial forces per unit length, exerted in the plane perpendicular to the wind direction at point *s*, according to the formula:

$$F_w(s) = m_e(s) \cdot (2 \cdot \pi \cdot n_{1,y})^2 \cdot \Phi_{i,y}(s) \cdot y_{F,\max} \,, \tag{3.8}$$

where $\Phi_{i,y}(s)$ is the natural mode shape of the structure normalized to unity at the point of maximum displacement, $y_{F,\max}$ is maximum displacement with time of the point at which $\Phi_{i,y}(s)$ equals 1.
Approach 1 (according to PN-EN 1991-1-4, Annex E) was used to determine the amplitude of vibration in the plane perpendicular to the wind direction:

$$\frac{y_{F,\max}}{b} = \frac{1}{St^2} \cdot \frac{1}{Sc} \cdot K \cdot K_w \cdot c_{lat} \,, \tag{3.9}$$

where S_c is Scruton number, equal to:

$$Sc = \frac{2 \cdot \delta_s \cdot m_e}{\rho \cdot b^2} \,, \tag{3.10}$$

K is mode shape factor equal to $K = 0.13$ for cantilevered structures, K_w refers to effective correlation length factor, for cantilevered structures given by the relation:

$$K_w = 3 \cdot \frac{L_1 / b}{\lambda} \cdot \left[1 - \frac{L_1 / b}{\lambda} + \frac{1}{3} \cdot \left(\frac{L_1 / b}{\lambda} \right)^2 \right], K_w \le 0.6 \,, \tag{3.11}$$

L_1 is correlation length for the first mode shape, c_{lat} describe lateral load factor, related to the Reynolds number, for the case considered equal to $c_{lat} = 0.2$.
The amplitude of vibration and the correlation length were determined by means of the iterative method.
The number of loading cycles imposed by vortex-induced vibrations was calculated from the expression:

$$N = 2 \cdot T \cdot n_{1,y} \cdot \varepsilon_0 \cdot \left(\frac{v_{crit}}{v_0} \right)^2 \cdot \exp\left(-\left(\frac{v_{crit}}{v_0} \right)^2 \right) \,, \tag{3.12}$$

where T is design working life of the structure in seconds, ε_0 is bandwidth factor allowing for the range of wind velocities causing vortex-induced vibrations; taken as equal to $\varepsilon_0 = 0.3$, v_0 refers to the modal value of the Weibull probability distribution assumed for the wind velocity in [m/s], multiplied by $\sqrt{2}$, equal to:

$$v_0 = 0.2 \cdot v_m \,. \tag{3.13}$$

3.3. Calculation model

The support structure was modeled using the Autodesk Robot Structural Analysis 2014 software, utilizing the finite element method, as a solid section structure and a shell structure. Six-degree-of-freedom (6DOF) solid section finite elements and triangular and quadrilateral shell finite elements were used. A support fixed in foundations was taken as the structural arrangement in both models.
Wind loads imposed on members were modeled as evenly distributed linear forces, while the load caused by antennas and supports as concentrated forces. In the shell structure model, wind loads were modeled as the surface loading per unit area.
The fatigue analysis was performed based on the calculation model developed in the Consteel 12 software as a shell structure. Shell finite elements in the shape of a triangle of side 100 mm on average were used.
Joints were analyzed with the aid of the IDEA StatiCa 9 software using the finite element method. Internal forces in each member were replaced with the load of a node in a local arrangement of connected rods.

3.4. Analysis of load-carrying capacity

The load-carrying capacity of the support structure for telecommunication equipment was determined according to PN-EN 50341.
Members were considered as solid-wall shell-type poles with a thin-wall cross-section in the shape of an octadecagonal hollow section for which the criterion of limit slenderness for the class 4 cross-section is:

$$\frac{b}{t} > 42\varepsilon\,, \tag{3.14}$$

where b and t are wall length and thickness respectively, ε = square root of 235/f_y and f_y is the nominal value of the yield strength in N/mm^2.
The characteristics of polygonal cross-sections were calculated from the formulas:
- area:

$$A = (d - t)\sin\left(\frac{\pi}{n_k}\right) n_k t\,, \tag{3.15}$$

– moment of inertia:

$$I = \frac{n_k}{192}\tan\left(\frac{\pi}{n_k}\right)\left(3 + \tan\left(\frac{\pi}{n_k}\right)^2\right)\left(d_f^4 - (d_f - 2t)^4\right), \tag{3.16}$$

– elastic section modulus:

$$W_{el} = \frac{I}{\frac{d - t}{2}}, \tag{3.17}$$

where d describes outside diameter across angles of the polygon, n_k refers to number of sides and d_f is diameter at the crown, equals to:

$$d_f = d\cos\left(\frac{\pi}{n_k}\right) - . \tag{3.18}$$

The load-carrying capacity of class 3 polygonal cross-sections, without openings, will be satisfactory if the following condition is met:

$$\frac{N_{Ed}}{A} + \frac{M_{Ed}}{W_{el}} \leq \frac{f_y}{\gamma_{M1}} . \tag{3.19}$$

where N_{Ed} and M_{Ed} are design normal force and bending moment, A and W_{el} are gross cross-section area and elastic section modulus, and γ_{M1} is partial factor for resistance, for S355 steel equal to 1.15.
Tables 2 and 3 below include characteristics of cross-sections, design forces, and verification of the condition of load-carrying capacity at 11 points of the tower.

Table 2. Characteristics and effort of cross-sections 1 to 6.

Cross section		1	2	3	4	5	6
Diameter, [mm]	d	1170	1138	1091	1043	996	948
Thickness, [mm]	t	6	6	6	6	6	6
Wall length, [mm]	b	203.2	197.6	189.5	181.1	173.0	164.6
Number of sides, [-]	n_k	18	18	18	18	18	18
Diameter at the crown, [mm]	d_f	1152.2	1120.7	1074.4	1027.2	980.9	933.6
Gross cross-section, [cm^2]	A	218.3	212.3	203.5	194.5	185.7	176.7
Moment of interia, [cm^4]	I	362128.8	333074.3	293283.5	256053.5	222790.2	191928.1
Elastic section modulus, [cm^3]	W_{el}	6222.1	5884.7	5406.1	4938.4	4500.8	4074.9
Yield strength, [MPa]	f_y	355	355	355	355	355	355
Epsilon, [-]	ε	0.814	0.814	0.814	0.814	0.814	0.814
Cross section class check		3 class	3 class	3 class	3 class	3 class	3 class
Normal force, [kN]	N_{Ed}	74.02	57.77	55.13	52.6	50.19	47.88
Bending moment, [kNm]	M_{Ed}	420.31	222.49	194.81	169.03	145.13	123.07
$N_{Ed}/A + M_{ed}/W_{el,}$ [MPa]		70.94	40.53	38.74	36.93	34.95	32.91
$f_y/\gamma_{MI,}$ [MPa]		308.70	308.70	308.70	308.70	308.70	308.70
Cross-section effort, [%]		23.0%	13.1%	12.6%	12.0%	11.3%	10.7%

Table 3. Characteristics and effort of cross-sections 7 to 11.

Cross section		7	8	9	10	11
Diameter, [mm]	d	901	853	806	758	245
Thickness, [mm]	t	5	5	5	5	12
Wall length, [mm]	b	156.5	148.1	140.0	131.6	42.5
Number of sides, [-]	n_k	18	18	18	18	18
Diameter at the crown, [mm]	d_f	887.3	840.0	793.8	746.5	241.3
Gross cross-section, [cm^2]	A	140.0	132.5	125.2	117.7	87.4
Moment of interia, [cm^4]	I	137638.6	116680.7	98334.1	81693.2	5812.3
Elastic section modulus, [cm^3]	W_{el}	3072.3	2751.9	2455.3	2169.8	498.9
Yield strength, [MPa]	f_y	355	355	355	355	355
Epsilon, [-]	ε	0.814	0.814	0.814	0.814	0.814
Cross section class check		3 class	3 class	3 class	3 class	3 class
Normal force, [kN]	N_{Ed}	45.69	43.62	41.66	37.22	30.63
Bending moment, [kNm]	M_{Ed}	102.8	84.28	67.45	52.24	38.61
$N_{Ed}/A + M_{ed}/W_{el,}$ [MPa]		36.72	33.92	30.80	27.24	80.89
$f_y/\gamma_{M1,}$ [MPa]		308.70	308.70	308.70	308.70	308.70
Cross-section effort, [%]		11.9%	11.0%	10.0%	8.8%	26.2%

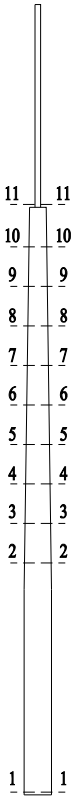

The distribution of stresses reduced according to the Huber hypothesis was checked at the point where the cross-section suddenly changes (Fig. 2) and by the openings (Fig. 3); the distribution was then compared with the yield strength of steel.

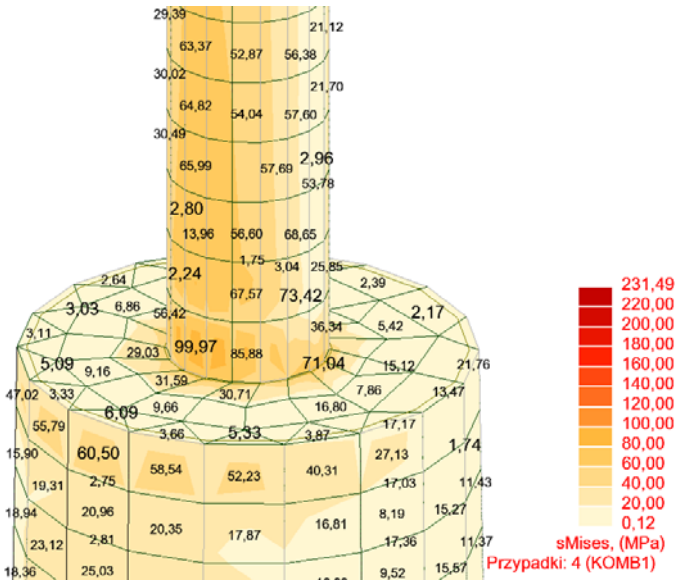

Fig. 2. Distribution of stresses reduced according to the Huber hypothesis at the point where the cross-section suddenly changes

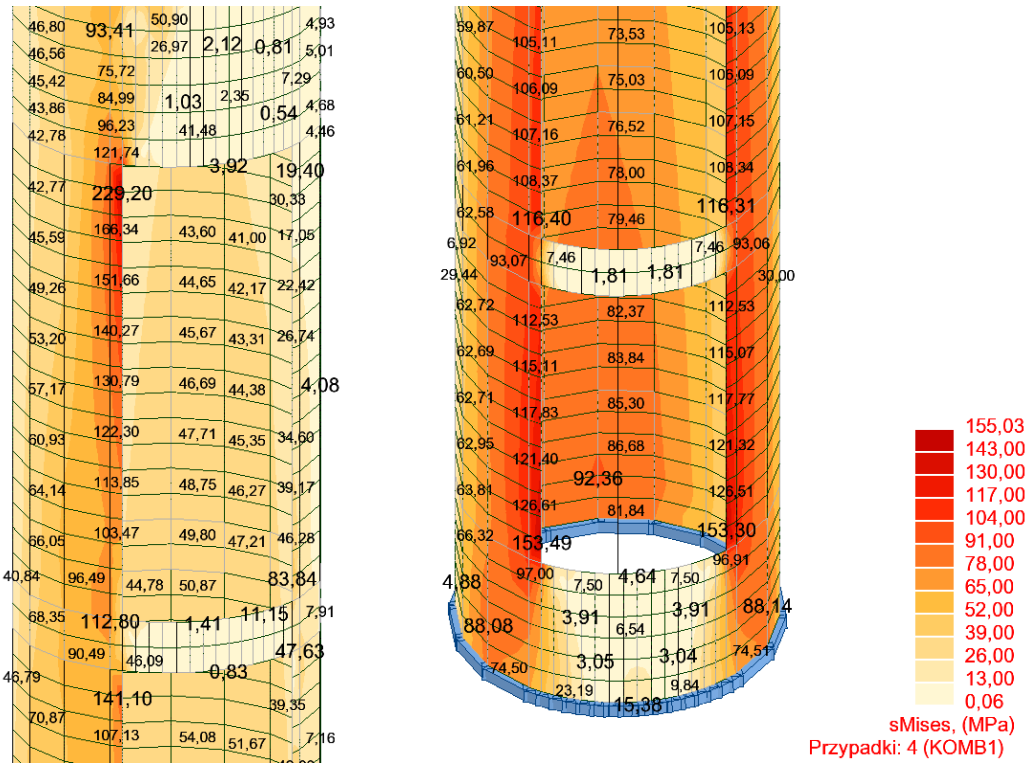

Fig. 3. Distribution of stresses reduced according to the Huber hypothesis by the openings

4. FATIGUE ANALYSIS

Nominal, modified nominal or geometric stress ranges due to frequent loads $\psi_1 Q_k$ should not exceed the following values:

$$\Delta\sigma \le 1.5 \cdot f_y , \tag{4.1}$$

where $\psi_1 = 0.2$ for wind actions.
It also should be demonstrated that for fatigue loading the following load-carrying capacity conditions are satisfied:

$$\frac{\gamma_{Ff} \cdot \Delta\sigma_{E,2}}{\Delta\sigma_C / \gamma_{Mf}} \le 1.0 . \tag{4.2}$$

where γ_{Ff} is partial factor for equivalent constant-amplitude stress ranges, γ_{Ff} = 1.0 (according to PN-EN 1993-3-1), γ_{Mf} is partial factor for fatigue strength, taken as γ_{Mf} = 1.15 for low consequence of failure of a structure assessed using the safe-life method, $\Delta\sigma_c$ is the reference value of the fatigue strength at N = 2 million cycles, $\Delta\sigma_{E,2}$ refers to equivalent constant-amplitude stress range related to 2 million cycles, according to the relation:

$$\Delta\sigma_{E,2} = \lambda \cdot \Delta\sigma_E . \tag{4.3}$$

$\Delta\sigma_E$ is stress range related to N number of cycles, λ is equivalence factor given by the formula:

$$\lambda = \left(\frac{N}{2 \cdot 10^6} \right)^{\frac{1}{m}}, \tag{4.4}$$

where m is slope of the S-N curve for the case considered $m = 5$. For cantilevered structures, areas exposed to maximum fatigue stress ranges include the area of the joint with the foundation. For the structure considered, since the joint was reinforced by stiffening with lateral ribs, maximum stresses will occur in the cross-section above the ribs. The reference value of the fatigue strength for circular hollow sections is $\Delta\sigma_c = 160.0$ MPa. For the least favorable case of fatigue loading (load directions are shown in Fig. 5), the equivalent stress range is equal to $\Delta\sigma_{E,2} = 178.5$ MPa, so:

$$\frac{\gamma_{Ff} \cdot \Delta\sigma_{E,2}}{\Delta\sigma_C / \gamma_{Mf}} = 1.28 \ > \ 1.0, \tag{4.5}$$

thus, the condition is not satisfied.
The solution is to design joint stiffening with larger lateral ribs. Figure 4 shows the differences in equivalent stresses without and with stiffening.

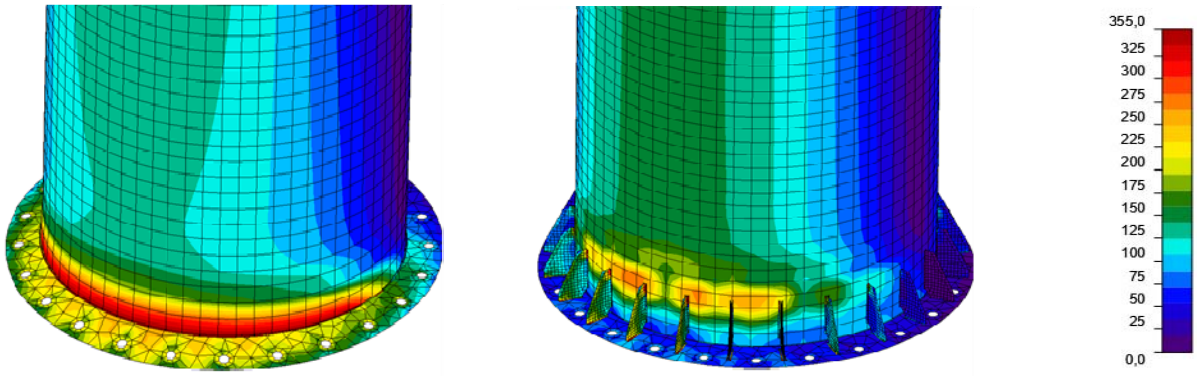

Fig. 4. Equivalent stresses in the tower base, stresses values in MPa.

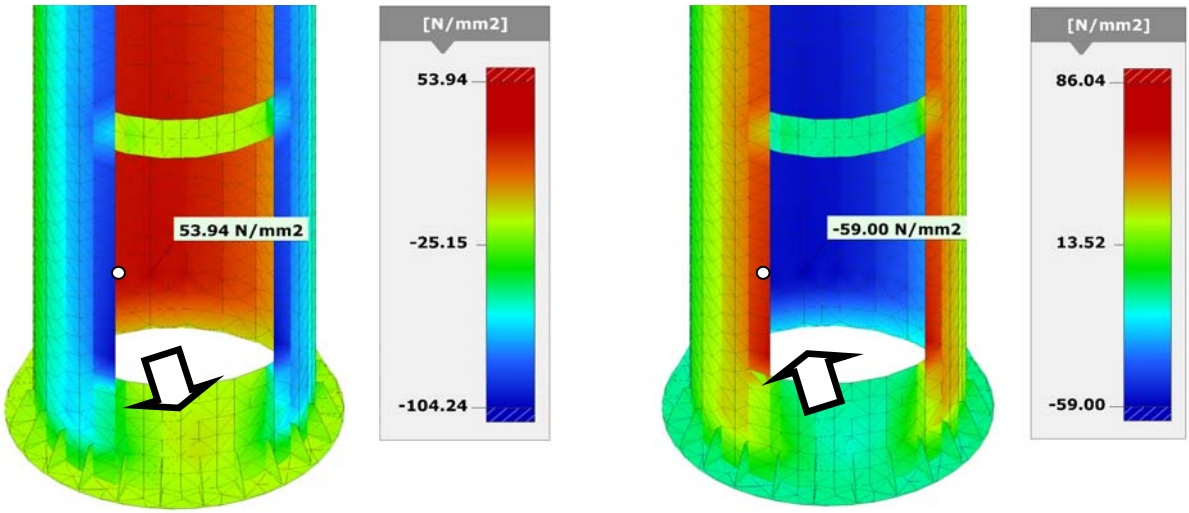

Fig. 5. Stress pattern at the joint with the foundation

4. RESULTS AND CONCLUSIONS

Based on the analyses, the following conclusions can be drawn:

- The analyses indicated that the structural fatigue resulting from potential vortex excitation is crucial for monopole tower structures. Special attention should be paid to the connection between the tower's core and base where high values of stress were observed.
- One aspect that must not be neglected when designing solid-wall structures is technical openings of various types which make the cross-section weaker and should be always accounted for in the structural analysis. In the analyzed structure there is a stress concentration in the vicinity of the opening in segment S-4, providing access to telecommunications equipment serving the base station. To reinforce the edges of the openings in order to reduce stresses, L-sections, welded along the whole length of the segment should be designed on the inner side of the circular hollow section along the edge.
- The load-carrying capacity with respect to fatigue is exceeded by about 30%. To keep the load-carrying capacity, larger stiffening ribs at the joint of the tower core and the foundation should be provided.
- In order to reduce lateral vibrations of the structure caused by vortex excitation, and thus to satisfy the condition of the load-carrying capacity of the structure with respect to fatigue, the system cover of the upper segment of the tower should be equipped with turbulence mixers to disturb the regularity of vortex shedding at the upper part of the structure.
- Vortex excitation will occur only if the system beautification cover is mounted on the upper segment of the tower with antennas and equipment. If the telecommunication equipment is left without the cover, lateral vibrations will not occur and thus all the conditions of the load-carrying capacity of the structure will be met. It should be noted, however, that in this case wind actions on the tower core and the effort of each segment and joint would increase and the aesthetic qualities of the structure would deteriorate.

REFERENCES

Smith, B.W. 2007. *Communication Structures*. Thomas Telford.

Sockel, H. 1994. *Wind-excited vibration of structures*. Wien: Springer-Verlag.

PN-EN 1991-1-4: 2005. Eurocode 1 – Part 1-4: General actions. Wind actions.

PN-EN 1993-3-1. Eurocode 3 – Design od steel structures – Part 3-1: Towers, masts and chimneys – Towers and masts.

PN-EN 50341-1. Overhead electrical lines exceeding AC 1 kV — Part 1: General requirements – Common specifications.

KEYWORDS

AUTOR INDEX